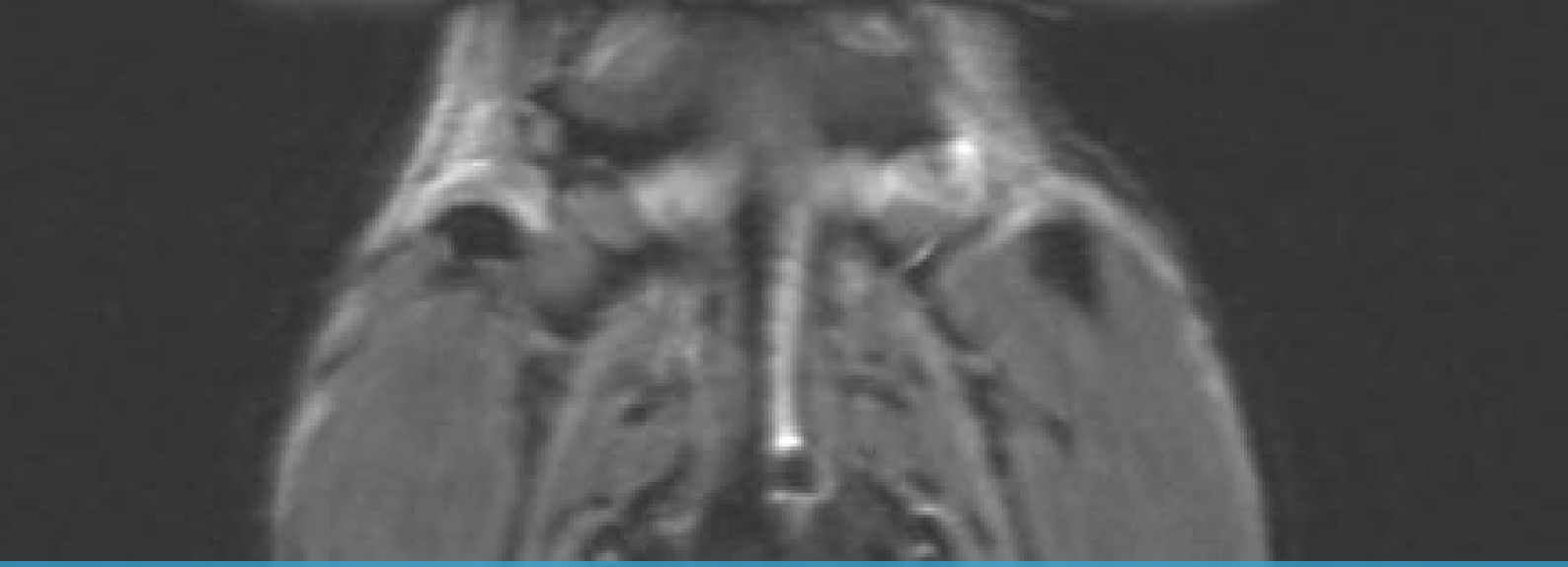

5th Annual Meeting of the ISMRM Iberian Chapter

Barcelona, 3rd - 4th July 2025

ISMRM | Iberian CHAPTER

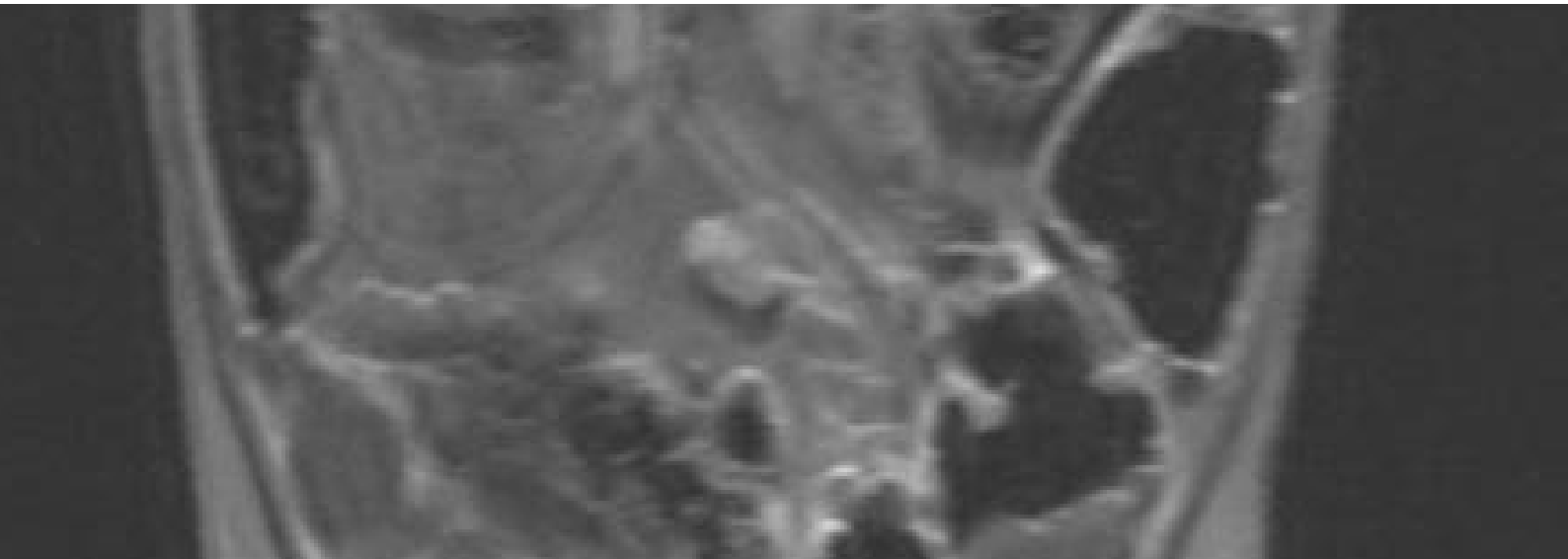

Index

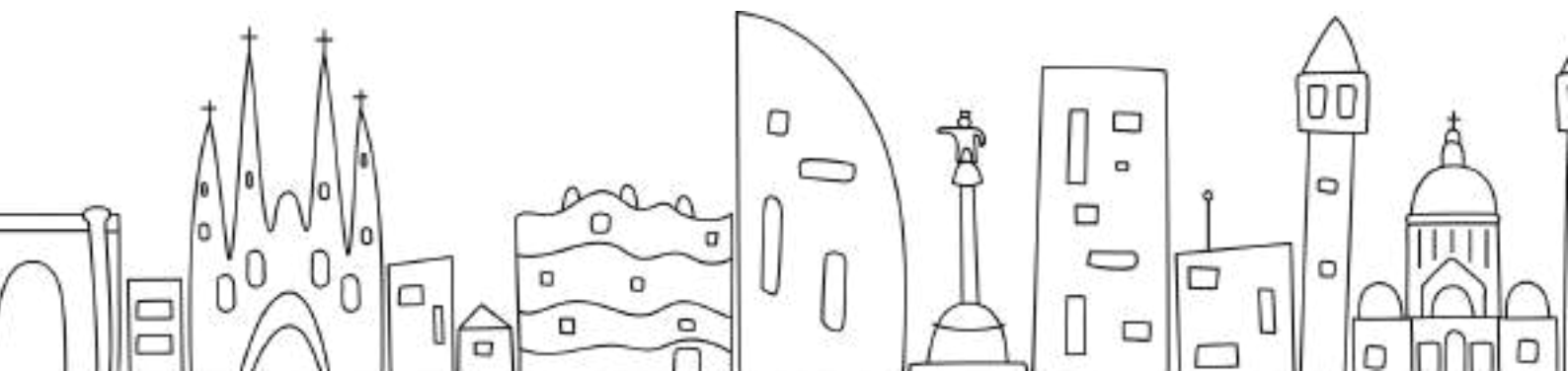

A message from the ISMRM Iberian Chapter

Dear Iberian MR Researchers,

It is with great pleasure that, on behalf of the ISMRM Iberian Chapter Committee, I warmly welcome you to our 5th Annual Chapter Meeting, taking place this year in the beautiful city of Barcelona, hosted at the Institute for Bioengineering of Catalonia. The venue offers not only state-of-the-art facilities but also a vibrant and collaborative atmosphere that perfectly embodies the spirit of our community.

This year's meeting promises to deliver an outstanding scientific program, enriched by insightful presentations, dynamic discussions, and ample opportunities for networking and collaboration. We are confident that these three days will inspire new ideas, foster connections, and contribute meaningfully to the advancement of MR research. Hosting the meeting in one of Europe's most culturally rich and stimulating cities is an added privilege we are excited to share with you.

I would like to extend my sincere gratitude to the local organizing committee, led by Irene Marco Rius, for their exceptional dedication and hard work in preparing this congress. Their careful selection of speakers and meticulous planning have been crucial in shaping what we expect to be a memorable and successful event. Thanks to their efforts, we can look forward to three days filled with scientific exchange, technical innovation, and, of course, some well-deserved enjoyment in the wonderful city of Barcelona.

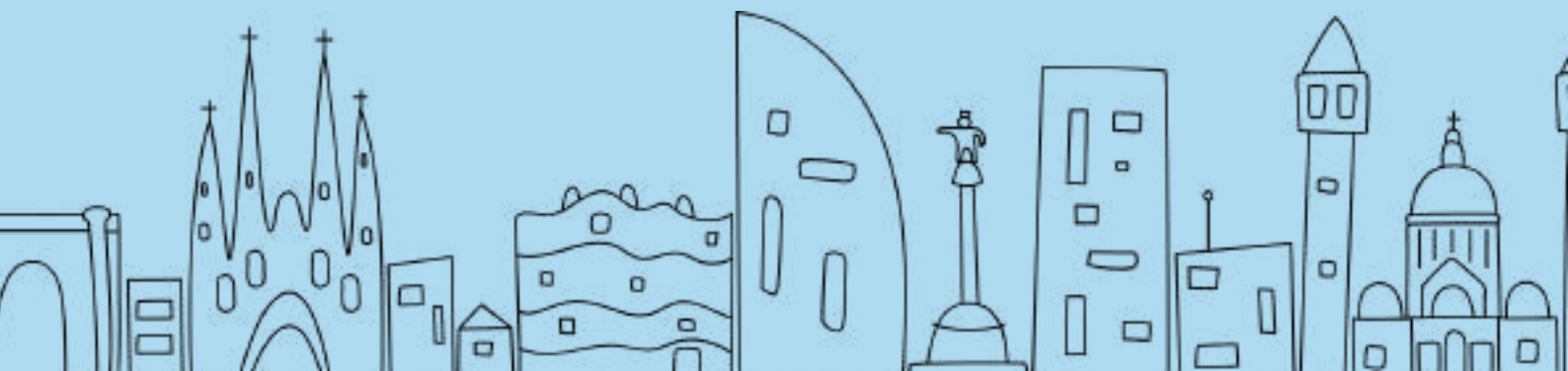

I also want to take this opportunity to thank each of you for your continued support and active engagement with the Chapter. It is thanks to your commitment, enthusiasm, and contributions that our community remains vibrant, dynamic, and ever-growing. Your involvement is the driving force behind the success of this Chapter and the progress of MR research in the Iberian Peninsula.

We look forward to connecting with you in person in Barcelona, to sharing knowledge, exchanging ideas, and working together to advance the field of MR.

Warm regards,

Silvia De Santis
Chair of the ISMRM Iberian Chapter Committee

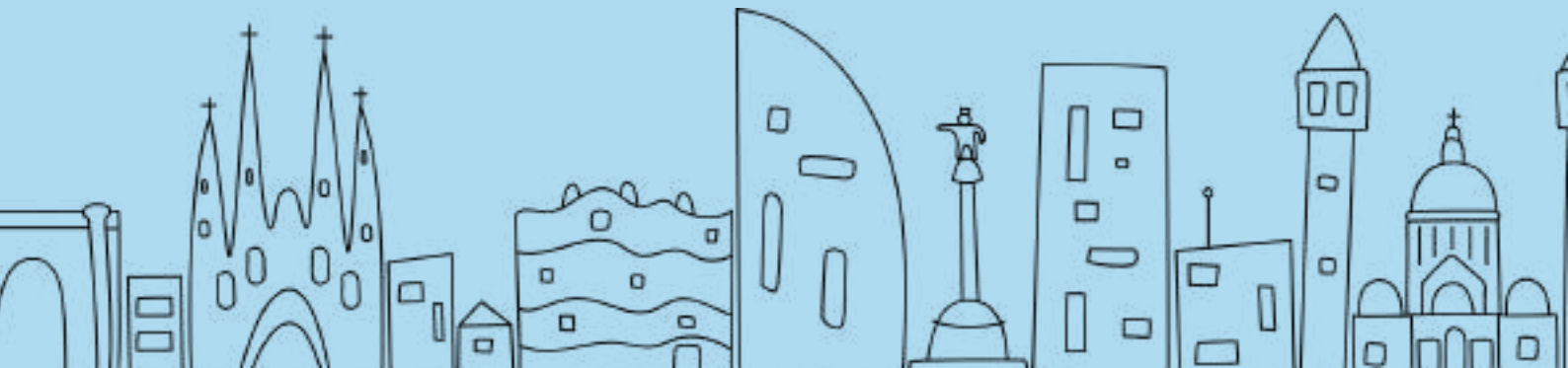

Welcome

Welcome to the 5th Annual Meeting of the ISMRM Iberian Chapter in Barcelona!

As Program Chair of the 2025 Annual Meeting, I am delighted to welcome you to the dynamic and inspiring city of Barcelona on June 3-4.

Barcelona is a city that embraces both the past and the future, where centuries-old architecture coexists with cutting-edge scientific research. Nestled between the sea and the mountains, its streets are alive with creativity, exploration and a spirit of collaboration. It is only fitting that our meeting is hosted at the Parc Científic de Barcelona (PCB), a hub where pioneering research meets entrepreneurial vision, and where science and innovation thrive side by side.

Once again, this year's meeting brings our community together around a shared mission: to push the boundaries of magnetic resonance imaging and spectroscopy, bridging the gap between fundamental research and clinical application. The program is structured to provide a comprehensive journey through the field, from foundational concepts to cutting-edge innovations.

The meeting will open with a pre-meeting educational workshop, offering a deep dive into the fundamentals of MRI theory, advanced fast imaging methods (including fMRI and diffusion MRI) and the latest developments in quantitative imaging and AI automation. This session will culminate in a hands-on workshop using IBEC's preclinical 3T MRI scanner, providing participants with a unique opportunity to connect theory with practice.

Over the following two days, the program will feature a diverse and stimulating mix of plenary lectures, oral and poster sessions, industry pitches and ample networking opportunities. The plenary talks will highlight trustworthy AI for brain MRI analysis, dynamic assessment of cancer metabolism through multi-nuclear MRI, and the latest breakthroughs in preclinical molecular imaging.

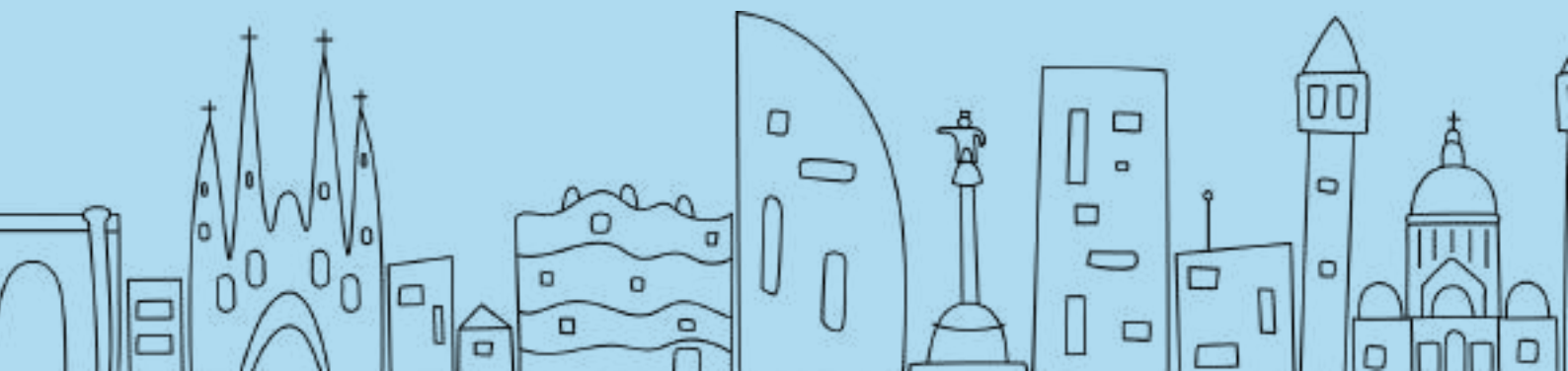

These sessions will set the stage for focused discussions on both clinical and preclinical applications, showcasing how emerging technologies are reshaping the landscape of MRI and MR.

The poster teasers and industry pitches will further amplify the meeting's dynamic atmosphere, providing a platform for sharing innovative ideas, new methodologies, and technological advances from our vibrant community. Designed to spark discussion, stimulate collaboration, and inspire new approaches, this program promises to be both informative and transformative.

But this meeting is not just about science. It's also a space for networking and collaboration. We invite you to meet someone new at each coffee break and to join us for the networking event, where you can relax, exchange ideas and enjoy the flavors of Catalonia. As always, take the opportunity to explore the city's renowned cultural heritage, from the artistic wonders of Gaudí to the lively neighborhoods and Mediterranean shores.

The 5th Annual Meeting of the ISMRM Iberian Chapter promises to be a celebration of scientific excellence, innovation and community spirit. I look forward to sharing these days of discovery and connection with all of you in Barcelona.
See you at the conference!

Irene Marco Rius
Program Chair of the 5th Annual Meeting of the ISMRM Iberian Chapter

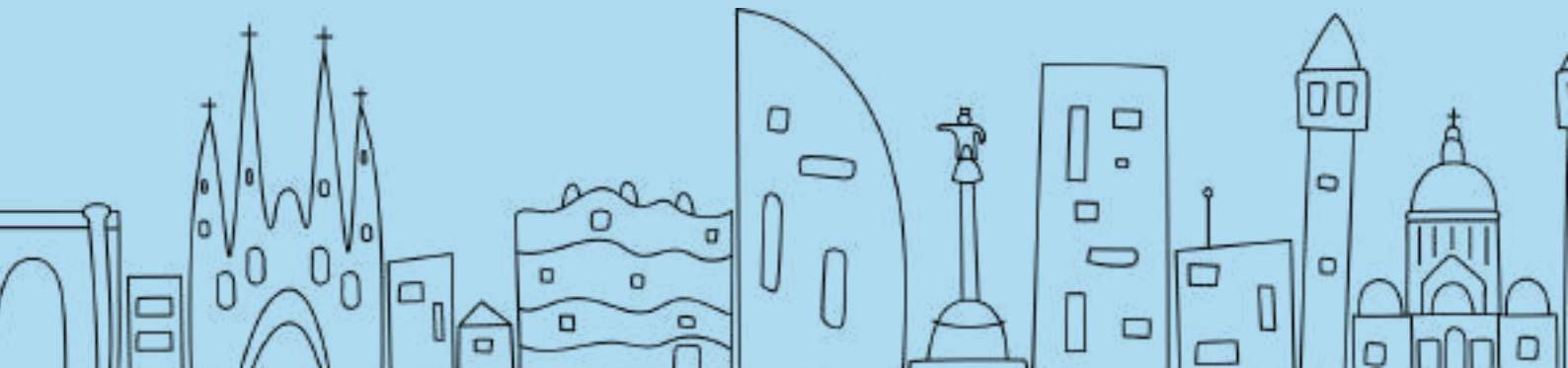

Get to know Barcelona

Barcelona welcomes you with open arms, a vibrant city where millenary history meets the most creative modernity. Located between the Mediterranean Sea and the hills of Collserola, this Catalan jewel invites you to discover its unmistakable identity, its unique architecture, its delicious gastronomy and its welcoming spirit.

From the majestic works of Antoni Gaudí, such as the iconic Sagrada Familia or the colorful Park Güell, to the lively streets of the Gothic Quarter, every corner of Barcelona tells a story. Strolling along Las Ramblas, enjoying an afternoon on the Barceloneta beach or getting lost among the boutiques and tapas bars of El Born is just the beginning.

This city seduces not only for its beauty, but also for its cosmopolitan soul. Here, tradition and innovation coexist in perfect harmony. Whether you come for culture, leisure, business or simply for pleasure, Barcelona has something for everyone.

Welcome to an unforgettable experience! Welcome to Barcelona!

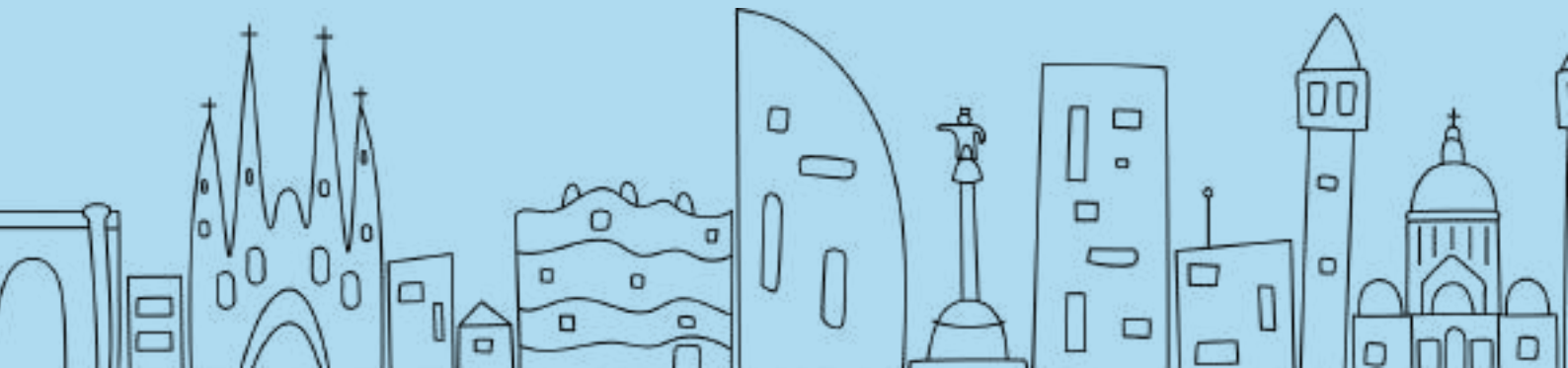

Organization

Iberian Chapter Executive Committee

Silvia De Santis (UMH)
Andrada Ianus (KCL)
Margarida Julià-Sapé (UAB)
José Ángel Pineda-Pardo (HM CINAC)
Gabriel Ramos Llorden (HMS)
Verónica Aramendia (UN)
Irene Guadilla (UVa)
Raquel González Alday (IIBM)
Irene Marco Rius (IBEC)

Local Organizing Committee

Irene Marco Rius (IBEC)
Maria Alejandra Ortega Machuca (IBEC)
Ana Paula Candiota (UAB)
Margarida Julià-Sapé (UAB)
Emma Muñoz Moreno (IDIBAPS)
Silvia Lope-Piedrafita (UAB)
Ignasi Barba Vert (VHIO)
Marina Benito (UCM)
Francesco Grussu (VHIO)
David Gómez Cabeza (IBEC)

Scientific Committee

Irene Marco Rius (IBEC)
Maria Alejandra Ortega Machuca (IBEC)
Ana Paula Candiota (UAB)
Margarida Julià-Sapé (UAB)
Emma Muñoz Moreno (IDIBAPS)
Silvia Lope-Piedrafita (UAB)
Ignasi Barba Vert (VHIO)
Marina Benito (UCM)
Francesco Grussu (VHIO)
David Gómez Cabeza (IBEC)
Silvia de Santis (UMH)
Andrada Ianus (KCL)
Irene Guadilla (UVA)

Web design, Artwork & Booklet

Eider Vidal (IBEC)

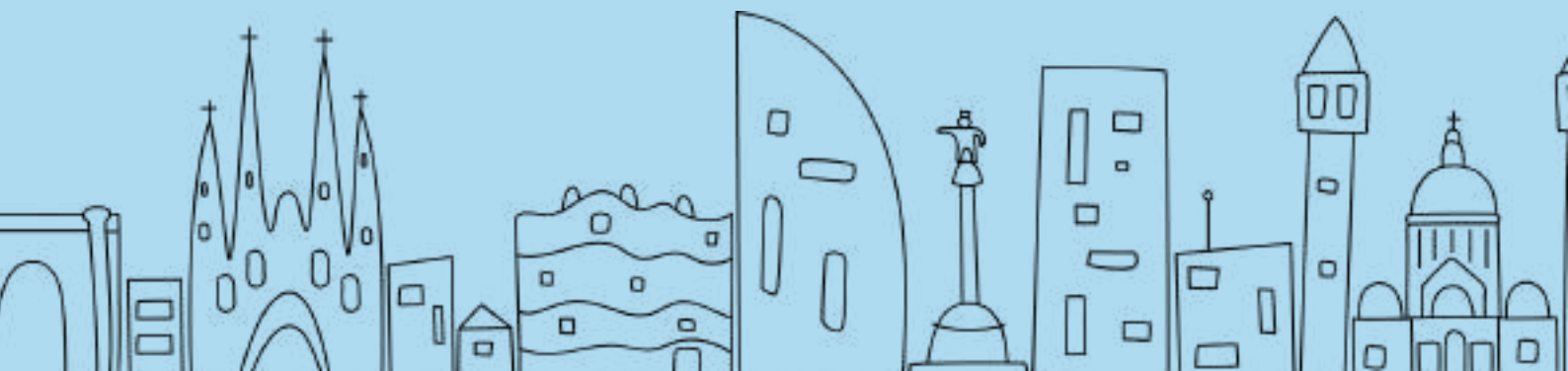

The Reviewers

Andrada Ianus
Nuria Arias Ramos
Ana Paula Candiota
Jesús Pacheco Torres
Marta Vidorreta
Irene Guadilla
Álvaro Planchuelo-Gómez
José Vitor Oliveira Sereno
Marta Correira
Hugo Alexandre Ferreira
Marina Benito Vicente
Carlos Macarro
Teresa Matias Correia
César Caballero Gaudes
Noam Shemesh
Sónia Isabel Gonçalves
Angel Torrado-Carvajal
Tiago Fernandes
M.Carmen Martínez-Bisbal
Elisa Moya-Sáez
Emma Muñoz-Moreno
Francesco Grussu
Ramón Iglesias Rey
Gina Caetano
Diego Hernando
Margarida Julià Sapé
Rui Simões
Gulnur Ungan
Manuel Blesa Cabez
David Gomez-Cabeza
Rita G Nunes
Athanasios Grigoriou
Catarina Passarinho
Alonso Garcia Ruiz
Davide Emanuel Rodrigues Freitas
Susana Merino-Caviedes
João Duarte
Anna Voronova
Miguel López Aguirre
Ricardo Corredor Jerez
Silvia Lope Piedrafita
Verónica Aramendía-Vidaurreta

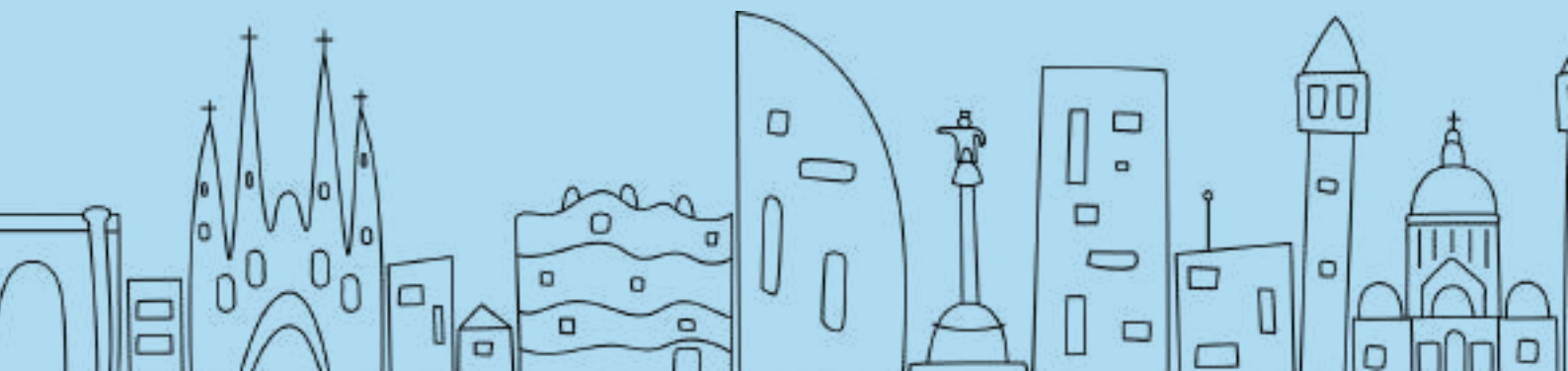

Venue

IBEC Institute for Bioengineering of Catalonia, Barcelona
C/ Baldiri Reixac 10-12
08028 Barcelona

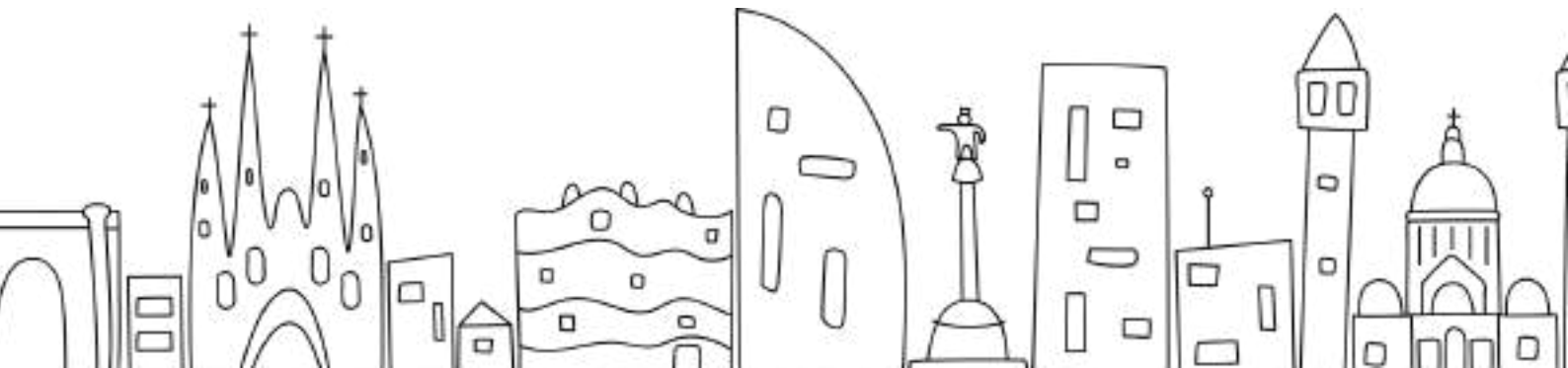

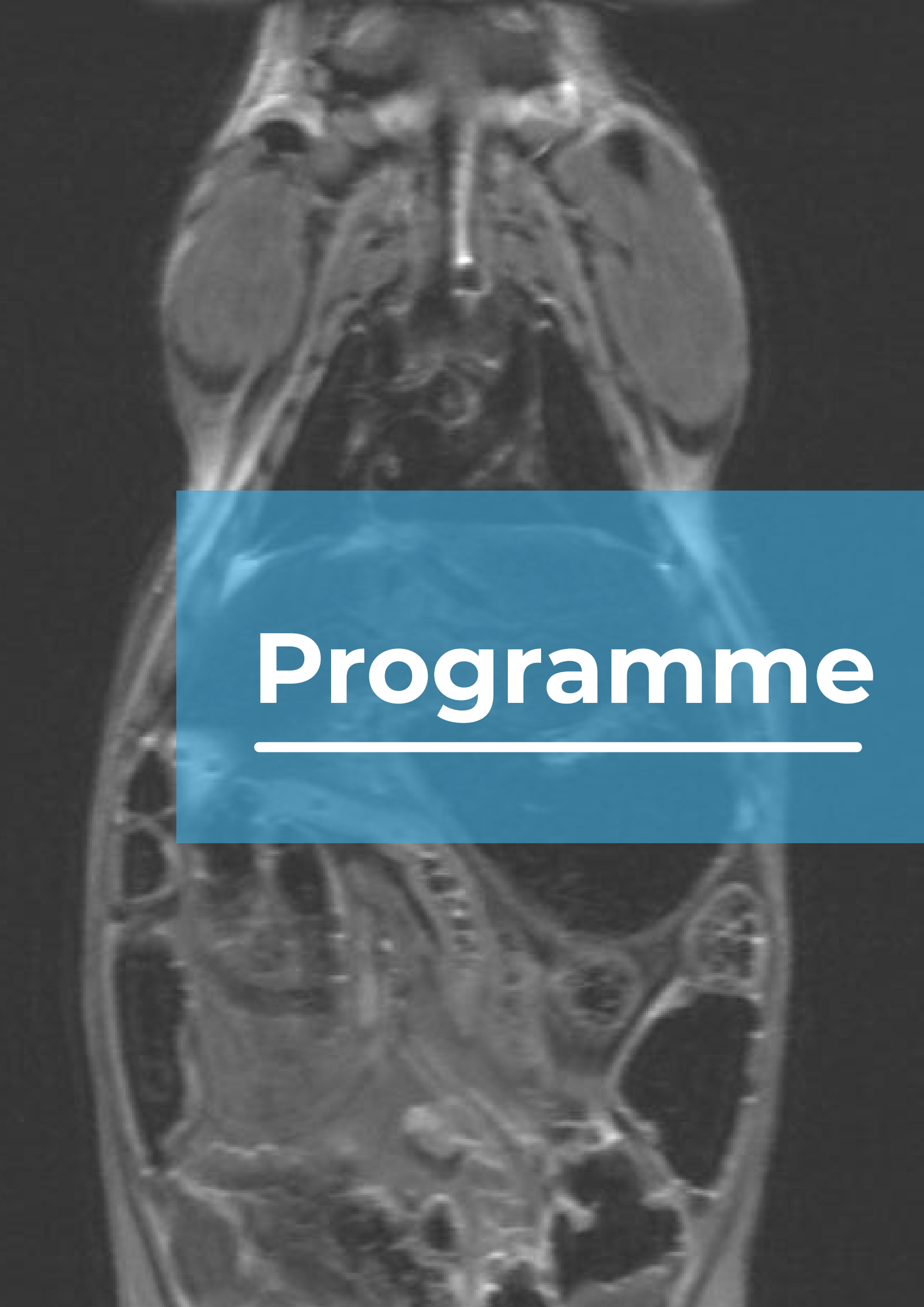

Programme

Workshop - 2nd July

5th Annual Meeting of the ISMRM Iberian Chapter

Moderator: David Gómez Cabeza

13.00h	MRI Basics (Theory and Acquisition) Speaker: Marina Benito – UCM
13.50h	MRI Fast Imaging (Functional MRI and diffusion MRI) Speaker: Andrada Ianus (King's College London)
14.40h	Coffee Break
15.10h	MRI QUIZ! Speaker: David Gómez Cabeza (IBEC)
15.40h	Quantitative Imaging and AI Automation Speaker: Francesco Grussu (VHIO)
16.30h	MRI Basics Worksop in IBEC's 3T Bruker RMI Practical Session – Sponsored by IBEC Speaker: David Gomez Cabeza – (IBEC)

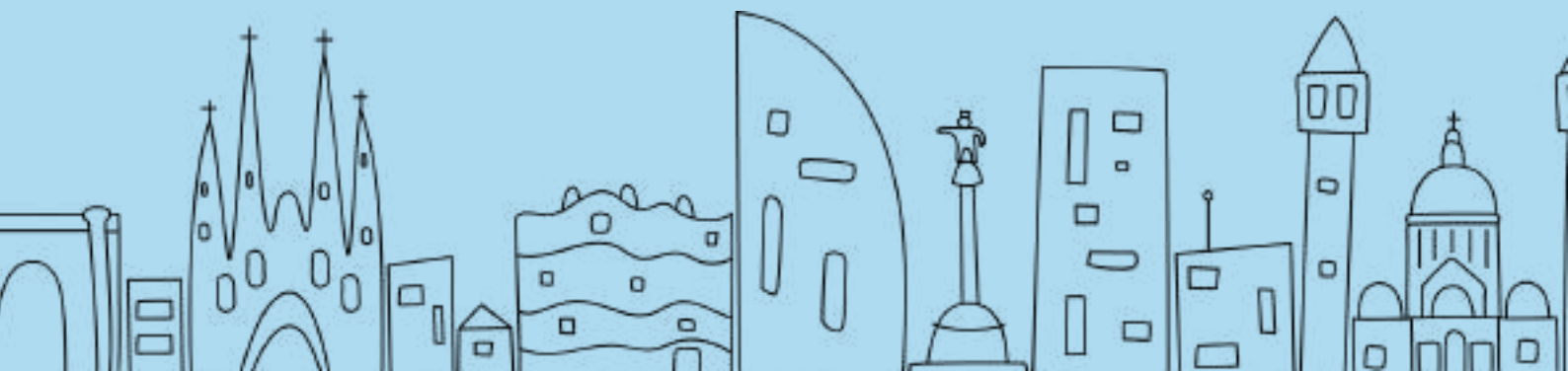

3rd July

5th Annual Meeting of the ISMRM Iberian Chapter

10.00h Registration

11.00h **Opening session:** Silvia De Santis (Instituto de Neurociencias de Alicante) and Irene Marco Rius (IBEC). “Introduction and welcome from the Chapter and Local committees”

11.30h **Plenary Talk:** Meritxell Bach (EPFL, Switzerland). “Beyond performance: trustworthy AI in brain MR image analysis through quality control and uncertainty quantification”
Moderator: Andrada Ianus and Ana Fauto

12.30h **Industry Pitches** – *Moderator: Ana Paula Candiota*

- 12:30-12:50: Platinum sponsor. MRSolutions, “Advances on MRI technology for the Iberian chapter community” (20 min)
- 12:50-13:00: Gold sponsor. ParaLab, “Advances on MRI technology for the Iberian chapter community” (10 min)

13.00h Lunch

14.00h **Oral Session (Clinical Session)** – 8 min presentation + 2 min Q&A.
Moderator: Francesco Grussu and Athanasios Grigoriou

- Teresa Matías Correia – Fully Automated Deep Learning and Radiomics Pipeline for Assessing Myocardial Infarction and Microvascular Obstruction – Quantitative Bio-Imaging Lab, CCMAR, Faro, Portugal
- Pablo García Cristobal – Neuroimaging with an elliptical bore portable MRI designed for neuromodulation with focused ultrasound.- Institute for Molecular Instrumentation and Imaging (i3M)

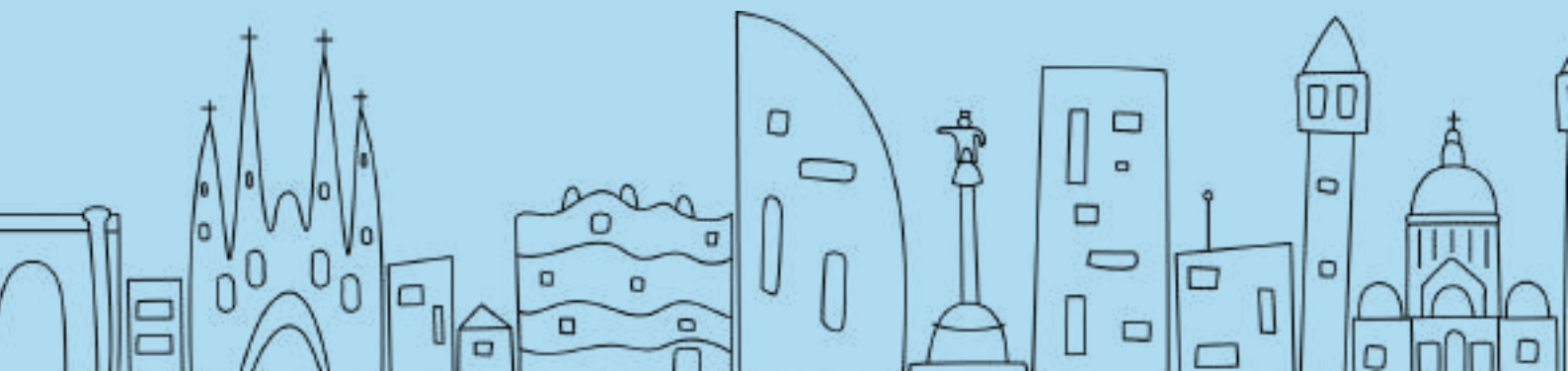

3rd July

5th Annual Meeting of the ISMRM Iberian Chapter

- Elias José Faro Gomez – Enhancing Hypoxic-Ischemic Encephalopathy Classification through Region-Specific Brain MRI Segmentation – Universidad Politécnica de Madrid
- Tomasz Pieciak – Synthesizing realistic diffusion-weighted MR data for machine learning – Universidad de Valladolid
- Verónica Aramendía Vidaurreta – Motion Correction Strategies in Renal Arterial Spin Labeling Perfusion: Qualitative and Quantitative Performance Evaluation – Clínica Universidad de Navarra
- Catarina Passarinho – Transfer Learning for cross-dataset brain tumor segmentation in post-operative MRI – Instituto Superior Técnico

15.00h **Poster Teaser Clinical MRI** (1 slide – 1min).
Moderator: Ignasi Barba and Elisa Moya-Sáez

15.45h Coffee break + **Poster Session Clinical**

20.00h Dinner at “La Pomarada”

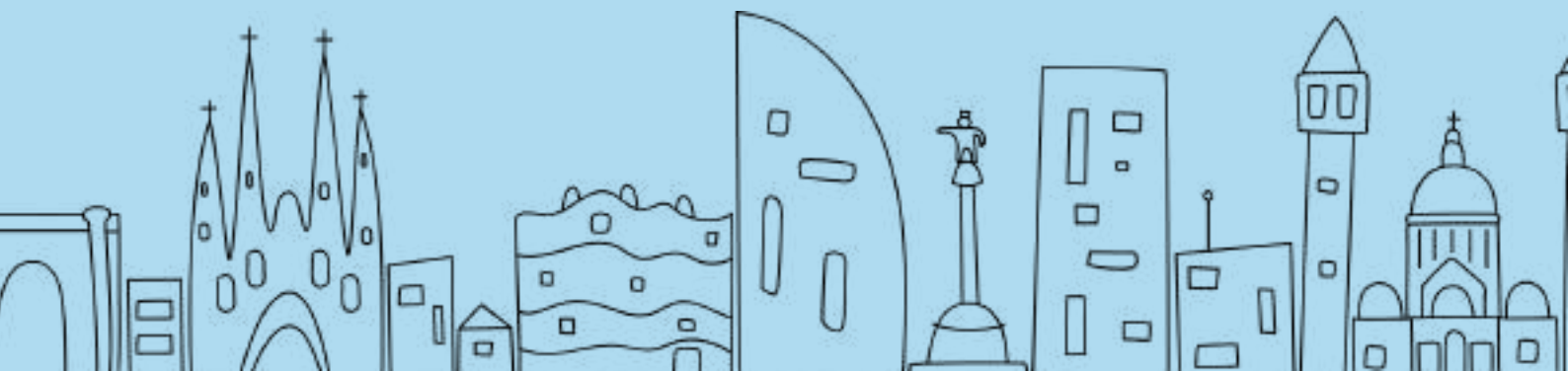

4th July

5th Annual Meeting of the ISMRM Iberian Chapter

09.00h **Plenary Talk** (Sebastián Cerdán Lecture): Rui V Simões (Universidade do Porto, Portugal) – Dynamic Assessment of cancer metabolism with multi-nuclear MRI
Moderator: Silvia Lope Piedrafita and Nuria Arias Ramos

10.00h **Oral Session -Preclinical Session** (8min presentation + 2 min Q&A)
Moderator: Irene Guadilla and Raquel González-Alday

- Silvia Lope Piedrafita – Applying longitudinal MRI for tumor evaluation in two immunocompetent chicken chorioallantoic membrane (CAM) cancer xenograft models- Universitat Autònoma de Barcelona
- Pilar Sango Solanas – Methodological development of MR Elastography for liver fibrosis in a murine animal model – CREATIS, Université de Lyon
- Rafael Neto Henriques – Correlation Tensor Imaging at 3T for In Vivo Mouse Brain Imaging – Champalimaud Research, Champalimaud Foundation
- Elena Espinós-Soler – Sexual dimorphism in aging trajectories as measured through resting state functional connectivity and diffusion-weighted MRI – Instituto de Neurociencias de Alicante, UMH-CSIC
- David Gómez Cabeza – Hyperpolarisation-enhanced MRSI for Metabolic Imaging in Organ-on-a-Chip Devices – Institute for Bioengineering of Catalonia (IBEC)
- Gerard Martí Juan – Fetpype: An Open-Source pipeline for reproducible Fetal Brain MRI Analysis – Universitat Pompeu Fabra (UPF)

11.00h Coffee break

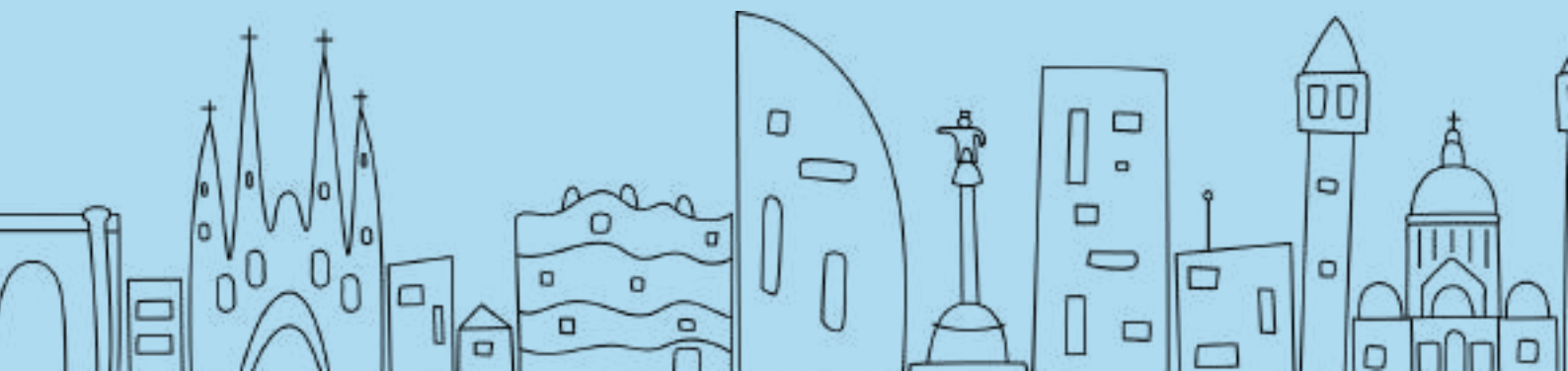

4th July

5th Annual Meeting of the ISMRM Iberian Chapter

11.45h **Industry Pitches**
Moderator: David Gomez Cabeza

- 11:45-11:55: Gold sponsor. NVision,"Simplifying In Vivo Metabolic Imaging: Robust and easy-to-use Hyperpolarization" (10 min)
- 11:55-12:00: Silver sponsor. Bruker, "Advances on MRI technology for the Iberian chapter community" (5min)

12.00h **Plenary Talk:** André Martins (Universitat Tubingen, Germany) – Latest Advances in Preclinical Molecular Imaging
Moderator: Marina Benito Vicente and Lili Fanni Toth

13.00h Lunch

14.30h **Poster Teaser PreClinical MRI**
Moderator: Emma Muñoz and Margarida Alves
27 power pitches

15.15h Coffee Break **– Poster Session – PreClinical**

16.30h **Round Table Discussion:** "Bringing advanced MRI and MRS from research to clinic".
Moderator: Irene Marco-Rius & Silvia De Santis.
Panel: Meritxell Bach-Cuadra, Rui V Simões, André F. Martins

17.30h **Closing session**

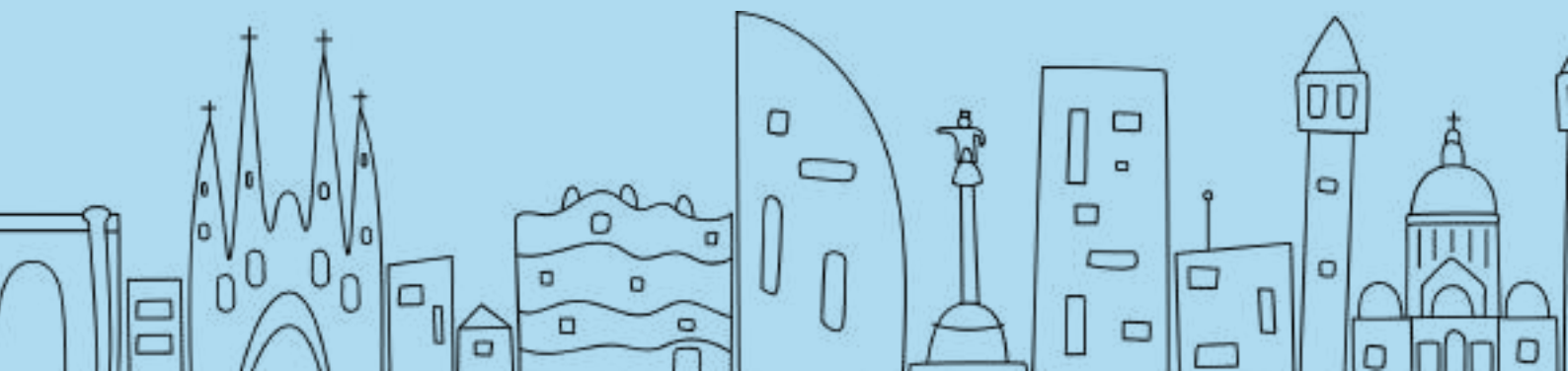

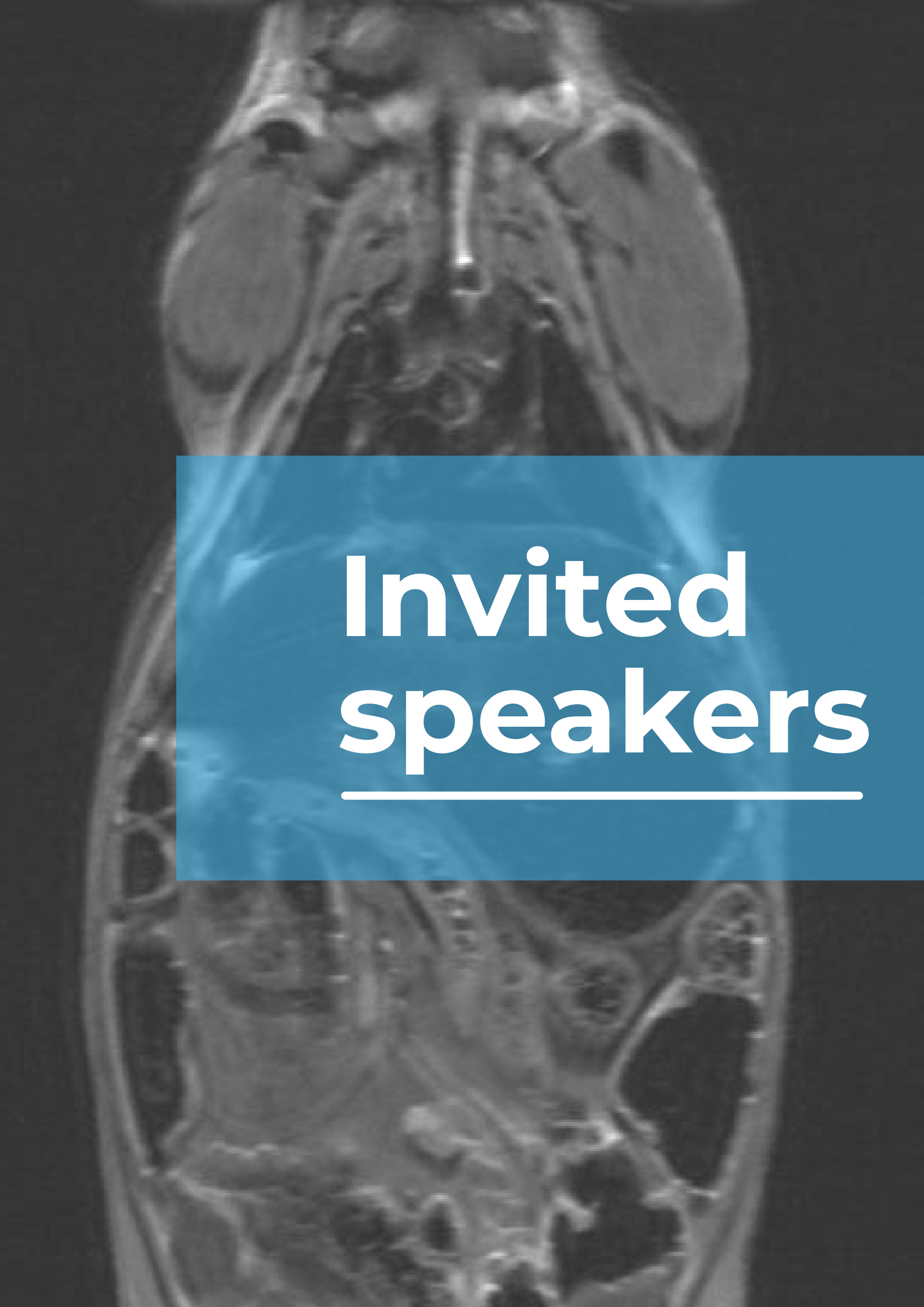

Invited speakers

INVITED SPEAKER

MERITXELL BACH

Center for Biomedical Imaging

Beyond performance: trustworthy AI in brain MR image analysis through quality control and uncertainty quantification

INVITED SPEAKER

RUI VASCO SIMÕES

Institute for Research and Innovation in Health

Dynamic Assessment of cancer metabolism with multi-nuclear MRI

INVITED SPEAKER

ANDRÉ F. MARTINS

University Hospital Tübingen

Latest Advances in Preclinical Molecular Imaging
Moderator: Marina Benito Vicente

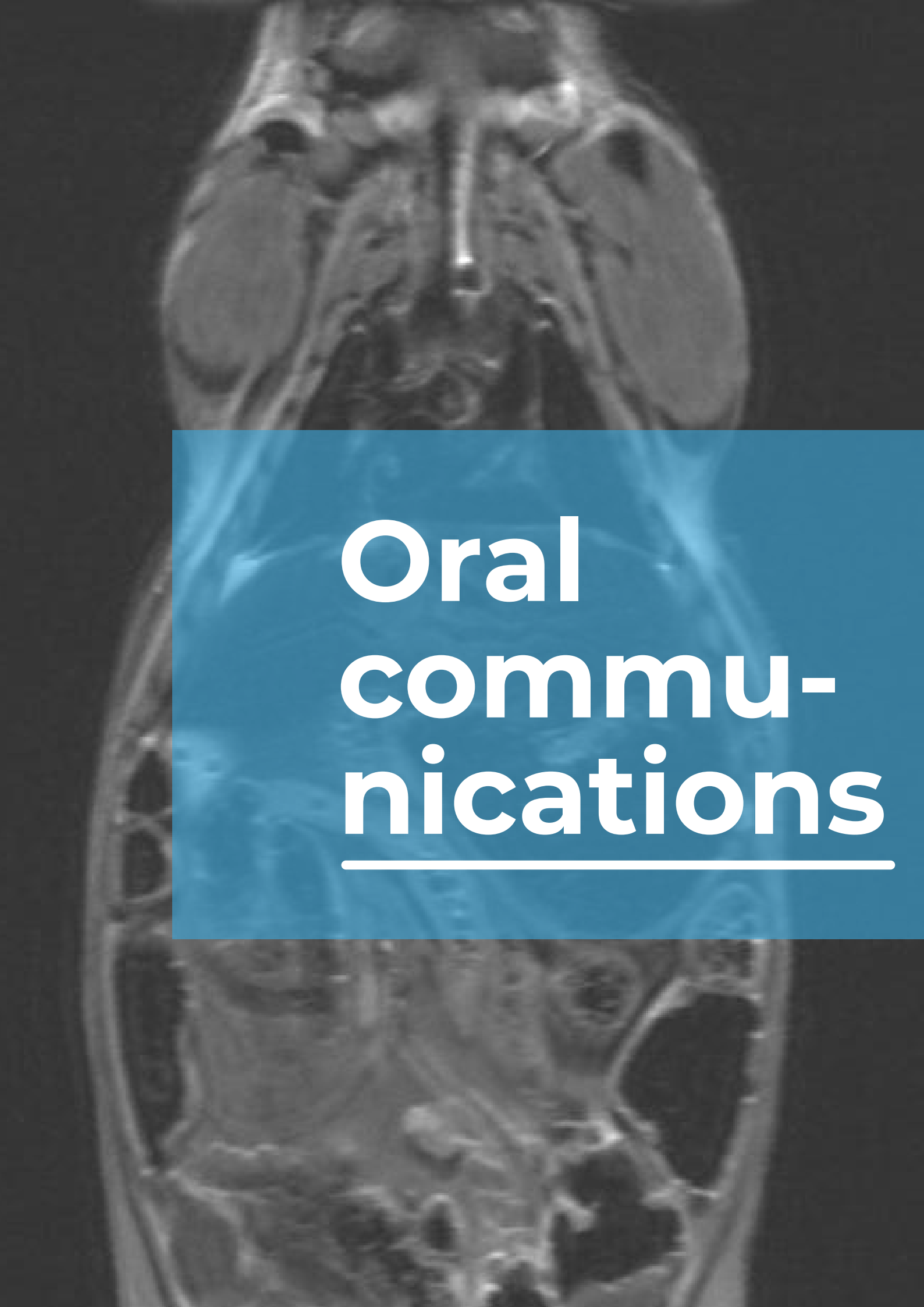

Oral communications

Fully Automated Deep Learning and Radiomics Pipeline for Assessing Myocardial Infarction and Microvascular Obstruction

João Santinha[1], Minh Nhat Trinh[2], Teresa Matias Correia[2,3*]

[1]Champalimaud Foundation, Lisbon, Portugal; [2] Centro de Ciências do Mar - CCMAR, Faro, Portugal; [3]School of Biomedical Engineering and Imaging Sciences, King's College London, London, United Kingdom *tmcorreia@ualg.pt

INTRODUCTION: Late Gadolinium Enhancement (LGE) is the current non-invasive reference standard for detecting myocardial viability after myocardial infarction (MI)[1]. LGE also shows the presence and extent of microvascular obstruction (MVO) or no-reflow, a marker of severe myocardial injury[2]. Automatic segmentation and classification techniques have been developed to identify regions of LGE uptake; however, they typically do not address MVO areas.[3,4] We introduce a RAdiomics model for Myocardial Infarction detection (RAMI.dl), which combines deep learning (DL)-based segmentation and radiomics LGE feature extraction to automatically detect and quantify MI and MVO.
METHODS: Clinical data 100 patients (33 normal, 67/40 pathological/MVO) from the EMIDEC LGE dataset[4] and corresponding segmentations (myocardium, MI, MVO) were divided into stratified training/testing sets. **Segmentation** Tiramisu U-Net with Focal Active Contour Loss[5] was used to segment regions of interest to extract radiomic features. **Radiomics** Features were extracted using original, Laplacian of Gaussian (LoG), wavelet decompositions, gradients, and 2D local binary patterns. These were used to construct RAMI.dl, a logistic regression with lasso regularization. RAMI was trained to automatically distinguish: 1) normal and pathological cases from image features extracted from DL-based myocardium segmentation and 2) MI and MVO cases considering image features extracted from DL-based MI segmentation. SHapley Additive exPlanations (SHAP) were used to identify key features. Segmentation was assessed using Dice score, Hausdorff distance, and volume differences. Predictive accuracy was evaluated with sensitivity, specificity, and area under the curve (AUC) metrics on cross-validation and held-out test sets.
RESULTS & DISCUSSION: RAMI.dl exhibited excellent performance with AUC of 0.94 ± 0.04 and 0.83 on the cross-validation and held-out test, respectively. It achieved sensitivities of 76% ± 10% and 65% on the cross-validation and held-out test sets, and remarkable specificities of 96% ± 7% and 100%, respectively. For MI and MVO differentiation, on the cross-validation and held-out test, the model yielded AUC 0.87 ± 0.11 and 0.85, sensitivity 70 ± 12 and 80, specificity 0.88 ± 0.13 and 90, respectively. Representative cases, illustrated in Fig 2, show radiomics maps, accurate segmentations and volume estimates. In summary, RAMI.dl combines deep learning segmentation with radiomics prediction to enable accurate MI and MVO detection and quantification, providing important diagnostic and prognostic information without requiring user input.

Acknowledgements Research supported by FCT UIDB/04326/2020 (DOI:10.54499/UIDB/04326/2020), IDP/04326/2020 (DOI:10.54499/UIDP/04326/2020), LA/P/0101/2020 (DOI:10.54499/LA/P/0101/2020) and "la Caixa" Foundation and FCT I.P. [LCF/PR/HR22/00533].

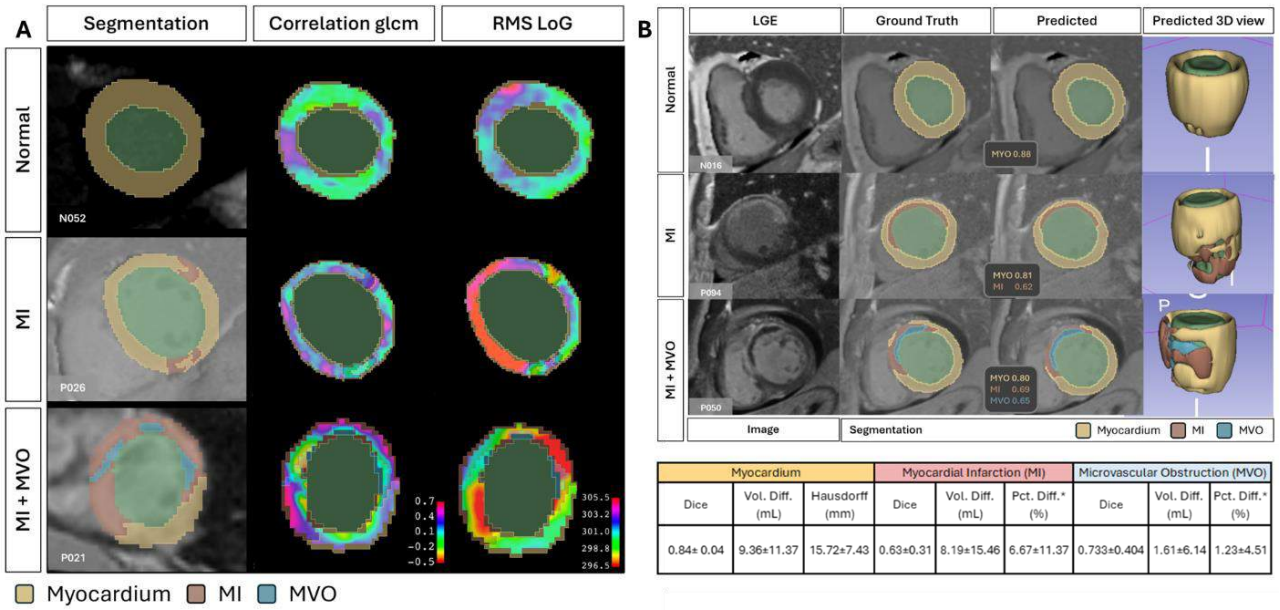

Myocardium			Myocardial Infarction (MI)			Microvascular Obstruction (MVO)		
Dice	Vol. Diff. (mL)	Hausdorff (mm)	Dice	Vol. Diff. (mL)	Pct. Diff.* (%)	Dice	Vol. Diff. (mL)	Pct. Diff.* (%)
0.84± 0.04	9.36±11.37	15.72±7.43	0.63±0.31	8.19±15.46	6.67±11.37	0.733±0.404	1.61±6.14	1.23±4.51

Fig 1. A) (Column 1) Segmentations for 3 representative cases: normal, MI only and MI with MVO; (**Column 2**) Gray-level co-occurrence matrix (glcm) **correlation radiomics maps**; (**Column 3**) First-order root mean squared (RMS) extracted from **Laplacian of Gaussian** (LoG) maps. MI cases have higher values than normal cases, while the MI + MVO has lower values, showing the importance of this feature for detecting MVO. **B) DL-based segmentations** (**Column 1**) LGE images; (**Column 2**) ground truth segmentations; (**Column 3**) DL segmentation; (**Column 4**) whole-heart view with Dice scores. (**bottom**) Quantitative metrics for the 3D segmentation.

REFERENCES **1** Ismail *et al*. Front Cardiovasc Med 9:826283 (2022). **2** Pineda *et al*. AJR Am J Roentgenol 191:73-9 (2008). **3** Lourenço *et al*. Lect Notes Comp Sci 12592 (2021). **4**. Lalande *et al*. Data 5, 89 (2020). **5** Trinh *et al*. RIVF 635-40 (2022).

Neuroimaging with an elliptical bore portable MRI designed for neuromodulation with focused ultrasound.

Pablo García-Cristóbal[1*], Teresa Guallart-Naval[1], Jose Borreguero[1], Eduardo Pallás[1], Pablo Benlloch[1,2], Laia Porcar[2], José M. Algarín[1], Fernando Galve[1], Marina Fernández-García[1], Jesús Conejero[1], Luiz Guilherme[1], Lucas Swistunow[1], Rubén Bosch[1], Beatrice Lena[3], Andrew Webb[3], Joseba Alonso[1]

[1] MRILab, Institute for Molecular Imaging and Instrumentation (i3M), Spanish National Research Council (CSIC) and Universitat Politècnica de València (UPV), 46022 Valencia, Spain; [2] PhysioMRI Tech S.L., 46022 Valencia, Spain; [3]C.J. Gorter MRI Center, Leiden University Medical Center, Leiden, Netherlands * **pablo.garcia-cristobal@i3m.upv.es**

INTRODUCTION: Recent advances demonstrate the significant impact that affordable, portable MRI scanners [1] can have in expanding diagnostic access, particularly in low- and middle-income countries (LMICs) [2]. Building on results with our initial portable MRI prototype [1], we have developed an advanced model capable of head imaging. Major re-engineering aspects include a shorter, elliptical-bore magnet [3] that better accommodates the natural shape of the human body. In Figure 1 we can see the system during a brain scan.
Furthermore, it was later adapted to be used as a guiding system for Focused Ultrasound-based (MRgFUS) neuromodulation [4]. This setup is intended to be used in macaque subjects, to test its preclinical validity. Figure 1b shows the resulting setup.

METHODS: For neuroimaging, we employed a RARE sequence. To suppress artifacts caused by eddy currents, we analyzed odd and even echoes separately. Images were acquired with a spatial resolution of 1.6 × 1.6 × 5 mm³ within a field of view (FOV) of 20 × 22 × 19 cm³, using an acquisition bandwidth of 46 kHz. T1-weighted images were acquired with a repetition time (TR) of 600 ms, an echo time (TE) of 16 ms, and an echo train length (ETL) of 8, following an in-out k-space trajectory, with a total acquisition time of 6 minutes. For T2-weighted images, the parameters were TR = 2500 ms, TE = 20 ms, and ETL = 16, using an out-center-out trajectory, with an acquisition time of 11 minutes. Additionally, we acquired images with an inversion pulse, using TR = 1200 ms, inversion time (TI) = 120 ms, TE = 20 ms, and ETL = 8, also with an in-out trajectory, with a total acquisition time of 11 minutes. To correct the distortions, we apply a magnetic-field-based correction algorithm, SPDS [5].
The MRgFUS setup employs a larger RF coil consisting of an elliptical solenoid with 20 wire turns, a length of 26 cm and a short- and long-axis length of 19.8 and 26.8 cm respectively. A water-filled pool containing the transducer is placed inside and coupled to the subject's head by an elastic thin membrane. To position the transducer, a robotic setup consisting of three linear stages (one per axis), and one hexapod is integrated, connecting to the FUS element by a pole, so that the magnetic field of the main magnet does not interfere with the robots' electronics.
For accurate positioning we employ an initial transversal 3D RARE sequence, with an isotropic cubic FOV of 28 cm3 and a voxel size of 2 × 2 × 2.3 mm. The remaining parameters are selected to accelerate the acquisition while visualizing major anatomical features of the subject and the transducer pool: TR = 600 ms , TE = 10 ms and ETL = 30, for a total acquisition time of under 5 minutes per scan. The resulting image is post-processed, and the subject is co-registered to a pre-existing CT scan, where the desired position of the transducer is marked. This co-registration allows us to know the displacements needed between the current position of the transducer and the desired position for the treatment. Once this movement is done, a second image, with the same parameters, is acquired to check the correct positioning of the transducer.

RESULTS & DISCUSSION: Figure 2 shows images of healthy brains from volunteers using three different types of contrast. In all images, the main anatomical structures of the brain can be distinguished. The T1-weighted image provides a high signal-to-noise ratio (SNR), ensuring sharp details. The T2-weighted and STIR images offer greater contrast between white matter, gray matter, and cerebrospinal fluid, making these structures more distinguishable.
Figure 3 shows images of a macaque phantom in the MRgFUS system. Both the phantom and the spheroids designed to locate the transducer are visible. Using images to determine the accuracy of movements using the MR images, we find errors of around 1 millimeter in-plane, and 2 mm between image slices.

CONCLUSION: We have developed an advanced portable MRI system capable of head imaging, integrating a novel magnet design and a US-compatible system. Our results demonstrate that the system provides neuroimaging with different contrast types, effectively distinguishing key brain structures. These advancements pave the way for broader diagnostic accessibility, particularly in resource-limited settings. Preclinical studies are still pending, but preliminary results with the MRgFUS setup show its viability as a cost-efficient alternative to its high-field counterpart. Its final validation will be carried out in the upcoming months, where an extensive study using a cohort of macaques will be subjected to a FUS neuromodulation treatment plan.

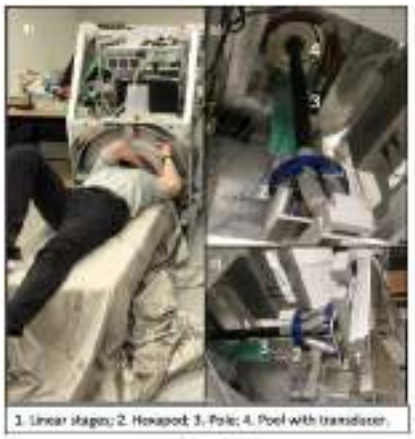

Figure 1.

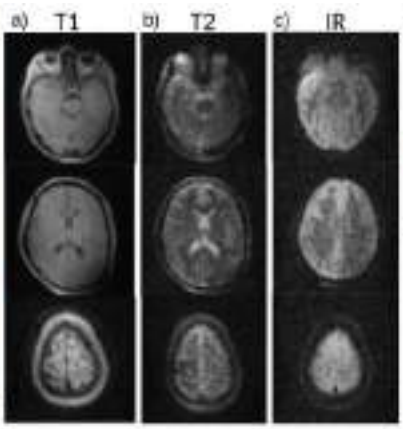

Figure 2.

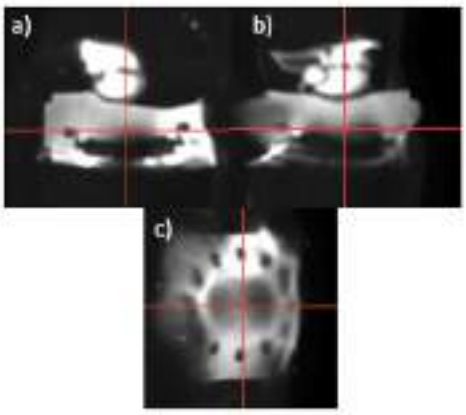

Figure 3.

Figure 1 – a) Portable MRI prototype with an elliptical bore with a volunteer. b) Back view of the scanner where the hexapod (blue) supported by the 3 linear stages can be seen, as well as the pole (black) that helps them move the transductor located in the pool (white). c Side view of the robot setup. **Figure 2 -** Images of healthy volunteers. a) 3D-RARE sequence T1-weighted. b) 3D-RARE sequence T2-weighted. c) 3D-STIR sequence. **Figure 3 – a)** Sagittal view of the pool and macaque phantom, where the transducer is seen, with the spheroids that form the positioning constellation. **b)** Coronal view, where the macaque and the "shadows" produced by the metallic elements are visible. **c)** Axial view showing where the spheroid constellation forming a ring.

References

1. Guallart-Naval T et al. Sci Rep. 2022;12:13147. **2.** Obungoloch J et al. NMR Biomed. 2023;36(7):e4917. **3.** Galve F et al. NMR Biomed. 2024;e5258. **4.** Lu H et al. Meta-Radiology. 2024;2(1). **5.** Borreguero J et al. Magn Reson Med. 2024;

Enhancing Hypoxic-Ischemic Encephalopathy Classification through Region-Specific Brain MRI Segmentation

Elias J. Faro Gómez[1], Alejandra Aguado-Del-Hoyo[2], Belén Bernardo-Atienza[3], Dorotea Blanco-Bravo[3], Juan J. Gómez-Valverde[1,4] and Lucilio Cordero Grande[1,4]

[1]Biomedical Image Technologies, ETSI Telecomunicación, Universidad Politécnica de Madrid, Madrid,Spain, [2]Radiology Service, Hospital General Universitario Gregorio Marañón, Madrid, Spain, [3]Neonatology Service, Hospital General Universitario Gregorio Marañón, Madrid, Spain, [4]CIBER-BBN, ISCIII, Madrid, Spain

Abstract

INTRODUCTION: Accurate classification of neonatal HIE severity is essential for clinical decision-making and outcome prediction [1]. While existing scoring systems have shown strong predictive potential, they are time-consuming and prone to observer variability [2, 3]. Automating scoring through advanced imaging could lead to more consistent assessments. Namely, this study investigates whether refined brain region segmentations enhance HIE classification accuracy. Using a public neonatal dataset and a clinical cohort, we study the added value of region-specific segmentation in distinguishing mild from severe cases.

METHODS: Automatic segmentation. The nnU-Net [4] was trained on 679 annotated T2- and T1-weighted MRI volumes from the developing Human Connectome Project dataset [5] to segment 12 neonatal brain regions, including 6 clinically relevant for HIE, White Matter (WM), deep Gray Matter (dGM), Posterior Limb of the Internal Capsule (PLIC), Basal Ganglia (BG), and Thalamus with high (Th-H) and low (Th-L) intensity [1]. The model was trained for 500 epochs using default nnU-Net 2D settings and applied to a clinical dataset of 71 neonates with mild to severe HIE. **Classification of severity.** The clinical dataset was slightly imbalanced, so a 3-fold stratified cross-validation was used. Various classification experiments were conducted: (I) Deep Learning (DL) Classification. A DenseNet model was trained using two aproaches: (a) 2D, pretrained on ImageNet and (b) 3D, no pretraining available. In both cases, extensive tests were performed to optimize the hyperparameters for maximized performance. (II) Radiomics classification. Features were extracted using Pyradiomics [6] removing features with correlation > 0.9 from: (a) A whole-brain mask and (b) The 6 HIE-relevant regions. We conducted two experiments: one with feature selection and another without. For the former, mutual information analysis was applied, retaining features with values greater than 0.2 for T2- and 0.1 for T1-weighted images. Additionally, ridge (α=0.01) and Lasso (α=0.1) regularization were respectively applied to T2 and T1 features. Furthermore, ANOVA-based feature selection was used to identify the five most important features. An ensemble approach combining, including Random Forest, Logistic Regression, Gradient Boosting, and Multiayer Perceptron, was adopted to improve robustness and reduce model bias.

RESULTS & DISCUSSION: Segmenting the six key regions improves prediction accuracy, AUC, and G-Mean compared to using only a whole-brain mask (Fig. 1, left), emphasizing the relevance of region-specific analysis. Feature selection is not strictly necessary, as models without it perform similarly, though selecting five key features slightly enhances T1-based predictions, warranting further study. Supervised DL results were comparable to radiomics when using a whole-brain mask, suggesting that DL does not inherently outperform radiomics under these conditions. Incorporating segmentations in DL models may improve performance, though a larger cohort could be needed. Directionality of key features identified by SHAP (Fig. 1, right) appears potentially consistent with trend towards lower image conspicuity from PLIC myelin and abnormal thalamic intensities in the presence of lesion [7]. Similarly promising results have been reported by other approaches [8]. However, data and pipeline standardization for automatic lesion detection in HIE is an on-going work, demanding further statistical analysis and validation, to which we expect to contribute with our future research.

Modality	Experiment	Reduction	Accuracy	AUC	G-Mean
T2	Rad Segs	Yes	**0.915±0.034**	0.999±0.000	**0.911±0.042**
	Rad Segs	No	0.887±0.021	**0.910±0.035**	0.875±0.028
	DL 2D	No	0.845±0.053	0.960±0.041	0.829±0.050
	Rad	No	0.831±0.034	0.867±0.028	0.805±0.022
	DL 3D	No	0.830±0.038	0.892±0.054	0.811±0.039
	Rad	Yes	0.732±0.051	0.743±0.030	0.712±0.045
T1	Rad Segs	Yes	**0.888±0.038**	**0.921±0.021**	**0.870±0.045**
	Rad Segs	No	0.831±0.008	0.871±0.006	0.818±0.002
	Rad	No	0.803±0.016	0.841±0.036	0.801±0.026
	DL 3D	No	0.803±0.070	0.785±0.036	0.795±0.065
	DL 2D	No	0.802±0.056	0.793±0.115	0.796±0.058
	Rad	Yes	0.691±0.076	0.739±0.051	0.627±0.089

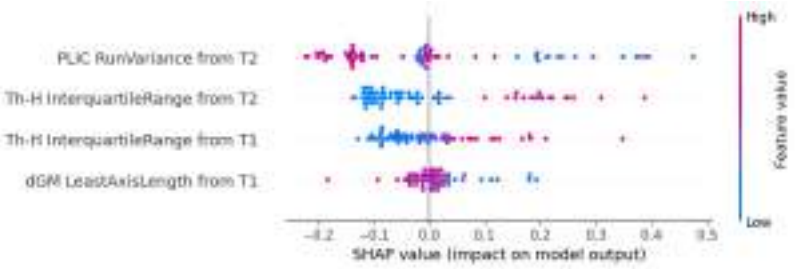

Figure 1 – (Left) Summary of DL and radiomic results using T2 and T1. 'Rad': radiomic experiment with a whole brain mask. 'Rad Segs': radiomic experiment with the 6 clinically relevant regions. (Right) Beeswarm plot of SHAP values showing most important features for both modalities. Higher SHAP values (shift to the right) are associated with more severe lesions.

Acknowledgements. The authors gratefully acknowledge the Universidad Politécnica de Madrid for providing computing resources on Magerit Supercomputer and funding from the MCIN / AEI/ 10.13039/501100011033 / FEDER, UE, under Project PID2021-129022OA-I00.

References

[1] M Martinez-Biarge et al. "Predicting motor outcome and death in term hypoxic-ischemic encephalopathy". Neurology 76.24 (2011), pp. 2055–2061. [2] S. Shankaran et al. "Brain injury following trial of hypothermia for neonatal hypoxic–ischaemic encephalopathy". Archives of Disease in Childhood - Fetal and Neonatal Edition 97.6 (2012), F398–F404. [3] LC. Weeke et al. "A Novel Magnetic Resonance Imaging Score Predicts Neurodevelopmental Outcome After Perinatal Asphyxia and Therapeutic Hypothermia". The Journal of Pediatrics 192 (2018), 33–40.e2. [4] F Isensee et al. "nnU-Net: a self-configuring method for deep learning-based biomedical image segmentation." Nature Methods 18.2 (2021). [5] A. Makropoulos et al. "The developing human connectome project: A minimal processing pipeline for neonatal cortical surface reconstruction". NeuroImage 173 (2018), pp. 88–112. [6] Joost J.M. van Griethuysen et al. "Computational Radiomics System to Decode the Radiographic Phenotype". Cancer Research 77.21 (2017), e104–e107. [7] JJM et al. "Neuroimaging in the term newborn with neonatal encephalopathy". Seminars in Fetal and Neonatal Medicine 26.5 (2021). [8] T. Brochet et al. "Neonatal Hypoxic Ischemic Encephalopathy Severity Grading Using Multimodal Swin Transformer". 2024 IEEE International Symposium on Biomedical Imaging. 2024, pp. 1–4.

Synthesizing realistic diffusion-weighted MR data for machine learning

Tomasz Pieciak[1,*], Santiago Aja-Fernández[1], Antonio Tristán-Vega[1]

[1]LPI, ETSI Telecomunicación, Universidad de Valladolid, Valladolid, Spain; *tpieciak@tel.uva.es

Abstract

INTRODUCTION: Machine learning algorithms require an extensive amount of labelled datasets to train and validate the models adequately for clinical applications[1]. However, obtaining the references for diffusion-weighted magnetic resonance (DW-MR) data is challenging owing to the quantifiable nature of the signal. To this end, one can estimate the pseudo-reference labels using the parametric methods[2-4] or establish them through *in silico* experiments under predefined diffusional properties[4,5]. This work: 1) analytically derives a new formulation for the extra-cellular perpendicular diffusivity, 2) introduces the voxel selection method with minimally dispersed fibres, 3) models intrinsic brain parameters *via* the gamma distribution, and 4) introduces a scheme for synthesising realistic DW signals from *in vivo* measurements.
METHODS: Analysis: assuming the intra- and extra-cellular longitudinal diffusivities are equal $\lambda_{||,\text{ic}}=\lambda_{||,\text{ec}}=\lambda_{||}$ and intra-cellular transverse diffusivity $\lambda_{\perp,\text{ic}}=0$, we express the perpendicular signal decay *via* Eq. [1] with $T_{2,\text{eff}}$ being the effective relaxation. Now, if $v_{\text{ic}}\propto f_{\text{ic}}\exp(-TE/T_{2,\text{a}})$, we define the extra-cellular transverse diffusivity $\lambda_{\perp,\text{ec}}$ (Eq. [2]) and find optimal b_0^{opt} using Eq. [3] for each pair $(v_{\text{ic},0},\lambda_{\perp,0})$. Synthesis: the DW-MR signal is synthesized using Eq. [4] with a kernel given by Eq. [5], where f FWVF is the free-water volume fraction, $D_{\text{iso}}=3\times10^{-3}\,\text{mm}^2/\text{s}$, and $W(\boldsymbol{n})$ is the Watson orientation function.
MATERIALS: MICRA data[6], 3F/3M, acquired using a 3T Connectom scanner at 300 mT/m. Δ/δ: 24/7ms, *b*-values: 200, 500, 1200, 2400, 4000, 6000 s/mm^2 with 20, 20, 30, 61, 61, 61 gradients, voxel size: 2×2×2mm^3 , TE=59ms, TR=3000ms.
RESULTS & DISCUSSION: We estimated FWVF[7], v_{ic} , OD[8], $\lambda_{||}$, $\lambda_{\perp}$[9] and c_l[10]. From the results in **Fig. 1a**, we selected the least dispersed and the most linear diffusivity regions, and illustrated the histograms of factor $\zeta=\text{OD}^2+c_l^2$ in **Fig. 1b**. **Fig. 1c** shows the accepted for analysis voxels, **Fig. 1d** illustrates visual inspections of the measures, histograms and fitted gamma distributions. Next, **Fig. 1e** presents the optimized parameter b_0^{opt} according to Eq. [3] with the mode $b_0^{\text{opt},*}$. **Fig. 1f** depicts the synthesized DW-MR signals for a single voxel, **Fig. 1g** shows the spherical average signal as a function of *b*-value. The proposal allows for estimating $\lambda_{\perp,\text{ec}}$ from a standard DW-MR acquisition and then synthesising brain-originated signals assuming a realistic parameter variability (not fixed!) in the brain for a wide range of *b*-values.

Analysis: $\exp(-\text{TE}/T_{2,\text{eff}})\exp(b\lambda_{\perp})\simeq f_{\text{ic}}\exp(-\text{TE}/T_{2,\text{a}})+(1-f_{\text{ic}})\exp(-\text{TE}/T_{2,\text{e}})\exp(-b\lambda_{\perp,\text{ec}})$ [1] $\quad\lambda_{\perp,\text{ec}}(b|v_{\text{ic}},\lambda_{\perp})=b^{-1}\log\left(\frac{1-v_{\text{ic}}}{\exp(-b\lambda_{\perp})-v_{\text{ic}}}\right)$ [2]

$$b_0^{\text{opt}}=\underset{b_0>0}{\text{argmin}}\int_0^{b_{\max}}\left(\exp(-b\lambda_{\perp,0})-v_{\text{ic},0}-(1-v_{\text{ic},0})\exp(-b\lambda_{\perp,\text{ec}}(b_0|v_{\text{ic},0},\lambda_{\perp,0}))\right)^2 db \quad [3]$$

Synthesis: $\frac{S(b,\mathbf{g})}{S(0)}=f\exp(-bD_{\text{iso}})+(1-f)\int_{\mathbb{S}}\mathcal{K}(b,\mathbf{g}^T\mathbf{n})W(\mathbf{n})d\mathbf{n}$ [4] $\quad\mathcal{K}(b,\varphi)=v_{\text{ic}}\exp(-b\lambda_{||}\varphi^2)+(1-v_{\text{ic}})\exp\left(-b(\lambda_{||}-\lambda_{\perp,\text{ec}})\varphi^2\right)\exp(-b\lambda_{\perp,\text{ec}})$ [5]

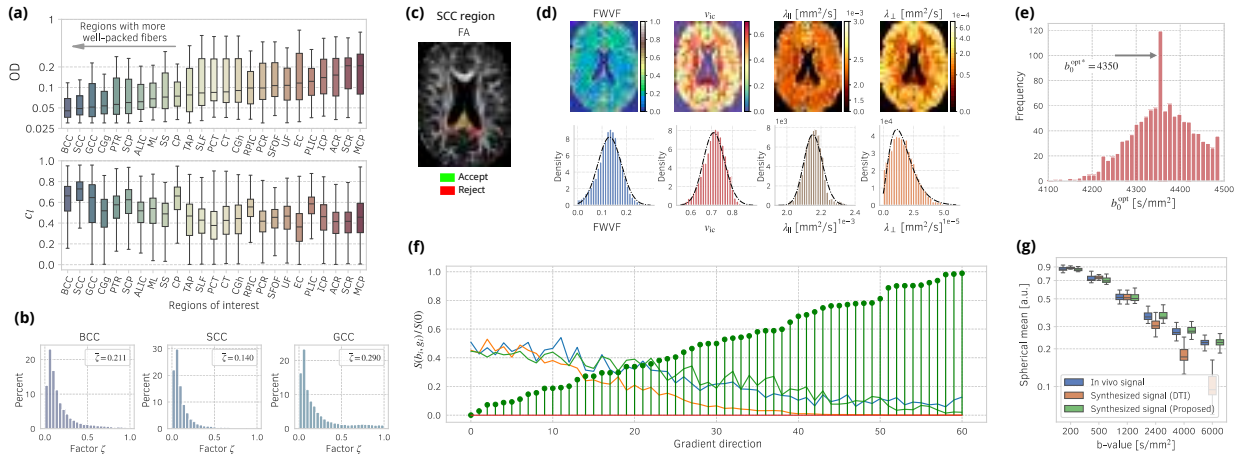

Figure 1 – (a) Orientation dispersion (OD) and Westin's linear measure c_l calculated for WM regions and aggregated over all subjects. **(b)** Histograms of the factor $\zeta=\text{OD}^2+c_l^2$ with its mean $\overline{\zeta}$. **(c)** Accepted/rejected voxel (below a quantile 0.25). **(d)** Estimated parameters from sub-01/ses-03, histograms generated from the accepted voxel and fitted gamma distributions *via* the maximum likelihood. **(e)** Histogram of optimized *b*-values b_0^{opt}. **(f)** Synthesized DW signal at $b=6000\text{s/mm}^2$ for a selected voxel from the SCC. Green stem plot represents the inner product computed between the gradient direction **g** and a unit vector identified with the main direction of longitudinal diffusion $\lambda_{||}$. **(g)** Spherical means computed for *in vivo* and *in silico* data synthesized *via* the Diffusion Tensor Imaging (DTI) and the proposal.

References

1. Dinsdale N.K, *Neuron*, 110(23), 2022. **2.** Golkov V., *IEEE TMI*, 35(5), 2016. **3.** Ye C., *MEDIA*, 61, 2020. **4.** Karimi D., *NeuroImage*, 239, 2021. **5.** Gyori N.G., *MRM*, 87(2), 2022. **6.** Koller K., *Neuroimage*, 225, 2021. **7.** Tristán-Vega A., *MRM*, 87(2), 2022. **8.** Daducci, *NeuroImage*, 105, 2015. **9.** Tristán-Vega, *NeuroImage*, 227, 2021. **10.** Westin, *MEDIA*, 6(2), 2002.

Acknowledgements

Funding: Junta de Castilla y León and Fondo Social Europeo Plus (FSE+) under research grant VA156P24, Ministerio de Ciencia e Innovación of Spain with researchgrants PID2021-124407NB-I00 and TED2021-130758B-I00, Polish National Agency for Academic Exchange for grant PPN/BEK/2019/1/00421, Ministry of Science and Higher Education (Poland) under the scholarship for outstanding young scientists (692/STYP/13/2018).

Motion Correction Strategies in Renal Arterial Spin Labeling Perfusion: Qualitative and Quantitative Performance Evaluation

Veronica Aramendía-Vidaurreta[1-2], Rebeca Echeverría Chasco[1-2], Marta Vidorreta[3], Leyre García Ruiz[1-2], Peter Speier[4], María A. Fernandez-Seara[1]

[1]Department of Radiology, Clínica Universidad de Navarra. Pamplona, Spain. [2]IdiSNA, Instituto de Investigación Sanitaria de Navarra, Spain. [3]Siemens Healthcare. Madrid, Spain. [4]Siemens Healthcare, Erlangen, Germany

INTRODUCTION: Renal blood flow (RBF) can be noninvasively measured with arterial spin labeling (ASL) by magnetically labeling blood water. However, motion limits its clinical use, requiring correction before quantification

METHODS:

Retrospective data: 77 datasets were analyzed on a 3T Siemens Skyra MR scanner from 19 subjects (healthy individuals, chronic kidney disease patients and kidney transplant recipients). A pseudo-continuous ASL (pCASL) sequence with a 2D spin-echo EPI readout was analyzed to quantify perfusion[1]. Datasets varied in background suppression levels, number of slices, post-labeling delays and total number of label-control pairs. Perfusion-weighted images (PWI) were generated by subtracting control and label images and pixelwise RBF maps were obtained using the single compartment model[2]. Temporal signal-to-noise ratio (tSNR) was calculated as a quality metric. Datasets were visually reviewed and categorized into motion (75%) and no motion (25%).

Registration: Two algorithms were evaluated: (1) groupwise, implemented offline in Elastix[1,3,4], minimizing a principal component analysis-based metric, aligning all images simultaneously, and (2) pairwise, implemented in the Siemens image calculation environment (ICE) of the sequence reconstruction pipeline[5], maximizing a normalized mutual information metric performed consecutively between temporally adjacent images.

Qualitative Assessment: Two experts rated all datasets by visualizing all images before and after registration for motion corrupted datasets (categories: failed, not improved, improved) and no motion datasets (categories: failed, same). Additionally, the rating “improved+” was used to denote instances where one algorithm clearly outperformed the other. Registered datasets by the two algorithms were presented randomly to ensure unbiased evaluation.

Quantitative Assessment: A subset of 25 motion-corrupted datasets was analyzed. Two images were selected: the reference used in the pairwise approach, and the image with maximum kidney motion prior to registration. In both images, one kidney was manually segmented before and after each type of registration. The following metrics were computed from the obtained segmentations: Dice coefficient, False Positive ratio (FP), False Negative ratio (FN)[5], absolute motion in the right-left (TRL) and superior-inferior (TSI) direction, and the Euclidean distance of the kidney center (computed as the centroid of the bounding box) between the reference and registered images. Additionally, in all datasets, tSNR, PWI and RBF measurements were compared between algorithms.

Statistical analysis: Cohen’s kappa, ANOVA or Aligned Rank Transform-ANOVA with post-hoc t-test or Wilcoxon signed rank tests. Significance-level=0.05.

RESULTS & DISCUSSION: A significantly higher Dice coefficient was obtained after registration with both methods compared to the values obtained before registration, indicating better overlap between the segmented kidneys. FP and FN ratios were significantly reduced after registration, with no significant differences between methods. Euclidean distance showed significant differences before and after registration and between algorithms, while TRL and TSI metrics showed no significant differences, likely due to the cohort variability. tSNR was higher after registration., although non-significant differences were observed (p=0.058). Image quality of RBF maps was visibly enhanced (see Figure 1). Overall, metrics were more improved after pairwise registration and presented less variability across subjects. No cases were rated as “failed” indicating neither algorithm introduced discernible errors. Almost all datasets (90%-100%) corrected motion to some degree with both algorithms. The pairwise registration was better than groupwise registration in 40% of cases, while groupwise was better than pairwise registration in 2% of cases. Observer agreement was perfect in the “no-motion” group (Cohen’s-kappa=1) and very high in the "motion" group. (Cohen's-kappa=0.82 (CI-95% 0.59 -1)).

CONCLUSION: The pairwise registration shows promise for minimizing motion in ASL RBF measurements.

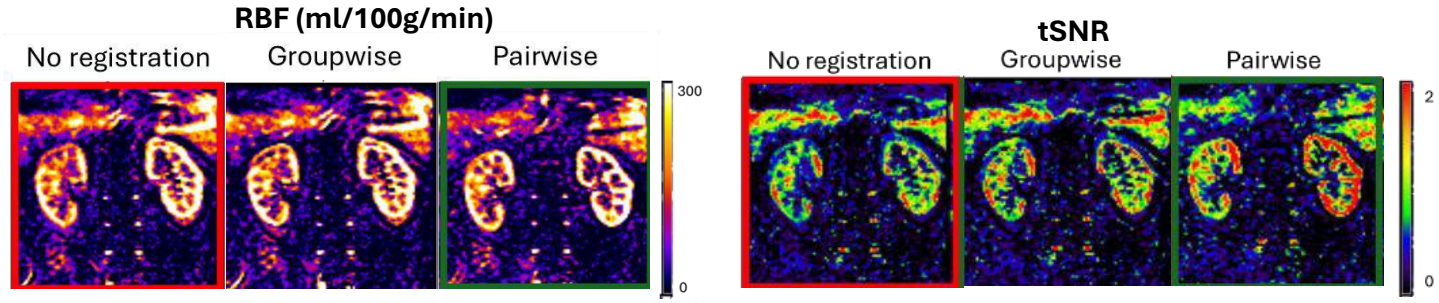

Figure 1: Pixelwise RBF and tSNR maps for one representative subject with motion before and after registration.

REFERENCES: 1 Echeverria-Chasco, et al. 2023. doi: 10.1002/nbm.4832; 2. Alsop, et al. 2015. doi:10.1002/mrm.25197; 3. Huizinga, et al. 2016 doi:10.1016/j.media.2015.12.004; 4. Klein, et al. 2010. doi:10.1109/TMI.2009.2035616; 5. Xue, et al. 2008; doi:10.1007/978-3-540-85990-1_5; 6. Wobbrock, et al. 2011 In: 29th Annual ACM CHI Conference on Human Factors in Computing Systems; 2011:143-14

ACKNOWLEDGEMENTS: This project was supported by Siemens Healthcare and the Government of Navarra under the frame of ERA PerMed (ERAPERMED2020-326 - RESPECT).

Transfer Learning for cross-dataset brain tumor segmentation in post-operative MRI

Catarina Passarinho[1,2], Oscar Lally[3], Ana Matoso[1,4], Marta P. Loureiro[1,2], José Maria Moreira[4], Patrícia Figueiredo[1], Rita G. Nunes[1]

[1] Institute for Systems and Robotics – Lisboa and Department of Bioengineering, Instituto Superior Técnico, Universidade de Lisboa, Lisbon, Portugal; [2] Hospital da Luz, Luz Saúde, Lisbon, Portugal; [3] King's College London, London, United Kingdom; [4] Hospital da Luz Learning Health, Luz Saúde, Lisbon, Portugal.

INTRODUCTION: High-grade glioma (HGG) segmentation is crucial for precise therapy planning and monitoring progression. Although manual annotation by experts remains the gold standard, automated methods have proven to be valuable alternatives to distinguish between tumor regions[1], which is essential for targeted treatments. Despite extensive research on glioma segmentation, most studies have been performed on pre-operative imaging[2]. Post-operative tumor segmentation is more challenging due to changes caused by surgery and radiotherapy, in addition to the intrinsically hazy tumor margins and the limited availability of public post-treatment annotated datasets[3,4]. This work evaluates whether transfer learning (TL) applied to models first trained on pre-operative data improves performance in post-operative tumor segmentation.
METHODS: Three publicly available glioma datasets were used: BraTS2021 (N=1251, pre-operative), LUMIERE (N=490 after curation, post-operative), and BraTS2024 (N=1350, post-operative), all including T1, T2, FLAIR, and contrast-enhanced T1 (T1CE) MRI scans for each glioma patient and segmentation labels for three nested subregions: enhancing tumor (ET), tumor core (TC), and whole tumor (WT), including edema. Image alignment to a common space, bias field correction and brain extraction steps were applied to all datasets. Two promising segmentation architectures implemented in MONAI[5] were first trained on BraTS2021: 1) ResNet-based architecture that uses autoencoder regularization[6]; and 2) Swin UNETR[7], a U-shaped network with a Swin transformer as the encoder. Previous work showed that an ensemble model combining WT and TC gradings from the ResNet and the ET classification from the Swin UNETR significantly outperformed the individual models on the pre-operative BraTS2021 images[8]. Here, the same ensemble approach was used with TL, where the model weights from the initial round of training on BraTS2021 were consecutively fine-tuned on LUMIERE and BraTS2024 post-operative data. Model accuracy was assessed using Dice Similarity Coefficients (DSC) of each segmented region with the corresponding reference label, thus providing insights into model performance across pre- and post-operative contexts and different datasets.
RESULTS & DISCUSSION: The obtained DSC showed statistically significant performance differences across the three models trained for each test subset (t-tests with *p*-values<<<0.05). Segmentation accuracy on the BraTS2021 declined after TL on LUMIERE, but drastically improved after TL on BraTS2024, highlighting the similarities between both BraTS datasets. TL on LUMIERE significantly improved accuracy on its test set, but subsequent TL on BraTS2024 caused a notable drop in performance on LUMIERE. These results are likely due to the larger dataset size of BraTS2024 but also emphasize the challenge of sequential learning in deep neural networks, leading to catastrophic forgetting, even when the overall task remains the same. Both rounds of TL significantly improved performance on the BraTS2024 test set, suggesting the model was able to apply learned knowledge from LUMIERE effectively. Future work will explore the impact of elastic weight consolidation, a strategy against catastrophic forgetting, which aims to retain previously learned features and maintain performance across tasks and datasets.

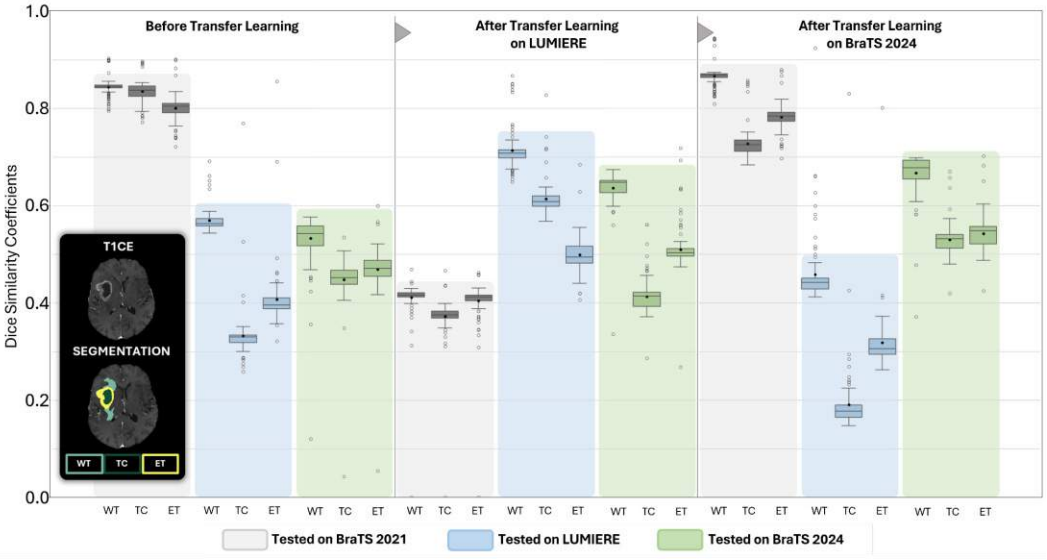

Figure 1 – Dice similarity coefficient distributions for each tumor region - whole tumor (WT), tumor core (TC) and enhancing tumor (ET) - across the BraTS2021 (grey), LUMIERE (blue), and BraTS2024 (green) test sets before transfer learning, after transfer learning on the LUMIERE dataset, and after transfer learning on the BraTS2024 dataset.

Acknowledgements

Funded by LARSyS-FCT through 10.54499/LA/P/0083/2020, 10.54499/UIDP/50009/2020, 10.54499/UIDB/50009/2020 and 2022.13185.BD.

References

1. Omuro A, DeAngelis LM. Glioblastoma and other malignant gliomas: a clinical review. JAMA. 2013. | 2. Işın A, et al. Review of MRI-based Brain Tumor Image Segmentation Using Deep Learning Methods. Procedia Computer Science. 2016. | 3.Hoebel KV, et al. Expert-centered Evaluation of Deep Learning Algorithms for Brain Tumor Segmentation. Radiol Artif Intell. 2024. | 4.Correia de Verdier M, et al. The 2024 Brain Tumor Segmentation (BraTS) challenge: glioma segmentation on post-treatment MRI. 10.48550/arXiv.2405.18368. 2024. | 5.https://monai.io/ | 6.Myronenko, A. 3D MRI Brain Tumor Segmentation Using Autoencoder Regularization. BrainLes 2018. 2019. | 7.Hatamizadeh A, et al. Swin UNETR: Swin Transformers for Semantic Segmentation of Brain Tumors in MRI Images. 10.48550/arXiv.2201.01266. 2022. | 8.Passarinho C., et al. Improved automated segmentation of glioblastoma with ensemble learning. #P241 ESMRMB, 2023.

Applying longitudinal MRI for tumor evaluation in two immunocompetent chicken chorioallantoic membrane (CAM) cancer xenograft models

Núria Profitós-Pelejà[1], Margarida Julià-Sapé[2,3,4], Ana Paula Candiota[2,4], Gaël Roué[1], Silvia Lope-Piedrafita[2,4]*

[1]Lymphoma Translational group, Josep Carreras Leukaemia Research Institute, Badalona (Barcelona), Spain; [2]Dept. de Bioquímica i Biología Molecular, UAB, Spain; [3]Institut de Biotecnologia i Biomedicina (IBB), UAB, Spain; [4]CIBER de Bioingeniería, Biomateriales y Nanomedicina, Spain. *Silvia.Lope@uab.cat

Abstract

INTRODUCTION: The chicken embryo chorioallantoic membrane (CAM) assay has emerged as a valuable preclinical model, significantly advancing the principles of the 3Rs (Replacement, Reduction, Refinement) in scientific research, with no ethical approval required in Spain if terminated by embryonic day (ED) 16. CAM models offer an alternative to traditional, immunocompromised, and costly animal models, providing robust and clinically relevant data [1]. In cancer research, the CAM assay is widely used, among others, for the study of tumor growth and metastasis, angiogenesis, drug acute toxicity and efficacy, enabling the evaluation of a wide range of therapeutics in a timely and cost-effective manner [2]. However, evaluations such as tumor volume or angiogenesis are performed only at endpoint, after excision of the tumors and surrounding tissues, lacking critical intermediate data, which could be highly relevant, especially in preclinical drug efficacy assessment. In this study, we evaluate the feasibility of non-invasive longitudinal MRI acquisitions in CAM-derived pancreatic cancer and lymphoma xenograft models, to gain intermediate insights into tumor progression.

METHODS: OCI-Ly1 (Lymphoma) and PaTu (Pancreatic cancer) tumor cells were engrafted onto the upper chorioallantoic membrane of fertilized white Leghorn chicken egg on ED 9, using standard procedures [3]. MRI was performed at 7T (Bruker Biospec 70/30) on ED 14 and 16. Following a 60-min incubation at 4 ºC to minimize embryo movements, the egg was placed in the scanner at room temperature, and an actively decoupled 15 mm diameter surface coil (SC) was affixed on the eggshell above the tumor site. The SC was used for signal detection, and a 72 mm volume coil for transmission. Doble T2-weighted images were acquired with a RARE sequence (TE_{eff}, 36 ms and 132 ms; TR, 5 s; 1.5&0.5 mm slices; MTX 256x256; FOV, 5x5 cm^2). For tumor volume assessment, regions of interest were manually delineated on each slice where the tumor was visible.

RESULTS & DISCUSSION: No adverse effects were observed in the chicken embryos following both MRI examinations. Tumor and its vascularized system showed more contrast at T2w-132ms TE images than at 36 ms TE. The pancreatic tumor grew more deeply, while the lymphoma grew more superficially. Additionally, pancreatic tumors exhibited increased vasculature branches compared to lymphoma. Remarkably, there was a reduction in tumor volume overtime, which was more pronounced in the pancreatic tumor (ED14 vs ED16; pancreatic: 47,3 mm^3 vs 38.1 mm^3; lymphoma: 41,9 mm^3 vs 38,9 mm^3). Thus, longitudinal approaches can increase statistical power by minimizing between-subject variability and enabling the identification of trends and changes that may be overlooked in endpoint studies.

CONCLUSION: We successfully conducted longitudinal MRI on two types of tumor xenografts grown on CAM membranes, with no observable adverse effects on the chicken embryos. This demonstrates the feasibility of this approach for future drug screening and therapy optimization studies. Coupling the CAM assay with longitudinal MRI analysis may offer a promising alternative for studying individual tumor biology and accelerating the development of tailored anticancer therapies.

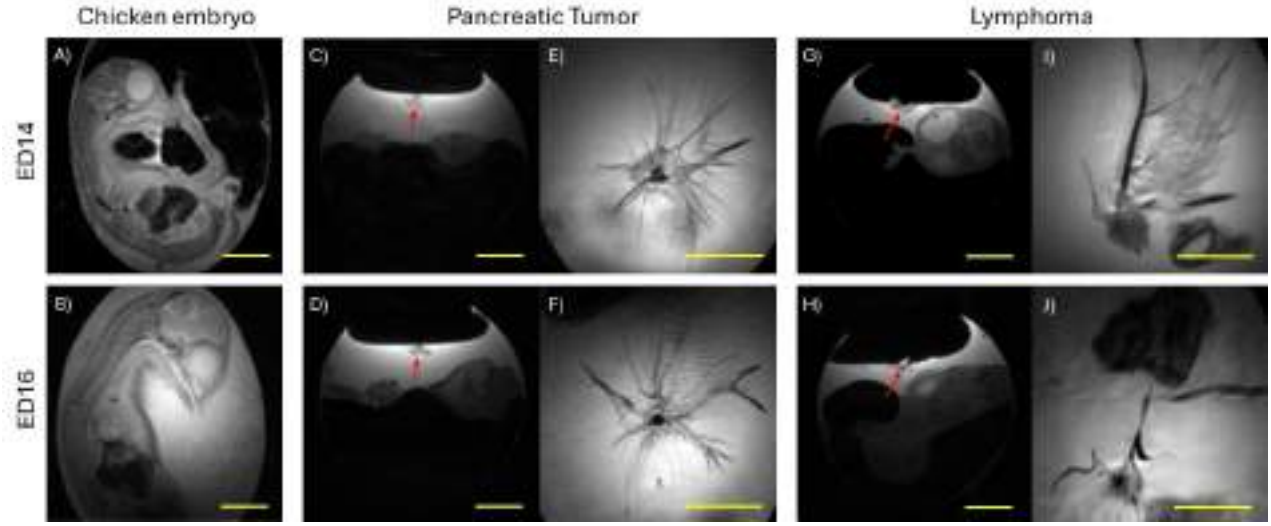

Figure 1 – Representative CAM T2w images at ED 14 (top) and ED 16 (bottom) for pancreatic (middle panels) and lymphoma (right panels) tumors. A,B) CAM coronal slices through the sagittal embryo plane. Axial (C,D,G,H) and coronal (E,F,I,J) sections through the tumor. Arrows pointing tumor masses. 1 cm scale bars.

References

1. Nowak-Sliwinska et al. 2014 *Angiogenesis* 17(4): 779; **2.** Fischer et al. 2022 C*ancers* 15, 191; **3.** Lima Ribeiro et al. 2023 *Front. Immunol.* 14:1130052

Methodological development of MR Elastography for liver fibrosis in a murine animal model

Pilar Sango Solanas, Tiffany Bakir, Kevin Tse Ve Koon, Olivier Beuf

INSA Lyon, Université Lyon 1, CNRS, Inserm, CREATIS UMR 5220, U1294, 69621 Villeurbanne, FRANCE
pilar.sango@creatis.univ-lyon1.fr

Abstract: Metabolic dysfunction-associated steatotic liver disease (MASLD) affects 30% of the global population and can progress to severe fibrosis. While MR elastography (MRE) enables non-invasive liver stiffness measurement, standard MRE sequences have long echo times, limiting imaging quality in short-T2 tissues, such as iron-overloaded livers. To address this, we developed a novel MRE strategy (RARE OC MRE) using optimized RF pulses to replace motion-encoding gradients, allowing for very short TE. In vivo experiments on healthy mice demonstrated the reproducibility of this method, with higher SNR compared to conventional MRE. Future work will assess its robustness in an iron-overload murine model.

INTRODUCTION: Metabolic dysfunction-associated steatotic liver disease (MASLD) affects approximately 30% of the global population[1] and can progress to severe fibrosis and cirrhosis. Since liver fibrosis is often asymptomatic, early detection is challenging, with most patients diagnosed at an advanced stage. While liver biopsy remains the gold standard for diagnosis, it is invasive and prone to sampling errors. Given these limitations, non-invasive diagnostic methods are crucial. MRI is therefore a highly valuable tool, offering high-quality soft-tissue imaging and facilitating the identification of diagnostic biomarkers for liver fibrosis. In this context, MR Elastography (MRE) can quantify biomechanical properties of tissues from the encoding into the phase of the MRI signal of external mechanically-generated shear waves propagating through tissues[2]. Liver stiffness can thus be measured and it is correlated to the level of liver fibrosis, enabling the staging of hepatic fibrosis with high sensitivity[3]. However, the standard MRE sequence has long echo times due to the presence of motion-encoding gradients (MEGs), resulting in insufficient image quality for exploring short T2 tissues, such as the liver with iron overload[4]. To overcome this limitation, we work on the methodological development of motion encoding strategies and MRE sequences. For this purpose, we developed an MRE strategy where an optimized RF pulse, applied with a constant gradient, replaces the MEGs yielding to very short TE and therefore allowing the biomechanical characterization of short T2 tissues[5]. This study aims to validate the proposed strategy (RARE OC MRE) trough *in vivo* mice liver experiments.

METHODS: Four healthy female mice were examined in accordance with ethical guidelines. They were anesthetized with isoflurane (2-3%), with continuous monitoring of their respiration and temperature. MRE acquisitions at 300 Hz were performed at 7-day intervals, comparing the G' moduli obtained using a RARE MEG MRE and a RARE OC MRE sequences. In the latter, RF pulses optimized via an Optimal Control (OC) algorithm ensure both slice selection and motion encoding. Phase images were processed (unwrapping, temporal Fourier transform, spatial filtering) to enable the reconstruction of elastograms. The storage modulus G' was measured in homogeneous liver ROIs and the variations between D1 and D7 (ΔG') was determined to assess reproducibility.

RESULTS & DISCUSSION: Figure 1 illustrates the magnitude, wave, and elastogram images compared for a mouse at Day 1 and Day 7. Table 1 summarizes the mean G' values, standard deviations, G' variations and SNRs for each mouse and acquisition method. Test-retest reproducibility is demonstrated by the little variation of G' measurements between D1 and D7 for both acquisition methods. In conclusion, the proposed RARE OC MRE strategy enables reproducible quantification of liver stiffness, with a significantly higher SNR compared to the RARE MEG MRE method. The next step will be to test this approach on a murine model with iron overload to assess its robustness in this context.

Sequence	Mouse	Test = D1 Re-test = D7	G' (kPa) ± SD	ΔG' (%)	SNR
RARE MEG MRE	1	D1	2.09 ± 0.33	2,4	36
		D7	2.14 ± 0.47		31.3
	2	D1	1.99 ± 0.28	1	26
		D7	2.01 ± 0.22		30.9
	3	D1	2.08 ± 0.23	1,9	35.8
		D7	2.11 ± 0.25		33.2
	4	D1	1.85 ± 0.36	1,1	37.5
		D7	1.87 ± 0.31		42.9
RARE OC MRE	1	D1	2.11 ± 0.28	0	75.9
		D7	2.11 ± 0.27		69.3
	2	D1	2.04 ± 0.21	2,5	64.8
		D7	1.99 ± 0.18		70.6
	3	D1	1.96 ± 0.18	2,5	74.9
		D7	2.01 ± 0.22		76.3
	4	D1	1.84 ± 0.18	2,6	79.2
		D7	1.92 ± 0.21		86.6

Table 1. Obtained results for both MRE methods

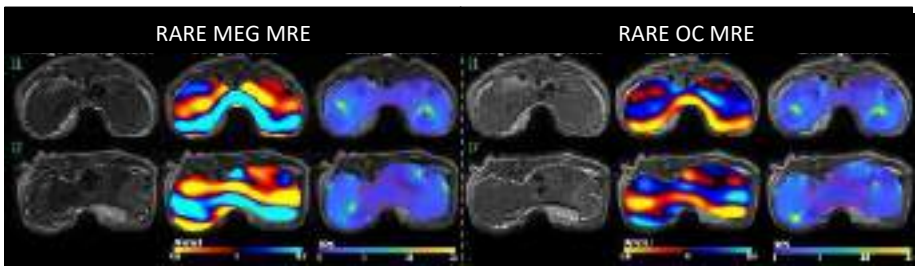

Figure 1. Magnitude, phase images and elastograms (kPa) obtained with both MRE methods at D1 and D7 for the same mouse.

References: [1]Younossi et al. 2023 *Hepatology*; [2]Muthupillai et al. 1995 *Science*; [3]Morisaka et al. 2018 *JMRI*; [4]Ghoz et al. 2019 *Quant. Imaging Med. Sur*; [5] Sango-Solanas et al. 2024 *NMR in Biomed*.

Correlation Tensor Imaging at 3T for In Vivo Mouse Brain Imaging

Rafael N. Henriques[1*], Andrada Ianus[2,1,3], Noam Shemesh[1], Rui V. Simões[4]

[1]Champalimaud Research, Champalimaud Foundation, Lisbon, PT, [2]Imaging Physics and Engineering Research Department, School of Biomedical Engineering and Imaging Sciences, King's College London, London, UK; [3]Algarve Biomedical Center, University of Algarve, Faro, PT; [4]Institute for Research & Innovation in Health (i3S), University of Porto, Porto, PT
*rafael.henriques@neuro.fchampalimaud.org

Abstract

INTRODUCTION: Correlation Tensor MRI (CTI) is a novel diffusion MRI technique that enhances microstructural characterization without relying on conventional model assumptions[1,2]. By extracting unique information from advanced double diffusion encoding (DDE) sequences[3,4], CTI enables a complete separation of different diffusional kurtosis sources, including the often-overlooked microscopic kurtosis (K_μ), which has shown significant relevance in pathologies[5,6]. However, CTI's initial development was performed on high-field preclinical scanners, limiting its direct translatability to clinical field strengths. In this study, we implemented CTI on a state-of-the-art 3T preclinical scanner equipped with a cryoprobe and demonstrated its feasibility for in vivo mouse brain imaging.
METHODS: All animal experiments were preapproved by institutional and national authorities, and carried out according to European Directive 2010/63. Brain MRI acquisitions were performed on mice (C57BL6j background) under anesthesia (1.5-2% isoflurane, 31% oxygen), using a Bruker BioSpec 3T Maxwell scanner, equipped with a 2-channel cryogenic RF coil, and an in-house developed DDE-EPI pulse sequence (ParaVison 360). DDE experiments were performed for 633 different pairs of gradient intensities (b_1, b_2) and directions according to the requirements for CTI reconstruction[2] (acquisition parameters: maximum b-value (b_1+b_2) = 2.5 ms/μm^2; Δ = 10 ms; δ = 4 ms; τ_m = 12ms; TR/TE = 2500/46ms; resolution = 150×150×600μm; partial FT = 1.39; single-shot EPI; total acquisition time = 26min). To quantify the repeatability, acquisitions were repeated twice. A third dataset was also acquired to assess the potential of CTI at an unprecedented in vivo resolution = 118×118×600 μm (partial FT = 1.60; remaining parameters unchanged). For SNR enhancement, complex signals of all datasets were denoised per channel using the Threshold PCA (TPCA)[7].
RESULTS & DISCUSSION: CTI maps revealed the expected high anisotropic kurtosis (K_{aniso}) values in white matter and elevated isotropic kurtosis (K_{iso}) values in voxels near the ventricles, likely due to partial volume effects between tissue and cerebrospinal fluid (Fig. 1A). Kμ maps showed that this source of non-Gaussian diffusion accounted for approximately 30% of total kurtosis in white matter and 60% in gray matter, corroborating previous reports highlighting μK's relevance in tissue microstructure assessment[2,5,8]. Repeat acquisitions demonstrated high reproducibility across all CTI estimates (Fig. 1B). Acquisitions at the higher spatial resolution (118×118 μm) produced CTI maps with visual quality comparable to the lower-resolution data, particularly in cortical brain regions (Fig. 1C).
CONCLUSION: This study demonstrates the feasibility of performing in vivo CTI on 3T preclinical scanners, supporting its role in translational research applications. The 3T and cryoprobe combination offers a promising alternative to high-field preclinical MRI systems, facilitating the translation of microstructural insights from animal model studies to patients.

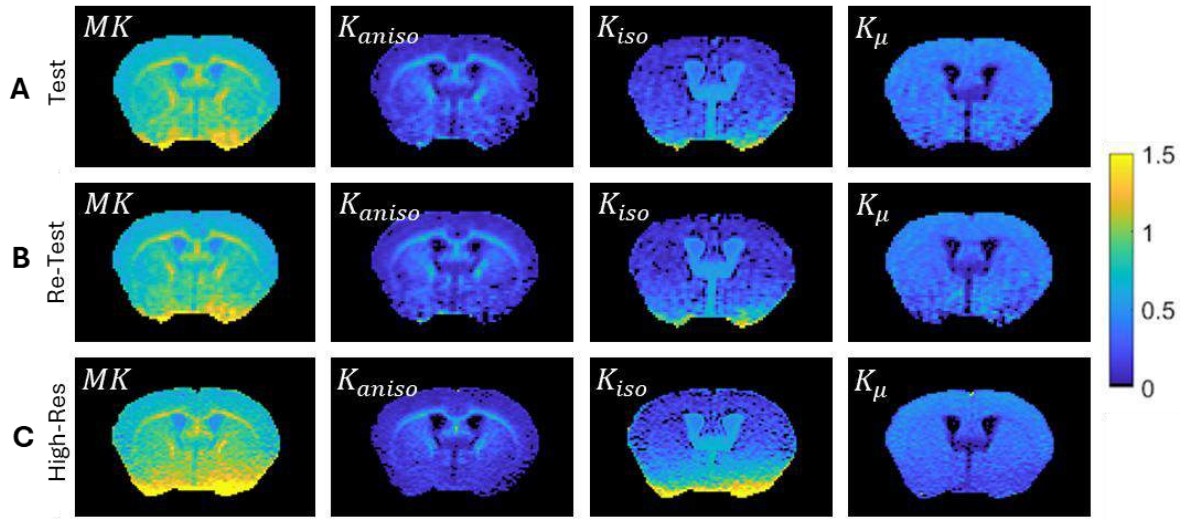

Figure 1 – Representative CTI maps for test-retest data (A and B) and for the higher resolution data (C). From left to right, the following is shown: total mean kurtosis (K_t); anisotropic kurtosis (K_{aniso}); isotropic kurtosis (K_{iso}); and microscopic kurtosis (K_μ).

References

1. Henriques et al. NIMG 2020; 211, 116605; **2.** Henriques et al. MRM 2021; 86(6), 3111-3130; **3.** Cory et al. Polym Prepr. 1990; 31, 149; **4.** Mitra Phys Rev B. 1995; 51, 15074-15078; **5** Alves et al. NIMG 2022; 247, 118833. **6** Henriques et al. Proc. Intl. Soc. Mag. Reson. Med. 2023, 3933. **7** Henriques et al. Imaging Neuroscience 2023 ; 1 : 1-26. **8** Novello et al. NIMG 2022; 254, 119137

Sexual dimorphism in aging trajectories as measured through resting state functional connectivity and diffusion-weighted MRI

Elena Espinós-Soler[1]*, Egoa Ugarte-Pérez[1], Antonio Cerdán-Cerdá[1], Aroa S. Maroto[1], Santiago Canals[2], Silvia De Santis[1]

Instituto de Neurociencias de Alicante [1]Molecular Neurobiology and Neuropathology; [2]Cellular and Systems Neurobiology; *eespinos@umh.es

INTRODUCTION: Characterizing functional connectivity (FC) in ageing is crucial for understanding how neural networks change over time, identifying early markers of degeneration, and developing interventions to promote cognitive health and brain resilience in older adults. In addition, studying sex-specific trajectories is crucial to uncover sex-dependent vulnerabilities.

MRI provides a unique opportunity to characterize aging trajectories in a non-invasive manner and with high resolution. While human studies have uncovered several age- and sex-specific patterns [1,2], we need preclinical models to dig into their neurobiological correlates and test interventions.

METHODS: Longitudinal resting state fMRI and diffusion weighted MR with b-value 1000s/mm^2 were acquired on a 7T Bruker scanner in 17 Wistar rats of both sexes (9 females) from 91 to 731 postnatal days, corresponding to young, adult and old age (total 71 scans). After image preprocessing, resting state networks (RSNs) were extracted by group independent component analysis. Using generalized linear model, brain FC in each network was investigated as a function of age, sex and their interaction using FSL randomise. In addition, MD and FA maps from diffusion tensor model were extracted in each ROI and correlated with FC across RSNs at all ages.

RESULTS & DISCUSSION: Remarkably, our rodent model of aging displays several key characteristics seen in human fMRI studies. Connectivity between networks decreases in number and strength with age (Fig. 1a), while FC within networks follows a U-shaped trajectory (Fig. 1b). This increase in connectivity in senescence is more pronounced in frontal regions (Fig. 1c), in agreement with the PASA theory [3]. Interestingly, we uncovered a novel interaction between age and sex in frontal and superior regions, paralleled by sex-specific MD trends in the same areas (Fig. 1d), where a Bayesian model selection supports separate models for each sex. Females display more hyperconnectivity and better behavior in Morris Water Maze task in the elderly (data not shown), indicating a compensatory effect [4]. Finally, FA in white matter and MD in grey matter at earlier ages predict FC at later ages (Fig. 1e), indicating that microstructural changes precede functional outcomes.

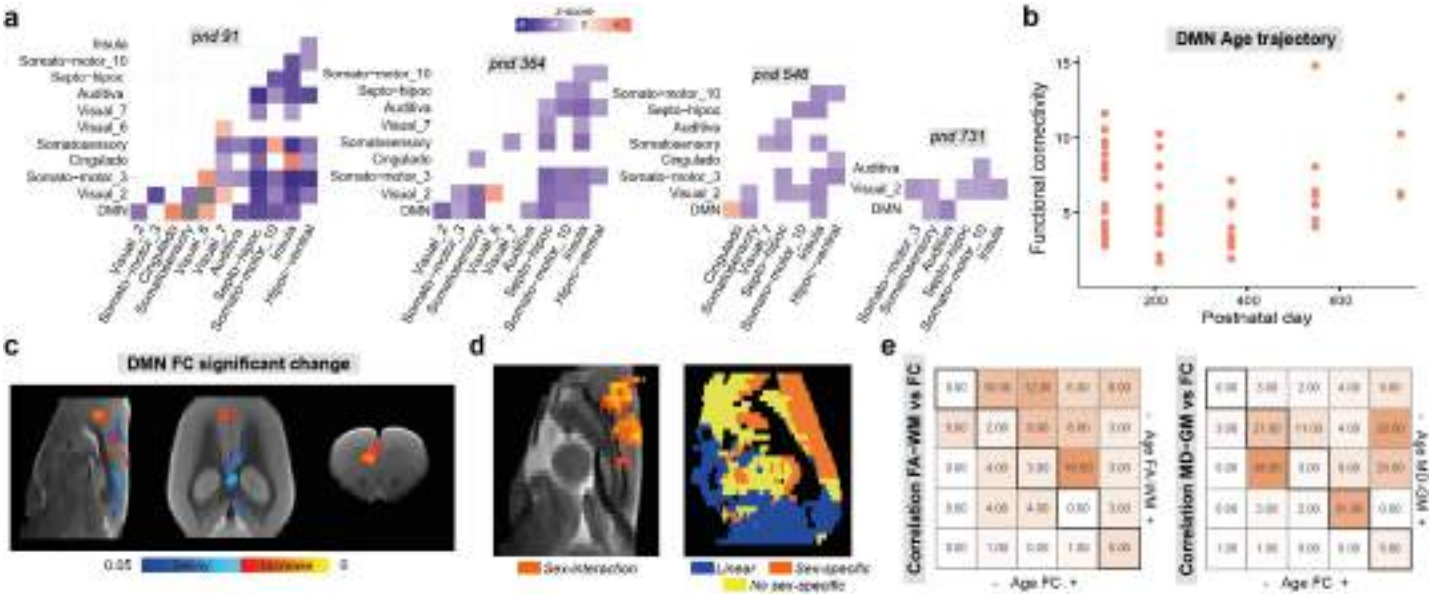

Figure 1 – a) Both number and strength of connections between different networks decreases over time. **b)** FC has U-shaped trend in different RSN, as shown in DMN. **c)** The decay in FC (pnd 91-400) is more pronounced in medial areas (blue) while the increase (pnd 400-731) is localized in anterior regions (red). **d)** Left: significant interactions between age and sex are localized in anterior networks such as the DMN, Insula, etc. Right: MD in anterior-superior areas best match a sex-specific second order model with age, and not a model combining both sexes. **e)** Number of significant correlations between FC and FA (left) and FC and MD (right) when testing different age pairs, summed over different regions. Preferential localization above the diagonal means that structural parameters at earlier ages are significantly correlated with functional connectivity at later ages.

References

1. MacDonald, M. E., & Pike, G. B. (2021). MRI of healthy brain aging: A review. NMR in biomedicine, 34(9), e4564. https://doi.org/10.1002/nbm.4564 ; **2.** Ficek-Tani, B., Horien, C., Ju, S., Xu, W., Li, N., Lacadie, C., Shen, X., Scheinost, D., Constable, T., & Fredericks, C. (2023). Sex differences in default mode network connectivity in healthy aging adults. Cerebral cortex (New York, N.Y.: 1991), 33(10), 6139–6151. https://doi.org/10.1093/cercor/bhac491 **3.** Davis, S. W., Dennis, N. A., Daselaar, S. M., Fleck, M. S., & Cabeza, R. (2008). Que PASA? The posterior-anterior shift in aging. Cerebral cortex (New York, N.Y.: 199[11), 18(5), 1201–1209. https://doi.org/10.1093/cercor/bhm155; **4.** Deery, H.A., Liang, E.X., Siddiqui, M.N. et al. Reconfiguration of metabolic connectivity in ageing. Commun Biol 7, 1600 (2024). https://doi.org/10.1038/s42003-024-07223-0

Hyperpolarisation-enhanced MRSI for Metabolic Imaging in Organ-on-a-Chip Devices

David Gómez Cabeza[1], Lluís Mangas-Florencio[1], Marc Azagra[1], Gergő Matajsz[1], **Irene Marco-Rius**[1]*

[1]Molecular Imaging for Precision Medicine, Institute for Bioengineering of Catalonia (IBEC), Barcelona, Spain
*[imarco@ibecbarcelona.eu]

Abstract

INTRODUCTION:
Organ-on-a-chip (OoC) platforms are microfluidic devices in which cells can be cultured in a 3D environment to replicate the structure and function of human organs. These microfluidic devices allow experiments to be carried out with a high degree of repeatability and experimental control and provide a route to personalised medicine and to replace animal testing. Many diseases affect cellular metabolism (e.g., cancers), and the changes in metabolic flux provide a marker to track the disease progression and response to treatment. In this work we are developing a multi-sample OoC platform to study the metabolic activity of cell-laden 3D structures noninvasively and with sufficient spatial resolution to distinguish each sample.
METHODS: We used dissolution Dynamic Nuclear Polarisation (dDNP) to hyperpolarise the metabolite [1-^{13}C]pyruvate and followed its metabolic conversion into lactate upon injection of pyruvate into a eight-well microfluidic platform containing immortalized human hepatocellular carcinoma cells (HepG2) under different metabolic conditions. Conventionally, dDNP experiments are restricted to 1 study sample for each dDNP injection (be it an animal or cells in a test tube). Our aim is to increase the experimental throughput and to use a more relevant biological model than cells. After the hyperpolarised sample filled the eight wells, we performed 8x16-voxel 13C chemical shift imaging and were able to spatially distinguish the eight samples.
RESULTS & DISCUSSION: We successfully parallelised the acquisition of metabolic imaging, understanding the role of rich media, cell lysis and extracellular NADH in converting pyruvate to lactate. With this type of voxel spectroscopic metabolic imaging provided by CSI, we observed three different phenomena in a single experiment. First, we observed the increase of lactate production in a rich media supplemented with Glu and Gln due to an increase in glycolytic activity, as previously reported in literature[1]. Second, extracellular NADH helps adjust the redox balance, in alive (indirectly) and lysed (directly) cells, resulting in an increase in lactate production[2]. Third, by lysing cells (and adding NADH), the metabolism of lactate was significantly increased thanks to avoiding the main limiting factor of the reaction, the transport of pyruvate into the cell tanks to the MCT1 transporter[3]. Yet, despite the advantages of the strategy, better detection coils with large areas (we employed a volume coil) and better *k*-space sampling with low pulsing are required to improve the resolution and aim for temporal imaging [4]. Nonetheless, our results are the first to show such level of parallelisation with high spatial resolution for cellular studies using microfluidics and HP-MRSI, contributing to incorporating hyperpolarised NMR into the field of precision medicine.

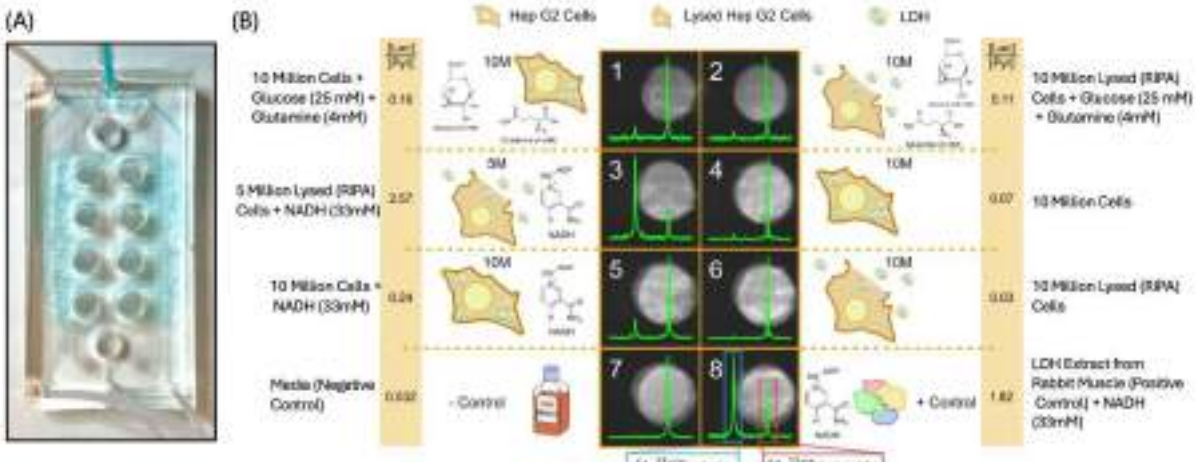

Figure 1 – (A) Photograph of the microfluidic chip. (B) 1H-MRI with 13C-MRSI spectra overlaid acquired with Chemical shift imaging. The condition (i.e. cell count, lysed/intact, media composition) studied in each well is indicated.

References

1. *M. Grashei, P. Biechl, et. al. Cancers, 14(7):1845, 2022.*
2. *W. Xiao, R. Wang, et. al. Antioxidants & redox signalling, 28(3):251–272, 2018*
3. *Y. Rao, S. Gammon, et. al. Proceedings of the National Academy of Sciences, 117(36):22378–22389, 2020*
4. Yeste, J., Azagra, M., Ortega, M. A., Portela, A., Matajsz, G., Herrero-Gómez, A., Kim, Y., Sriram, R., Kurhanewicz, J., Vigneron, D. B., **Marco-Rius, I.** *Parallel detection of chemical reactions in a microfluidic platform using hyperpolarized nuclear magnetic resonance.* Lab Chip. **2023.** 23. 4950-4958.

Fetpype: An Open-Source pipeline for reproducible Fetal Brain MRI Analysis

Gerard Martí-Juan[1,†], Thomas Sánchez[2,3,†], David Meunier[4], Steven Jia[4], Meritxell Bach Cuadra[2,3], Miguel A. González Ballester[1,5], Oscar Camara[1], Elisenda Eixarch[6,7,8], Gemma Piella[1], Guillaume Auzias [4*]

[1] BCN MedTech, Department of Engineering, Universitat Pompeu Fabra, Barcelona, Spain; [2] CIBM - Center for Biomedical Imaging, Switzerland; [3] Department of Diagnostic and Interventional Radiology, Lausanne University Hospital and University of Lausanne, Switzerland; [4] Aix-Marseille Université, CNRS, Institut de Neurosciences de La Timone, Marseille, France; [5] ICREA, Barcelona, Spain; [6] BCNatal Fetal Medicine Research Center (Hospital Clínic and Hospital Sant Joan de Déu); [7] Institut d'Investigacions Biomèdiques August Pi i Sunyer (IDIBAPS), Barcelona, Spain; [8] Centre for Biomedical Research on Rare Diseases (CIBERER), Barcelona, Spain; *guillaume.auzias@univ-amu.fr; † These authors contributed equally to this work.

Abstract

INTRODUCTION: Fetal brain Magnetic Resonance Imaging (MRI) is crucial for assessing neurodevelopment in utero. However, analyzing this data presents significant challenges due to fetal motion, low signal-to-noise ratio, and the need for complex multi-step processing, including motion correction, super-resolution reconstruction, and segmentation. While various specialized tools exist for individual steps, integrating them into robust, reproducible, and user-friendly workflows that go from raw image to volume and surface analysis is not straightforward. This lack of standardization hinders reproducibility across studies and limits the adoption of advanced analysis techniques for researchers and clinicians. To address these challenges, we introduce Fetpype, an open-source Python library designed to streamline and standardize the preprocessing and analysis of fetal brain MRI data**.**

METHODS: Fetpype integrates several established neuroimaging software principles and tools to create a cohesive and extensible framework, which we summarize in four points. (1) Data Standardization: Fetpype expects input data organized according to the Brain Imaging Data Structure (BIDS) standard, promoting interoperability and simplifying data management. (2) Containerization: Individual processing tools are encapsulated within Docker or Singularity containers. This ensures reproducibility and reduces installation issues, providing a better experience for the end user. (3) Workflow Management: The Nipype library is used to construct processing workflows: it provides a robust interface for combining different steps from different containers or packages, facilitating data caching and parallelization, and allowing pipelines to be easily shareable. (4) Configuration: Pipeline configuration is managed using simple YAML files, allowing users to easily select between different modules or parameters without directly modifying the code**.** The current implementation of Fetpype integrates modules for data preprocessing, high resolution reconstruction (NeSVoR [1], SVRTK, or NiftyMIC), and segmentation (using existing, popular pipelines like BOUNTI [2] or the developing human connectome project pipeline).

RESULTS & DISCUSSION: Fetpype offers a valuable resource for the fetal MRI community by providing a standardized, reproducible and flexible open-source platform for preprocessing and analysis. The pipeline is already being used across three different sites, for more than 320 subjects. We believe this tool can facilitate research, improve comparability between studies, and foster collaboration. The pipeline is publicly available on GitHub (https://github.com/fetpype/fetpype), and its open-source nature and modular design facilitate community involvement: researchers can integrate their own tools by creating corresponding Nipype interfaces and container wrappers, following the package contribution guidelines. We welcome the ISMRM community to use, test, and contribute to Fetpype.

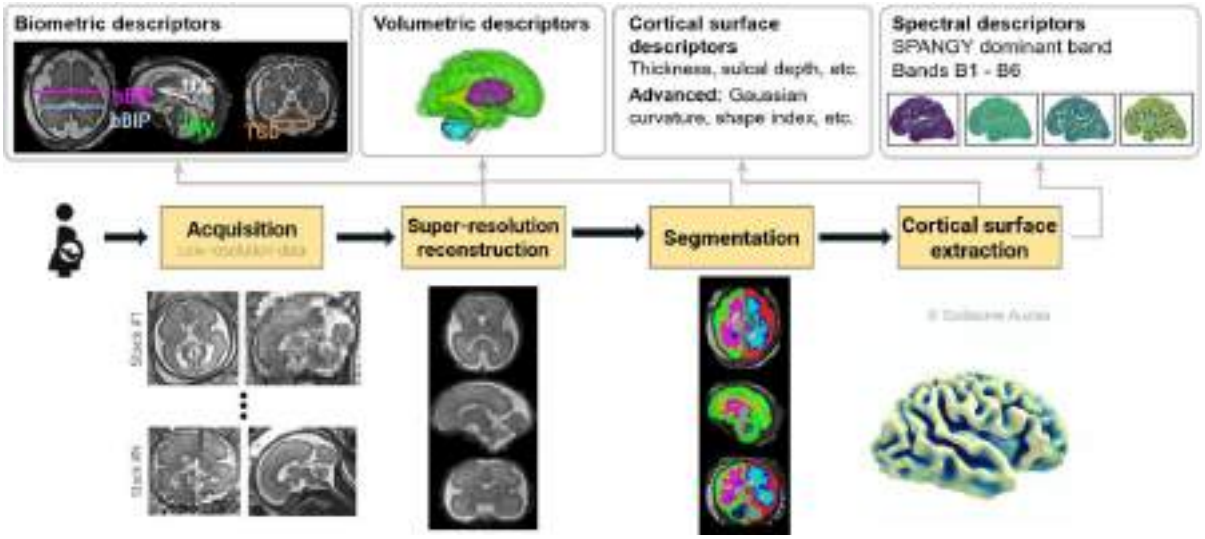

Figure 1 – Overview of the fetal brain MRI processing workflow that would be integrated within Fetpype, from acquisition to surface extraction.

References

[1] J. Xu *et al.*, "NeSVoR: Implicit Neural Representation for Slice-to-Volume Reconstruction in MRI," in *IEEE Transactions on Medical Imaging*, vol. 42, no. 6, pp. 1707-1719, June 2023, doi: 10.1109/TMI.2023.323621

[2] A. Uus. *et al.* "BOUNTI: Brain vOlumetry and aUtomated parcellatioN for 3D feTal MRI", in *eLife* 12:RP88818, 2023, doi: 10.7554/eLife.88818.1

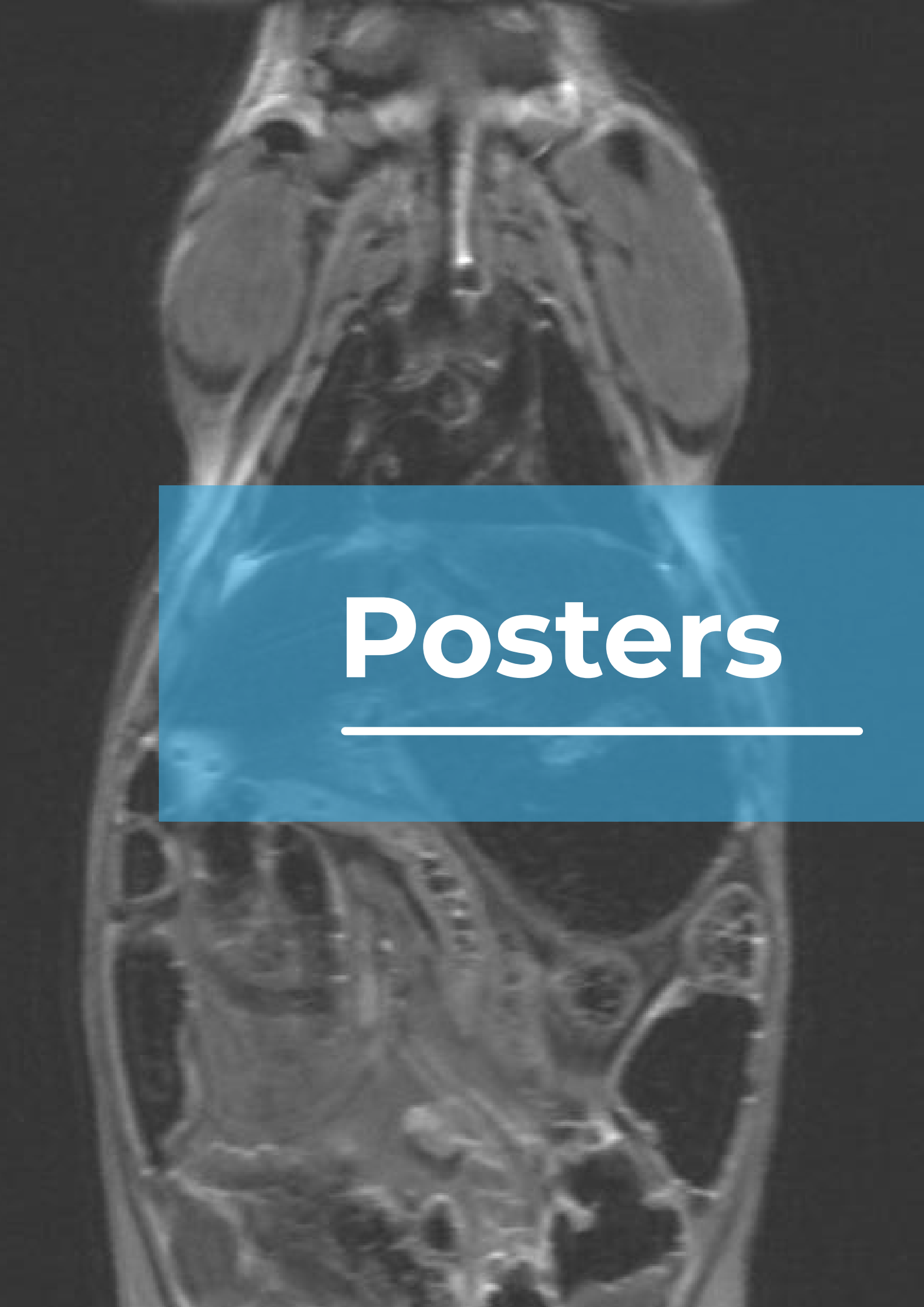

Posters

3rd July - Clinical Session

Poster	First name	Last name	Title
P1	Sergio Manuel	Solis Barquero	Splenic Switch-Off as a marker of adequate adenosine response in stress perfusion cardiac magnetic resonance using T1 mapping
P2	Elisa	Moya-Sáez	A motion-corrected reconstruction for highly undersampled perfusion CMR
P3	Alexandra	Santos	White matter microstructure is differentially impacted by cerebral amyloid angiopathy, neurofibrillary tangles and neuritic plaques co-pathology
P4	M. Carmen	Martínez-Bisbal	Study of the vulnerability of atheroma plaques in explants by NMR spectroscopy
P5	Alessandra	Gallo	Unsupervised learning in migraine using advanced diffusion metrics
P6	Sydney	Williams	Hardware Testing for Dynamic Field Probe Integration into a 7 Tesla Head Coil
P7	Ana	Matoso	Benchmarking Deep Learning Approaches for RANO Criteria Classification in Glioblastoma
P8	Jose	Borreguero Morata	Correction of distortions created by fields inhomogeneities in a Halbach scanner
P9	Lili Fanni	Toth	Conventional MR spectroscopy sequences combined with machine learning allow distinguishing between IDH mutation and grade in astrocytomas
P10	Marta	Padrela Loureiro	Can Patch-Based Harmonization in Radiomics of Longitudinal Glioblastoma MRI Improve Tumor Region Labelling?
P11	Begoña	Garate	Optimization of the magnetization transfer pulse parameters for neuromelanin contrast enhancement in the substantia nigra
P12	Carles	Roqué Greoles	Detection of spatial artifacts on resting state functional magnetic resonance data
P13	Jorge	Rueda Ramos	A comparative study of deep learning models to synthesize post-contrast imaging

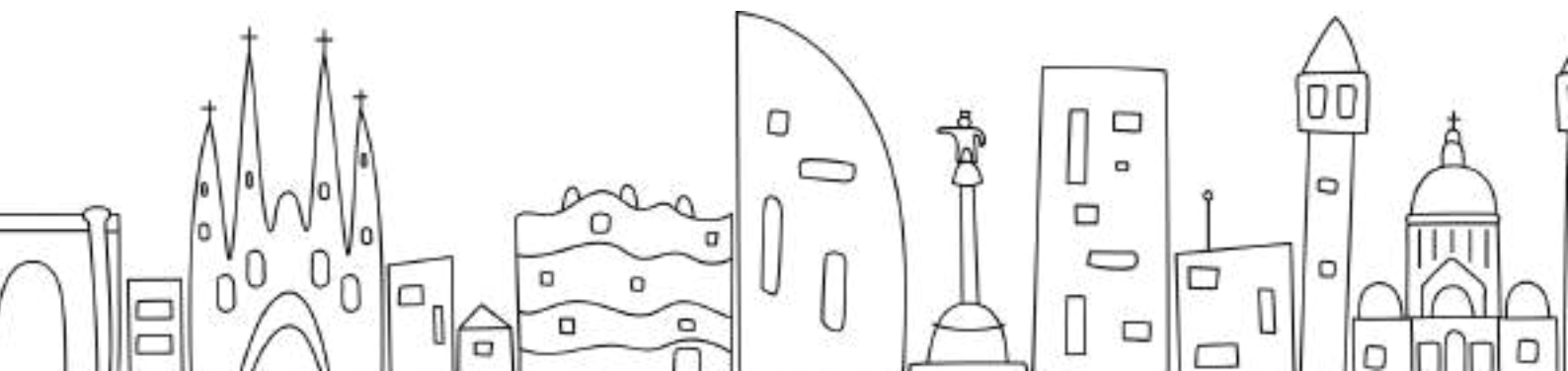

P14	Lucianna	Lopes do Couto	New perspectives for the analysis of intrinsic fMRI data and the improvement of automated diagnosis of Autism spectrum disorders: application of non-standard connectivity metrics, deconvolution approaches, and classifiers
P15	Andreia	Gaspar	Open-MOLLI for All: Advancing Open-Source, Vendor-Agnostic T1-mapping One System at a Time, Now on GE!
P16	Pablo	Villacorta-Aylagas	A Free and Open-Source Web Application for Pulse Sequence Development and Simulation
P17	Ana	Fouto	High-resolution advanced diffusion MRI of rectal cancer surgical specimens: correlating microstructural characteristics with histology
P18	Iñigo	Herrero Vidaurre	Olfactory functional MRI: Application to evaluate brain activation patterns in women with sexual interest-arousal disorders
P19	Andrea	Cabero-Arnold	Using ADC-Based Measurements to Predict Functional Recovery and Malignant Infarction in Acute Ischemic Stroke of the Anterior Circulation
P20	Marina	Mas Argemí	Whole-brain functional connectivity in the A4 and LEARN datasets to study preclinical Alzheimer?s Disease
P21	Benito	Farina	A Radiomics-Based Signature for Identifying Successful Response to TMZ Treatment in Murine GL261 Glioblastoma: leveraging the peritumoral zone
P22	Paula	Caballero Lillo	Different Models, Different Brain Age Gaps in Chronic Musculoskeletal Pain
P23	Irene	Guadilla	White matter alterations after physiotherapy intervention in chronic musculoskeletal pain patients using free-water corrected DTI
P24	Verónica	Aramendía-Vidaurreta	A Multicenter Kidney Research Study about the Participant Insights on Data Sharing and Artificial Intelligence
P25	Cèlia	Cruz Escalera	A Framework for Organizing and Processing DWI Data in the FTLDNI Database
P26	Helena	Sánchez Ulloa	Deep learning segmentation for morphological assessment of optic nerve integrity in optic neuritis

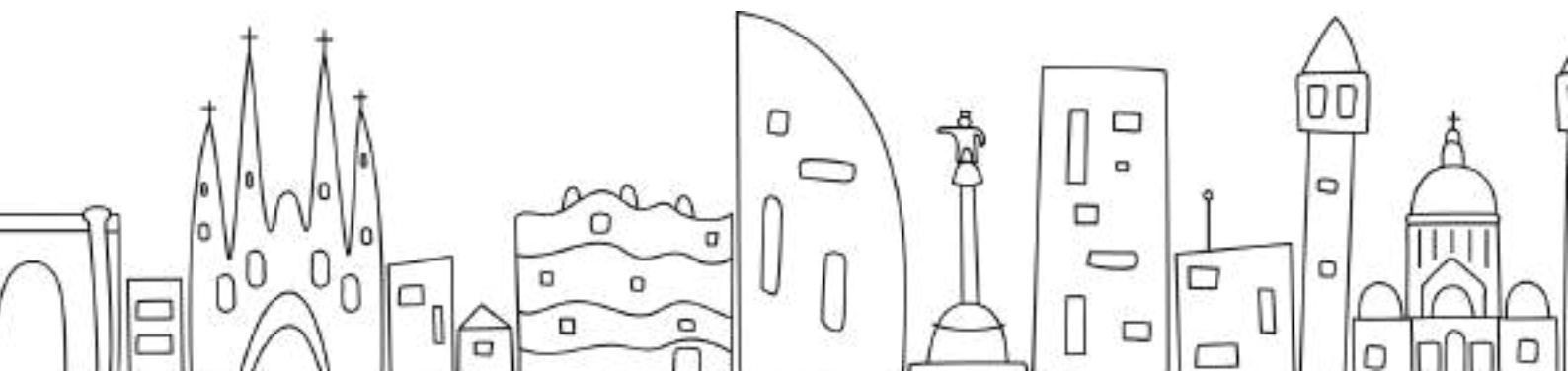

4th July - Preclinical Session

Poster	First name	Last name	Title
P27	Catarina	Neves de Carvalho	Accelerated EPG-based myocardial T1 mapping with PENGUIN
P28	Egoa	Ugarte Pérez	Microstructural MRI trajectories in healthy aging: sexual dimorphism, functional and behavioral correlates
P29	Maximilian	Eggl	Efficient Model Fitting of Diffusion MRI via Simulation-Based Inference
P30	Vega	Lloveras Monserrat	Tumor detection via MRI using metal-free organic radical dendrimers as contrast agents
P31	Vicent	Ribas	Hyperpolarized NMR Reveals Distinct Liver Metabolic Alterations in Female Mouse Models of Obesity
P32	Paula	Carretero Navarro	Study of the relationship between tumor metabolism modulators, IDO1, IDH and ChK-?, and the expression of the immune checkpoint, PDL1, in glioblastoma models.
P33	Ana	Gomes	Quantification of healthy aging of BM vasculature by DCE-MRI
P34	Raquel	González-Alday	Evaluating neuroinflammation in-vivo in a mouse model using multiparametric MRI, with ex-vivo insights from immunofluorescence and HRMAS spectroscopy
P35	Raquel	González-Alday	Resomapper: a user friendly and versatile pipeline for multiparametric MRI data processing and mapping
P36	Patricia	Martínez-Tazo	Leveraging the MouseX DW-ALLEN atlas and the QUINT workflow to match MR and histological data in a mouse model of neurodegeneration
P37	Marta	Rodrigo Díaz	Diet-induced obese mice show altered cerebral mean diffusivity and FA values during fasting
P38	Lluís	Mangas Florencio	A Custom Bioreactor for dDNP-NMR Studies of 3D Cell Models
P39	Adriana	Ferreiro De Aguiar	Cerebral magnetic resonance imaging insights into bariatric surgery-induced changes in obese mice
P40	Darwin	Córdova-Ascurra	Neuroinflammation and Metabolic changes induced by medium-term High-fat diet in an IL-1R1KO murine model: An MRI-based study

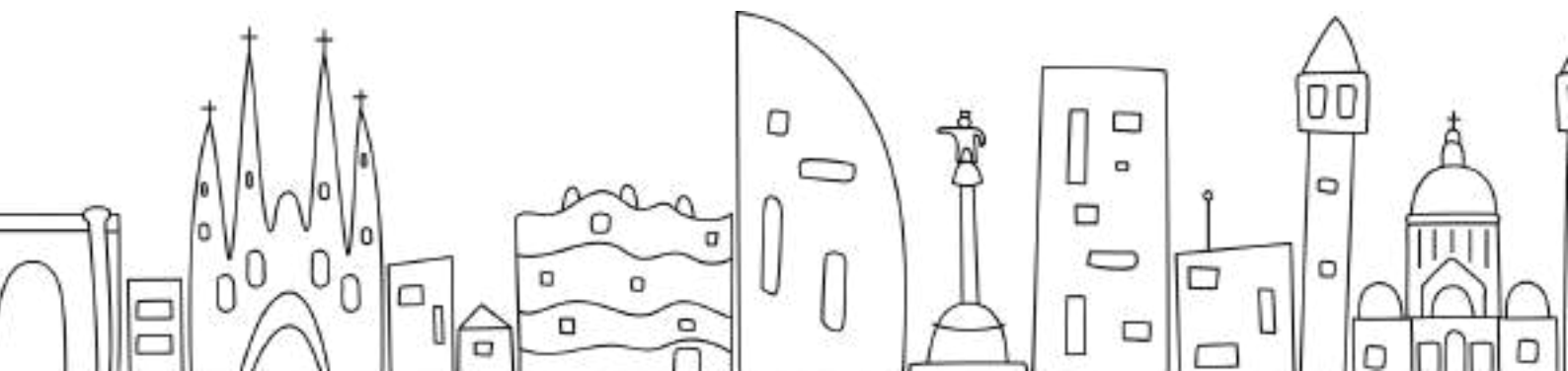

P41	Guillem	París	Towards Robust Diffusion MRI Biomarkers: A Reliability and Repeatability Study
P42	Ana Paula	Candiota	Advanced AI strategies to estimate inflection point of response/relapse in preclinical GL261 glioblastoma using T2w MRI data
P43	Clàudia	Calvet-Soler	T2* MRI hiperintensity in a rat model of intracerebral hemorrhage are related to dynamic changes in perilesional edema and clot formation
P44	Ana Paula	Candiota	Bridging 3T and 7T MR: Towards Unified Metabolic Profiling for Preclinical Brain Tumor Studies
P45	Alejandro	Hinojosa-Moscoso	Fear conditioning pathways: Psychophysiological interaction analysis of the basolateral amygdala
P46	Andrea	Díaz Pérez	T2 heterogeneity analysis of the infarcted region reveals a new aspect of cerebroprotection by SAHA in stroke
P47	Gergo	Matajsz	13C metabolic imaging in chorioallantoic membrane (CAM) assays: methods development and optimisation
P48	Rui	Simoes	Advanced Diffusion MRI in the Mouse Brain in vivo at 3 Tesla
P49	Athanasios	Grigoriou	Simplicity is a virtue: histology-informed model comparison selects simple diffusion representations in a colorectal cancer metastasis specimen
P50	M. Carmen	Martínez-Bisbal	micro-MRI as a tool to determine neurodevelopmental changes derived from Afadin protein perturbation
P51	José	Vidal Gancedo	New metal-free MRI contrast agents based on organic radical dendrimers
P52	Ramón	Iglesias Rey	2D Glioblastoma Segmentation in Rat and Mouse Models Using U-Net Architecture
P53	Justino	Rodríguez Galván	Diffusion MRI Simulation Takes Advantage of Higher Order Models than DTI

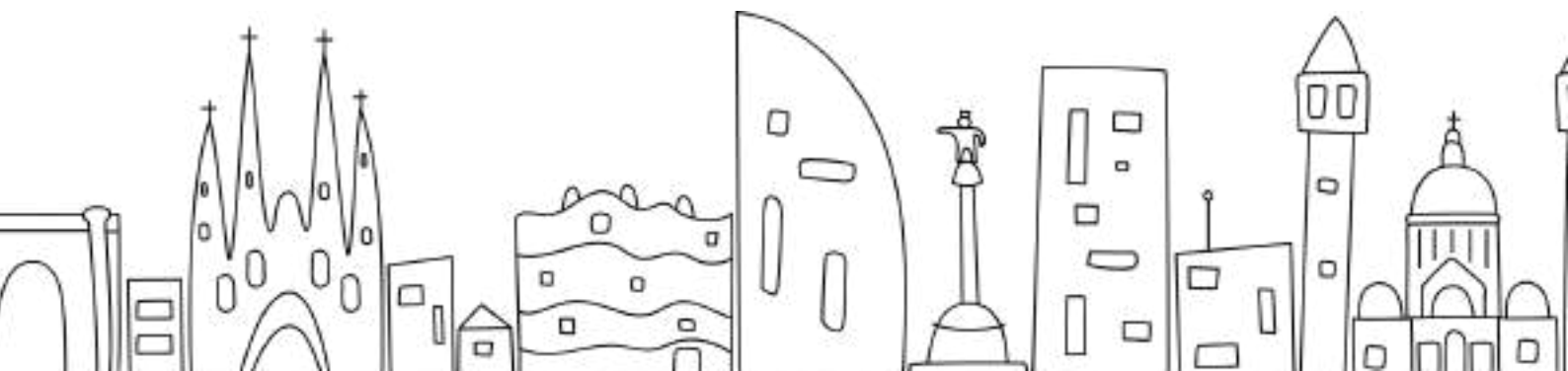

Splenic Switch-Off as a marker of adequate adenosine response in stress perfusion cardiac magnetic resonance using T1 mapping

Sergio M. Solis-Barquero[1-2], Verónica Aramendia-Vidaurreta[1-2], Ana Ezponda[1], Marta Vidorreta[3], Marina Pascual[4], Gorka Bastarrika[1], María A. Fernández-Seara[1-2*]

[1]Department of Radiology, Clínica Universidad de Navarra, Pamplona, Spain; [2]IdiSNA, Instituto de Investigación Sanitaria de Navarra, Spain; [3]Siemens Healthcare, Madrid, Spain; [4]Department of Cardiology, Clínica Universidad de Navarra, Pamplona, Spain *mfseara@unav.es

Abstract

INTRODUCTION: Stress perfusion cardiac magnetic resonance (CMR) uses adenosine to detect ischemia. One third of false-negative CMR results are related to inadequate adenosine response.[1] Guidelines recommend a heart-rate increase of 10 beats-per-minute (BPM), after three minutes of adenosine infusion for stress acquisition. However, this not always indicates increased myocardial perfusion.[2] Splenic switch-off, defined as splenic perfusion decrease, may be a potential marker of adequate stress.[3] It has been assessed using contrast first-pass,[3] ASL,[4] PET,[5] and through a reduction in splenic T1 values from rest to stress.[6] Only two studies have explored T1 mapping as a marker of switch-off.[6,7] Moreover, the authors of the first study have raised doubts about the validity of their results.[8]Thus, this study aimed to further investigate splenic T1 mapping for assessing splenic switch-off, given the limited existing data.

METHODS: Study was approved by local Ethics Committee. All participants gave written informed consent to participate. Adult patients (>18 years) scheduled for CMR were prospectively recruited. Scans were performed using a 1.5T Aera MRI (Siemens) with an 18-channel body and 32-channel spine coils. Fixed adenosine dose of 140 µg/kg/min was used for stress imaging. T1 mapping used a MOLLI 5(3)3(0) sequence.[9] Motion-corrected T1 maps were automatically generated and mean splenic rest and stress T1 values were obtained from manually drawn ROIs covering visible splenic tissue. $\Delta T1_{spleen}$ was computed ($T1_{stress}$-$T1_{rest}$). Automatically segmented perfusion maps were generated by an ECG-triggered bSSFP sequence for rest and stress first-pass imaging (60 images/heartbeats, free-breathing, gadolinium dose:0.75mmol/kg).[10] Semi-quantitative splenic perfusion analysis was performed on motion-corrected images, and ΔSI_{spleen} (percentage change in signal intensity normalized by baseline) was calculated.

Switch-off classification was conducted by two independent radiologists based on first-pass images (reference standard). Normality was tested with Shapiro-Wilk. Splenic T1 was analyzed using ART[11] (non-normal distribution), followed by mixed-ANOVA for rest vs. stress condition and switch-off vs. failed switch-off groups. ART-C[12] with Bonferroni correction was used for post-hoc comparisons between rest and stress within each group when interaction was significant. ΔT1 and ΔSI differences between groups were tested using Wilcoxon rank-sum tests. Spearman's rank correlation assessed relationships between ΔSI and ΔT1 values. ROC curves were generated for ΔT1 and ΔSI data, with AUC and Youden Index calculated for switch-off detection. All tests were carried-out in RStudio, statistical significance was set at p <0.05.13

RESULTS & DISCUSSION: Fifty-nine patients were scanned, with twelve patients excluded due to incomplete scans, heart conditions outside the scope, or not visible spleen. The final cohort included forty-seven patients (thirty-five males, mean age=65±13 years), and 74.5% experienced splenic switch-off. Similar switch-off proportion (72%) has been reported.[5] Splenic T1 post-hoc showed statistically significant differences between the conditions only for the switch-off group (p<0.001), where splenic T1 values decreased from rest to stress. Statistically significant differences were obtained between groups for $\Delta T1_{spleen}$(p=0.001) and ΔSI_{spleen}(p<0.001) and a statistically significant correlation was found between the two parameters. Statistically significant differences in $\Delta T1_{spleen}$ and ΔSI_{spleen} between groups align with previous findings.[3,6,7] The $\Delta T1_{spleen}$ threshold was lower than previous reports (≥30ms).[6 7] Lower splenic T1 values during stress likely resulted from adenosine-induced vasoconstriction reducing splenic perfusion, as T1 is affected by blood volume (water content).[13] Further studies should explore adenosine's effect on splenic T1 beyond blood volume reduction. This work suggests that splenic T1 values can identify splenic switch-off during adenosine stress CMR in a clinical population.

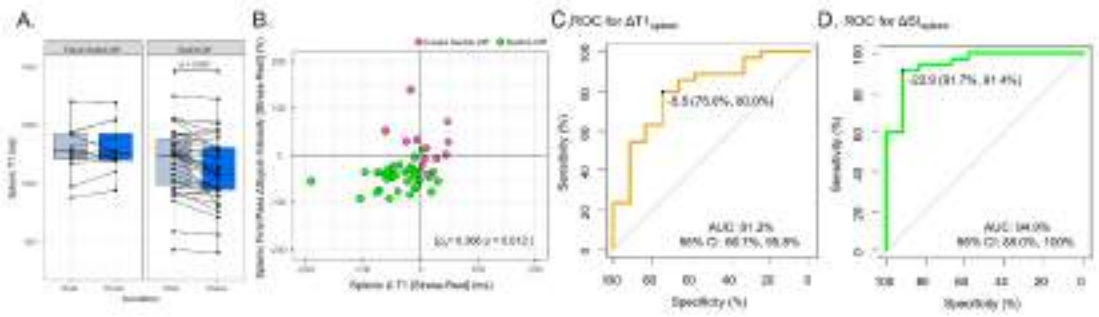

Figure 1 – A. Boxplot for splenic T1 measurements in switch-off and failed switch-off. **B.** Correlation between ΔT1 and ΔSI for splenic switch-off and failed splenic switch-off groups. **C.** ROC curves for ΔT1 for the classification of switch-off and **D.** ROC curve for ΔSI for the classification of switch-

References

1. Kidambi A, et al. Journal of Magnetic Resonance Imaging 2016; 43: 566–573.; **2.** Modi BN, et al. International Journal of Cardiovascular Imaging 2018; 34: 1117–1125.; **3.** Manisty C, et al. Radiology 2015; 276: 732–740. **4.** Aramendía-Vidaurreta V, et al. Journal of Magnetic Resonance Imaging 2022. doi:10.1002/jmri.28460.; **5.** Patriki D, et al. Journal of Cardiovascular Magnetic Resonance 2021; 23. doi:10.1186/s12968-020-00696-y.; **6.** Liu A, et al. Journal of Cardiovascular Magnetic Resonance 2017; 19: 1–10.; **7.** Wan FF, et al. Cardiovascular Imaging Asia 2022; 6: 88.; **8.** Liu A, Journal of Cardiovascular Magnetic Resonance 2023; 25. doi:10.1186/s12968-023-00935-y.; **9.** Messroghli DR, et al. Magn Reson Med 2004; 52: 141–146.; 10. Kellman P, et al. Journal of Cardiovascular Magnetic Resonance 2017; 19. doi:10.1186/s12968-017-0355-5.; **11**. Wobbrock JO, 29th Annual ACM CHI Conference on Human Factors in Computing Systems. 2011, pp 143–146.; **12.** Elkin LA, UIST 2021 - Proceedings of the 34th Annual ACM Symposium on User Interface Software and Technology. Association for Computing Machinery, Inc, 2021, pp 754–768.; **13.** Levick C, et al. PLoS One 2019; 14. doi:10.1371/journal.pone.0221066.

A motion-corrected reconstruction for highly undersampled perfusion CMR

Elisa Moya-Sáez[1*], Rosa-María Menchón-Lara[1,2], Rita G. Nunes[3], Teresa M. Correia[4,5], Carlos Alberola-López[1]

[1]LPI, University of Valladolid, Spain; [2]Universidad Politécnica de Cartagena, Spain; [3]ISR–Lisboa and Department of Bioengineering, IST, University of Lisbon, Portugal; [4]Center of Marine Sciences-CCMAR, Faro, Portugal; [5]School of Biomedical Engineering and Imaging Sciences, King's College London, UK *elisa.moya@uva.es

Abstract

INTRODUCTION: First-pass perfusion cardiac MR (pCMR) facilitates the non-invasive diagnosis of coronary artery disease by acquiring dynamic images during the rapid passage of a contrast bolus through the heart[1]. A trade-off exists between heart coverage and temporal/spatial resolution. To alleviate this shortcoming, undersampled acquisitions followed by constrained reconstruction methods have been proposed. Also, there is a growing preference for acquiring images during free-breathing, as it offers increased reliability and enhanced patient comfort. In this context, the incorporation of motion correction (MoCo) approaches becomes essential for both free-breathing acquisitions and for correcting residual motion due to imperfect breath-holding. However, MoCo tends to degrade as acceleration increases. This work proposes a pipeline for a motion-corrected reconstruction of highly undersampled pCMR acquisitions. A novel rigid MoCo step, formulated exclusively in k-space, is proposed.

METHODS: **Data** Three patients underwent a REST pCMR acquisition on a Philips 3T Achieva scanner. Acquisitions parameters were: in-plane resolution = 1.6 × 1.6 mm^2, FOV = 320×320 mm^2, slice thickness = 10 mm, 32 coils, and scan time = 1 min. A radial sampling was used with 10 spokes per frame (acceleration factor ~20x); however, prior to any other step, the k-space was gridded onto a Cartesian grid. Sensitivity maps were estimated using ESPIRIT[2].

Proposed approach: The main steps of the motion-corrected reconstruction pipeline are: 1) Rigid MoCo in k-space with K-CC-MoCo[3]; this method performs a pairwise registration formulated exclusively in k-space with the normalized cross correlation as the registration metric defined between a synthetic reference and the k-spaces of each frame. To focus the minimization on the heart region, a ROVir coil-compression approach[4] is employed. 2) Low Rank + Sparse (L+S) reconstruction[5] of the rigidly motion-corrected k-space. 3) Pair-wise non-rigid image-based MoCo of the reconstructed dynamic images to correct for slight residual motion[6].

RESULTS & DISCUSSION: Figure 1 shows the results for the motion-corrected reconstructions in a representative patient in which bulk motion caused by imperfect breath-holding is observable. The results show that the application of MoCo approaches notably reduces blurring when all the frames of the dynamic images are combined. Also, we should highlight that the rigid MoCo step in k-space becomes crucial for an accurate overall MoCo; specifically, the non-rigid motion-corrected images that were reconstructed without this first step (Fig 1.C) present a poorer correction compared to the images obtained with the three-steps proposed approach (Fig 1.D).

ACKNOWLEDGMENTS Work supported by “la Caixa” Foundation and FCT with project [LCF/PR/HR22/00533t].

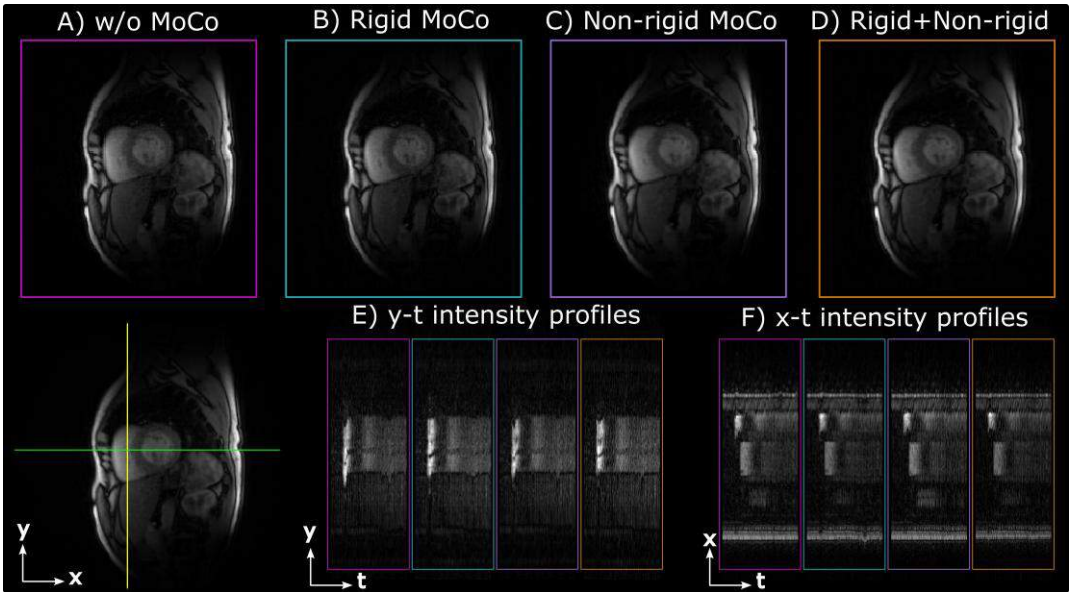

Figure 1 – Sum along frames of the reconstructed dynamic images for the pipelines A) without MoCo, B) with only rigid k-space-based MoCo. C) with only non-rigid image-based MoCo, and D) with both rigid (in k-space) and non-rigid (in image-space) MoCo. Also, intensity profiles for E) y-t direction (yellow line, foot-head) and F) x-t direction (green line, right-left).

References

1. Fair M.J., et al. J Cardiovasc Magn Reson. 2015;17(1),68; **2.** Uecker M., et al. Magn Reson Med 2021;71(3),990-1001; **3.** Moya-Sáez E., et al. ISMRM 2025. **4.** Kim D., et al. Magn Reson Med 2021; 86(1),197-212; **5.** Otazo, R., et al; Magn Reson Med 2015;*73*(3),1125-1136; **6.** Menchón-Lara R.M., et al. Signal Processing 2023;202,108771.

White matter microstructure is differentially impacted by cerebral amyloid angiopathy, neurofibrillary tangles and neuritic plaques co-pathology

Alexandra Santos[1], Francisco C. Almeida[1], Kathryn Gauthreaux[2], Charles N. Mock[2], Walter A. Kukull[2], John F. Crary[3], Tiago Gil Oliveira[1]

[1]Life and Health Sciences Research Institute, University of Minho, Braga; [2]National Alzheimer's Coordinating Center, University of Washington; [3]Neuropathology Brain Bank & Research Core, Icahn School of Medicine, Mount Sinai. *tiago@med.uminho.pt

Abstract

INTRODUCTION:
White matter (WM) is affected by and serves as a pathway to neurofibrillary tangles (NFTs) propagation in Alzheimer's disease (AD). Additional neuropathological changes frequently coexist in AD, alongside NFTs and neuritic plaques (NPs) accumulation, further accelerating the progression of dementia. For instance, cerebral amyloid angiopathy (CAA) associates with NPs to exacerbate NFTs accumulation [1]. We aim to study how these co-pathologies differently affect WM integrity in AD.

METHODS:
We performed a cross-sectional study of antemortem diffusion tensor imaging (DTI) data according to participants' postmortem NFTs, NPs and CAA neuropathology, from the National Alzheimer's Coordinating Center (NACC) dataset. Our study cohort comprised 26 AD participants, with MRI and autopsy data collected within a maximum interval of four years. DTI metrics were compared between neuropathology-defined groups and correlated to Clinical Dementia Rating (CDR) scores and hippocampal volumes. MRI data provided by the NACC was acquired at multiple Alzheimer's Disease Research Centers on 3T scanners. The DTI preprocessing pipeline included threshold principal component analysis denoising, and corrections for Gibbs ringing, EPI distortions, eddy currents, and motion using DIPY, FSL, and ANTs. DTI metrics were extracted for regions defined by the JHU-ICBM-DTI-48 WM atlas. Hippocampal volumes were obtained from volumetric T1-weighted images using FreeSurfer.

RESULTS & DISCUSSION:
We found statistically significant asymmetric DTI changes in several WM regions between Braak NFTs stages III/IV and V/VI, and across CAA pathological burden, with increased mean, radial and axial diffusivities. CAA demonstrated a greater WM impact on the posterior right hemisphere while NFTs had greater impact on the left hemisphere (Fig.1). This posterior predominance of CAA effects has also been observed in previous studies [2]. CAA-NFTs co-pathology effects were observed in the splenium of the corpus callosum, as significant changes were observed in both CAA and NFTs analyses (Fig.1) but disappeared after correction for the co-pathology. DTI metrics correlated significantly with CDR scores and hippocampal volumes across multiple regions among the ones identified as exhibiting neuropathology-related diffusivity changes, supporting the concept that these WM changes may reflect a worsening of disease outcomes. Our results suggest that WM integrity is differentially impacted by AD neuropathology, with CAA and NFTs influencing each other's effects on WM microstructure, highlighting the importance of considering the influence of CAA co-pathology on WM degeneration in AD.

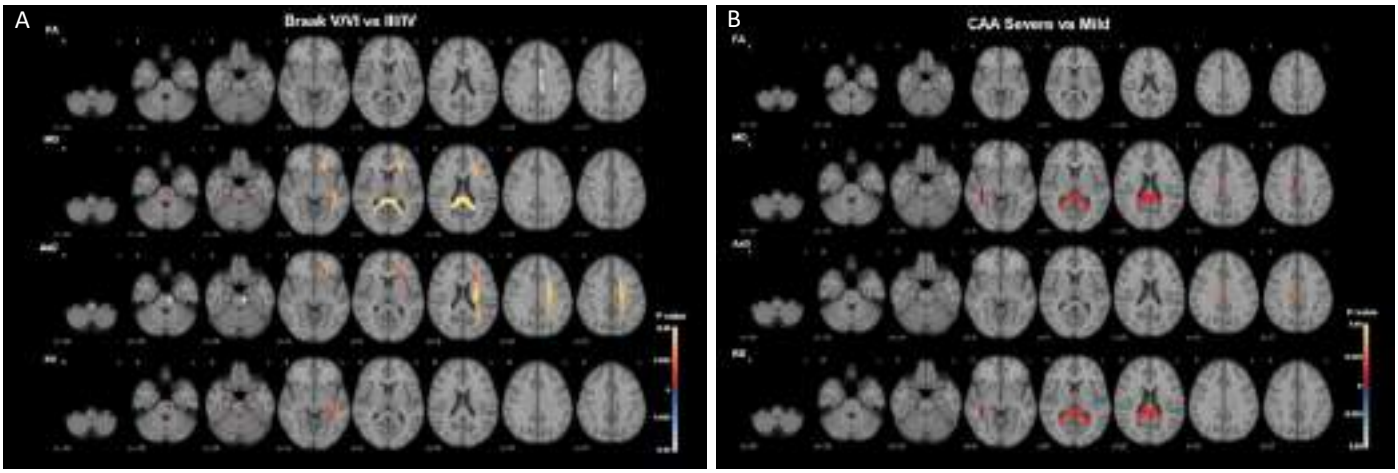

Figure 1 – Asymmetric regional changes in WM integrity across advanced Braak stages and CAA severity in AD. Axial views of WM ROIs with differences in DTI metrics linear model residuals for age, sex and MRI-to-death interval, between Braak stages III/IV and V/VI (A) and severe and mild CAA (B), overlaid on the MNI 152 T1 template. Only statistically significant comparisons ($p < 0.05$ according to the Wilcoxon test (A) and Kruskal-Wallis followed by Dunn's post-hoc test (B) are shown.

References

1. Godrich D, Pasteris J, Martin ER, Rundek T, Schellenberg G, Foroud T, et al. Cerebral amyloid angiopathy impacts neurofibrillary tangle burden and cognition. Brain Commun. 2024;6(6):fcae369; **2.** Deasy L, Laurent-Chabalier S, Wacongne A, Parvu T, Mura T, Thouvenot E, et al. Diagnostic Accuracy of Posterior/Anterior Periventricular WMH Ratio to Differentiate CAA From Hypertensive Arteriopathy. Stroke. 2024;55(8):2086-93.

Study of the vulnerability of atheroma plaques in explants by NMR spectroscopy

Carmen Mezquita-Blanch[1,2], Marina Botello-Marabotto[1,3,4], M. Carmen Martínez-Bisbal[1,2,3,4*], Pilar Medina[5], Andrea Bernardos[1,4,6,7], Ramón Martínez-Máñez[1,3,4,6,7], Manuel Miralles[5,8,9], Emma Plana Andani[5,8]

[1] Instituto Interuniversitario de Investigación de Reconocimiento Molecular y Desarrollo Tecnológico (IDM), Universitat Politècnica de València - Universitat de València, Valencia, Spain; [2] Departamento de Química Física, Universitat de València, Valencia, Spain; [3] Unidad Mixta de Investigación en Nanomedicina y Sensores, Instituto de Investigación Sanitaria La Fe (IISLAFE), Universitat Politècnica de València, Valencia, Spain; [4] CIBER de Bioingeniería, Biomateriales y Nanomedicina, Instituto de Salud Carlos III, Spain; [5] Grupo Acreditado de Hemostasia, Trombosis, Arteriosclerosis y Biología Vascular, Instituto de Investigación Sanitaria La Fe (IISLAFE), Valencia, Spain [6] Unidad Mixta UPV-CIPF de Investigación en Mecanismos de Enfermedades y Nanomedicina, Universitat Politècnica de València, Centro de Investigación Príncipe Felipe, Valencia, Spain [7] Departamento de Química, Universitat Politècnica de València, Valencia, Spain [8] Servicio de Angiología y Cirugía Vascular, Hospital Universitario y Politécnico La Fe, Valencia, Spain [9] Departamento de Cirugía, Facultad de Medicina, Universitat de València, Valencia, Spain; *carmen.martinez-bisbal@uv.es

Abstract

INTRODUCTION: Carotid artery stenosis is mainly produced by the progressive accumulation of atherosclerotic plaque in the vascular wall. Lipids, low density proteins, expression of chemokines and adhesion molecules, and migration of monocytes and lymphocytes into the plaque are hallmarks of atheroma plaques. These plaques have variable embolic propensity depending on the composition and vulnerability of plaque, rather than the severity of the stenosis (1). NMR spectroscopy has been previously used in our group to determine biomarkers of plaque vulnerability in atheroma plaques and serum from patients (2). High sensitivity (100 % and 88.37 %) and specificity (91.6 % and 77.78 %) in plaque and serum, respectively have been found (2) with several metabolites participating in the discriminant models. Given the complexity of both serum and plaque matrices, finding a circulating metabolite profile that accurately reflects local dysregulation remained challenging. Therefore, to specifically identify metabolites released from atheroma plaques, we have designed the current study involving the analysis and longitudinal assessment of conditioned media from explanted plaque tissue.

METHODS: Atheroma plaques were obtained, during standard endarterectomy procedures, from symptomatic and asymptomatic patients (n=29) recruited by the Angiology and Vascular Surgery Service from the Hospital Universitario y Politécnico La Fe, Valencia, Spain. Symptomatology was defined as transient ischaemic attack, *amaurosis fugax*, and stroke occurred at most 21 days before surgery. A 2 mm cross-section fragment of the plaque (explant) was incubated in DMEM (5 mL) supplemented with antibiotic (penicillin and streptomycin). Aliquots from 500 µl of conditioned media were collected at 24 h, 48 h and 5 days, and processed according to previous protocols (3). Samples were resuspended in deuterated buffer and underwent NMR spectroscopy study in a 600 MHz NMR spectrometer (Bruker DRX 600 MHz, U26 NMR: Biomedical Applications II platform from Nanbiosis, Research Infrastructures & Services of CIBERBBN, Universitat de València). After acquisition, spectra underwent phase, baseline and chemical shift correction with Mnova V.15 (4) Processed spectra were saved as text and were loaded in PLS_Toolbox Solo 9.3 (2024) software (5). Spectra were binned and PCA and PLS-DA were conducted.

RESULTS & DISCUSSION: The unsupervised analysis showed differences between the spectra acquired at each time, being samples obtained at 5 days the most different. Samples collected at 48 h were studied by PLS-DA to identify different profiles between symptomatic and asymptomatic patients. In a first model, all the variables were considered, and a low performance was reached. To reduce the number of variables and to increase the performance of the model, the variables with VIP>1 were selected yielding a model with high sensitivity and specificity (100 and 95% respectively). These findings indicate that, after 48 hours, explant conditioned media exhibit differences related to symptomatology, potentially facilitating the identification of biomarkers transferred from atheroma plaques to serum related with plaque vulnerability

Acknowledgments: MCIN/AEI/10.13039/501100011033/ and by European Regional Development Fund - A way of doing Europe project PID2021-126304OB-C41 and PID2021-128141OBC22, Instituto de Salud Carlos (ISCIII) project PI20/01171 and PI24/01607, and Generalitat Valenciana project CIPROM/2021/007.

References

1. Hansson et al., doi: 10.1038/ni.2001; **2**. Botello-Marabotto et al., doi: 10.1016/j.talanta.2024.127211; **3.** Kostidis et al., doi: 10.1016/j.aca.2017.05.011 **4.** Mestrelab Research S.L. Santiago de Compostela, Spain; **5.** Eigenvector Research, Inc., Manson,

Unsupervised learning in migraine using advanced diffusion metrics

Alessandra Gallo[1]*, Antonio Tristán-Vega[1], Ángel L. Guerrero[2,3], David García-Azorín[3,4], Santiago Aja-Fernández[1], Rodrigo de Luis-García[1], Álvaro Planchuelo-Gómez[1]

[1]LPI, Universidad de Valladolid, Valladolid, Spain; [2]Headache Unit, Hospital Clínico Universitario de Valladolid, Valladolid, Spain; [3]Department of Medicine, Universidad de Valladolid, Valladolid, Spain; [4]Department of Neurology, Hospital Clínico Universitario de Valladolid, Valladolid, Spain *[alessandra.gallo@uva.es]

INTRODUCTION: Migraine is a highly prevalent neurological disorder with significant heterogeneity in its clinical presentation [1]. The current classification of migraine is unspecific to the clinical heterogeneity, being exclusively based on the monthly headache frequency, and there are no biomarkers for its diagnosis and progression [2]. This study aims to provide an alternative classification of migraine sub-types by using machine learning applied to diffusion MRI data.
METHODS: A total of 107 migraine patients (56 chronic migraine [CM], 51 episodic migraine [EM]), involved in previous studies [3], were recruited from the Headache Unit at Hospital Clínico Universitario de Valladolid (Spain). MRI data were acquired using a Philips Achieva 3T scanner, including T1- and diffusion-weighted imaging with b = 1000 s/mm^2 sequences. Diffusion metrics were extracted from 48 white matter regions based on the JHU ICBM-DTI-81 White Matter Atlas [4] using three computational approaches: AMURA [5], MISFIT [6] and Moments-based MISFIT. The first and third sets of measurements included return-to-origin (RTOP), return-to-axis (RTAP) and return-to-plane (RTPP) probabilities. The second set, obtained with MISFIT, included propagator anisotropy (PA), generalized moment of order 2 (q-space Mean Squared Displacement or QMSD), non-gaussianity (NG), diffusion anisotropy (DiA), and the axial apparent moment of order 1/2 (MUA). The cluster extraction procedure, shown in Figure 1(a), was then applied to twelve datasets, resulting from the combination of four types of diffusion descriptors (AMURA, MISFIT, moment-based MISFIT and DTI) with three groups of subjects (all patients with migraine, CM and EM). Additionally, the clusters were extracted using four diffusion tensor imaging (DTI) parameters: fractional anisotropy (FA), and mean (MD), radial (RD) and axial diffusivity (AD). The clinical characteristics were compared between the extracted clusters.
RESULTS & DISCUSSION: The optimal number of clusters was consistently two in all cases, independently of the technique used. The clusters extracted for any clustering technique differed depending on the set of diffusion metrics, as shown with illustrative examples in Figure 1(b). In some cases, the distribution of patients in each cluster and the clinical characteristics slightly differed between the clustering methods, but no major differences were found. Comparing the clinical features of the clusters for the three datasets, AMURA identified more statistically significant clinical differences than MISFIT for RTAP, RTOP, and RTPP (four vs. three), being particularly sensitive to migraine duration (years lived with migraine, months since onset of CM), age, and migraine classification (CM and EM) at the time of MRI acquisition. In contrast, MISFIT was more effective in differentiating migraine subgroups based on characteristics unrelated to time, showing higher sensitivity to medication overuse headache (MOH) and migraine frequency in CM, or sex. Regarding DTI results, significant differences between clusters were found for less variables, specifically sex, duration of migraine and headache frequency. These results suggest that AMURA is more appropriate for evaluating long-term migraine progression, while MISFIT would be better for the identification of subgroups associated with headache-specific features, particularly MOH and migraine frequency. Unsupervised learning techniques offer important insights into the pathophysiology of migraine and can provide a basis for predicting long-term clinical outcomes.

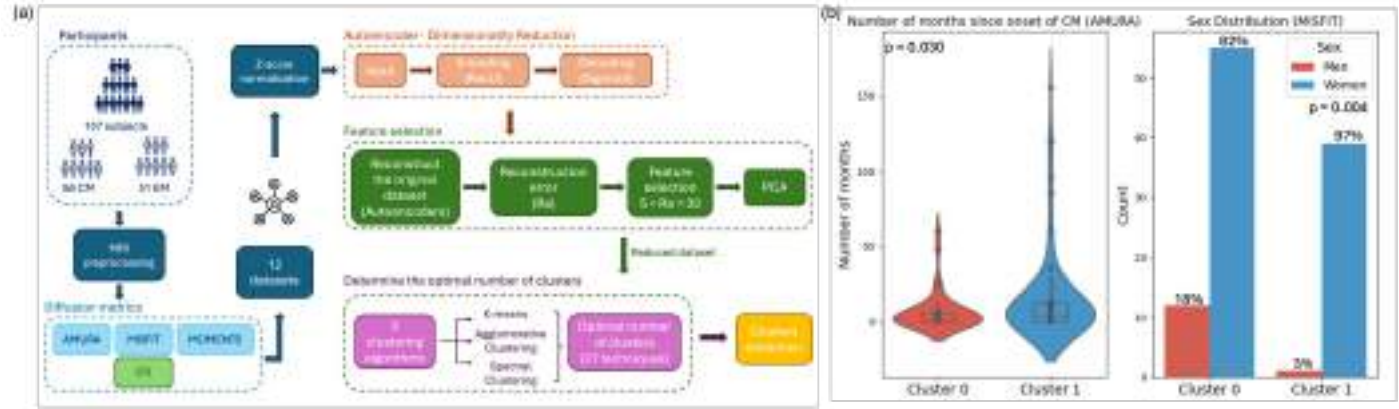

Figure 1 - (a) Processing pipeline to obtain unsupervised clusters. Schematic diagram showing the steps conducted to extract unsupervised clusters from diverse migraine groups. The twelve datasets refer to three different clinical groups and three sets of diffusion descriptors. (b) Comparison of clinical characteristics between clusters. Violin plots comparing the number of months since the onset of CM between the clusters of the AMURA dataset, and barplots representing the distribution of the patients by sex in the clusters of the MISFIT dataset.

References: **1.** Schürks et al. Cephalalgia(2011)-31:861; **2.** Headache Classification Committee. Cephalalgia(2018)-38:1-211; **3.** Planchuelo-Gómez et al. J Headache Pain(2020)-21:1; **4.** Oishi et al. NeuroImage(2008)-43:447-457; **5.** Aja-Fernández et al. PLoS One(2020)-15:e0229526; **6.** Tristán-Vega et al. Neuroimage(2021)-227:117616

Acknowledgements: This research was funded by grant PID2021-124407NB-I00 (Ministerio de Ciencia e Innovación and NextGenerationEU).

Hardware Testing for Dynamic Field Probe Integration into a 7 Tesla Head Coil

Sydney Nicole Williams[1*,2], Christian Mirkes[3], Paul McElhinney[4], Belinda Ding[5], Simon Gross[3], Kerrin J. Pine[6], Roland Müller[7], Nikolaus Weiskopf[6,8,9], Harald E. Möller[7,8], Shajan Gunamony[2,4]

[1]PROMISE Lab, Universidad Rey Juan Carlos, Móstoles, Spain; [2]Imaging Centre of Excellence, University of Glasgow, Glasgow, UK; [3]Skope Magnetic Resonance Technologies AG, Zurich, Switzerland; [4]MR CoilTech Ltd., Glasgow, UK; [5]Siemens Healthcare Ltd., Camberley, UK; [6]Department of Neurophysics, Max Planck Institute for Human Cognitive and Brain Sciences, Leipzig, Germany; [7]NMR Methods & Development Group, Max Planck Institute for Human Cognitive and Brain Sciences, Leipzig, Germany; [8]Felix Bloch Institute for Solid State Physics, Leipzig University, Leipzig, Germany; [9]Wellcome Centre for Human Neuroimaging, Institute of Neurology, University College London, London, UK. [*sydney.williams@urjc.es]

Abstract

INTRODUCTION: Ultra-high field MRI (UHF, ≥ 7T) has impressive benefits due to increased signal-to-noise ratio (SNR) which can yield higher resolution imaging. Nevertheless, UHF faces challenges like greater specific absorption rate (SAR) and inhomogeneities in the static and radiofrequency (RF) fields[1]. Parallel transmission (pTx) is a hardware-based solution for correcting RF field non-uniformity by using multiple transmit elements to generate independent RF fields that allow for spatial mitigation and homogenization and to have greater control over power deposition[2]. pTx coils can be complemented with high numbers of receive elements to further boost SNR at UHF[3]. Recently, hardware advances have enabled the integration of dynamic field probes into multi-transmit, multi-receive RF coils, offering the further capability of measuring static magnetic and gradient field fluctuations[4].This abstract discusses key hardware tests to ensure RF coil performance and safety in a 16-transmit (Tx), 64-receive (Rx) coil with integrated field probes.

METHODS: Simulation and Phantoms: A numerical model (CST Design Studio, Dassault Systèmes, France) was constructed of the 16Tx/64Rx coils with the field probes, modeled as shielded enclosures, precisely located and oriented as mounted on the receive array. Receive elements were excluded from simulation[5]. RF transmit and temperature maps were measured with and without probes, and the model SAR Q-matrices[6] were simulated using three body models.

Field Mapping: The transmit array was characterized in an agar-sugar head-and-shoulders phantom with presaturated TurboFLASH B_1^+-mapping[7] (TE/TR=1.9/300ms,FOV/Resolution/SliceThickness=230 mm/3.6 mm /5 mm,TA=27 sec) on a 7T Magnetom Terra Scanner (Siemens Healthineers, Erlangen, Germany). The receive array was assessed by SNR mapping following Ref. 8 and was performed in a spherical oil phantom. Both B_1^+ and SNR mapping procedures were conducted before and after the field probes were integrated into the coil.

Thermometry: Temperature maps were with the proton resonance frequency shift technique[9] in thermometry phantom with a 3D gradient-echo (TE/TR/FA=25/30 ms/20°, FOV/Resolution/TA=192 mm /3 mm /TA=2:02 min). A 10 min sequence with RF-only at the maximum power permitted for RF heating. Temperature maps were generated into B_1^+ modes, circularly polarized (CP) and zero phase.

Virtual Observation Point (VOPs): The simulated coil model Q-matrices were compressed to generate a set of 161 VOPS with an overestimation of 20% of local SAR with respect to the "worst case" configuration[10].

RESULTS & DISCUSSION: Figure 1 explores the effect of field probes on coil performance, electromagnetic fields, and local SAR. For the transmit array (1A), the change in B_1^+ map with and without field probes is small (~1-2%). In the temperature maps (1B,1C), the experimental maps (acquired only with field probes integrated in the coil), show agreement with simulations despite confounding artifacts of receive array heating and an air bubble. For the receive array (1D), again little differences are found without and with probes. After confirming model validity, the generated VOPs could be validated (1E) to allow for accurate and conservative overestimation of local SAR using pTx.

By characterizing the transmit, receive, and temperature distributions of the 16Tx/64Rx coil with and without dynamic field probes we have shown that the probes introduce negligible effects on coil performance. With full testing and VOP validation, this coil was approved for human imaging with in vivo results presented at the 2025 ISMRM Annual Meeting in Hawaii[11].

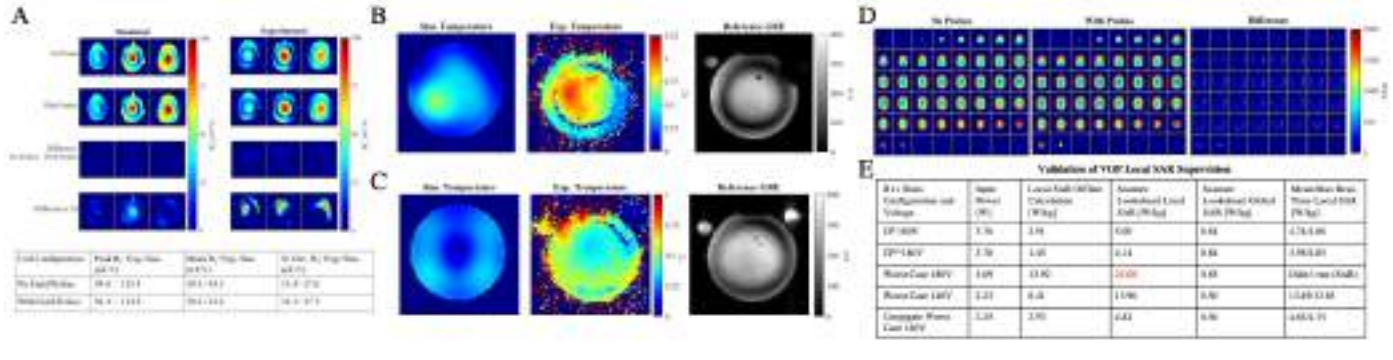

Figure 1 – Simulated and experimental hardware validation data. A) Comparison of simulated (left) and measured (right) B_1^+ maps without (top row), with (top middle row) field probes, and their difference images (middle bottom, bottom rows) along with quantitative statistics. B) Sim. and exp. temperature maps measured in circular polarization (CP) B_1^+ mode. C) Sim. and exp. temperature maps measured in zero phase B_1^+ mode. D) Comparison of exp. SNR maps measured without and with probes, and their difference image. E) Experimental validation of compressed VOPs for local SAR estimation in pTx modes on the scanner. As anticipated, scanner SAR estimates are always more conservative than offline calculations.

References

1. Kraff O and Quick HH, *JMRI* 2017; **2.** Williams SN, McElhinney P, and Gunamony S, *Phys. Med. Biol.,* 2023; **3.** Feinberg DA et al., *Nature Methods* 2024; **4.** Skope MRT, *ISMRM* 2023; **5.** McElhinney P et al., *ISMRM* 2021; **6.** Graesslin et al., *MRM* 2012; **7.** Fautz HP et al., *ISMRM* 2008; **8.** Kellman et al., *MRM* 2005; **19.** Ehses P, *MRM*, 2008. **10.** Eichfelder et al., *MRM* 2011; **11.** Pine K., *ISMRM* 2025.

Benchmarking Deep Learning Approaches for RANO Criteria Classification in Glioblastoma

Ana Matoso[1,2], Catarina Passarinho[1], Marta P. Loureiro[1], José Maria Moreira[2], Patrícia Figueiredo[1], Rita G. Nunes[1]

[1]Institute for Systems and Robotics – Lisboa; [2]Hospital da Luz Learning Health, Lisbon, Portugal; *anamatoso@tecnico.ulisboa.pt

Abstract

INTRODUCTION: Glioblastomas (GBM) are the most aggressive type of glioma, having a 5-year survival rate of 6.9%[1]. Treatment typically involves surgery, followed by radiotherapy and chemotherapy, and frequent magnetic resonance imaging (MRI) scans to monitor response[2]. Radiologists evaluate these scans using the Response Assessment in Neuro-Oncology (RANO) criteria[3] to categorize the tumor into one of four labels based on imaging and clinical features: complete response, partial response, stable disease, and progressive disease. This assessment is very complex and time-consuming, as it involves the integration of various clinical information and sometimes manual segmentation. Since deep learning (DL) has been widely used to tackle biomedical classification problems[4], this work aimed to implement the first DL pipeline for the classification of RANO criteria based on two consecutive MRI acquisitions.

METHODS: The models were trained and tested on the open dataset LUMIERE[5]. Five approaches were implemented and compared to identify the best methodology: 1) inputting subtraction of images of consecutive time points, instead of individual time points, 2) using different combinations of imaging modalities, 3) implementing different DL model architectures, 4) employing different pretraining tasks, and 5) adding patient clinical data to the inputs. To evaluate performance on this highly unbalanced dataset, a five-fold cross-validation approach was employed, and the following metrics were calculated: Balanced Accuracy, Precision, Recall, and F1-Score. Two explainability methods were applied: Saliency maps[6] and Grad-CAM[7].

RESULTS & DISCUSSION: The pipeline that achieved the best performance used a Densenet264, considering only T1-weighted, T2-weighted, and Fluid Attenuated Inversion Recovery (FLAIR) images as input without any pretraining and without inputting clinical data. A median Balanced Accuracy of 50.96% was achieved (reaching a maximum of 58% in one of the folds), although with a median F1-Score of 0.1335. Using Saliency Maps, the tumor region was often successfully highlighted. In contrast, Grad-CAM typically failed to highlight the tumor region, with exceptions observed in the Complete Response and Progressive Disease classes, where it effectively identified the tumor region. This difference could be attributed to Grad-CAM's reliance on higher-level feature maps, which might encode complex and abstract representations that are more challenging to interpret visually.

These results set a benchmark for future studies on glioblastoma treatment response assessment based on the RANO criteria. The modest results emphasize the difficulty of this task, likely affected by a heterogeneity of factors (such as the complex tumor environment) that might play a role when assessing the tumor's response to treatment.

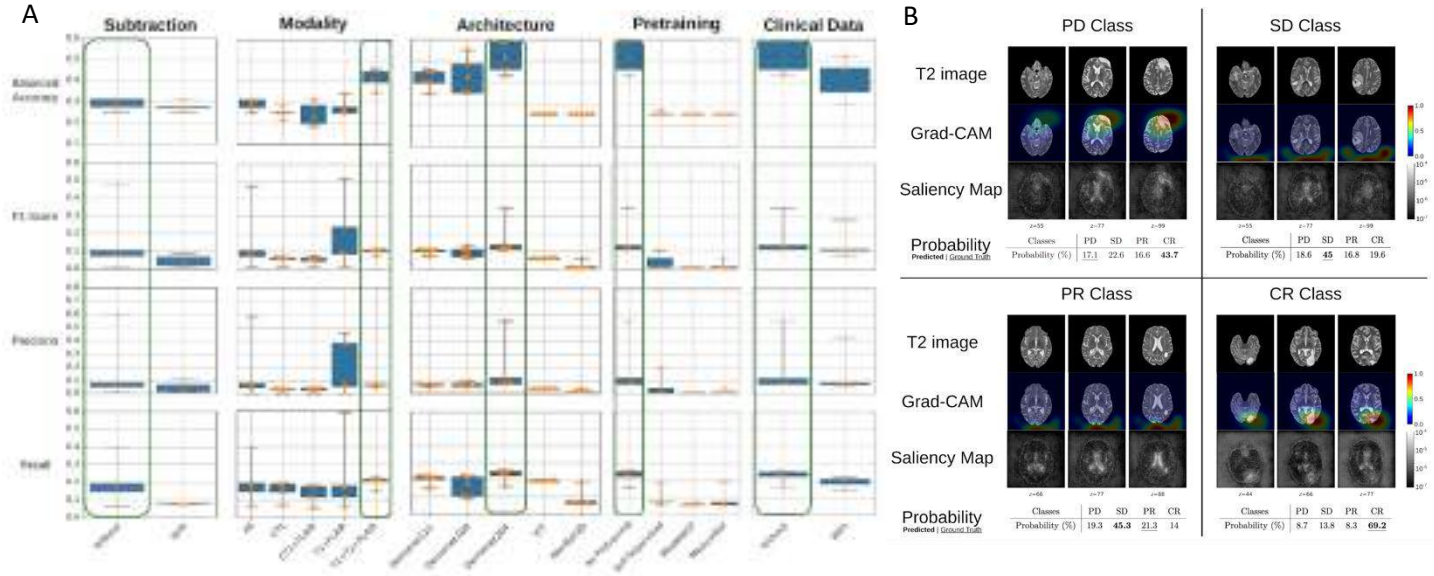

Figure 1 - (A) Performance metrics for each option in each approach tested. In green, the best option. (B) Explainability methods (Grad-CAM and Saliency maps) applied to an example of each class and the respective probabilities of that example being classified into each of the four classes. PD= Progressive Disease; SD=Stable Disease; PR=Partial Response; CR=Complete Response.

Acknowledgments: This work was supported by the Portuguese Science Foundation through grant 2023.03810.BDANA, 2022.13185.BD, and UI/BD/154928/2023. This work was also supported by LARSyS FCT funding (DOI: 10.54499/LA/P/0083/2020, 10.54499/UIDP/50009/2020, and 10.54499/UIDB/50009/2020).

References

1. Ostrom QT, et al. (2022). Neuro-Oncology; **2.** Horbinski C, et al (2023). Journal of the National Comprehensive Cancer Network; **3.** Wen PY, et al. (2010) JCO; **4.** Shaver MM, et al. (2019) Cancers; **5.** Suter Y, et al (2022) Scientific Data; **6.** Kokhlikyan N, et al (2020) arxiv; **7.** Selvaraju RR, et al (2020). Int J Comput Vis

Correction of distortions created by fields inhomogeneities in a Halbach scanner

J. Borreguero[1], E.G. Castañón[1], T. Guallart-Naval, M. Fernández[1], H. Ortega, F. Galve[1], J.M. Algarín[1] y J. Alonso[1].

[1] Institute for Molecular Imaging and Instrumentation (i3M, CSIC & UPV). Valencia, España.

INTRODUCTION: Halbach mandalas have proven to be excellent tools for producing low-field (<100 mT) MRI magnets, offering high portability, low weight, and cost-effectiveness [1]. However, these advantages come at the expense of certain geometrical distortions that may appear in the acquired images, as a consequence of B_0 inhomogeneities and non-linearities in gradient fields. To address the first, results crucially employ model-based reconstructions where the encoding matrix includes prior knowledge of spatial fluctuations in the involved fields. Here we present Single-Point Double-Shot (SPDS, [2]) method, which has proven to be essential for achieving robust and reliable B_0 mapping. Then, we tackle the non-linearities of the gradient fields by applying a geometrical co-registration method, consisting of an initial rigid registration followed by a B-spline protocol.

METHODS: **Approach 1: ART reconstruction with SPDS mapping for correction of B0 inhomogeneities.** First, we acquired a ΔB0(r) map with SPDS (Fig.1a, panel 1), which consists of two low-resolution pointwise images (à la SPRITE), ρ_1 and ρ_2, with different encoding times, T_{d1} and T_{d2}. In this sense, each image has a unique phase in every voxel, and thus the phase difference between the two images is an exact proxy for the B_0 field, given by $\Delta B0=(ph(\rho_2)- ph(\rho_1))/\gamma(T_{d2}-T_{d1})$. The sample is then scanned with an imaging sequence, as usual, to get k-space pairs as $\{k_i, s(k_i)\}$ (Fig.1a, panel 2). Finally, the information of ΔB_0 is used to construct the Encoding Matrix ($E_{i,j}$) as $E_{i,j}=exp\{-i[k_i \cdot r_j + \gamma \cdot \Delta B0(r_j) \cdot t(k_i)]\}$. Finally, we solve the system $s_i=E_{i,j} \cdot \rho_j$ iteratively with ART (Fig.1a, panel 3). This procedure is followed for standard MRI sequences (RARE in our case) for brain imaging of in-vivo subjects in a 90 mT Halbach scanner with 5,000 ppm [3]. **Approach 2: Deformable image registration methods for correction of gradient non-linearities.** Initially, a reticular phantom (shown in Fig 1c a)) filled with $CuSO_4$, is encoded and reconstructed with standard MRI protocolos. Additionally, we built a synthetic version of it, as a matrix of 0's and 1's which preserve the physical shapes and distances of the object. Following this, we employ both the synthetic and the measured phantoms, as fixed moving images, respectively, to test and evaluate a deformable registration protocol. This method basically takes the moving image and applies a certain number of geometrical transformations to convert it as much as possible into the object contained in the fixed image. The aligned files were then subjected to a b-spline non-linear transformation to correct the larger distortions. After fine adjustment of the parameters, we finally obtained a deformation field map for the whole volume of the scan, used then to batch correct a database that we have created containing a set of knee images acquired from real volunteers. In order to prove the validity of our co-registration procedure, we have tried to batch correct the distortions of one of our databases of knee images acquired from real volunteers. These images were acquired with the 72 mT Halbach system [1] using the same sequence that we used to measure our phantom.

RESULTS & DISCUSSION: Figure 1b demonstrates the performance of ART reconstruction with (bottom row) and without (middle row) B_0 knowledge generated by SPDS (top tow) for RARE sequences applied to a brain scan. It highlights significant improvements in Cartesian reconstructions when incorporating prior knowledge of the B0 field. Figure 3c-left shows the initial knee image, where inhomogeneities induces a distortion in the form of a bright curved line on the superior side. After applying our deformation field, said distortion is massively reduced, as we can see in Figure 3c-right. Additionally, the co-registration procedure does not alter the important information of the image, and we can observe the anatomical features of the knee clearly and without deformation.

References

[1] Guallart-Naval et al. *Portable magnetic resonance imaging of patients indoors, outdoors and at home*. Sci Reports. 2022. [2] Borreguero et al. *Zero-echo-time sequences in highly inhomogeneous fields*. Magnetic Resonance in Medicine. 2024. [3] Galve et al. *Elliptical Halbach magnet and gradient modules for low-field portable magnetic resonance imaging.* NMR in Biomedicine. 2024.

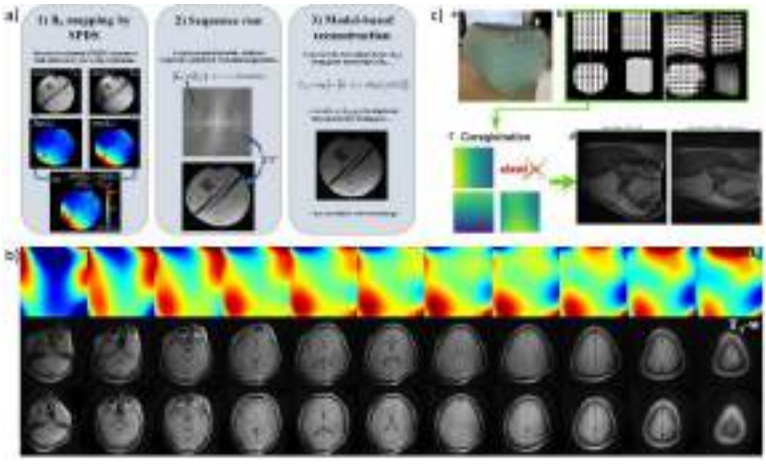

Fig.1. a) Diagram of the proposed procedure for imaging in highly inhomogeneous B0 fields, based on previous B0 mapping with SPDS and model-based reconstruction with ART. b) Application of SPDS mapping method followed by ART reconstruction of a RARE sequence applied for a brain of an in-vivo subject in a system with 5,000 ppm of inhomogeneity. c) Diagram of the proposed procedure for correction of distortions induced by gradient non-linearities following a co-registration process.

Conventional MR spectroscopy sequences combined with machine learning allow distinguishing between IDH mutation and grade in astrocytomas

Lili Tóth [1*], Carles Majós [2,3] Albert Pons-Escoda[2], Carles Arús[1,3], Margarida Julià-Sapé[1,3]

[1] Departament de Bioquímica i Biologia Molecular and Institut de Biotecnologia i Biomedicina (IBB), Universitat Autònoma de Barcelona (UAB), Cerdanyola del Vallès, Spain; [2] Grup de Neuro-oncologia, Institut d'Investigació Biomèdica de Bellvitge (IDIBELL), Hospital Universitari de Bellvitge, Barcelona, Spain; [3] Centro de Investigación Biomédica en Red en Bioingeniería, Biomateriales y Nanomedicina (CIBER-BBN), Spain *

Abstract

INTRODUCTION: Accurate grading and identification of IDH status in astrocytomas are essential for guiding therapeutic strategies and predicting patient prognosis. Their 2021 WHO classification emphasizes the importance of molecular markers, particularly IDH status, in tumor characterization[1]. Considering this, further investigation is needed to explore non-invasive diagnostic approaches. On the other hand, since 2012 when specific sequences were developed to detect the 2-hydroxyglutarate metabolite[2,3] conventional MRS sequences are not regarded as an option to detect the IDH mutation in gliomas. This study aims to re-evaluate the potential of magnetic resonance spectroscopy (MRS) in determining IDH status (mt: IDH mutated, wt: IDH wild type) and tumor grade (2, 3, or 4) by analyzing metabolite patterns across different astrocytoma subtypes, under the assumption that the effects of mutation and grade on the metabolic profile will affect the whole spectral pattern to allow for non-invasive discrimination.

METHODS: The study utilized Single Voxel (SV) MRS data collected at Hospital de Bellvitge with 1.5T Philips Ingenia and Intera scanners in Spain. Five classification tasks were performed on Short Echo (SE, 30 ms), Long Echo (LE, 136 ms), and concatenated SE+LE spectra. Sequential forward feature selection and linear discriminant analysis were used to identify features to distinguish between:1/Astrocitoma-IDH-mt-grade-2 (A2-mt) from Astrocitoma-IDH-NEC-grade-2 (A2-wt), 2/Astrocitoma-IDH-mt-grade-3 (A3-mt) from Astrocitoma-IDH-NEC-grade-3 (A3-wt), 3/A2+A3-mt from A2+A3+ Astrocitoma-IDH-mt-grade-4 (A4-mt), 4/A2 from A3, and 5/ A2+3 from A4. Classifiers were evaluated with area under the curve (AUC) and Balanced Error Rate (BER). The best classifier was defined by the smallest BER in the training phase.

RESULTS & DISCUSSION: After application of inclusion criteria, there were 71 cases with SV MRS available for analysis at SE (15 A2-mt, 12 A2-wt, 20 A3-mt, 13 A3-wt and 11 A4-mt) and 69 cases at LE (14 A2-mt, 13 A2-wt, 18 A3-mt, 13 A3-wt and 11 A4-mt). Recurring discriminative spectral features include creatine, choline and lipids at SE and lactate and Glx, at LE which can be seen on Figure 1. For the first question SE, and for the other questions the combined echo time, yielded the best classifiers. Notably, all AUC values for the best echo are quite high 0.938, 0.933, 0.834, 0.849 and 0.870 for the 5 questions, respectively. These findings support our claim that IDH status can be successfully determined for A2 and A3, while A2 can be differentiated from higher grades of astrocytoma without needing specialized sequences[4].

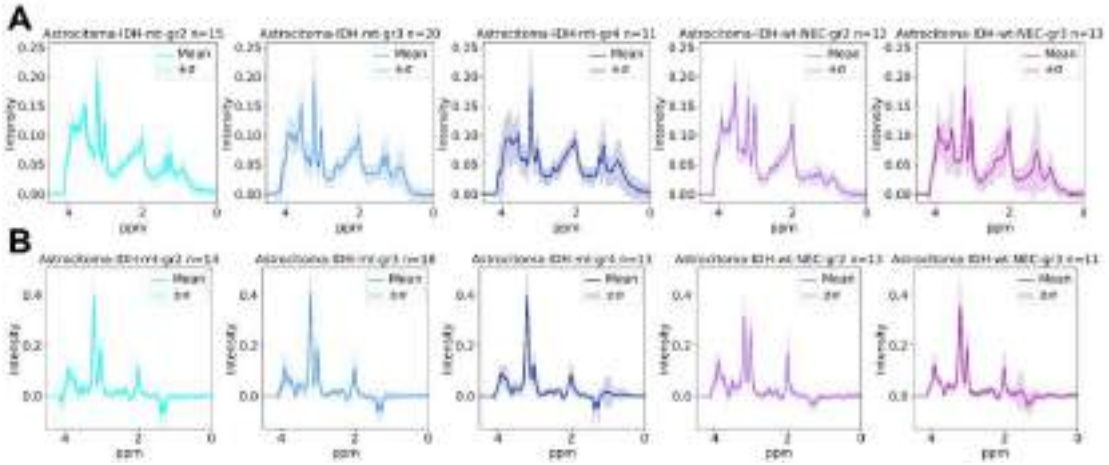

Figure 1 – Mean spectra of each tumor type. A: short echo (SE) spectra. B: long echo (LE) spectra.

References

1. Osborn, A. G., Louis, D. N., Poussaint, T. Y., Linscott, L. L. & Salzman, K. L. The 2021 World Health Organization Classification of Tumors of the Central Nervous System: What Neuroradiologists Need to Know. *American Journal of Neuroradiology* **43**, 928–937 (2022).
2. Choi, C. *et al.* 2-hydroxyglutarate detection by magnetic resonance spectroscopy in IDH-mutated patients with gliomas. *Nat Med* **18**, 624–629 (2012).
3. Andronesi, O. C. *et al.* Detection of 2-hydroxyglutarate in IDH-mutated glioma patients by in vivo spectral-editing and 2D correlation magnetic resonance spectroscopy. *Sci Transl Med* **4**, 116ra4 (2012).
4. Iida, T. *et al.* Grading of astrocytomas using the PRESTO (principles of echo-shifting with a train of observations) magnetic resonance imaging sequence. *Clinical Neurology and Neurosurgery* **173**, 91–95 (2018).

Can Patch-Based Harmonization in Radiomics of Longitudinal Glioblastoma MRI Improve Tumor Region Labelling?

Marta P. Loureiro[1]*, Catarina Passarinho[1], Ana Matoso[1], José Maria Moreira[2], Pedro Vilela[2], Patrícia Figueiredo[1], Rita G. Nunes[1]

[1]Institute for Systems and Robotics – Lisboa and Department of Bioengineering, Instituto Superior Técnico, Universidade de Lisboa, Lisbon, Portugal; [2]Hospital da Luz Learning Health, Luz Saúde, Lisbon, Portugal; [3]Imaging Department, Hospital da Luz, Lisbon, Portugal; *marta.padrela@tecnico.ulisboa.pt

Abstract

INTRODUCTION: Glioblastomas, the most common and aggressive primary brain tumours, are recurrently studied due to their significant impact on years of life lost and low survival rates, with an average 5-year survival of 6.6% [1]. MRI is an essential tool to diagnose and monitor treatment response in this condition [2]. Recent years have seen a rising interest in the extraction of radiomics features from MR images, used in Machine Learning tools to aid in these tasks. However, MRI intensities and MRI-derived radiomics features depend on acquisition and reconstruction protocols, leading to the necessity of data harmonization. Harmonizing medical imaging data is a growing necessity, propelled by clinical research addressing heterogeneous datasets of medical images and their radiomics features [3-5]. This work aims to assess the performance of ComBat, a widely used MRI harmonization method, when applied to radiomics features extracted from a longitudinal clinical dataset of glioblastoma patients.

METHODS: T2FLAIR and T1CE (contrast-enhanced) images from 40 glioblastoma patients were collected over several time points (comprising a total of 243 time points) in a clinical setting, using different scanner models and at various medical centres, resulting in acquisition parameters with high variability. Images underwent pre-processing, while segmentation into Enhancing Tumour (ET) and Edema was accomplished with HD-GLIO [6]. The images were then segmented into small patches (cubes of size 16 voxels), which were labelled as four tissue regions (*Normal*, *Edema*, *ET*, and *Edema & ET*). ComBat was applied to radiomics features extracted from these patches with PyRadiomics [7]. Two correlation analyses were performed. To assess batch effects before and after harmonization, we applied Canonical Correlation Analysis (CCA) [8], considering the radiomics features as the first group, and a linear model with the batch (same medical centre and scanner model), manufacturer and region as the second group. Patches were classified into one of the four tissue regions, using XGBoost, balanced accuracy as the evaluation metric, and weighted classes.

RESULTS & DISCUSSION: Our results show that ComBat effectively reduced batch effects while retaining biologically relevant information. Fig. 1 shows that data was grouped by batch prior to harmonization, but grouped by region after ComBat, proving that even small patches retain scanner effects without harmonization. Classification performance improved post-harmonization, achieving an average balanced accuracy of 0.92, compared to 0.91 without harmonization. This suggests that radiomics features can help predict the type of tissue present in a patch, which could eventually aid tumour segmentation tasks.

Acknowledgments: This work was supported by the Portuguese Science Foundation (FCT) through grants UI/BD/154928/2023, 2023.03810.BDANA and 2022.13185.BD. This work was also supported by LARSyS FCT funding (DOI: 10.54499/LA/P/0083/2020, 10.54499/UIDP/50009/2020, and 10.54499/UIDB/50009/2020).

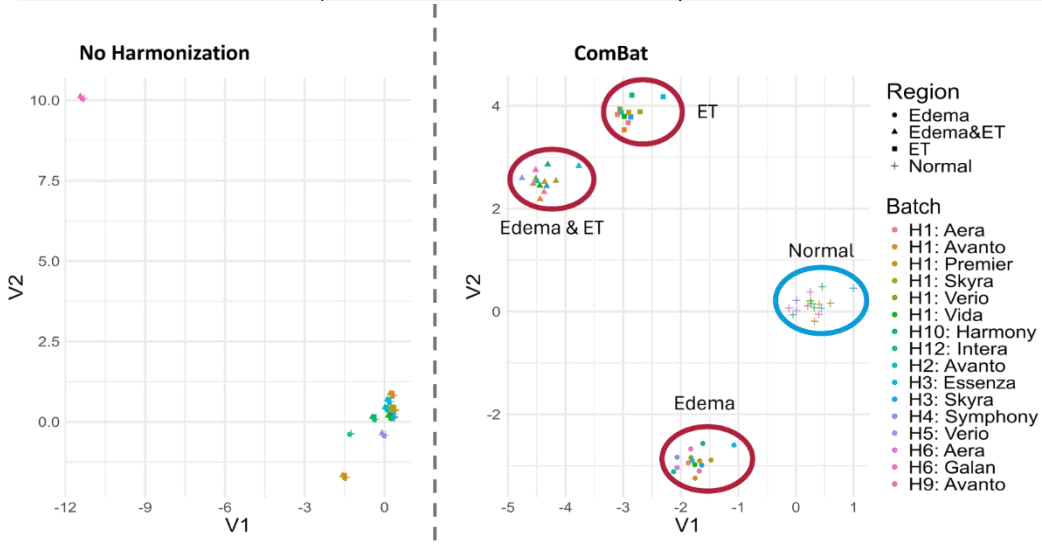

Figure 1 – Canonical Correlation Analysis (CCA) results for the first two canonical variables of the second group, V1 and V2, (categorical metadata: manufacturer, batch, and region) before and after harmonization with ComBat. Each point represents a categorical group (batch, manufacturer, or region) projected onto the first two canonical components. Note that the radiomics features were used as the first group. The different colours represent patches from different batches (defined by the hospital number and the scanner model), while different markers represent the different regions. Before harmonization, the data is organized by batch (represented by color), while after ComBat, region-based clustering becomes apparent (each region type is represented by a marker). ET: Enhancing Tumour.

References

1. Ostrom QT, et al. Neuro-Oncol. 2022. **2.** Gilard V, et al. J. Pers. Med. 2021. **3.** Carré A, et al. Sci. Rep. 2020. **4.** Shinohara RT, et al. NeuroImage: Clin. 2014. **5.** Fortin JP, et al. NeuroImage 2016. **6.** Kickingereder P, et al. Lancet Oncol. 2019. **7.** van Griethuysen, JJM, et al. Cancer Res. 2017. **8.** Zhuang X, et al. Hum Brain Mapp. 2020. **9.** Chen T, et al. *https://CRAN.R-project.org/package=xgboost.*

Optimization of the magnetization transfer pulse parameters for neuromelanin contrast enhancement in the substantia nigra

Begoña Garate Andikoetxea[1,2], Antonio Martin[1], Marta Vidorreta[3], María Cruz Rodríguez[1], María Asunción Fernández Seara[4] *

[1]Department of Neurology, Clínica Universidad de Navarra, Pamplona, Spain; [2]Universidad de Deusto, Bilbao, Spain; [3]Siemens Healthineers, Madrid, Spain; [4]Department of Radiology, Clínica Universidad de Navarra, Pamplona, Spain. * mfseara@unav.es

INTRODUCTION:

Neuromelanin MRI (NM-MRI) has explored T1 reduction [1], magnetization transfer (MT) or proton density (PD) weighted images [2] as a source of contrast ratio enhancement for the NM rich areas. Observing the heterogeneity of the MT approaches previously used, the goal of this work was to systematically optimize the parameters of a 3D GRE MT sequence to enhance NM contrast.

METHODS:

Experiment 1: 5 healthy controls (HC) (27±3 years, 3 females) were scanned on a 3T MAGNETOM Skyra MRI, using a 32-channel head coil. The protocol included a T1-weighted MPRAGE and the NM-sensitive 3D GRE with MT (TR=53 ms, TE=3.67 ms, FA=20°). The MT pulse was sinc-shaped, duration=10 ms and FA=500°. The MT frequency was varied (500, 1500, 2000, 4000, 10K and 100K Hz) to evaluate its effect on the contrast ratio.

Experiment 2:16 HCs (27±4 years, 11 females) were scanned using the same protocol. In this case the FA of the GRE readout excitation pulse was varied (5, 10, 20, 30 and 40 degrees), with MT ON and OFF (1200 Hz), to study the FA effect on the contrast ratio. Three echoes were acquired: TE1=3.67 ms, TE2=10.51 ms and TE3=17.35 ms.

The images were co-registered using SPM12 and the data was evaluated using Matlab scripts. The CR was calculated based on the signal intensities of the manually defined regions of interest (ROIs) in the NM region and the cerebral peduncles (PED) as: CR= ((S_NM-S_PED))/S_PED. Subsequently, the NM rich area volume was delineated by two trained observers. Tissue properties were estimated following a previously reported method [2]. Based on the group average results, simulations were employed to assess the optimal FA required to optimize the CR.

RESULTS & DISCUSSION:

In experiment 1, the highest CR was obtained for 500 and 1500 Hz (CR=0.28±0.02), with decreasing values for higher frequencies. In addition, significant differences were found between these two frequencies and 4000, 10K and 100 KHz. Figure1.A, one-way ANOVA and paired t-test results. In experiment 2, the maximum CR was obtained for MT ON and FA=5° (CR=0.42±0.05), Figure 1.B. Both FA and MT showed a significant main effect in the CR (two-way ANOVA and post-hoc tests), with no significant interaction. The same results were obtained for the volume analysis, with higher values measured for MT ON and FA=5°. All the post-hoc comparisons showed significant differences between the different FAs and MT ON/OFF condition for each FA, except the comparison between FAs of 5° and 10° with MT. The evaluated T1 and PD tissue properties were significantly lower with MT ON ($p<0.001$, paired samples t-tests), Figure 1.C. T2* did not showed significant differences. Finally, the simulation results aligned with the experimental measurements obtained in vivo, both in signal intensity and contrast ratio.

The first experiment showed that the CR did not vary significantly between 500, 1500 and 2000 Hz.

The second experiment revealed that with lower FA yielding greater CR (albeit lower signal) and facilitating the delineation of the NM-rich area volume as well as the MT. At the lowest flip angle, contrast was based on proton density differences as suggested previously [2], which was confirmed by the simulations. MT decreased the T1 and PD values of the brain tissues, further enhancing the PD based CR.

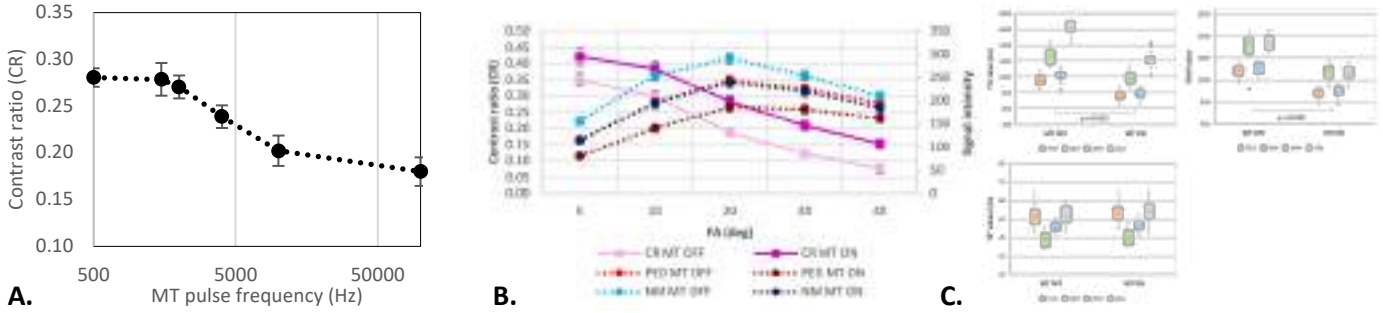

Figure 1 – Both experiments results. **A.** Group mean contrast ratio obtained for each MT frequency (expressed in logarithm scale), experiment 1. **B.** Signal intensities in the neuromelanin and peduncle regions and their contrast ratio measured with and without magnetization transfer, plotted as a function of GRE flip angle, experiment 2. **C.** Boxplots of the properties for each tissue with and without magnetization transfer, experiment 2.

References

1. Naying He et al, "Application of Neuromelanin MR Imaging in Parkinson Disease", Journal of Magnetic Resonance Imaging, Volume 57, Issue 2, 337-352, doi: 0.1002/jmri.28414 (2023); **2.** Liu et al, "Optimizing neuromelanin contrast in the substantia nigra and locus coeruleus using a magnetization transfer contrast prepared 3D gradient recalled echo sequence", Neuroimage 218, 116935, doi: 10.1016/j.neuroimage.2020.116935 (2020).

Detection of spatial artifacts on resting state functional magnetic resonance data

Carles Roqué[1], Marc Biosca[1], Roser Sala-Llonch[1,2], Raúl Tudela[2,1]

[1]*Institut de Neurociències, Departament de Biomedicina, Universitat de Barcelona. IDIBAPS. Barcelona, Spain.*
[2]*CIBER de Bioingeniería, Biomateriales y Nanomedicina, Instituto de Salud Carlos III, Barcelona, Spain*

Abstract

INTRODUCTION: Resting state functional magnetic resonance imaging (rs-fMRI) has shown potential to study changes in brain activity and connectivity. Nowadays this technique is applied to large datasets, which often combine many subjects acquired in different centers and at different time points. One of the drawbacks of this technique is that the rs-fMRI requires the acquisition of a large number of brain volumes in very short times, which are prone to be affected by different types of artifacts. Moreover, the analysis of rs-fMRI data requires curated pre-processing procedures obtain a clean and usable signal. In this context, it becomes fundamental to implement quality control (QC) strategies of the images to avoid artifacted datasets from the final analysis [1].
In this work we describe a spatial periodic artifact that appears in some sets of fMRI that remains underexplored in the literature and we propose an approach to easily detect it. Our method uses the 3D spatial Fourier transform (FT) in combination with spatial correlation analyses.

METHODS: We analyzed fMRI data of 1,178 participants from the A4 study [2] (ages 65-85 years) with normal cognition or very mild cognitive impairment. These were preprocessed in an automated fMRI pipeline combining in-house developed python scripts and tools from available packages as FSL, AFNI and ANTs. This pipeline already included a visual and automated QC to detect motion and segmentation artifacts. To further explore the presence of spatial artifacts, the preprocessed scans were evaluated by computing the 3D FT and correlation matrix between slices, all computed for each volume. The results were represented in summary figures, where the presence of peaks in the FT projections and/or the existence of correlated patterns within the image can be easily identified in a visual inspection.

RESULTS & DISCUSSION: We detected the presence of spatial artifacts in 21.9% of the subjects analyzed. Results show that artifacted images present high-frequency contributions in the FT amplitude, corresponding to the periodic noise in Figure [1.B]. The presence of secondary peaks in the FT amplitude are reported in the QC. Moreover, an increased correlation between the rows in slices has shown also to be linked to this type of spatial artifact.
We propose to integrate our pipeline to existing QC reports, mainly based on motion-related and segmentation artifacts, to obtain clean datasets for functional connectivity analyses. Further studies may try to fully automatize the detection and to use correction strategies.

Acknowledgments. The A4 Study is a public-private partnership, funded by the National Institute on Aging (NIA), Eli Lilly and Company, and other partners. We acknowledge the contributions of the A4 Study investigators, participants, and study sites.

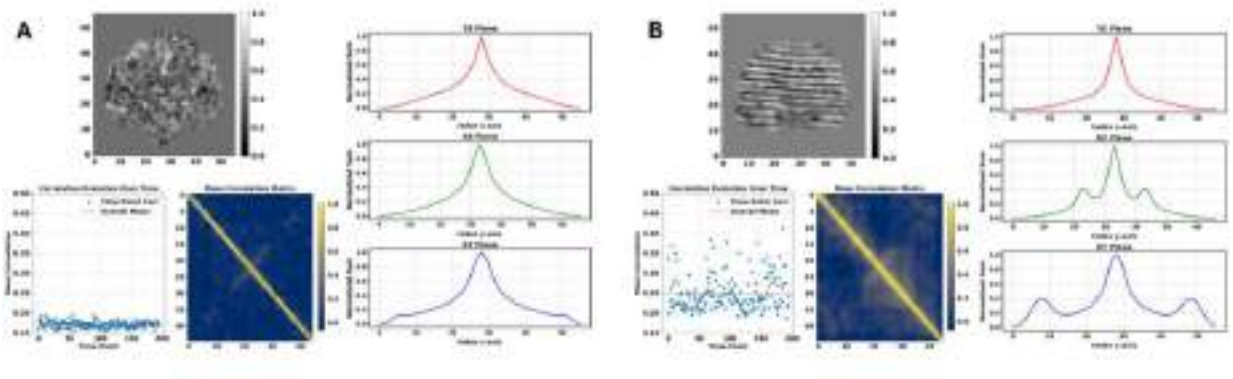

Figure 1 – Examples of non-artifacted (**A**) and artifacted (**B**) images in the QC report, respectively. Each example includes the slice with the highest correlation between rows, the average correlation of all the files for each time point of this slice, and its correlation matrix averaged for all the time points. The second column presents the projections on the three axis of the FT analysis. Higher correlation values and multiple peaks in the FT amplitude indicates the presence of artifacts.

References

[1]. Birn RM (2023) Quality control procedures and metrics for resting-state functional MRI. Front. Neuroimaging 2:1072927. doi: 10.3389/fnimg.2023.1072927

[**2].** Klinger HM, et al., Left Frontoparietal Control Network Connectivity Moderates the Effect of Amyloid on Cognitive Decline in Preclinical Alzheimer's Disease: The A4 Study. J Prev Alzheimers Dis. 2024; doi: 10.14283/jpad.2024.140.

A comparative study of deep learning models to synthesize post-contrast imaging

Jorge Rueda-Ramos[1], Elisa Moya-Sáez[1], Rodrigo de Luis-García[1], Laura Nuñez-González[2], Carlos Alberola-López[1], Juan Antonio Hernández-Tamames[2,3]

[1]LPI, University of Valladolid, Spain; [2]Radiology and Nuclear Medicine Department, Erasmus MC, The Netherlands; [3]Imaging Physics Department, TU Delft, The Netherlands.

Abstract

INTRODUCTION: Malignant glioma, the most common primary brain tumor in adults, is characterized by its heterogeneity and, in high-grade cases, its aggressiveness [1]. Its diagnosis is typically performed using MRI with gadolinium-based contrast agents, whose use presents drawbacks, such as potential adverse reactions, tissue accumulations, increased costs, and extended scan times, among others. In this study, we implement and compare different deep learning models to synthesize post-contrast MR weighted images in glioma patients from quantitative parametric maps obtained without the use of contrast agents.

METHODS: The dataset used was acquired at Erasmus MC, Rotterdam, The Netherlands on a 3T Sigma Premier GE scanner. It consists of a total of 15 glioma patients. For each of them, we have 4 weighted images: T1w, T2w, FLAIR, and post-T1w (ground truth), and the pre-contrast parametric maps: longitudinal relaxation time (T1), transversal relaxation time (T2), and proton density (PD), obtained using MAGiC [2]. In this work, these three maps are used as the inputs of the deep learning models compared, namely, a UNet [3] and a UNet with a Vision Transformer block (UNet-ViT). The former is based on a UNet neural network architecture with supervised learning whose inputs are the 2D maps. The latter is based on the same UNet neural network architecture, but it incorporates a ViT block in its bottleneck. Additionally, it is trained using self-supervised learning, since it incorporates a physical model (i.e., the theoretical equation of the applied pulse sequence) for network training, and the inputs are based on patches extracted from the input 2D maps. A visual comparison and a quality metric analysis with the structural similarity index (SSIM) and the peak-signal-to-noise-ratio (PSNR) are performed for the two deep learning models.

RESULTS & DISCUSSION: Figure 1 shows the boxplots of SSIM and PSNR metrics and, also, a visual representation for two representative patients of the ground truth acquired post-T1w images, the synthesized post-T1w for the UNet experiment, and the synthesized post-T1w for the UNet-ViT experiment. A significant improvement is observed between both experiments, which suggests that incorporating physical concepts (i.e., self-supervised learning), contributes to the optimization of the model. Additionally, the use of patches leverages the model to focus on small details, which improves the prediction of tumor enhancement, as observed in the figure (Fig. 1 d vs Fig. 1 e).

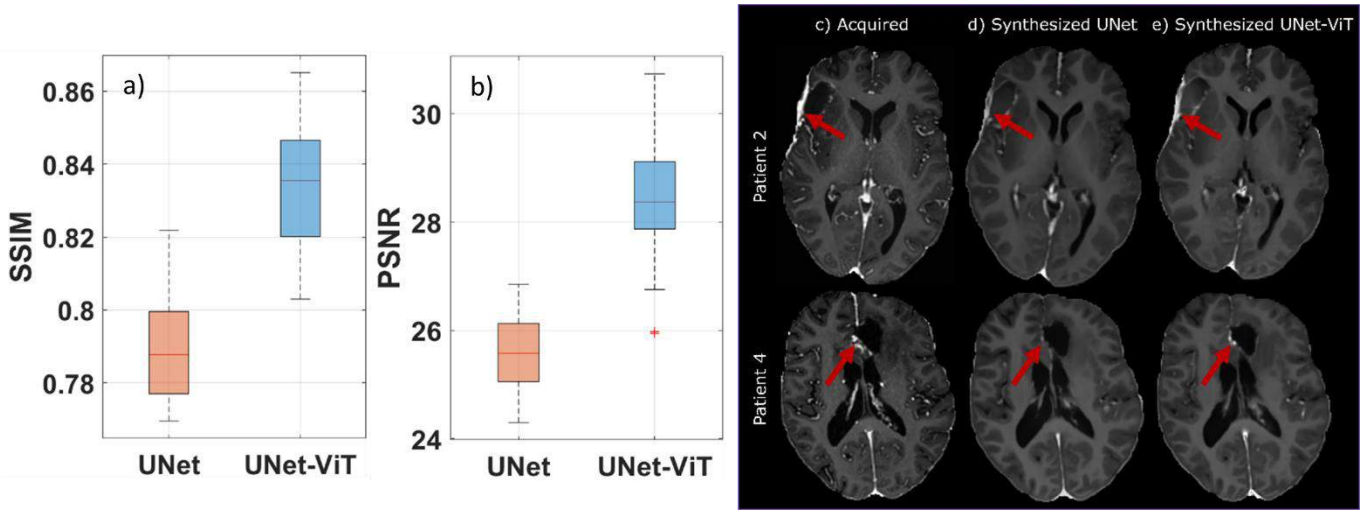

Figure 1 – On the left side, quality metrics a) SSIM and b) PSNR, calculated between the synthesized and acquired post-T1w images for the different experiments. Note that the background was not considered in the metric computations. On the right side, c) acquired post-T1w images and synthesized post-T1w images obtained with d) U-Net experiment and e) UNet-ViT experiment. The red arrows indicate tissues with enhancement.

References

1. Omuro A., et al. Journal of the American Medical Association 2013; 310(17), 1842-1850; **2.** Konar A. S., et al. Cancers 2022; *14*(15), 3624; **3.** Ronneberger O., et al. MICCAI 2015; part III 18 (pp. 234-241).

New perspectives for the analysis of intrinsic fMRI data and the improvement of automated diagnosis of Autism spectrum disorders: application of non-standard connectivity metrics, deconvolution approaches, and classifiers

Lucianna Lopes do Couto [1,2,*], Sofia Reimão [1], César Caballero-Gaudes [3], Alexandre Andrade [2]

[1] Faculty of Medicine of the University of Lisbon (FMUL), Lisbon, Portugal; [2] Institute of Biophysics and Biomedical Engineering (IBEB), Faculty of Sciences of the University of Lisbon (FCUL), Lisbon, Portugal; [3] Basque Center on Cognition, Brain and Language (BCBL), Donostia-San Sebastián, Spain;
* lucianna.couto@edu.ulisboa.pt

Abstract

INTRODUCTION: Autism spectrum disorders (ASD) are a group of neurodevelopmental conditions characterised by cognitive and/or behavioural impairment. The diagnostic process is multidisciplinary and time-consuming, involving mainly neuropsychological and imaging assessments; therefore, a fast and precise diagnostic is still challenging. In this context, the use of innovative methods to analyse intrinsic functional magnetic resonance imaging data (fMRI), such as non-standard connectivity metrics, deconvolution approaches to mitigate hemodynamic responses, automated diagnosis and biomarker identification, among others, are promising. The purpose of this work is to evaluate and compare intrinsic fMRI data from ASD subjects and typical controls, considering different non-standard connectivity metrics, deconvolution approaches, and machine learning classifiers for automated diagnosis.
METHODS: Data were obtained from the publicly available database ABIDE I Preprocessed (Autism Brain Imaging Data Exchange) [1]. Intrinsic fMRI timeseries (AAL atlas, 116 ROIs) [2] from 346 ASD subjects and 369 typical controls were deconvolved using two deconvolution approaches: Blind Deconvolution (BD) (MATLAB® rs-HRF toolbox) [3] and Paradigm Free Mapping (PFM) [4]. Functional connectivity matrices were obtained using six different connectivity metrics: Pearson's correlation without (PC) and with (Corr) time delay, Non-linear correlation coefficient (H2), Mutual information in time domain (MIT), Transfer entropy (TE) and Coherence (Coh) (MULAN toolbox) [5]. For each metric, two methods were adopted: bivariate, i.e., considering only the pairwise connections; and partial, i.e., calculating partial results to consider the influence of other ROIs. In addition, the connectivity direction was considered as well: for each metric, D indicates directed, and U indicates undirected connectivity [5]. All machine learning analyses, including evaluating the classification performance of classifiers in automated diagnosis of ASD, were performed with the Malini toolbox [6], considering features such as Accuracy and Confusion Matrix.
RESULTS & DISCUSSION: Considering all the connectivity metrics, their specific parameters and the deconvolution approaches used in this work, 168 groups were obtained for the analysis of automated diagnosis of ASD. For the Ridge Logistic Regression (RLR) classifier, for example, bivariate computations led to higher accuracies compared to partial computations. In terms of deconvolution approaches, BD performed better with more conventional connectivity metrics such as PC and Corr, while PFM performed better with MIT and TE. These results suggest that using deconvolution approaches and non-standard connectivity metrics in the analysis of intrinsic fMRI data may be a very useful strategy in the search for biomarkers in ASD, as they showed the potential to provide a more in-depth analysis.

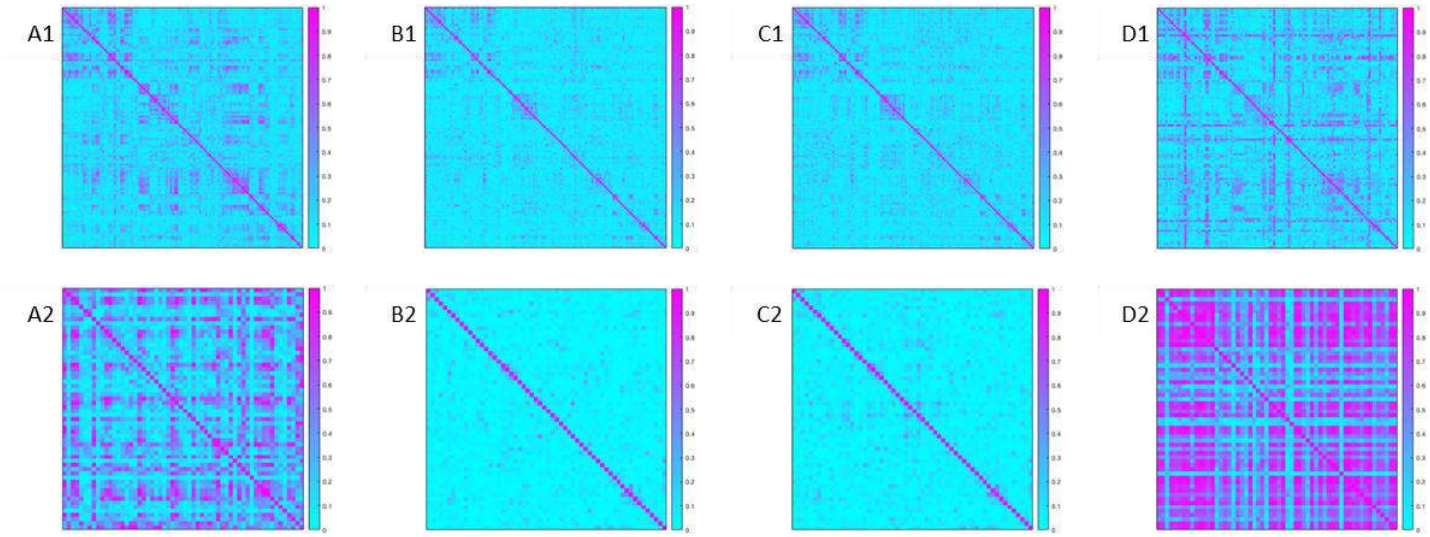

Figure 1. Functional connectivity matrices of a random ASD subject obtained using the metric Non-linear correlation coefficient (H2) and the deconvolution approaches BD and PFM. For each example, B indicates bivariate, P indicates partial, U indicates undirected. (A1) BH2U, non-deconvolved. (B1) BH2U, BD-deconvolved. (C1) BH2U, BD-fitted (adjusted). (D1) BH2U, PFM-deconvolved. (A2) PH2U, non-deconvolved. (B2) PH2U, BD-deconvolved. (C2) PH2U, BD-fitted (adjusted). (D2) PH2U, PFM-deconvolved.

References

[1] ABIDE I Preprocessed: http://preprocessed-connectomes-project.org/abide.
[2] Tzourio-Mazoyer N *et al*, 2002. doi:10.1006/nimg.2001.0978.
[3] Wu GR *et al*, 2013. doi:10.1016/j.media.2013.01.003.
[4] Gaudes CC *et al*, 2012. doi:10.1109/ISBI.2012.6235549.
[5] Wang HE *et al*, 2014. doi:10.3389/fnins.2014.00405.
[6] Lanka P *et al*, 2020. doi.org/10.1016/j.dib.2020.105213.

Open-MOLLI for All: Advancing Open-Source, Vendor-Agnostic T1-mapping One System at a Time, Now on GE!

Andreia S Gaspar[1], Paul JC Hughes[2], Jon-Fredrik Nielsen[3], Neil J Stewart[2], James M Wild[2], Teresa M Correia[4,5]. Rita G Nunes[1]

[1]Instituto de Sistemas e Robótica–Lisboa and Departamento de Bioengenharia, Instituto Superior Técnico, Universidade de Lisboa; Lisboa, Portugal; [2] POLARIS, Division of Clinical Medicine, School of Medicine & Population Health, University of Sheffield, Sheffield, United Kingdom [3]Functional MRI Laboratory, Department of Radiology, University of Michigan, MI, USA; [4]Centre of Marine Sciences Universidade do Algarve, Faro, Portugal; [5] School of Biomedical Engineering and Imaging Sciences King's College London, London, United Kingdom; *andreia.gaspar@tecnico.ulisboa.pt

INTRODUCTION: Standardization of MR quantitative measures is crucial for reproducible results that can be reliably used in the clinic to distinguish healthy from pathological tissues [1-3]. However, the implementation of techniques such as T1 mapping is known to vary between vendors, affecting reproducibility and hindering the method's applicability for clinical diagnostic and follow-up. Precise pulse sequence matching across centers and vendors has been shown to improve reproducibility [4] (e.g. VENUS [1] and Pulseq [5]).

The open-source myocardial T1 mapping (Open-MOLLI) sequence [6,7] was previously developed to enable reproducible cardiac T1-mapping. Open-MOLLI has since been tested in different Siemens systems (1.5 T and 3.0T) and compared to the vendor MOLLI implementations. It was shown to provide comparable myocardial T1 values with equivalent same-scan repeatability [8]. In this work, we extend the Open-MOLLI method and adapt the sequence to comply with specific GE requirements, demonstrating the feasibility to run it also on GE systems.

METHODS: MOLLI consists of an inversion-recovery (IR) sequence for quantitative T1 parameter estimation (T1 mapping). Open-MOLLI uses trigger scheme 5(3)3. It is publicly available at https://github.com/asgaspar/OpenMOLLI. Open-MOLLI was adapted for the GE system using TOPPE [9] by labelling the sequence into 4 blocks: the inversion pulse, the readout, the delay between readouts and the delay after inversion. The GE implementation of Open-MOLLI was tested on 2 healthy subjects (2M) in a 3T Signa PET-MR scanner using a 32 channel Head Coil.

The acquisition was performed in one axial brain slice, and the mean T1 was estimated in white (WM) and grey matter (GM) manually delineated regions of interest. Open-MOLLI with an under-sampling factor of 2 had the following parameters: field-of-view of 354 × 327 mm^2, matrix size 256×144, slice thickness of 8 mm, TR/TE=3.24/3.12 ms, flip angle of 35º, readout bandwidth 808 Hz/pixel, with shortest inversion time (TI) of 183 ms. The sequence timing was built according to a (simulated) heart rate of 60 bpm. Data reconstruction was performed offline using GRAPPA, and T1 estimation with 3-parameter analytic model using the magnitude signals was done in Matlab [3].

RESULTS & DISCUSSION: Open-MOLLI was successfully implemented on GE. Figure 1a shows the T1-weighted images obtained for 2 subjects. Figure 2b shows the T1 maps estimated for each subject. The mean T1 values for each region of interest are presented in Table 1, along with their standard deviations and the respective T1 literature values for GM and WM at 3.0T. The mean T1 over the two subjects was 772±22 ms for WM, and 1244±72 ms for GM, which is in agreement with the literature ($T1_{WM}$=860 ms and $T1_{GM}$=1200 ms)[10-13]. The work is a proof-of-concept of the applicability of Open-MOLLI to a vendor (GE) different from that in which it was originally implemented (Siemens). We were able to estimate T1 values for the brain (GM and WM) that are consistent with those reported in the literature at 3.0T. The adaptation of the Open-MOLLI T1-mapping sequence to the GE system required changes in the sequence that remain compatible with previously used Siemens systems. The current GE Open-MOLLI implementation still lacks the cardiac-triggering capabilities required for myocardial T1-mapping, which are the focus of ongoing work.

CONCLUSION: This work demonstrates the applicability of Open-MOLLI in GE systems, paving the way for future inter-scanner reproducibility studies.

a. Mean T1 (ms) per region

	Open-MOLLI		Literature [10]
	Subject 1	Subject 2	
White matter	788±92	757±70	860
Grey matter	1193±97	1295±116	1200

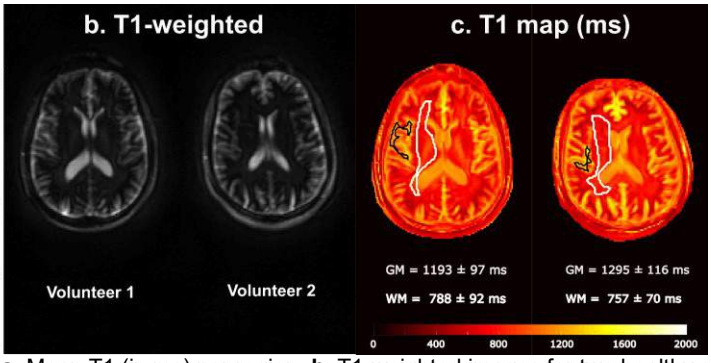

Figure 1 – T1 mapping in vivo with Open-MOLLI in GE: **a.** Mean T1 (in ms) per region; **b.** T1-weighted images for two healthy subjects with TI=183 ms, and respective, **c.** T1 maps (in ms). Region of interest for white matter (white) and grey matter (black) are represented, with respective mean T1 and standard deviation.

References: 1. Karakuzu A, et al. MRM. 2022;88(3):1212–28. **2.**Tong G, et al. MRI. 2021;87:7-18. **3.** Kellman P, et al. JMRI. 2014; 16: 2. **4.**Teixeira RPAG,et al. MRM. 2020; 84: 221-236. **5.** Layton KJ, et al. MRM. 2017;77:1544-1552. **6.** Gaspar AS, et al. MRM. 2024; 1-10. **7.** Messroghli DR, et al. JMRI. 2007;26(4):1081-1086. 8. Gaspar AS, et al. 14th ESMRMB, Spain; p. 0431. **9.** Nielsen J.-F, et al. MRM. 2018;79: 3128-3134. **10.** Clare S, et al. MRM. 2001;45: 630–4.

Acknowledgements: "la Caixa" Foundation and FCT, I.P [LCF/PR/HR22/00533]; **FCT** (SFRH/BD/120006/2016, PTDC/EMD/EMD/29686/2017; UIDP/50009/2020; UIDB/04326/2020 DOI:10.54499/UIDB/04326/2020, UIDP/04326/2020 DOI:10.54499/UIDP/04326/2020, LA/P/0101/2020 DOI:10.54499/LA/P/0101/2020, LISBOA-01-0145-FEDER-029686, DOI: 10.54499/LA/P/0083/2020,10.54499/UIDP/50009/2020,10.54499/UIDB/50009/2020.

A Free and Open-Source Web Application for Pulse Sequence Development and Simulation

Pablo Villacorta-Aylagas[1], Carlos Castillo-Passi[2], Pablo Irarrázaval[2], Federico Simmross-Wattenberg[1], Manuel Rodríguez-Cayetano[1], Carlos Alberola-López[1]

[1]Laboratorio de Procesado de Imagen, Universidad de Valladolid; [2]Instituto de Ingeniería Biomédica, Pontificia Universidad Católica de Chile;

Abstract

INTRODUCTION: Both pulse sequence design and acquisition simulation are essential disciplines in MRI research. In previous work [1], we introduced a graphical pulse sequence editor and a web version of the KomaMRI [2] simulator. The former, while useful, lacked flexibility for defining global parameters and included a 3D slice visualization tool not well suited for web environments. Regarding the latter, it allowed remote simulations but was not integrated with the sequence editor. This work therefore presents a complete and improved platform that integrates both components, enabling the design and simulation of advanced MRI sequences in a web-based environment free of local installations.
METHODS: A full-stack development has been carried out, addressing both the front-end and the back-end, as well as the communication mechanisms between them. Specifically, the front-end includes an improved version of the previously developed sequence editor, a 3D slice visualization tool, and two additional panels: one for visualizing the temporal sequence diagram and the other for displaying simulation results. This implementation combines the Qt framework with web technologies such as HTML, JavaScript, VTK.js, and WebAssembly. The back-end, developed in Julia, includes an HTTP server with a REST API, the KomaMRI simulator, and additional modules which include the database and front-end compiled files.
RESULTS & DISCUSSION: The tests conducted with the developed tool highlight its usefulness, interactivity, and smoothness, also demonstrating its ability to design and simulate arbitrarily complex pulse sequences without the need for local installations. Figure 1 displays the application layout, integrated within the Web browser.

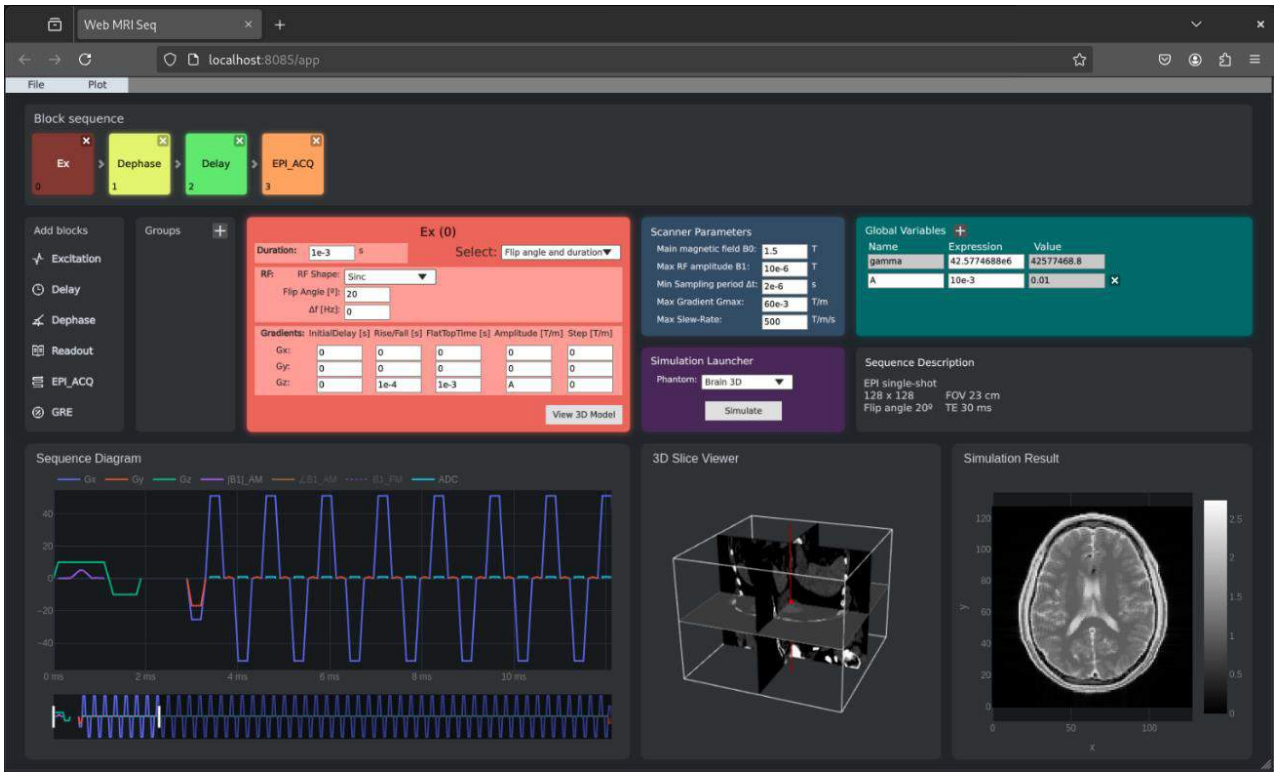

Figure 1 – Final layout of the web application. Upper panels handle sequence design and simulation launch in KomaMRI, while lower panels display the sequence diagram and simulation results.

References

1. P. Villacorta-Aylagas, I. Fernández-Arias, C. Castillo-Passi, P. Irarrázaval, F. Simmross-Wattenberg, M. Rodríguez-Cayetano, and C. Alberola-López, “A Web Version of KomaMRI. Sequence Editor and Remote Execution”, in ISMRM Iberian Chapter Annual Meeting 2023, Valladolid, Spain.

2. C. Castillo-Passi, R. Coronado, G. Varela-Mattatal, C. Alberola-López, R. Botnar, and P. Irarrázaval, “KomaMRI.jl: An open-source framework for general MRI simulations with GPU acceleration”, Magnetic Resonance in Medicine, vol. 90, no. 1, pp. 329-342, 2023.

High-resolution advanced diffusion MRI of rectal cancer surgical specimens: correlating microstructural characteristics with histology

Ana R Fouto[1*], Mireia Castillo-Martin[2], Shermann Moreira[2], Noam Shemesh[2], Laura Fernandez[2], Hasti Calá[2], Nuno Couto[2], Ignacio Herrando[2], Stephanie Nougaret[3], Raluca Popita[4], Jorge Brito[5], Susana Ouro[6], Miguel Chambel[2], Nikos Papanikolau[2], Amjad Parvaiz[2], Richard J. Heald[2], Inês Santiago[1,6] and Andrada Ianus[1,2,7]

[1] Algarve Biomedical Center, Faro, Portugal; [2] Champalimaud Foudation, Lisbon, Portugal; [3] Montpellier Cancer Research Institute (IRCM), France; [4] The Oncology Institute "Prof. Dr. Ion Chiricuță" Cluj-Napoca, Romania; [5] Centro Hospitalar Universitário do Algarve EPE, Portugal; [6] Hospital da Luz, Lisbon, Portugal; [7] King's College London, BMEIS School, London, UK. *ana.fouto@abcmedicalg.pt

INTRODUCTION: Clinical MRI is commonly used for diagnosing rectal cancer, with T_2-weighted images being the primary modality for staging and restaging after neoadjuvant therapy (NAT) [1,2]. Diffusion MRI (dMRI), which provides information on tissue microstructure and cellularity, is recommended as an adjunct for assessing tumour response. However, studies have demonstrated its potential to enhance tissue characterization significantly [3,4,5]. This study maps the diffusion characteristics of various rectal wall components using high-resolution advanced dMRI of total mesorectal excision (TME) specimens post-NAT; and evaluates its ability to differentiate several tissue types.

METHODS: All experiments were approved by the institutional ethics committee.

Specimen preparation for ex-vivo MRI: Four patients diagnosed with rectal cancer underwent TME after NAT. Surgical specimens were immersed in 10% buffered formalin for ~36h, then rinsed, immersed in 1xPBS for 4h, and mounted in a cylindrical container covered with Fomblin (a MR-invisible fluid). Samples were imaged with a 9.4T Bruker Biospec scanner (at 22 ºC; 86 mm transmit/receive). Specimens were pseudonymized by Champalimaud Foundation Biobank.

Histopathology examination: The rectum was cut in 5mm sections (grossing stage), and areas of interest embedded in paraffin. H&E-stained slides were digitalized (Philips Ultra-Fast Scanner 1.6) and matched with the grossing images. A pathologist with 23 years of experience identified distinct tissues on the histology slices which were aligned with corresponding MRI slices based on morphological landmarks and confirmed by a radiologist with 13 years of experience.

dMRI data: 2D standard DTI: TR/TE=11000/24 ms; 130 slices; matrix size: 140 x 130; isotropic resolution of 0.5 mm^3, 2 b0 images, 2 b-values (1500 s/mm^2, 3000 s/mm^2) and 15 diffusion directions. Diffusion and kurtosis tensor parameters were mapped voxelwise using a linear least squares (LLS) algorithm in Matlab. Regions of interest (ROIs) for mucosa, submucosa, muscle layers, tumour and fibrous tissue were defined on MRI following MRI-histopathology correlation (Fig. 1a). To evaluate differences between mean value across six tissue types of each diffusion parameter, we used a Linear Mixed-effects Model on JASP, with FDR correction for multiple comparisons.

RESULTS & DISCUSSION: Our findings showed significant differences in diffusion parameters, specifically fractional anisotropy (FA), mean diffusivity (MD), and mean kurtosis (MK) across various tissue types (Fig. 1b). Muscle tissue exhibits the highest FA values, while tumor and fibrous tissue demonstrate increased FA compared to healthy mucosa. Tumour regions also exhibit lower MD values compared to fibrous tissue, indicating increased cellularity and restricted diffusion. MK values show less tissue differences, with potentially lower values in fibrous tissue compared to tumour areas. Colour coded FA maps further provide information about the tumour invasion in the muscle layer (Fig. 1c).

CONCLUSION: DTI/DKI metrics can improve tissue mapping for rectal cancer (re)staging beyond conventional DWI.

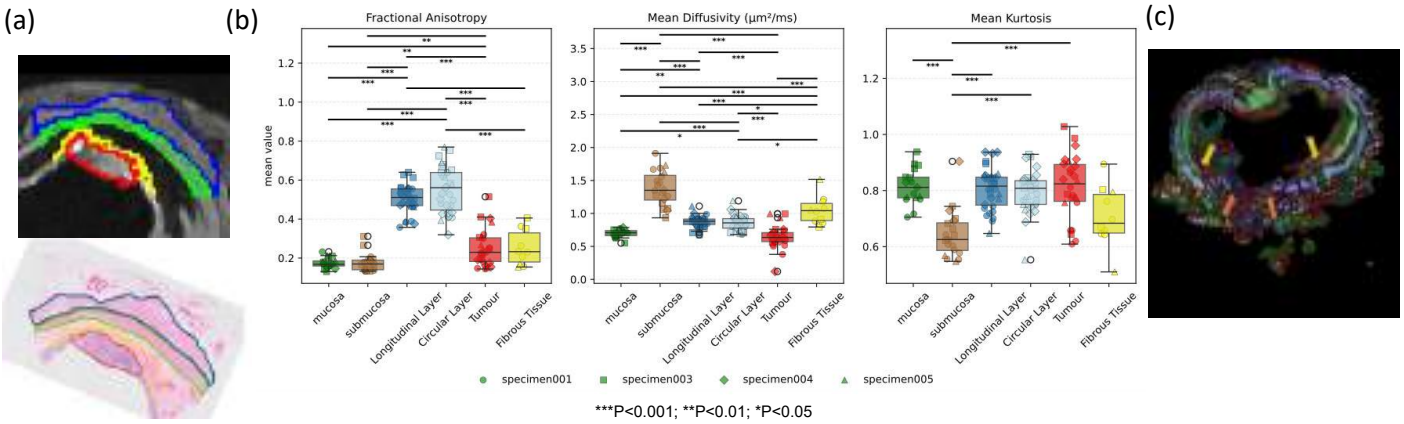

Figure 1 – (a) An illustrative example of the defined ROIs on MRI (top) and matching histological slice (bottom). The colored lines represent the different tissue ROIs: Longitudinal muscle layer (dark-blue); Circular muscle layer (light blue); Tumour (red) and Fibrous Tissue (yellow). (b) Boxplots showing the pairwise significant differences across the various rectal wall layers, as well as tumour and fibrous regions, for FA; MD and MK maps. (c) The color-coded FA map showing the directionality of the principal DT eigenvector overlaid on the FA map. Yellow and orange arrows indicate interruption of longitudinal and circular muscle layers, respectively, due to persistent in-depth tumour invasion.

References

1. Horvat N, et al. Radiographics. 2019;39: 367–387. **2.** Santiago I, et al. Insights Imaging. 2021;12: 114. **3.** Fokkinga, E, et al. JMRI 60.4 (2024): 1278-1304. **4.** Schurink, N.W. et al, Br J Radiol, (2019): 92(1096):20180655; **5.** Pham T. T. et al, Sci Rep (2019): 27;9:9311

Acknowledgements: This work has been funded by Fundação para a Ciência e a Tecnologia (2023.02201.RESTART; THCS/0003/2023) under the framework the co-fund partnership of Transforming Health and Care Systems, THCS, (GAN° 101095654 of the EU Horizon Europe Research and Innovation Programme).

Olfactory functional MRI: Application to evaluate brain activation patterns in women with sexual interest-arousal disorders

I. Herrero-Vidaurre[1], L. Ribera-Torres[2], J. Otero[3,4], R. Farre[3,4], C. Castelo-Branco[2,4], E. Muñoz-Moreno[1].

1 Magnetic Resonance Imaging Core Facility, IDIBAPS, Barcelona, Spain. 2 Clinical Institute of Gynecology, Obstetrics and Neonatology, Hospital Clinic de Barcelona, IDIBAPS, Universitat de Barcelona, Barcelona, Spain. 3 Unitat de Biofísica i Bioenginyeria, Facultat de Medicina i Ciències de la Salut, Universitat de Barcelona. 4 IDIBAPS, Barcelona, Spain

Introduction: Olfactory functions such as odor detection or response to olfactory stimuli can be assessed by functional MRI and contribute to the understanding of brain and behavior under different conditions. However, in comparison to other sensory domains, fMRI under olfactory stimulation has been less explored, in part due to the need for specific olfactory delivery systems. We performed olfactory-based fMRI using a custom-built system and applied it to evaluate the response to pheromone in female sexual dysfunction (FSD) subjects before and after treatment. FSD significantly impacts quality of life, with the most common subtype being hypoactive sexual desire disorder (FSIAD), characterized by a persistent lack of sexual desire or fantasies. Its causes are not fully understood but likely involve neuroendocrine, psychiatric, and behavioral factors. Only two studies have directly compared brain activity in women with and without FSIAD (3, 4). This study hypothesizes that FSD and the improvement in sexual dysfunction observed with ospemifene treatment is associated to changes in the response to pheromone, that can be measurable through olfactory stimulus-based fMRI (5).

Methods: We conducted fMRI analyses to study brain activation patterns before and after ospemifene treatment, in a cohort of 15 women with FSD (9 with ospemifene treatment, 6 with placebo). Participants were exposed to alternating scents—pheromones, clean air, and Phenyl Ethyl Alcohol (PEA) —using an open-source, low-cost, custom-built olfactory delivery system compatible with the fMRI setting. The fMRI protocol followed a standard block design with 12 one-minute alternating scent exposures. Head movement was minimized using individually molded foam supports. Prior to functional imaging, a high-resolution T1-weighted structural scan was acquired to exclude anatomical abnormalities and enable accurate localization of brain activity. Functional images were preprocessed with motion correction, EPI correction with T1 and a registration to the MNI152 atlas (6). First level analysis was performed afterwards, to obtain each subject activation in response to each odor in comparison with clean air, followed by a dual regression and randomization. The activation before and after treatment in each treatment group (ospemifene and placebo) was compared using voxel-wise randomize with TFCE correction. Significance was defined as $p<0.005$.

Results, discussion and conclusion: Fig 1.A shows the mean activation map in response to pheromone and PEA, showing a similar pattern of activation in areas related to olfaction, but with some differences in more occipital regions. Regarding the treatment effect, in women who received ospemifene, decreased brain activation was observed after treatment in response to both pheromone (fig.1B) and PEA odors (Fig 1C). Specifically, changes were noted in the frontal pole and medial frontal cortex for the pheromone, and in the insula, parietal operculum, and planum temporal for PEA. In the placebo group, changes between pre- and post-treatment were smaller. Reduced activation to pheromone was seen in the frontal pole (compared to no stimulus) and in both the frontal pole and cingulate gyrus (compared to PEA). In conclusion, ospemifene appears to modulate brain responses to olfactory stimuli in women with hypoactive sexual desire disorder, that can be detected by fMRI analysis.

Figures

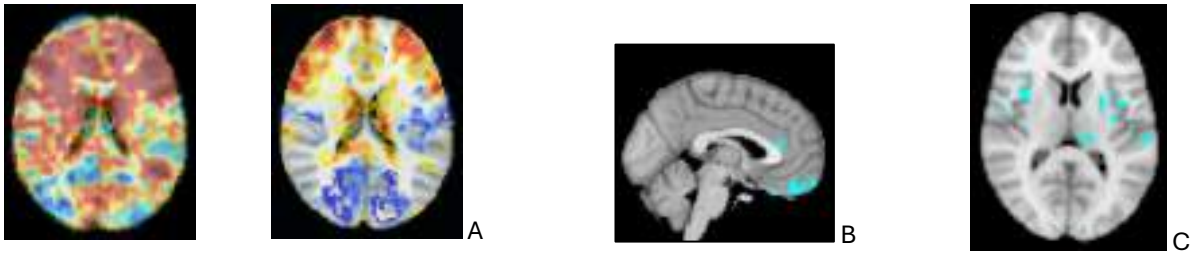

Fig. 1: (A) Mean of first level analysis of activations in PEA and Pheromone vs Rest. (B) Areas of decreased activations after treatment in response to pheromone. (C) Areas of decreased activations after treatment in response to PEA.

1. American Psychiatric Association. 2013. 2. Hayes RD et al. 2. J Sex Med 2008; 5:777–87. 3. Neuroscience 2009; 158:484–502, Arnow et al. 4. Neuroimage 2000; 12:314–25, Caselli et al. 5. Neuroscience Letters, Volume 735, 2020, 135166, Han et al. 6. https://brainmap.org/training/BrettTransform.html

Using ADC-Based Measurements to Predict Functional Recovery and Malignant Infarction in Acute Ischemic Stroke of the Anterior Circulation

[Cabero-Arnold, Andrea][1,2*], [Rossi, Sergio Soeren][3], [Rodríguez Vázquez, Alejandro] [1,2], [Laredo, Carlos][1,2], [Doncel- Moriano, Antonio][1,2],[Ramis, Dario J][1,2], [Moraleja, David][1,2],[Rosa, Irene][1,2],[Renú, Arturo][1,2],[Urra, Xabier][1,2],[Chamorro, Angel][1,2]

[1][Comprehensive Stroke Center, Department ofNeuroscience, Hospital Clinic, Barcelona, Spain]; [2][Fundació de Recerca Clínic Barcelona - Institut d'InvestigacionsBiomèdiques August Pi i Sunyer (IDIBAPS), Barcelona, Spain]; [3][Research Unit of Neurology, Department of Medicine and Surgery, Università Campus Bio-Medico di Roma, Rome, Italy,]; *[cabero@recerca.clinic.cat]

Abstract

INTRODUCTION: Predicting functional outcomes and complications, such as malignant Middle Cerebral artery Infarction (MCI), remains challenging in Acute Ischemic Stroke (AIS). Advances in the treatment of patients with even the largest ischemic lesions suggest that ischemic lesions may be heterogeneous.[1] Apparent Diffusion Coefficient (ADC) sequences provide insights into ischemic lesion microstructure.[2] This study evaluated the prognostic potential of ADC-derived variables in moderate-severe anterior circulation AIS patients.

METHODS: 78 patients imaged within 48 hours post-stroke were retrospectively analyzed. DWI sequences were processed to segment lesion volumes and extract ADC maps, ADC signal intensity (Intensity Score), interquartile range (IQR), and ADC_{rel500} (Lesion volume <$500\times10^{-6}mm^2/s$ relative to total lesion volume). Clinical outcomes at 90 days were assessed using mRS. Logistic regression models, including combined models, were developed to predict functional independence (mRS≤2) and MCI, evaluating their added value beyond lesion volume quantification.

RESULTS & DISCUSSION: 55 patients (71%) had poor functional outcomes, 11 (14%) developed MCI, and 23 (29%) died. Larger ADC_{rel500} volumes, higher Intensity Scores, and wider IQRs were associated with worse mRS ($p<0.05$). Combined models (AUC 0.894 for mRS and 0.896 for MCI) significantly outperformed lesion volume model (AUC 0.821 for mRS and 0.822 for MCI) according to Likelihood Ratio Test ($p<0.01$) (Fig.1).

ADC-derived metrics, by capturing ischemic lesion dynamics and heterogeneity—encompassing cytotoxic and vasogenic edema—may reflect early blood-brain barrier disruption and neurovascular unit dysfunction. These insights may enable early identification of high-risk patients, improve risk stratification and guide personalized AIS therapies.

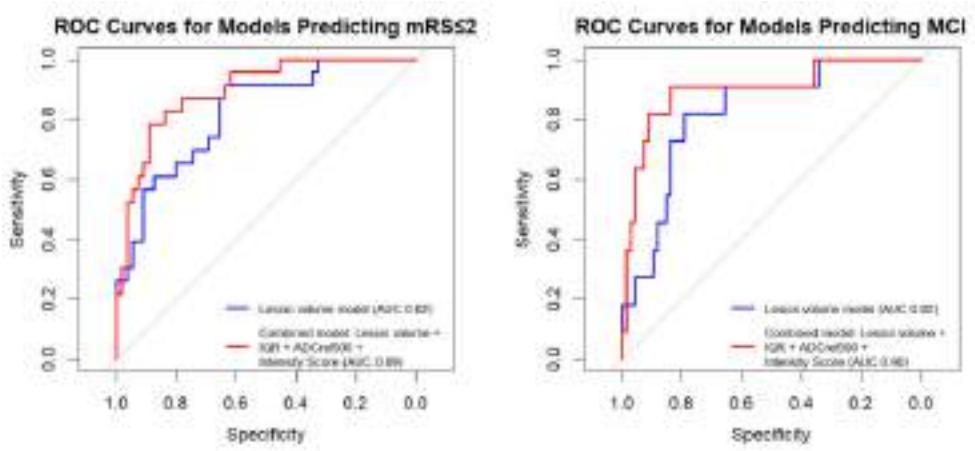

Figure 1 – ROC Curves for Models Predicting (A) modified Rankin Score≤2 and (B) MCI.

References

1. Lu, Q., Zheng, L., Nie, X., Wang, M., Duan, W., Liu, X., ... & Liu, L. (2025). Clinical Severity and Outcomes in Large Infarcts With Endovascular Therapy: A Post Hoc Analysis of the ANGEL-ASPECT Trial. *Stroke*, *56*(4), 1048-1053. **2.** Rana, A. K., Wardlaw, J. M., Armitage, P. A., & Bastin, M. E. (2003). Apparent diffusion coefficient (ADC) measurements may be more reliable and reproducible than lesion volume on diffusion-weighted images from patients with acute ischaemic stroke–implications for study design. Magnetic resonance imaging, 21(6), 617-624.

Whole-brain functional connectivity in the A4 and LEARN datasets to study preclinical Alzheimer's Disease

Marina Mas-Argemí[1], Raúl Tudela[2,1], Marc Biosca[1], Roser Sala-Llonch[1,2].

[1]*Institut de Neurociències, Departament de Biomedicina, Universitat de Barcelona. IDIBAPS. Barcelona, Spain.*
[2]*CIBER de Bioingeniería, Biomateriales y Nanomedicina, Instituto de Salud Carlos III, Barcelona, Spain*

INTRODUCTION: Resting-state functional magnetic resonance imaging (fMRI) allows studying functional connectivity (FC), offering the opportunity to analyze, providing insights into brain organization, several conditions and disease. In the context of Alzheimer's Disease (AD), brain changes have been described before clinical symptoms, as abnormal Amyloid levels, and altered structure and function. Here, we studied fMRI data of a large cohort of adults, with and without the presence of amyloid in the brain.

METHODS: We analyzed fMRI data of 1890 participants from the A4 and LEARN-NE studies [1] (ages 65-85 y) with normal cognition or very mild cognitive impairment, presenting normal (LEARN) or slightly elevated (A4) amyloid levels as observed on Amyloid PET scans. Additional data included demographics, cognitive assessments, and APOE genotyping. Images were preprocessed with an automated fMRI pipeline combining in-house developed python scripts and tools from available packages as FSL, AFNI and ANTs. All images were passed through accurate visual and quantitative quality control (QC). We performed group Independent Component Analysis (ICA) to derive a set of common Resting State Networks (RSNs), followed by dual regression and FSLNETS approach to generate individual FC matrices, calculated as partial correlation between RSNs' timeseries. We applied general lineal models to study differences between groups and correlations with age and amyloid levels.

RESULTS & DISCUSSION: A total of 395 subjects from LEARN and 897 subjects from the A4 study passed the QC and were considered for further analyses. With an ICA we identified 20 RSNs over a total of 30 components (Figure 1A). We found FC differences ($p<0.05$) between groups, with subjects with amyloid positivity showing less connectivity. We also found both positive and negative relationships with age, suggesting whole-brain functional reorganization.
Overall, we demonstrate that the functional architecture at rest might have important implications in driving the effect of amyloid pathology and age effect in the brain at preclinical disease stages. The analysis of the functional connectivity as a whole aims to have a remarkable role in the early diagnosis of AD.

Acknowledgments
The A4 Study is a public-private partnership, funded by the National Institute on Aging (NIA), Eli Lilly and Company, and other partners. We acknowledge the contributions of the A4 Study investigators, participants, and study sites.

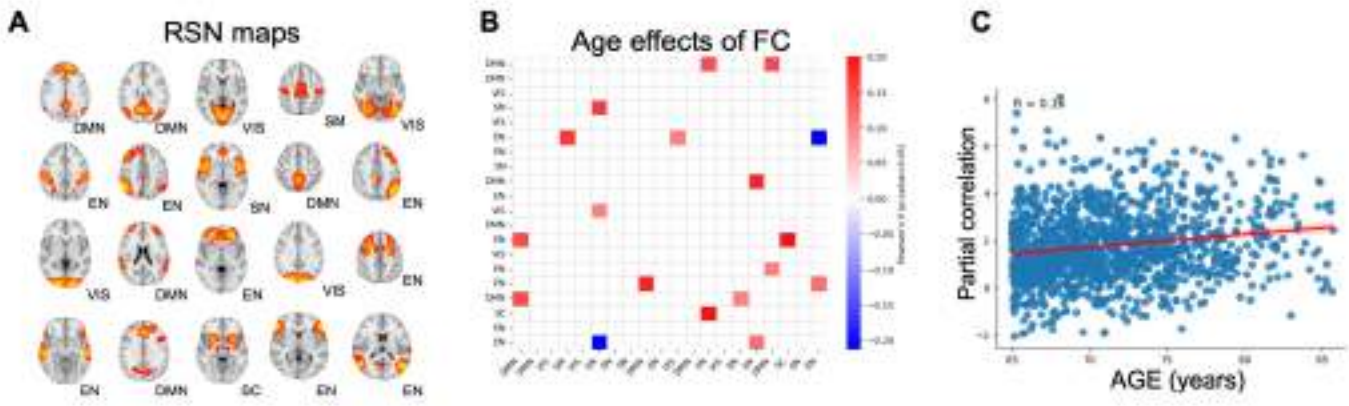

Figure 1 – A. Spatial maps of the identified RSNs; **B.** Matrix showing correlations between brain connectivity and age (only significant edges with $p<0.05$ are shown). **C.** Scatter plot of a sample edge showing positive effect of age on the connectivity.

References

[1] Sperling RA, Donohue MC, Raman R, Rafii MS, Johnson K, Masters CL, van Dyck CH, Iwatsubo T, Marshall GA, Yaari R, Mancini M, Holdridge KC, Case M, Sims JR, Aisen PS; A4 Study Team. Trial of Solanezumab in Preclinical Alzheimer's Disease. N Engl J Med. 2023 Sep 21;389(12):1096-1107. doi: 10.1056/NEJMoa2305032. Epub 2023 Jul 17. PMID: 37458272; PMCID: PMC10559996.

A Radiomics-Based Signature for Identifying Successful Response to TMZ Treatment in Murine GL261 Glioblastoma: leveraging the peritumoral zone

Benito Farina[1,2], Juan E. Ortuño[2,1], Andrés Santos[1,2], Ana Paula Candiota[2,3], María J. Ledesma-Carbayo[1,2]*

[1]Biomedical Image Technologies, ETSI Telecomunicación, Universidad Politécnica de Madrid, Madrid, Spain; [2]CIBER-BBN, Instituto de Salud Carlos III, Madrid, Spain; [3]Departament. de Bioquímica i Biología Molecular (Unitat Biociències), Universitat Autònoma de Barcelona, Cerdanyola del Vallès, Spain. *mj.ledesma@upm.es

Abstract

INTRODUCTION: Glioblastoma (GB) is the most aggressive primary brain tumor in adults, characterized by high invasiveness and poor prognosis [1]. Magnetic Resonance Imaging (MRI) is crucial for characterizing GBM, but distinguishing early treatment effects from tumor progression remains challenging. Temozolomide (TMZ) is the standard chemotherapy for GB, yet its effectiveness varies, underscoring the need for advanced biomarkers to assess treatment response, allowing for an early switch to a second line treatment [2]. This study evaluates the potential of T2-weighted MRI-derived radiomic features to identify local tissue changes in TMZ-treated GL261 GB-bearing mice showing transient response, from untreated controls in which tumors are showing uncontrolled proliferation, regardless of tumor volumes. **METHODS:** GL261 tumors were generated through intracranial injection as described by us [3]. TMZ was administered (60mg/kg) to treated groups starting at day 11 post-implantation, with protocols described in [3] and [4]. T2w MRI studies were performed at 7T with a RARE sequence (TR/TEeff = 4200/36ms). T2-weighted MRI data were collected from 60 mice (31 TMZ-treated, 29 controls), and radiomic features (51 features/case) were extracted from three regions: tumor core, dilated peritumoral borders (3.5 mm radius), and combined tumor regions (Figure 1). Image intensities were normalized (0–250 range), and feature discretization was tested with bin widths of 2, 4, and 6. A training set (30 mice: 17 treated, 13 controls) was used to develop supervised machine learning models (Random Forest, SVM, Logistic Regression) with ANOVA-based feature selection and hyperparameter optimization (GridSearchCV, 5-fold cross-validation). The other 30 mice were used as an independent test set. **RESULTS & DISCUSSION:** Models relying solely on tumor core or tumor edge features showed poor classification (low AUC/accuracy), while combined tumor-peritumor features enabled robust discrimination. The optimized Random Forest classifier achieved an AUC of 0.92 and accuracy of 0.93 on the test set (30 mice: 14 treated, 16 controls), with texture-based features dominating the predictive signature. These findings support the idea that the peritumoral zone contains molecular/cellular alterations involved in proliferation, invasion, and recurrence [5]. Moreover, microglial cells have been described in peritumoral zones, and depending on their phenotype, they can have different impact on tumor response to therapy. The changes in molecular characteristics and cell populations, as well as local effects on tumors, can be potentially spotted with advanced imaging approaches [6] which are not currently considered in standard pipelines. TMZ-treated mice that were followed-up until endpoint presented prolonged survival time (43±10 days, n=11), and some mice (n=4) showed total tumor remission, compared with the standard survival of untreated mice (ca. 21 days, UAB data, n>100), confirming the treatment efficacy. It is worth mentioning that in most cases, the study was not conducted to endpoint since euthanasia was done for validation purposes. However, data were obtained during a clear response (TMZ-treated) or exponential tumor growth (control mice). Although control mice do not fully represent a “tumor progression after treatment” group, this approach could pave the way for future studies in this direction. **CONCLUSION:** These results suggest that radiomic heterogeneity within the tumor and its peritumoral area is critical for distinguishing treatment effects triggered in TMZ-treated mice, which presented, as expected, relevant differences from control animals. The model’s predictive potential arises from its ability to capture microenvironmental heterogeneity reflective of TMZ-induced biological changes, which are linked to treatment response.

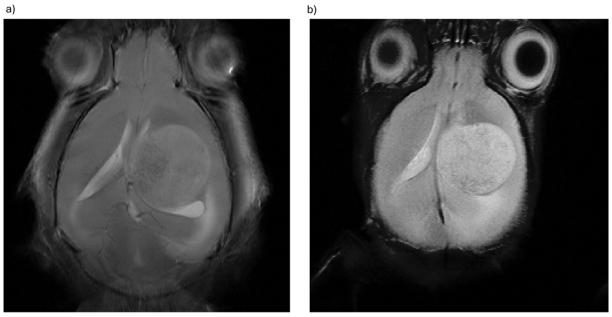

Figure 1 – MRI images at day 16: (a) Control case, (b) Treated case.

1. M. Reni, et al, “Central nervous system gliomas,” Critical Reviews in Oncology/Hematology, vol. 113. Elsevier Ireland Ltd, pp. 213–234, 01-May-2017.; **2.** A. Karachi, et al, *Neuro. Oncol.*, 20(12): 1566–1572, 2018. **3.** Arias-Ramos N, et al. Metabolites. 2017;7(2):20**. 4.** Wu S, -et al. NMR Biomed. 2020;33(4):e4229. **5.** Ballestín A, et al. Front Immunol. 2024;15:1347877. **6.** Altieri R, et al. Brain Sci. 2021;11(2):200.

Different Models, Different Brain Age Gaps in Chronic Musculoskeletal Pain

Paula Caballero-Lillo[1,2], Rafael Navarro-González[1,2], Álvaro Planchuelo-Gómez[1], Irene Guadilla[1], Santiago Aja Fernández[1], Federico Montero[3] and Rodrigo de Luis-García[1]

1. Laboratorio de Procesado de Imagen, Universidad de Valladolid, Valladolid, Spain
2. Headache Unit, Hospital Clínico Universitario de Valladolid, Valladolid, Spain
3. Active Pain Coping Strategies Unit, Primary Care Area of Eastern Valladolid, Valladolid, Spain

INTRODUCTION: Chronic musculoskeletal pain (MSKP) has been associated with neuroplastic changes that may affect brain structure and function. Brain age prediction serves as a promising biomarker to characterize such alterations [1]. This study investigates brain age differences between healthy controls and MSKP patients with chronic back pain using four distinct models: the model developed by David A. Wood (with and without fine-tuning), Pyment, and an in-house model based on morphological features. Cross-sectional and longitudinal analyses were conducted to evaluate baseline differences and potential brain aging trajectories over time.

METHODS: MRI data were acquired on a 3T scanner (Universidad de Valladolid) from 53 healthy controls and 38 MSKP patients. A second scan was obtained for 32 of the patients after a six-month interval.

Four brain age models were used: the David A. Wood model[2] trained on an external dataset; the same model after fine-tuning using local data from the LPI database (n = 187) ; Pyment [3]; and an in-house model, a single-layer MLP trained on 4,268 open-access T1w MRI cases. This model uses 314 brain features extracted with FastSurfer (7.4.1) [4].

Brain Age Gap (BAG = predicted age – chronological age) was analyzed using ANCOVA or a robust linear model if ANCOVA assumptions were not met. Sex and estimated total intracranial volume (eTIV) were included as covariates. Age was either corrected in the predictions or included as a covariate.

RESULTS & DISCUSSION: Two of the brain age models employed (original David A. Wood and Pyment) revealed a statistically significant different brain age gap between healthy controls and MSK patients (p=0.045 and p=0.019, respectively). The Pyment model also detected differences in second acquisition (p=0.0006). Surprisingly, differences indicated lower brain age in MSK patients. The other two models (fine-tuned David A. Wood and in-house model) revealed no differences. Also, no significant differences in the brain age gap were found longitudinally with any of the models. These findings suggest that, although brain age could be a useful biomarker in chronic pain, results may critically depend on the chosen brain age model and the specific patient group considered [5]. Further research is needed to elucidate the existence and nature of these possible differences

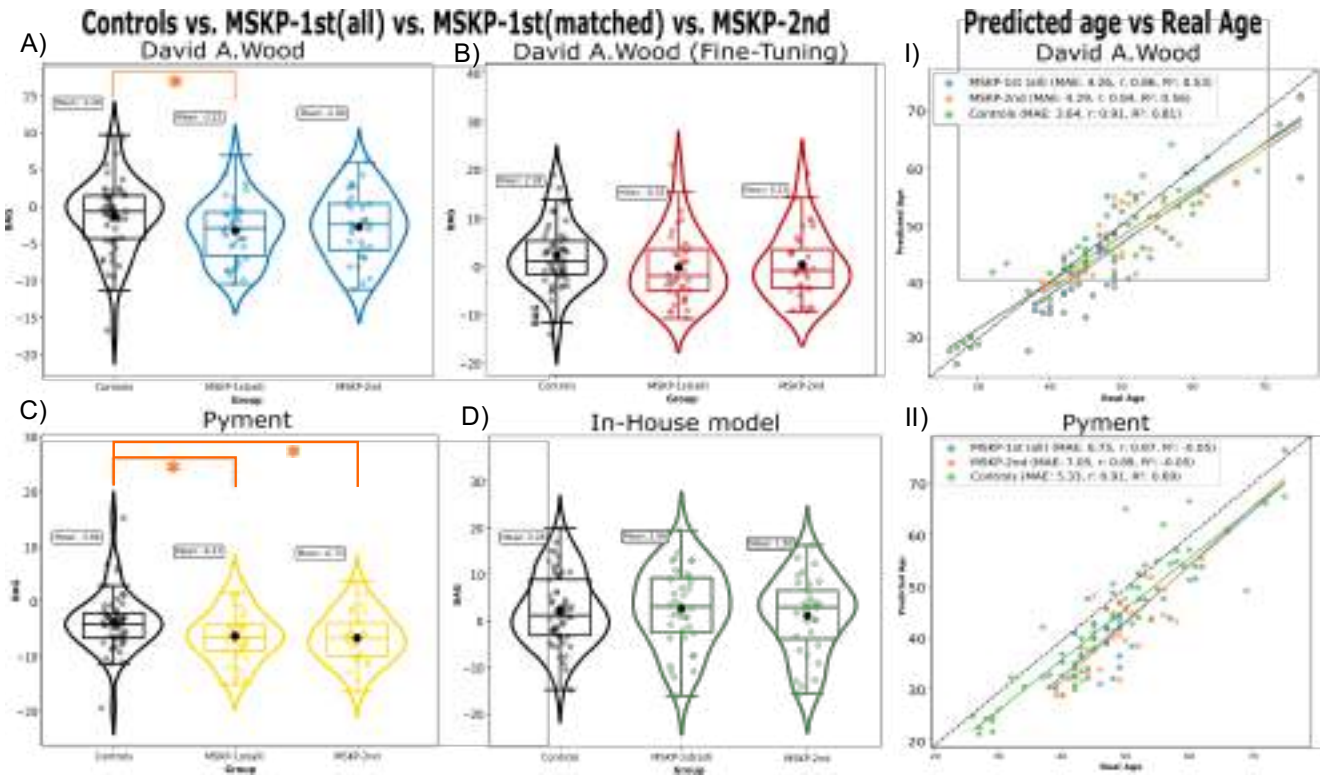

***Figure 1**. (a–d) Brain Age Gap (BAG) comparisons between healthy controls and MSKP patients across four models: (a) David A. Wood, (b) David A. Wood Fine-Tuning, (c) Pyment, (d) In-house model. Asterisks (*) indicate significant group differences. (I–II) Scatter plots showing predicted brain age vs. real age at the first and second acquisition for MSKP patients and healthy controls.*

References: **1**.Gary, Z. Yu, et al. *Brain Research* 1755 (2021): 147263. **2**. Wood, David A., et al. *Human Brain Mapping* 45.4 (2024): e26625.2997–3011. **3.** Leonardsen, Esten H., et al. *NeuroImage* 256 (2022): 119210. **4**. Henschel, Leonie, et al. *NeuroImage* 219 (2020): 117012. **5**.Hung, Peter Shih-Ping, et al. *Pain* 163.8 (2022): 1468–1478

White matter alterations after physiotherapy intervention in chronic musculoskeletal pain patients using free-water corrected DTI

Irene Guadilla*[1], Álvaro Planchuelo-Gómez[1], Antonio Tristán-Vega[1], Federico Montero[2], Rodrigo de Luis García[1], Santiago Aja-Fernández[1]

[1] Laboratorio de Procesado de Imagen, Universidad de Valladolid, Spain; [2] Unidad de Estrategias de Afrontamiento Activos del dolor, Gerencia de Atención Primaria de Valladolid Este, SACYL, Spain.
*irene.guadilla@uva.es

Abstract

INTRODUCTION: Chronic musculoskeletal pain (CMP) is the leading cause of disability in western societies[1]. Surgery and pharmacological therapy are the most common treatments, but recent advances have led to non-pharmacological treatments involving pain education and physical exercise. In this work we studied the white matter (WM) before and after one such non-pharmacological treatment, in order to assess the extent of possible brain changes. Since chronic pain is related to neuroinflammation, we will consider both standard DTI and Free-Water (FW) corrected metrics for the analysis.

METHODS: Diffusion MRI data were acquired in a 3T scanner at the Universidad de Valladolid with a 32-channel head coil, using two non-diffusion weighted volumes (b=0s/mm^2) and 2 shells (b= 500, 6 directions and 1000 s/mm^2, 61 directions). CMP patients with low back pain (n=35, 28/7 females/males, 50±8years), were studied in two sessions: the first was pre-intervention (t_0) and the second post-intervention (t_1). After the first session, patients went under a physiotherapy-based intervention during six weeks, following the protocol in Galan-Martín et al.[2] Datasets were pre-processed, and FW maps calculated with the dMRI-Lab toolbox[3]. In parallel, the FW fraction was subtracted from the diffusion signal and DTI parameters were recalculated. Registration fails and the lack of some physiological data caused the final number of subjects to be 29. WM regions of interest (ROI) were identified using the Johns Hopkins University ICBM-DTI-81 WM Labels Atlas[4] and the average diffusion values were calculated per ROI for each subject. Longitudinal analysis was performed with a linear mixed-effects model in R. The fixed effects were the time between sessions (longitudinal coefficient), the evolution (whether the patient's condition improves considering the visual analogue scale), age, sex and interaction between time and phenotype to analyze the progression separately. P-values were corrected for multiple comparisons using FDR.

RESULTS & DISCUSSION: The statistical analysis revealed significant differences in some WM tracts for the DTI parameters and FW values (Fig.1A). At t_0, significant differences between the patients that improved and those that did not improve were only observed using DTI, with significant higher MD and RD values for those patients that improved, but at t_1 significant differences were detected using FW-DTI. The FA values estimated with FW-DTI were significantly lower at t_1, and the rest of the diffusion parameters presented increases and decreases in some WM tracts. The FW fraction showed significant higher values in those patients that improved after the integrated therapy programs.

In this study, the estimation of the FW fraction and the correction of the diffusion signal reveal alterations in the WM that were not detected with DTI. We demonstrate that patients with CMP exhibited significant changes of the diffusion parameters in the WM tracts after the integrated therapy program. Patients who did not improve their condition after the therapy showed a higher rate of change in the diffusion parameters, which may indicate a greater evolution of WM damage. More analyses are required to determine the physiological processes that could explain these WM alterations.

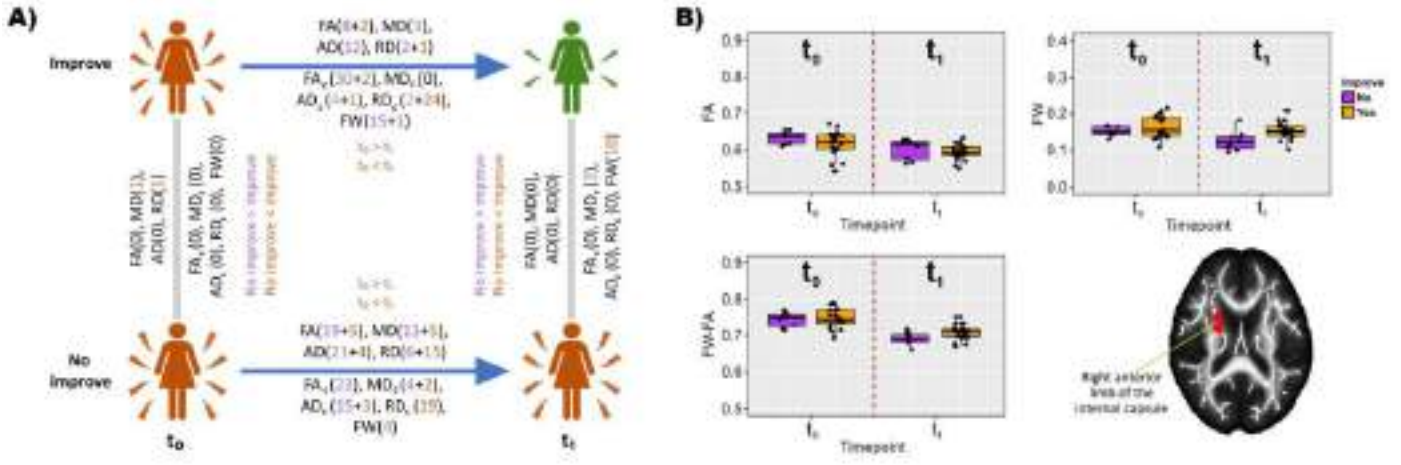

Figure 1. A) Summary of the number of WM tracts with significant differences after the correction for multiple comparisons in the diffusion parameters from both mathematical approaches (DTI: above arrows, and FW-DTI below the arrows). **B)** Boxplots of the fractional anisotropy (FA), fractional anisotropy after the FW correction (FW-FA) and FW fraction of the right anterior limb of the internal capsule.

References

1. Borchgrevink et al. The Journal of Pain (2022). **2.** Galan-Martín et al. Journal of Clinical Medicine (2020). **3.** Tristán-Vega et al. Magn Reson Med (2021). **4.** Oishi et al. Neuroimage (2008).

A Multicenter Kidney Research Study about the Participant Insights on Data Sharing and Artificial Intelligence

Veronica Aramendía-Vidaurreta[1-2], Leyre García Ruiz[1-2], Malene Aastrup[3], Michela Bozzetto[4], Paolo Brambilla[5], Rebeca Echeverria-Chasco[1-2], Esben S.S. Hansen[3], Larisa Micu[6], Jose María Mora-Gutierrez[7], Siria Pasini[4], Anish Raj[8,9], Steffen Ringgaard[3], , Anika Strittmatter[8,9], Tau Vendelboe[3], Giulia Villa[4], Iona Urdea[6], Nicolas Selby[12,] Niels Henrik Buus[10], Nuria Garcia-Fernandez[7], Matias Trillini[11], Susan T. Francis[12], Lucian-Mihai Itu[6], Christoffer Laustsen[3], Frank G. Zoellner[8,9], Anna Caroli[4], María A. Fernández-Seara[1-2]

1. Radiology Dep. Clínica Universidad de Navarra, Spain; 2.IDISNA, Spain, 3.The MR Research Centre, Aarhus University, Denmark, 4. Bioengineering Dep. IRCCS, Bergamo, Italy, 5.Radiology Unit, Bergamo, Italy, 6.Advanta Siemens, Romania, 7. Nephrology Dep.Clínica Universidad de Navarra, Spain, 8, Computer Assisted Clinical, Medicine Heidelberg University, Mannheim, Germany, 9., Mannheim Institute for Intelligent Systems in Medicine, Heidelberg University, Mannheim, Germany, 10. Renal Medicine Dep, Aarhus University Hospital, Denmark, 11. Centro di Ricerche Cliniche per le Malattie Rare "Aldo e Cele Daccò", IRCCS, Bergamo, Italy, 12.University of Nottingham, UK

INTRODUCTION: Data sharing in research promotes reproducibility, while artificial intelligence (AI) aids in processing complex clinical data. However, more research is needed on participant's attitudes toward data sharing and AI in clinical data, including MRI. This study aims to explore kidney research participant's views on data sharing and AI.

METHODS:

Survey design: included 42 questions (114 items) organized into three sections:

-*Data sharing*: Assessed concerns and attitudes towards data sharing[2].

-*AI*: Evaluated attitudes towards AI in medical research (concerns, effectiveness, and trust)[3].

-*Explanatory*: Collected demographics and data sharing/AI-related variables (trust, computer skills).

Survey distribution: 137 surveys were distributed to research participants (patients and healthy subjects) in clinical centers across Italy (N=36), UK (N=67) and Spain (N=34). Participants provided informed consent and responses were anonymous.

Data preprocessing: Rating scale responses were coded with lower values indicating negative opinions and higher values indicating positive opinions. Counts and percentages for each category were computed to evaluate overall responses. Explanatory variables, informed consent questions and overall opinions on the balance of benefits and drawbacks were excluded from the internal consistency and subject's overall opinion analyses.

Subject's overall opinion on data sharing and AI: Responses were normalized from -1 to 1, with 0 as neutral. Mean values were computed to derive a single metric representing the individual's overall opinion.

Survey internal consistency: Cronbach's alpha was calculated separately for data sharing and AI[4].

Regression analysis: A two-step regression analysis was performed to identify significant predictors of overall opinion on data sharing and AI: (1) Univariate Gaussian regression for each explanatory variable, (2) Multivariate Gaussian regression for variables with $p<0.10$, identifying significant predictors ($p<0.05$).

RESULTS & DISCUSSION: Figure 1A shows that many respondents perceived a major benefit of sharing clinical data to accelerate scientific answers. Figure 1B reveals no respondents selected "not at all" regarding trust on AI for analyzing clinical data, including MRI. Figure 1C shows that subject's overall opinion on data sharing (average score: 0.51±0.25) and AI (average score: 0.29±0.21) were positive (on a scale of -1 to 1).Cronbach's alpha was 0.93 [0.91-0.94] for data sharing and 0.90 [0.87–0.92] for AI, indicating excellent internal consistency of the survey indicating reliable measurement of participants' perceptions.

The data sharing regression model included four variables (education, family income, trust in people, and institutional trust). Institutional trust ($p<0.001$) and family income ($p=0.0579$) were significant, suggesting that higher trust and income increased the likelihood of sharing data. The AI regression model included health status, clinical category, participation experience, and AI knowledge. Clinical category ($p=0.04$) and AI knowledge ($p=0.02$) were significant, indicating that healthy volunteers and those with higher AI knowledge viewed AI more positively.

CONCLUSION: Participants in renal MRI studies generally hold positives views on data sharing and AI, consistent with existent literature. Key factors influencing these attitudes include institutional trust, participant clinical category and technical knowledge of AI.

(A) Sharing anonymized data can:

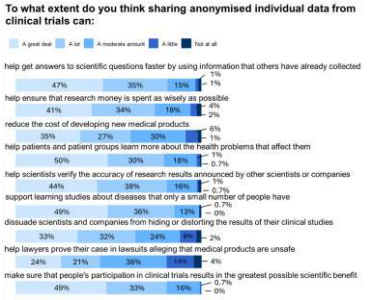

(B) Trust on AI:

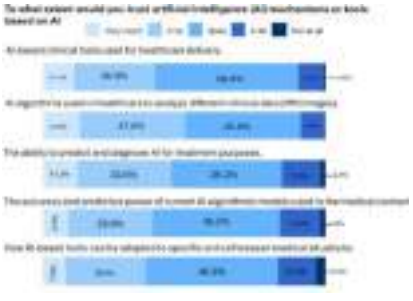

(C) Subject's overall opinion on:

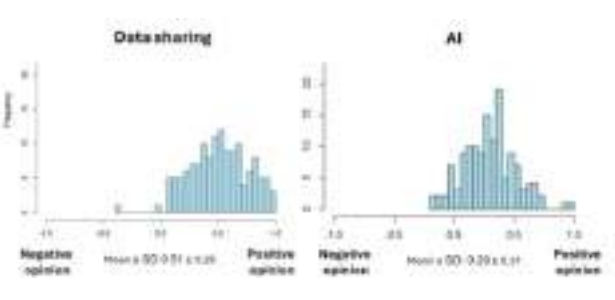

Figure 1: (A) Subject's overall opinion on data sharing and AI. (B) Impact of data sharing. Most respondents chose "a great deal" for its impact on faster science, health insights, and rare disease understanding. (C) Trust in AI. No respondents chose "not at all" trust in AI algorithms analyzing clinical data like MRIs.

REFERENCES: 1. Bhandari A, et al. Clin Imaging. 2021, 2. Mello MM, et al. N Engl J Med. 2018, 3. Ongena YP, et al. Eur Radiol. 2020,4. Cronbach LJ. Psychometrika. 1951.

ACKNOWLEDGEMENTS: Funding: This project was supported by the Government of Navarra, Italian Ministry of Health, German Federal Ministry of Education and Research (grant number 01KU2102), and Innovation Fund Denmark under the frame of ERA PerMed (ERAPERMED2020-326 - RESPECT).

A Framework for Organizing and Processing DWI Data in the FTLDNI Database

Cèlia Cruz-Escalera[1,3], Raúl Tudela[2,3], Roser Sala-Llonch[2,3], Agnès Pérez-Millan[4]*, for the Frontotemporal Lobar Degeneration Neuroimaging Initiative

[1]Universitat Rovira i Virgili, [2]CIBER de Bioingeniería, Biomateriales y Nanomedicina, Instituto de Salud Carlos III, Barcelona, Spain, [3]Institut de Neurociències, Departament de Biomedicina, Universitat de Barcelona. IDIBAPS. Barcelona, Spain, [4]eHealth Center, Faculty of Computer Science, Multimedia and Telecommunications, Universitat Oberta de Catalunya, 08016 Barcelona, Spain

INTRODUCTION: The availability of large neuroimaging datasets has become crucial for modeling patterns and trajectories in neurodegenerative disease, offering opportunities for data reusability and open science. Structural T1 MRI images are straightforward to use. However, other modalities, such as diffusion MRI (DWI), represent more challenges in terms of data pruning, harmonization, and pipeline generation. We present a methodology to enable the automatic use of the DWI data available in the Frontotemporal Lobar Degeneration Neuroimaging Initiative (FTLDNI) (https://memory.ucsf.edu/research-trials/research/allftd) database in research setting and their processing

METHODS: We have implemented a full pipeline including: (1) data exploration and selective download, (2) BIDS[1] standardization and data organization, and (3) Image preprocessing. A summary of the pipeline is shown in Figure 1. All the procedures were implemented in Python using specific tools available in the HD-BET[2] and FSL-FDT toolboxes. First, we download all the T1-weighted and DWI images available in the NIFD project through the Image and Data Archive (IDA) platform (https://ida.loni.usc.edu/login.jsp). All these images are cleaned and organized within the database. Then, they are transformed from DICOM to NIFTI format and organized to follow the BIDS specification. Specifically, we implemented an automated protocol to derive FA and MD maps from the diffusion input images using a tensor (DTI) approach, including eddy current artifacts and motion correction.

RESULTS & DISCUSSION: The entire dataset contains images from 246 patients from four different centers, where each patient has multiple images corresponding to different visits. We cleaned and filtered all these images to retain only T1-weighted and one DWI images from each visit. After the application of the automatic BIDS transformation to organize the database into a research setting, we performed an exploratory analysis to identify usable data across centers and protocols. From this analysis, the larger homogeneous set of images was selected to implement our processing pipeline. This set consisted of 534 images from 262 participants from a single center, with across 1 to 6 sessions per participant. All the selected images were acquired using a 64-direction DWI protocol.
We applied our automated processing pipeline to this subset, computing FA and MD maps (Figure 1), as common diffusion measurement. These maps were visually inspected for validation.
We are currently working on automatically obtaining all the FA and MD maps for all the datasets, including basic automatic quality control, minimizing the number of images requiring visual validation. Further analyses would include implementing the protocol in the selected subsample and examining patterns and differences across groups.
Code available at: https://github.com/celiacruzescalera/DWI-pipeline

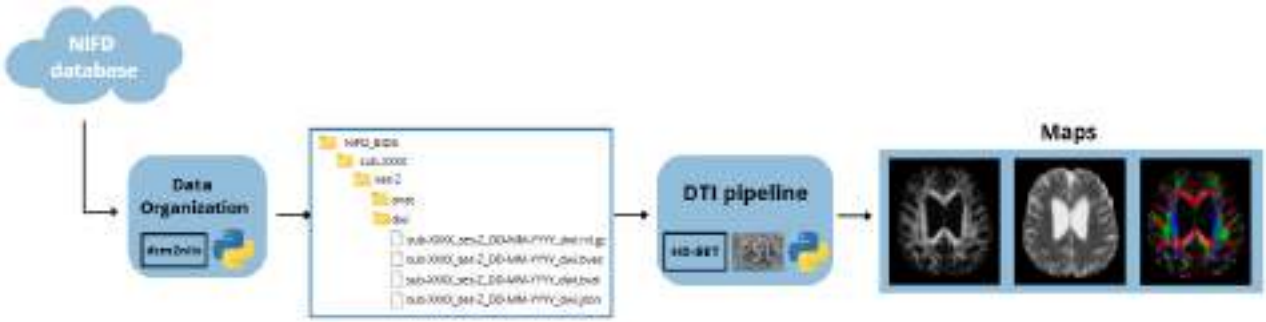

Figure 1 – Data base processing pipeline. The images downloaded from the NIFD database are transformed from DICOM to NIFTI format and organized to follow the BIDS specification. Then, an automated protocol to derive FA and MD maps from the diffusion input images using a tensor (DTI) approach, including eddy current artifacts and motion correction.

1. Gorgolewski, K., Auer, T., Calhoun, V. et al. The brain imaging data structure, a format for organizing and describing outputs of neuroimaging experiments. Sci Data 3, 160044 (2016). https://doi.org/10.1038/sdata.2016.44
2. Isensee, F., Jaeger, P. F., Kohl, S. A., Petersen, J., & Maier-Hein, K. H. (2021). nnU-Net: a self-configuring method for deep learning-based biomedical image segmentation. Nature methods, 18(2), 203-211.

Deep learning segmentation for morphological assessment of optic nerve integrity in optic neuritis

Helena Sánchez Ulloa[1,2], Paola Ajdinaj[3], Neus Mongay-Ochoa[4], Eugenio Funelli[5], Manel Alberich[2], Gemma Piella[1], Alex Rovira[2,6], Jaume Sastre-Garriga[4], Deborah Pareto[2,6]

[1]BCN Medtech, Department of Engineering, Barcelona (Spain); [2]Neuroradiology Group, Vall d'Hebron Institut Recerca, Barcelona (Spain); [3]Department of Neuroscience, imaging and clinical sciences, University G.D'Annunzio of Chieti (Italy); [4]Department of Neurology. Centre d'Esclerosi Múltiple de Catalunya (CEMCAT), Vall d'Hebron University Hospital, Barcelona (Spain); [5]University Milan-Bicocca (Italy); [6]Neuroradiology Section, Radiology Department (IDI), Vall d'Hebron University Hospital, Barcelona (Spain)

Abstract

INTRODUCTION:

Deep learning techniques, particularly convolutional neural networks, have shown promise in automating complex tasks such as anatomical structure segmentation, offering faster and more objective assessments. Among these, U-Net has emerged as a powerful tool for segmenting anatomical structures in medical images. Optic neuritis (ON) is one of the most common demyelinating manifestations of multiple sclerosis (MS), yet its segmentation primarily relies on manual methods that are time-consuming and subject to a certain degree of inter-rater variability. This highlights the need for an automated, deep learning-based approach to enhance standardization and accuracy. This study aims to develop a U-Net model to segment the optic nerve from conventional 3D T1-weighted magnetic resonance imaging (MRI) scans.

METHODS:

The cohort included healthy controls (HC, n=18) and subjects with MS with (n=16) and without ON (n=17). Ground truths were generated by manually outlining each optic nerve, for all subjects, based on the T1-weighted MRI. Before implementing the deep-learning model, a preprocessing pipeline was set up to crop automatically the optic nerve area, based on a predefined region of interest (ROI) drawn at the Montreal Neurological Institute template. Then, this ROI was brought to the native space, by inverting the normalization transformation matrix. This step was implemented with SPM software package.
For the deep-learning task, a 2D U-Net architecture with four encoding and decoding levels was implemented. The model incorporated batch normalization, ReLU activation, and a dropout rate of 0.2 to improve generalization. The network was trained using grayscale single-channel input with a binary segmentation output.
Patches of 32 x 32 voxels were generated for segmentation across different planes—sagittal (n=7954), axial (n=6066), and coronal (n= 9345)—allowing for a more comprehensive assessment of the optic nerve. The dataset was divided into training (70%), testing (15%), and validation (15%) sets.
To assess the model performance, the generated masks were compared to the ground truths by using the Dice coefficient as well as other metrics such as precision, recall, and accuracy.

RESULTS & DISCUSSION:

The single-plane segmentation approach yielded promising results, enhancing the detection of optic nerve structures and demonstrating strong generalization on the test set performance (see Table 1). Preliminary results indicate that the deep-learning model can successfully differentiate the optic nerve from surrounding tissues, despite the challenges posed by its size and similar gray tones to brain structures. Future work will focus on extending segmentation to multiple planes to further improve accuracy.

	Accuracy	Dice	Recall	Precision
Axial	0.98	0.51	0.20	0.28
Sagittal	0.99	0.44	0.37	0.41
Coronal	0.99	0.43	0.37	0.45

Table 1 – Segmentation performance across axial, coronal and sagittal plane.

Accelerated EPG-based myocardial T1 mapping with PENGUIN

Catarina N Carvalho[1,2 *], Andreia S Gaspar[2], Rita G Nunes[2], Teresa M Correia[1,3]

[1]Center of Marine Sciences (CCMAR), Faro, Portugal; [2]Institute for Systems and Robotics - Lisboa and Department of Bioengineering, Instituto Superior Técnico, Universidade de Lisboa, Lisbon, Portugal; [3]School of Biomedical Engineering and Imaging Sciences, King's College London, London, United Kingdom

*catarina.neves.carvalho@tecnico.ulisboa.pt

Abstract

INTRODUCTION: Model-based Deep Learning (DL) allows accelerating MRI reconstruction and quantitative mapping. Here, we propose a DL architecture that performs myocardial T1 mapping directly from accelerated k-space, which models the signal with the Extended Phase Graph (EPG) formulation, to allow more accurate quantification. The DL architecture is a modification of PhasE Graph sigNal and Gradients QUantitative Inference machiNe (PENGUIN)[1], with the following novelties: (a) quantitative mapping is performed directly from undersampled k-space; (b) signal intensity curves are simulated not only for a range of T1 values, but also for a range of regular heart rate (HR) values.

METHODS: PENGUIN (Figure 1a) combines a Recurrent Inference Machine[2] with a dictionary of EPG simulated signal evolution curves that provides the network with a pre-calculated signal model. PENGUIN performs J=2 inference steps to obtain J estimates of the T1 maps, considering the L1-norm loss function evaluated in the myocardium. Networks were trained for acceleration factors acc={4,8}, ADAM optimizer, learning rate=1e-4, for 300 epochs, C=64 and C=256 channels for acceleration factors 4 and 8, respectively. Data were obtained from MICCAI's 2023 CMR reconstruction challenge[3]. T1 mapping was conducted following a 4-(1)-3-(1)-2 MOLLI sequence, short axis (SA) view only, FOV=360×307 mm^2, spatial resolution=1.4×1.4 mm^2, slice thickness=5.0 mm, TR=2.67 ms, TE=1.13 ms, partial Fourier=7/8, and GRAPPA factor of 2, on a 3T MAGNETOM Vida Siemens scanner. K-space data were undersampled retrospectively, following a radial k-t sampling trajectory with golden angle increments. EPG-based simulations were implemented for HR=[28,102] bpm, T1=0:1:2000 ms, T2=50 ms. Ground-truth T1 maps were obtained by performing a pattern recognition approach over the reconstructed, fully sampled signal intensity images, through dot product matching. Zero-filled (ZF) and Compressed Sensing (CS) reconstructions were performed to compare with PENGUIN.

RESULTS & DISCUSSION: PENGUIN's T1 maps (Figure 1b-c) achieved mean relative errors of 10.1±11.0% and 15.9±15.4%, and mean MSSIM scores of 0.999±0.001 and 0.998±0.001, for acc=4 and 8, respectively. PENGUIN is less resource-consuming than CS reconstruction, since the computational burden is moved to the preprocessing stage.

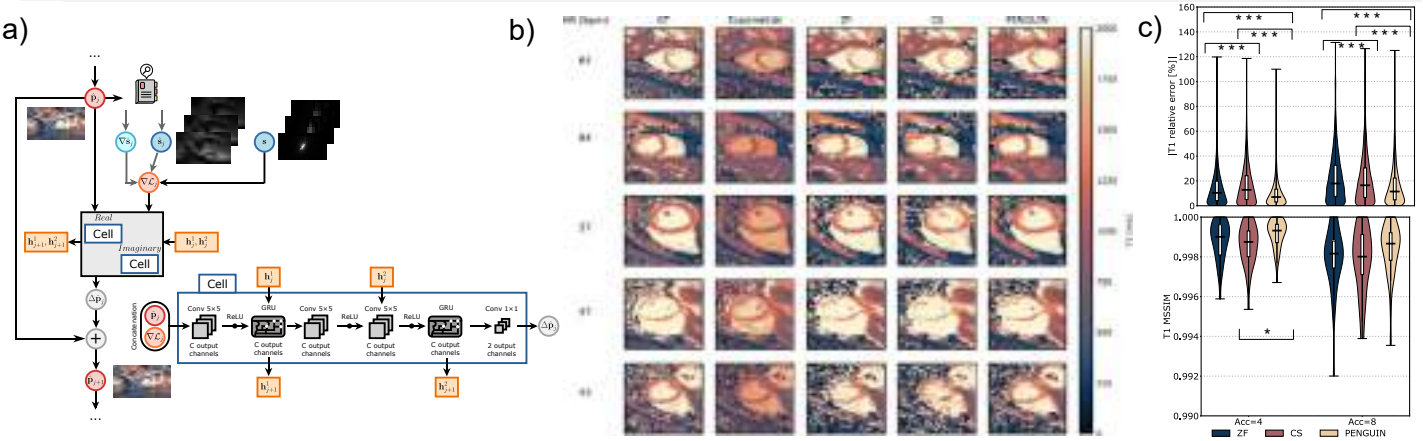

Figure 1 – (a) PENGUIN architecture for inference step j. The estimate p_j is given to the dictionary to obtain the signal-intensity and corresponding derivative of each T1 value in p_j. The gradient of the negative log-likelihood ΔL_j is calculated, concatenated to p_j and given as input to the network, which outputs the incremental update to the estimated maps. h_j: memory vectors. (b) T1 maps of 5 distinct test subjects (rows), acc=4; ground truth (GT), Exponential Fitting, zero-filled (ZF), compressed sensing (CS), and PENGUIN. (c) T1 relative errors and MSSIM scores obtained for all testing images; * (p-value<0.05) and *** (p-value<0.001).

References

1. Carvalho C, Gaspar A, Nunes R, Correia T. Diving into Extended Phase Graph-based Deep Learning for accurate T2 mapping with PENGUIN. In proceedings of 2023 ISMRM & ISMRT Annual Meeting & Exhibition; **2.** Putzky P, Welling M. Recurrent Inference Machines for Solving Inverse Problems. June 2017. **3.** Wang C, Lyu J, Wang S, et al. CMRxRecon: A publicly available k-space dataset and benchmark to advance deep learning for cardiac MRI. Sci Data. 2024;11(1):687.

Acknowledgements

This work was supported by: NVIDIA GPU hardware grant; "la Caixa" Foundation and FCT, I.P [LCF/PR/HR22/00533]; FCT (SFRH/BD/120006/2016, PTDC/EMD/EMD/29686/2017; UIDP/50009/2020), Programa Operacional Regional de Lisboa 2020 (LISBOA-01-0145-FEDER-029686), LARSyS funding (DOI: 10.54499/LA/P/0083/2020,10.54499/UIDP/50009/2020,10.54499/UIDB/50009/2020. This research was supported by FCT through projects UIDB/04326/2020 (DOI:10.54499/UIDB/04326/2020), UIDP/04326/2020 (DOI:10.54499/UIDP/04326/2020) and LA/P/0101/2020 (DOI:10.54499/LA/P/0101/2020).

Microstructural MRI trajectories in healthy aging: sexual dimorphism, functional and behavioral correlates

Egoa Ugarte Pérez[1*], Elena Espinós-Soler[1], Aroa S. Maroto[1], Antonio Cerdán-Cerdá[1], Santiago Canals Gamoneda[1], Silvia de Santis[1]

[1]Instituto de Neurociencias de Alicante, UMH-CSIC; *eugarte@umh.es

INTRODUCTION: Characterizing sex differences is crucial to identify resilient/vulnerable targets, and understand the differential susceptibilities to neurodegeneration. MRI enables non-invasive, detailed analysis of brain microstructural and functional trajectories. Previous results indicated that women experience a delayed onset of microstructural decline[1]; to understand the biological underpinning of this finding, here we measure longitudinally microstructural MRI biomarkers in a rat model of aging across the full lifespan. Additionally, to determine the impact of the structural sexual dimorphism on cognition, we assessed resting state functional connectivity (FC) and spatial memory performance using the Morris Water Maze (MWM).

METHODS: 30 Wistar rats (15 f) were scanned longitudinally over 2 years to collect diffusion-weighted (b-value 1000 and 2500 s/mm2) and resting state functional data (TR 2s). First, we extracted Mean Diffusivity (MD), Fractional Anisotropy (FA), Neurite Dispersion (NDisp) and Density (NDen) maps. Their trend with age was modeled ROI-wise using either linear, segmented with sex effect, or segmented separate for each sex regression models. Then, the best model was selected via a Bayesian information criterion. Segmented models capture: i) the breakpoint, the age when the curve inverts its trend towards reduced microstructural integrity, and ii) the slope after the breakpoint. Spatial patterns were tested by correlating slopes with the mean ROI coordinates. To assess FC, independent component analysis was used to extract resting-state networks, and age and sex effects were tested within each network. At the final time point, animals underwent 5 days of MWM test. Long-term memory was assessed by measuring the latency in finding the previous platform position, while latency in finding the new platform assessed short-term memory.

RESULTS & DISCUSSION: Females consistently exhibited a delayed mean breakpoint across all WM in FA, NDisp and NDen (Figure 1A), and across all GM regions in NDen (data not shown). In addition, males showed a mean faster rate of change once the breakpoint was reached, particularly in MD (Figure 1B). MD in males demonstrated a significant correlation between the slope and the mean Y-coordinate, indicating a ventro-dorsal gradient in the rate of change, while females showed a correlation along the Z-axis, demonstrating a posterior-anterior gradient (Figure 1C). Interestingly, posterior regions best fit to a linear model, while anterior and superior regions best fit to a sex-specific segmented regression model (Figure 1D). Functional analyses revealed an overall decline in FC with age until approximately one year, followed by an increase thereafter. This hyperconnectivity is more pronounced in anterior and superior regions, and in females (Figure 1E). Finally, behavioral analyses in the MWM revealed a significant sexual dimorphism in long-term but not short-term memory, with females displaying a significantly faster learning compared to males (Figure 1F). Taken together, our findings demonstrate that: i) the sexual dimorphism in microstructural aging trajectories observed in humans is conserved in rats; ii) it is preferentially localized in anterior and superior regions; iii) it is paralleled by sexually dysmorphic hyperconnectivity in the same spatial locations; and iv) translated in better performance in tasks heavily relying on prefrontal cortex.

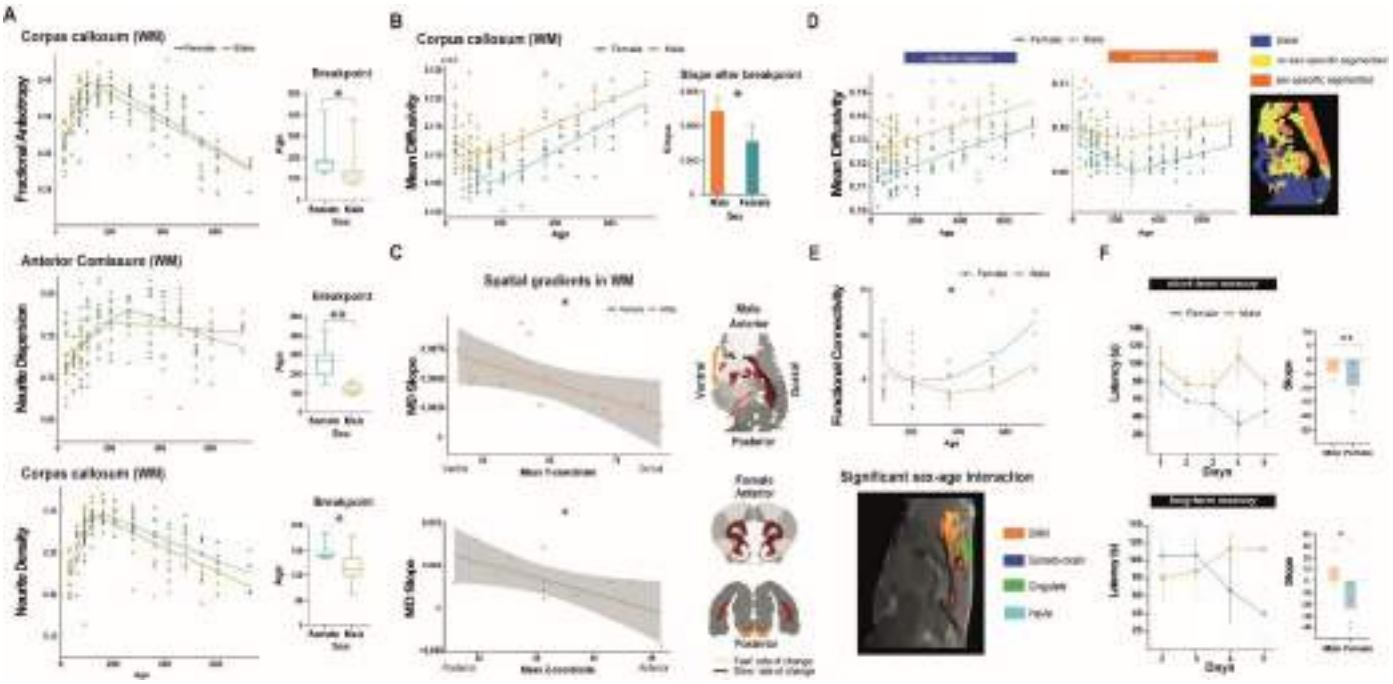

Figure 1. Sex-specific patterns in DWI, resting state FC and behavior. (A) Left: Example of aging curves in representative WM regions (FA, NDisp and NDen). Right: t-test between sexes show delayed breakpoint in females (blue) vs males (orange) for FA ($p<0.05$), NDisp ($p<0.01$) and NDen ($p<0.05$). (B) Left: MD trends in corpus callosum. Right: mean WM slopes show faster change in males ($p<0.05$). (C) For MD slope in WM, males show a significant correlation with the ventro-dorsal coordinate (orange) ($p<0.05$), while female with the antero-posterior coordinate (blue) ($p<0.05$). Yellow-brown gradient represents faster-slower slopes after breakpoint. (D) Posterior regions (left) for MD best follow a linear model, while anterior regions (right) follow a segmented model. This pattern is also depicted in the brain map on the right. (E) A representative trajectory of FC versus age for males (orange) and females (blue), showing a significant sex-age interaction, with females exhibiting significantly greater hyperconnectivity after one year (top). Age-related hyperconnectivity is mainly observed in anterior and superior regions (bottom), such as DMN, somato-motor, cingulate and insula networks. (F) Short-term memory performance shows no significant difference in the slope of the latency over days between sexes (top). In contrast, long-term memory performance reveals a significantly higher learning rate in females compared to males ($p < 0.05$) (bottom). *DMN= default mode network.*

REFERENCES: [1] Toschi N, Gisbert RA, Passamonti L, Canals S, De Santis S. Neurobiol Aging. 2020;86:191-200.

Efficient Model Fitting of Diffusion MRI via Simulation-Based Inference

Maximilian F. Eggl[1,2], Silvia De Santis[1]*

[1]Institute of Neuroscience, CSIC-UMH, Alicante; [2]University of Bonn Medical Center, Bonn *dsilvia@umh.es

Abstract

INTRODUCTION: Diffusion-weighted MRI (dw-MRI) is a key technique that enables non-invasive exploration of tissue microstructure [1]. When combined with advanced mathematical and biophysical models (e.g. AxCaliber [2]), it provides valuable diagnostic insight. However, these models require long, complex acquisitions due to noisy data and limitations of standard fitting using e.g. non-linear least squares (NLLS). We propose using simulation-based inference (SBI), specifically neural posterior estimation, to estimate model parameters from substantially reduced experimental acquisitions. In contrast to prior approaches relying on model-based fitting or post-hoc uncertainty quantification [3], this work employs amortized posterior estimation to directly infer model parameters from reduced acquisitions.

METHODS: We evaluate the efficacy of SBI on various diffusion models including DTI, DKI and AxCaliber. We leverage SBI to obtain reliable diffusion maps from far fewer samples than are required for robust NLLS fitting, more in line with the theoretical minimum - equal to the number of parameters under ideal identifiability and noise-free conditions. Neural density estimators were trained on simulated data by minimizing the negative log-likelihood of known parameters under the network-predicted posterior [4]. Once trained, the network can infer posteriors from experimental data, providing accurate parameter estimates where other methods are impractical.

RESULTS: Using the AxCaliber model, we evaluated SBI and NLLS on both in-silico data and in-vivo data using a reduced acquisition set (19 acquisitions - 1 B_0 and 6 for B > 0 repeated for three diffusion times - a 90% reduction from the full 273). In silico, SBI consistently outperformed NLLS across full and reduced acquisition schemes and noise levels (SNR = 2–30). In vivo results (five subjects from [5]) showed SBI maintained an accuracy > 0.7 (measured using the structural similarity index, SSIM) compared to full-data results for key model parameters, using only 10% of the full data. In contrast, NLLS achieved an average SSIM of just 0.4. Figure 1c demonstrates that SBI-derived restricted diffusion fraction maps retain anatomical fidelity and contrast at reduced acquisitions. Similar results were also achieved for DTI and DKI. These results establish SBI as an efficient, generalizable tool for accurate parameter estimation from sparse acquisitions, reducing scan time demands and broadening clinical accessibility.

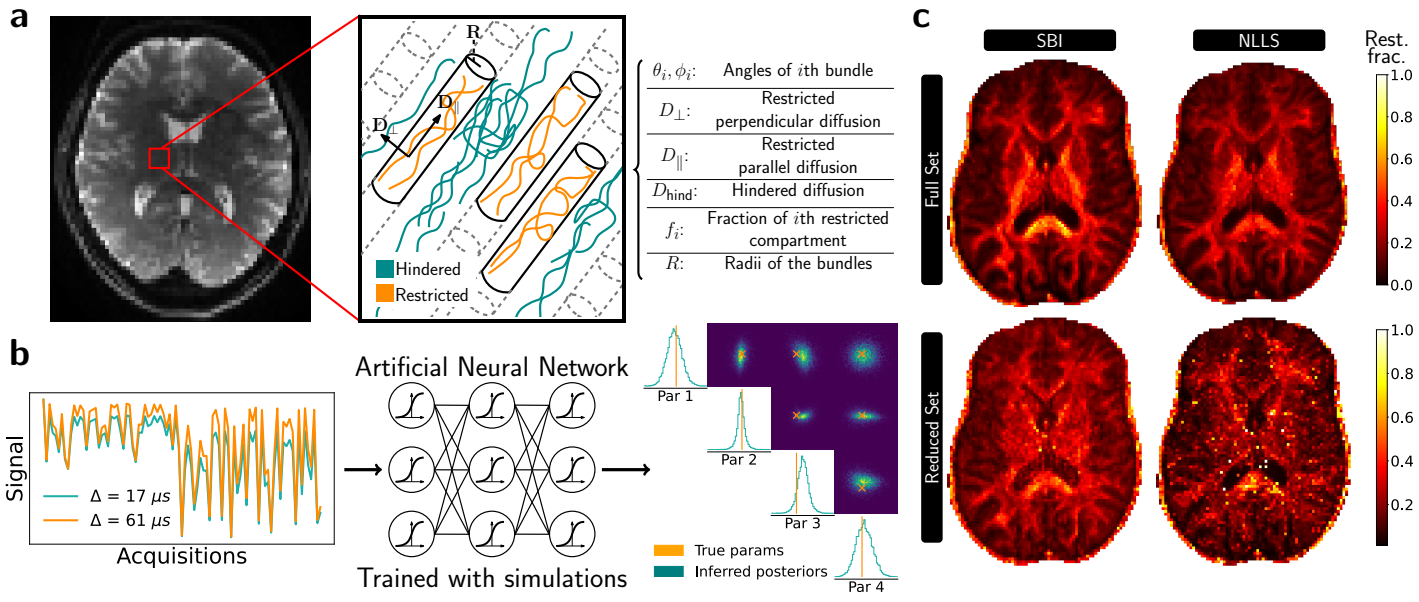

Figure 1 – a) Example schematic illustration of the AxCaliber model (hindered and restricted diffusion in orange and teal, respectively). Estimated parameters, such as restricted bundle angles or compartment fractions, serve as quantitative biomarkers of tissue integrity. **b)** Special acquisition schemes produce signals encoding microstructural fingerprints, which are input to neural density estimators pre-trained on simulations. The network infers posterior distributions over the model parameters for each experimental measurement. **c)** Example restricted fraction maps from a single axial slice, comparing SBI and NLLS fits using the AxCaliber model with full (273 acquisitions) and reduced (19 acquisitions) datasets. SBI preserves anatomical detail and parameter fidelity at 90% acquisition reduction, while NLLS exhibits a significant reduction in structural information.

References

1. Le Bihan et al., 2001 **2.** Assaf et al., 2008, **3.** Jallais & Palombo, 2024, **4.** Tejero-Cantero et al., 2025, **5.** Cerdá et al, 2024

Tumor detection via MRI using metal-free organic radical dendrimers as contrast agents.

Vega Lloveras,[1,2,*] Yufei Wu,[1] Ruben García Costas,[1] Ehsan Shirdel,[1] Xuejiao Wang,[1] Chuanting Zhou,[1] José Vidal-Gancedo.[1,2,*]

[1]Institut de Ciència de Materials de Barcelona, ICMAB-CSIC, Campus UAB, 08193 Bellaterra, Spain.
[2] CIBER de Bioingeniería, Biomateriales y Nanomedicina, Instituto de Salud Carlos III, 08913 Bellaterra, Spain.
*vega@icmab.es; j.vidal@icmab.es

Currently, gadolinium-based contrast agents (GBCAs) are the most commonly used MRI CAs in clinical settings. While historically considered safe, a well-established link emerged over the past decade between GBCA administration and the development of nephrogenic systemic fibrosis (NSF) in patients with renal impairment. Additionally, recent studies have reported the accumulation of residual Gd(III) ions in various organs—including the brain, bones, skin, liver, and kidneys—even in individuals with normal renal function and an intact blood-brain barrier (BBB). Given these concerns, the development of alternative imaging probes that circumvent GBCA-related toxicity is of paramount importance.

Persistent organic radicals present a promising alternative, as they exhibit paramagnetic properties similar to Gd-based CAs and function as T_1 contrast agents while avoiding the risks associated with metal accumulation. However, isolated organic radicals show low ability to generate contrast and can undergo rapid bioreduction.
Our strategy involves anchoring multiple organic radicals onto the surface of a dendrimeric macromolecule (radical dendrimers)[1-8], which enhances contrast capacity while also protecting the radicals from bioreduction, thereby improving their performance.

We have successfully synthesized various generations of radical dendrimers that are fully water-soluble and functionalized with nitroxide organic radicals at the periphery. Both *in vitro* and *in vivo* studies have demonstrated that these dendrimers provide contrast enhancement comparable to or even superior to GBCAs. Under *in vivo* conditions, radical dendrimers have effectively enhanced contrast in murine GL261 glioblastoma (GB) tumors, achieving similar imaging results to commercial Gd-based agents despite being administered at a fourfold lower dose[2] (Figure 1). They selectively accumulate in brain tumor tissues, enabling imaging over extended periods (≥2.5 h) compared to Gd chelates. Furthermore, the radicals on the dendrimers exhibit high stability in biological environments. These findings support the potential of radical dendrimers as a viable alternative to metal-based MRI contrast agents, particularly for glioblastoma imaging.

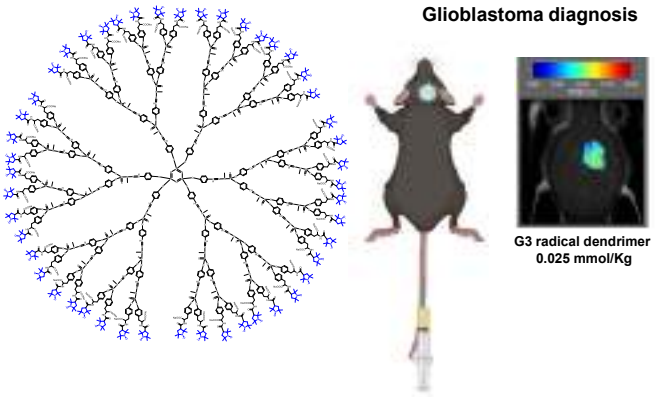

Figure 1. Left) Structure of the third generation of a radical dendrimer based on polyphosphorhydrazone dendrimer and proxyl organic radicals (in blue). Right) Color-code scale for relative contrast enhancement (RCE) of GL261 glioblastoma tumour-bearing mice with intravenous administration of the radical dendrimer at 0.025 mmol/Kg.

References:

1. L. Pinto, V. Lloveras, S. Zhang, F. Liko, J. Veciana, J.L. Muñoz-Gómez, J. Vidal-Gancedo. ACS *Appl. Bio Mater.* **2020**, *3*, 369.
2. S. Zhang, V. Lloveras, S. Lope, P. Calero, S. Wu, A. P. Candiota, J. Vidal-Gancedo. *Biomacromolecules* **2022**, *23*, 2767−2777.
3. S. Zhang, V. Lloveras, Y. Wu, J. Tolosa, J. C. García-Martínez, J. Vidal-Gancedo. *Pharmaceutics* **2023**, *15*, 1776.
4. Ch. Tian, S. Zhang, V. Lloveras, J. Vidal-Gancedo. *Adv. Ind. Eng. Polym. Res.* **2024**, *7*, 255-261.
5. Y. Wu, V. Lloveras, A. Morgado, E. Perez-Inestrosa, E. Babaliari, S. Psilodimitrakopoulos, Y. Vida, J. Vidal-Gancedo. *ACS Appl. Mater. Interfaces* **2024**,*16* (47), 65295-65306.
6. Y. Wu, V. Lloveras, S. Lope-Piedrafita, M. Mulero-Acevedo, A. P. Candiota, J. Vidal-Gancedo. *Acta Biomaterialia* **2025**,*192*, 461-472.
7. Y. Wu, V. Lloveras, S. Zhang, J. Tolosa, J. C García-Martínez, J. Vidal-Gancedo. *Dyes Pigm.* **2025**, *232*, 11248.
8. S. Zhang, V. Lloveras, Y. Wu, J. Vidal-Gancedo. *Eur. Polym. J.* **2025**, *235*, 113691.

Hyperpolarized NMR Reveals Distinct Liver Metabolic Alterations in Female Mouse Models of Obesity

Vicent Ribas[1, 2], Alba Herrero-Gómez[1], Helena Marí de Nova[2], David Gómez-Cabeza[1], Joan-Marc Servitja[2], Irene Marco-Rius[1]

[1]Institute for Bioengineering of Catalonia (IBEC), Barcelona; [2]Institut d'Investigacions Biomèdiques August Pi I Sunyer (IDIBAPS), Barcelona.
Vribas@ibecbarcelona.eu

INTRODUCTION:
Hyperpolarized nuclear magnetic resonance (HP-NMR) enables real-time, non-invasive metabolic assessment in vivo [**1, 2**], making it a valuable tool for investigating obesity-induced metabolic alterations. Despite the well-established impact of obesity on metabolism, its effects in female subjects remain underexplored **[3]**. Given the liver's central role in metabolic regulation, different types of obesity may drive distinct hepatic adaptations, particularly in key metabolic hubs such as pyruvate, which integrates glycolysis, mitochondrial respiration and amino acid metabolism [**4]**.
In this study, we employed HP-NMR to investigate how obesity alters hepatic pyruvate metabolism in female mice.

METHODS:
Obesity was induced in female C57Bl/6J mice through two different approaches: (1) a high-fat diet (HFD, 60% fat) for 20 weeks, and (2) genetically induced obesity in leptin-deficient (Ob/Ob) mice, maintained on a regular diet until 12–14 weeks of age. These groups were compared to lean control mice fed a low-fat diet for 20 weeks. All animals underwent metabolic characterization, including body weight assessment, glucose tolerance testing, and insulin sensitivity evaluation. At the study endpoint, HP-NMR was utilized to analyze hepatic 1-^{13}C-pyruvate metabolism **(figure 1**), when kinetic rate constants (Kp) for lactate, alanine, and bicarbonate production were determined using a mathematical fitting model.

RESULTS & DISCUSSION:
HP-NMR analysis revealed distinct metabolic alterations between obesity models. The 1-^{13}C-lactate production rate from hyperpolarized 1-^{13}C-pyruvate differed significantly between the two obesity groups. Compared to lean controls, 1-^{13}C-alanine kinetic rate was decreased in the Ob/Ob model but increased in the HFD-induced obesity model. Notably, bicarbonate production was detected exclusively in the Ob/Ob mice, suggesting enhanced mitochondrial metabolism, likely contributing to active triglyceride synthesis. These findings highlight HP-NMR as a powerful tool for elucidating metabolic adaptations in vivo, providing critical insights into obesity-associated hepatic metabolic reprogramming.

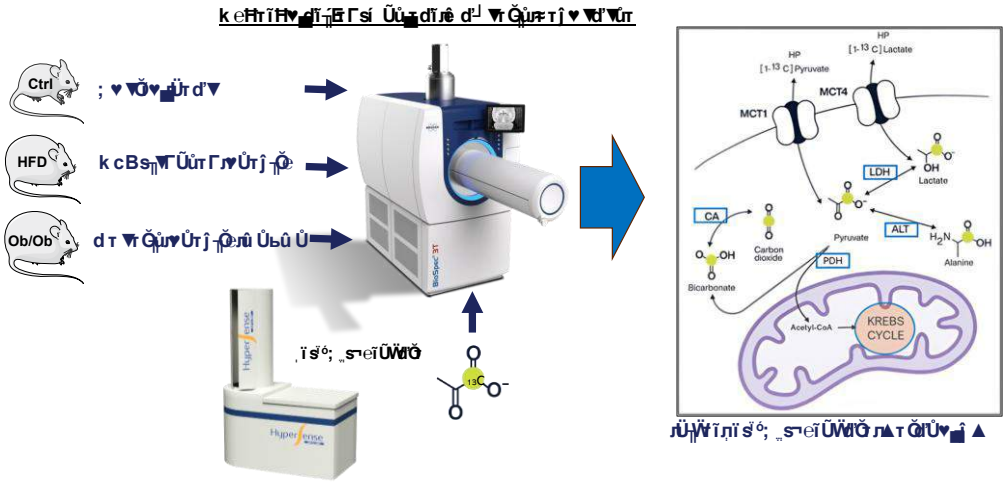

Figure 1 – Experimental outline and obesity mouse models for analysis of 1-^{13}C-pyruvate metabolism in the liver. The relative flow of liver pyruvate converted into lactate, alanine or bicarbonate was assessed by HP-NMR spectrometry.

Abstract References

[1]. Marco-Rius, I., & Comment, A. (2018). In Vivo Hyperpolarized 13C MRS and MRI applications. *EMagRes*, 7(4), 167–178. 1592
[2]. Marco-Rius, I., von Morze, C., Sriram, R; et al (2017). Monitoring acute metabolic changes in the liver and kidneys induced by fructose and glucose using hyperpolarized [2-13 C] dihydroxyacetone. *Magnetic Resonance in Medicine*, 77(1), 65–73;]. **[3].** Maric, I., Krieger, J.-P., van der Velden, P., et al. (2022). Sex and Species Differences in the Development of Diet-Induced Obesity and Metabolic Disturbances in Rodents. *Frontiers in Nutrition*, *9* (February), 1–14. [4]. Piraquive Agudelo, J., Kim, Y., Agarwal, S., Sriram, R., Bok, R.et al. (2023). Hyperpolarized [1-13 C] pyruvate MRSI to detect metabolic changes in liver in a methionine and choline-deficient diet rat model of fatty liver disease. *Magnetic Resonance in Medicine*.

Study of the relationship between tumor metabolism modulators, IDO1, IDH and ChK-α, and the expression of the immune checkpoint, PDL1, in glioblastoma models

Paula Carretero-Navarro[1], María José Guillén Gómez[1], Pilar López-Larrubia[1], Jesús Pacheco-Torres[1]*

[1]Instituto de Investigaciones Biomédicas Sols-Morreale CSIC-UAM, Madrid 28029, Spain; *jpacheco@iib.uam.es

Abstract

INTRODUCTION: Immune checkpoint blockade-based immunotherapies (IMT) have demonstrated efficacy in some tumors such as melanoma, but have failed in others like glioblastoma, and we don't know the reason. A possible cause is aberrant tumor metabolism that allows tumors to create an immunosuppressive microenvironment. Previous studies showed a relationship between immune checkpoint PD-L1 and key pieces of tumor metabolism. This work aims to investigate the existence of a relationship between aberrant tumor metabolism and acquired tumor immunoresistance.

METHODS: We modulated the immune-checkpoint PD-L1 and three key metabolic enzymes, ChK-α, IDO1 and IDH1, to assess their effect on the lipid profile of various GBM models. We used the murine glioma cell line GL261 wild type (GL261wt) and IDH mutated (GL261mIDH) along with human glioblastoma cell lines (SF10602ML). Cells were seeded and treated for 48h with metabolic inhibitors, or transfected with siRNAs against PD-L1 and ChK-α. Metabolic profiles were obtained through dual-phase metabolite extraction and subsequent ^{1}H high-resolution NMR. Spectra were acquired on a Bruker Avance Neo 11.7T NMR spectrometer. Integrals of the metabolites were determined and normalized to the TSP reference and the number of cells, from at least three experimental samples.

RESULTS & DISCUSSION: Decreasing PD-L1 expression depicted increased levels of lipids involved in tumor progression, such as cholesterol or phosphatidylcholine in SF10602ML and GL261mIDH cells. Downregulating Chk- α increased the levels of total lipids in GL261-WT cells. Furthermore, the pharmacological inhibition of IDO1 with 1MT showed a significant increase of cholesterol, phosphatidylcholine and total lipids in GL261-WT cell line. On the other hand, the inactivation of mIDH1 with AGI-5198 reduced the total level of lipids in murine cell lines carrying IDH1 mutation.

Our results showed the existence of an interrelationship between PD-L1 expression and lipid metabolism in glioblastoma cells, highlighting the influence of the genetic profile on this interrelationship. This study demonstrates that PD-L1 has pro-oncogenic functions that go beyond its traditional role as an immunomodulator, influencing tumor metabolism. Metabolism also impact immunoresistence, as it has been demonstrated that lipids can reprogram T cells infiltrating the tumor mass towards immunosuppressive and anti-inflammatory phenotypes. Therefore, the increase in lipid levels upon PD-L1 downregulation could be utilized by tumor cells to regain resistance against the natural immune response.

These results are highly relevant as they unveil a relationship between tumor metabolism and tumor acquired immuneresistance. The study of this relationship and the mechanisms that control it will allow us to understand why certain tumors do not respond to IMT, as well as rationally design new combinations of therapies seeking a synergistic effect.

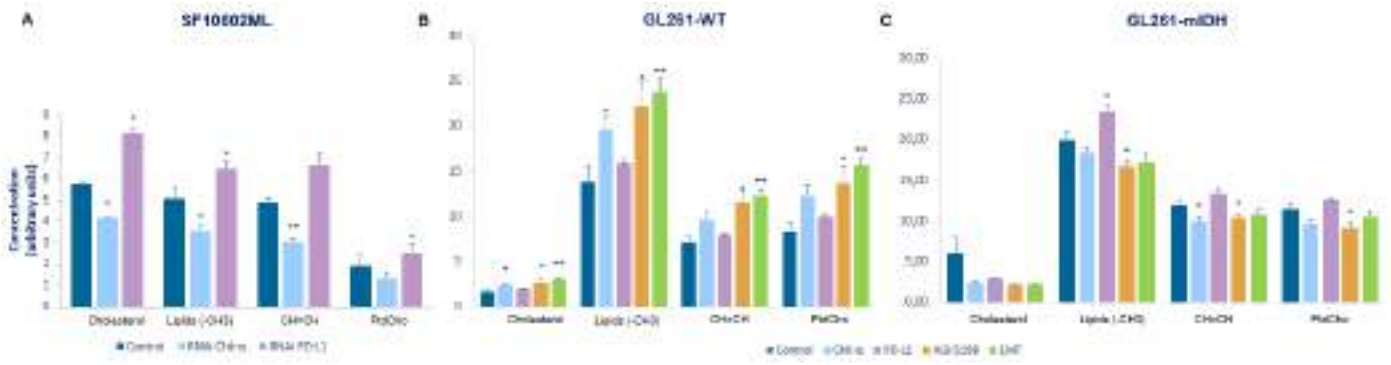

Figure 1 – Representation of lipid levels in SF10602ML cells (**A**), GL261-WT (**B)** and GL261-mIDH (**C**) cells. Control cells (dark blue), Chk-α siRNA-interfered cells (light blue), PD-L1 siRNA-interfered cells (lilac), AGI-5198-treated cells (orange) and 1MT-treated cells (green). It has been generated from the quantitative analysis of high-resolution MRS spectral data of lipid phases. The mean value ± standard error is represented, with n≥3. *p ≤ 0.05, **p ≤ 0.01, compared to control cells.

References

1. Pacheco-Torres, J., Penet, MF., Mironchik, Y. et al. The PD-L1 metabolic interactome intersects with choline metabolism and inflammation. Cancer Metab 2021; 9, 10. **2.** Yang T, Kong Z, Ma W. PD-1/PD-L1 immune checkpoint inhibitors in glioblastoma: clinical studies, challenges and potential. Hum Vaccin Immunother ;17(2):546-553.

Quantification of healthy aging of BM vasculature by DCE-MRI

Ana Gomes[1*], Dominique Bonnet[2], Bernard Siow[1]

[1]In Vivo Imaging, The Francis Crick, London, UK, [2]Haematopoietic Stem Cell Laboratory, The Francis Crick Institute, London, UK
*ana.gomes@crick.ac.uk

INTRODUCTION: Alterations in bone marrow (BM) vascular function can significantly impact the microenvironment in which hematopoietic cells reside, particularly hematopoietic stem/progenitor cells (HSPC). We have previously shown that DCE-MRI can be used to quantify bone marrow (BM) vascular changes induced by Acute Myeloid Leukemia [1]. In this study we focus on healthy NSG mice and expand on the findings of the previous study to characterize normal aging of the NSG BM vasculature.

METHODS: NSG mice were divided in groups according to age (2-3 months, 5-8 months, and 14-16 months). MRI was performed on a 9.4 T Bruker with a B-GA12SH gradient coil system and a 40 mm ID quadrature birdcage coil. DCE scans were performed using a FLASH (TR 17.639 ms; TE 1.859 ms; FA 10°; FOV 30x30x0.5 mm3 (128x128), Dotarem (0.4 mL/Kg, Guerbet, France) was injected 4 min after the start of the scan. Anesthesia was induced and maintained using isoflurane (1-4%) in room air supplemented with oxygen (80%/20%). Temperature and respiration rate were monitored using an SA Instruments system (Bayshore, NY, USA). MatLab 2019b was used for all DCE-MRI non model based analyses.

RESULTS & DISCUSSION:
Healthy aging alters BM vascular function (Fig1) Key changes in vascular function are already present at 6-8 months of age, and no significant changes were detected between 6-8 months and 14-16 months. Our study shows that healthy aged BM vasculature is characterized by slower blood inflow and increased leakiness. Lower blood flow can lead to hypoxia and inadequate nutrient delivery, potentially impairing HSPC function and skewing differentiation, while increased leakiness can disrupt the tightly controlled exchange between the vasculature and BM tissue, allowing inappropriate exposure to systemic signals or immune cells [2,3].
The importance of this dysfunction extends beyond basic hematopoiesis. Understanding the specific nature of BM vascular dysfunction—namely, low blood flow and leakiness—can offer insights into disease mechanisms and reveal new therapeutic targets. Strategies that normalize or restore vascular function in the BM may improve outcomes in conditions like myelodysplastic syndromes, leukemia, or even age-related hematopoietic decline [4]. Moreover, since the BM vasculature is uniquely specialized compared to other vascular beds, these findings highlight the need for tissue-specific approaches when studying or targeting vascular pathologies [5].

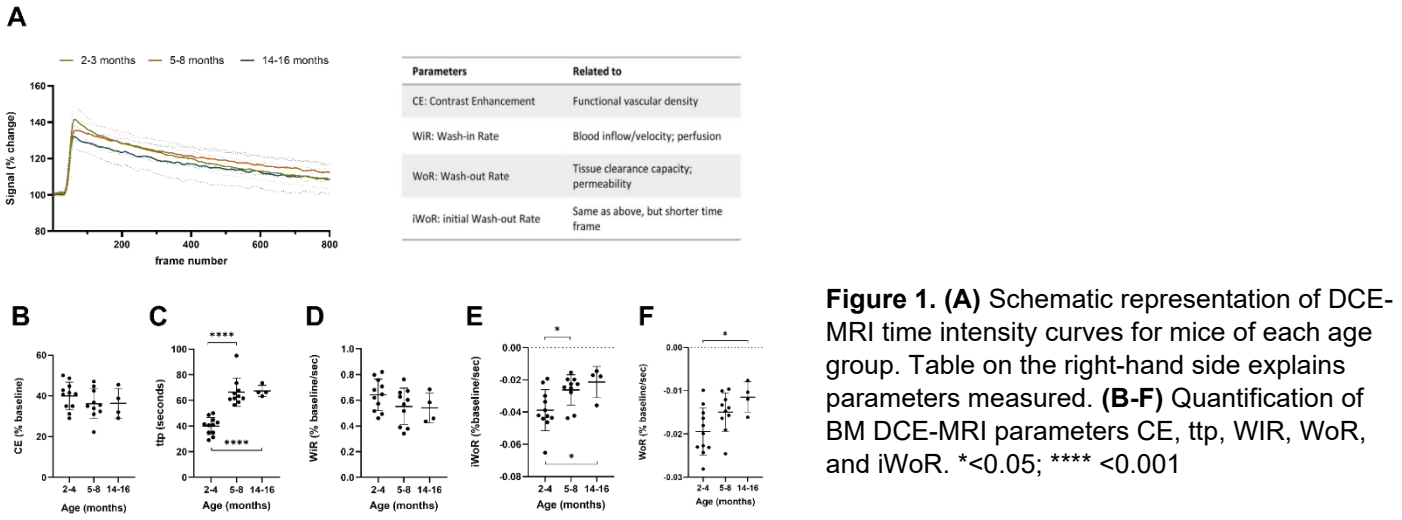

Figure 1. (A) Schematic representation of DCE-MRI time intensity curves for mice of each age group. Table on the right-hand side explains parameters measured. **(B-F)** Quantification of BM DCE-MRI parameters CE, ttp, WIR, WoR, and iWoR. *<0.05; **** <0.001

REFERENCES

[1] Gomes A. et al. Haematologica, 2021; 106(8); [2] Itkin, T. et al. Nature, 532(7599), 2016, 323–328; [3] Kusumbe, A. P. et al. Nature, 2014, 507(7492), 323–328; [4] Poulos, M. G. et al. Nature, 2016, 540(7633), 169–175. [5] Ramasamy, S. K. et al. Nature Communications, 2016, 7, 13601.

Evaluating neuroinflammation *in-vivo* in a mouse model using multiparametric MRI, with *ex-vivo* insights from immunofluorescence and HRMAS spectroscopy

Raquel González-Alday[1], Carla Dávila-Yagüe[1], Nuria Arias-Ramos[1], Blanca Lizarbe[1,2], Pilar López-Larrubia[1]*

[1]Instituto de Investigaciones Biomédicas Sols-Morreale (CSIC-UAM), Madrid, Spain; [2]Departamento de Bioquímica (UAM), Madrid, Spain; *plopez@iib.uam.es

Abstract

INTRODUCTION: Systemic administration of lipopolysaccharide (LPS) is a widely used murine model for studying neuroinflammation, with established microglia activation and cytokine production [1]. While MRI studies have primarily focused on rats or in diffusion-weighted imaging, the objective of this work is to characterize this model in mice using a multiparametric MRI approach to identify non-invasive biomarkers of neuroinflammation.

METHODS: C57BL/6J wild-type adult male and female mice were subjected to a single intraperitoneal injection of either saline or LPS derived from *Escherichia coli*, administered at a dose of 10mg/kg. MRI studies were conducted in a Bruker Biospec 7T system, acquiring baseline scans and subsequent scans at 3h and 24h post-administration. The multiparametric MRI protocol included T_2W images, T_2 and T_2* maps, magnetization transfer imaging (MTI) and diffusion tensor imaging (DTI). The multiparametric MRI maps were processed using Resomapper, an in-house developed Python pipeline that uses Dipy [2] for DTI fitting, they were co-registered using ANTsPy [3], and then a region of interest (ROI)-based analysis was performed using linear mixed effect models in the software R. The selected ROIs include the cortex (Cx), hippocampus, (HPC), thalamus (Thal), and hypothalamus (HTH). At the end of the study, mice were sacrificed either by high-power focused microwave for ^{1}H HRMAS spectroscopy or by intracardiac perfusion for immunofluorescence assays. In these assays, brain slices were stained with Iba1 to detect microglia and GFAP to detect astrocytes. Various morphology aspects of these cells were analyzed using an in-house developed ImageJ [4] macro.

RESULTS & DISCUSSION: The analysis of the MRI studies showed a significant decrease of mean diffusivity (MD) in LPS-treated mice after injection in all the studied brain areas, while the contrary effect was observed in control mice, with an increase of MD (**Figure 1**). The same behavior was observed in axial diffusivity (AD). The results of the immunofluorescence assays (**Figure 2**) confirm that in LPS-treated mice, a higher number of astrocytes and microglia, being the microglia cells also bigger and more circular than in controls, which confirms that the diffusivity in these mice is hindered by these reactive immune cells, explaining the MRI results of LPS-treated mice. The increased diffusivity in controls suggests a vasogenic effect caused by the saline injection, which might be masking a higher decrease in MD in LPS mice. A decrease over time in T_2 was observed in all mice, probably due to the effect of anesthesia. Finally, regarding the HRMAS analysis of the *ex-vivo* samples, the most notable differences were that a lower concentration of glucose was observed in all brain areas of LPS-treated mice than controls, and a higher concentration of glutamate in the cortex of these same mice was found (**Figure 3**). These differences are expected to be caused by the toxic effect of LPS and the reactive state of astrocytes and microglia. More work is currently in progress to better understand these results and to combine the information of all MRI maps into a more advanced analysis.

Figure 1

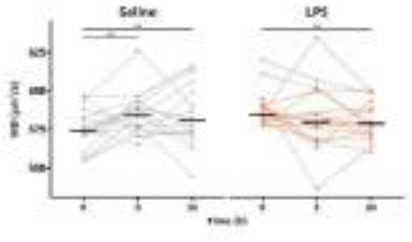

Figure 2

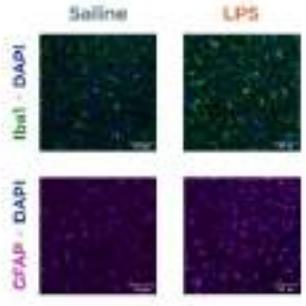

Figure 3

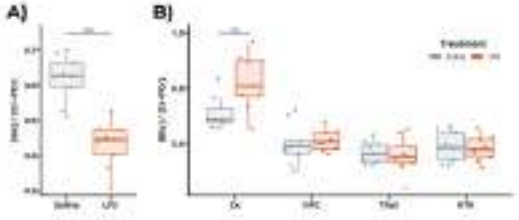

Figure 1 – Mean diffusivity before and 3h and 24h after injection (average of all brain areas for each subject is represented).
Figure 2 – Immunofluorescence images of microglia (Iba1) and astrocytes (GFAP) in a section of hippocampus.
Figure 3 – Relative metabolite concentrations obtained by HRMAS spectroscopy of ex-vivo samples. A) Average of glucose concentration along all brain areas. B) Glutamate concentration by brain area.

References

1. A. Skrzypczak-Wiercioch, K. Sałat, *Molecules*. 27, 5481 (2022); **2.** E. Garyfallidis *et al.*, *Front. Neuroinformatics*. 8 (2014); **3.** N. J. Tustison *et al.*, *Sci. Rep.* 11, 9068 (2021); **4.** J. Schindelin *et al.*, *Nat. Methods*. **9**, 676–682 (2012)

Resomapper: a user friendly and versatile pipeline for multiparametric MRI data processing and mapping

Raquel González-Alday[1], Adriana Ferreiro[1], Nuria Arias-Ramos[1], Blanca Lizarbe[1,2], Pilar López-Larrubia[1]*

[1]Instituto de Investigaciones Biomédicas Sols-Morreale (CSIC-UAM), Madrid, Spain; [2]Departamento de Bioquímica (UAM), Madrid, Spain;
*plopez@iib.uam.es

Abstract

INTRODUCTION: Magnetic resonance imaging (MRI) is essential in research and clinical settings, with quantitative MRI (qMRI) improving reproducibility and sensitivity. However, qMRI processing can be challenging, especially for users with limited coding experience. We introduce Resomapper, an open-source, cross-platform tool that integrates well-established processing libraries into a unified, user-friendly workflow, simplifying qMRI analysis and promoting accessibility, reproducibility, and data sharing.

METHODS: Resomapper is a Python-based tool designed for user-friendly multiparametric MRI processing. It integrates well-established libraries, including Nibabel [1] and SimpleITK [2] for image and data handling, Dipy [3] for diffusion modeling, and others. The software supports T_1, T_2, and T_2* relaxometry, magnetization transfer imaging (MTI), diffusion tensor imaging (DTI), and simple apparent diffusion coefficient (ADC) fitting. To enhance data quality, Resomapper includes preprocessing options such as denoising, Gibbs artifact removal, and bias field correction. Users can process data via an interactive sequential pipeline or an automated JSON-configured workflow, both executable through simple command-line instructions (see **Figure 1** for an overview of the workflow). Resomapper ensures compatibility by converting raw MRI data from different formats (DICOM, Bruker, MR Solutions) into the standardized NIfTI format within a BIDS-like structure [4], enhancing reproducibility, scalability, and data management efficiency. As an example of application of the software, we present a brain MRI study carried out on healthy, adult C57BL/6J mice, both males and females (n=34). MRI acquisitions were conducted in a Bruker Biospec 7T system, with a multiparametric MRI protocol including anatomical T_2W images, T_2 and T_2* maps, MTI and DTI. The studies were processed with Resomapper and then co-registered using ANTsPy [3]. Finally, a region of interest (ROI)-based analysis was performed to check for differences between sex and brain areas. The selected ROIs include the cortex (Cx), hippocampus, (HPC), thalamus (Thal), and hypothalamus (HTH).

RESULTS & DISCUSSION: The results of the preclinical MRI studies are shown in **Figure 2**. Expected differences were found between brain regions in all parameters, and in addition, a small significant sex difference was observed in T_2*, being the values found in the thalamus and hypothalamus higher in female mice than in males. This might mean that anesthesia affects differently across sex (T_2* is the last acquisition in the MRI protocol, in this case). Moreover, this example serves as a reference for other multiparametric MRI studies in mice, demonstrating the feasibility of using Resomapper for standardized multiparametric qMRI analysis. By integrating multiple processing tools into a single, user-friendly framework, Resomapper simplifies qMRI workflows and facilitates reproducible, high-quality image analysis. Its support for diverse preprocessing techniques, multiple imaging modalities, and standardized data formats makes it a valuable tool for researchers with varying levels of programming expertise. Future work will focus on expanding modality support, improving automation, and enhancing compatibility with clinical datasets.

Figure 1

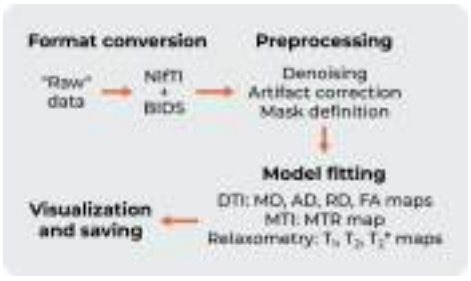

Figure 2

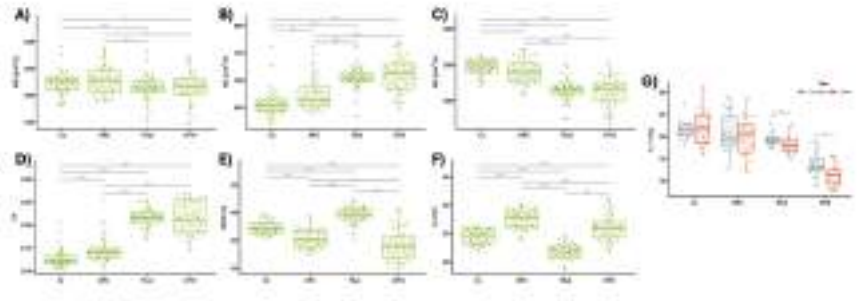

Figure 1 – Schematic of the workflow implemented in Resomapper.
Figure 2 – MRI results across different brain areas. Males and females are represented together in A) – F), where no sex differences were found, to illustrate differences between areas. For T_2*, in G), females vs males are represented to illustrate the difference found in the thalamus and hypothalamus.

References

1. M. Brett *et al.*, nipy/nibabel: 5.3.1 (2024); **2.** B. C. Lowekamp *et al.*, *Front. Neuroinformatics*. 7 (2013); **3.** E. Garyfallidis *et al.*, *Front. Neuroinformatics*. 8 (2014); **4.** K. J. Gorgolewski *et al.*, *Sci. Data*. 3, 160044 (2016).

Leveraging the MouseX DW-ALLEN atlas and the QUINT workflow to match MR and histological data in a mouse model of neurodegeneration

Patricia Martínez-Tazo, Aroa S.Maroto, Silvia De Santis

Instituto de Neurociencias de Alicante, Molecular Neurobiology and Neuropathology, Alicante, Spain. *patricia.martinezt@umh.es

Abstract

INTRODUCTION: Working within the same reference space in neuroimaging is crucial to integrate and compare different techniques effectively. The Allen Mouse Brain Atlas (AMBA), as the largest open resource for mouse brain data, plays a central role in this process. Given the pressing need of validating MRI data's underpinning biology, matching histological and MRI data is of key importance. To this end, we have adapted the parcellation of the QUINT workflow [1]- which brings AMBA parcellation over histological brain slides- to match the same regions and resolution as the MouseX DW-ALLEN atlas [2]. This enables us to overlay the AMBA onto histological slides and analyze MRI-derived parameters alongside their histological validation using the same parcellation, ultimately uncovering the underlying biology of MRI contrast. As a proof of concept, we have applied the framework to test associations between MRI markers and reactive periplaque microglia in the APP/PS1 mouse models of Alzheimer's disease.

METHODS: APP/PS1 mice (n=11) were scanned on a 7T Bruker scanner at 9 months, when pathology is reportedly spread to cortical and hippocampal areas [3]. Whole brain gray matter was characterized by relaxometry, and by conventional and advanced diffusion-weighted MRI to extract diffusion tensor imaging markers, and markers sensitive to microglia morphology. Parcellation was done according to the MouseX-DW-ALLEN Atlas [2] as illustrated in *Figure1a*. A subset was perfused right after MRI acquisition for histological processing, and immunofluorescence staining was used to stain microglia (Iba-1). A representative slice per subject was processed following our modified QUINT workflow: i) DAPI staining was registered to AMBA space; ii) Iba-1 staining was thresholded and segmented for periplaque microglia quantification; and iii) microglia load was quantified region-wise (workflow shown in *Figure1a,* results in *Figure1b*). Next, we tested correlations between MRI markers and periplaque microglia load (*Figure1c*), revealing significant association between microglia load and FA (R^2*=-0.52; pvalue=0.016*); AD (R^2*=-0.46; pvalue=0.036*); T2* (R^2*=-0.63; pvalue=0.002*); and stick dispersion KW (R^2*=-0.47; pvalue=0.031*) .

RESULTS & DISCUSSION: Quantification of periplaque microglia confirms the presence of pathology in cortical and hippocampal regions (*Figure1b*), as guided by MouseX parcellation. Notably, a significant negative correlation was reported between MRI-derived stick dispersion and periplaque microglia count per region (*Figure1c*), supporting sensitivity of this parameter to process retraction following plaque-associated microglia reactivity. In addition, reduced T2* in areas of reactive microglia is compatible with iron accumulation [5]. This workflow enables testing correlation between MRI biomarkers and histological markers under a common anatomical division, thus holding a great potential to elucidate disease-specific microstructural biomarkers.

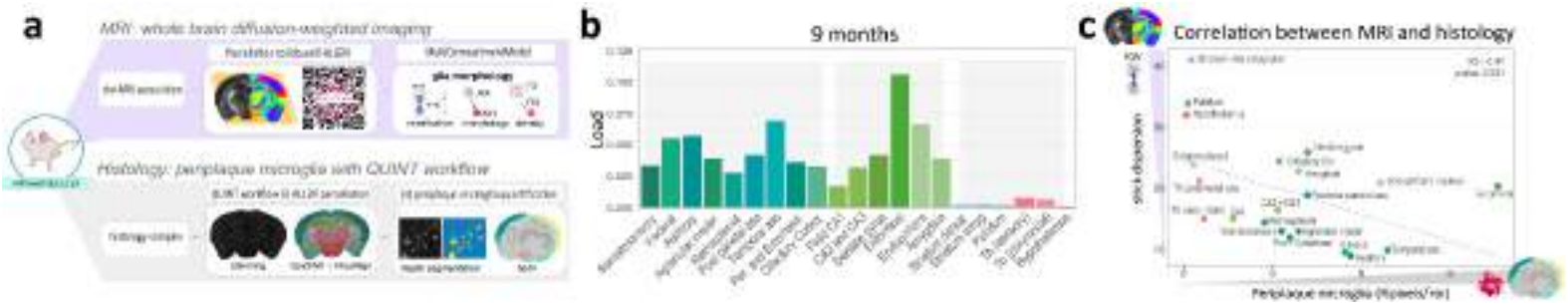

Figure 1. **a) Data acquisition and analysis** workflow for MRI and histological data. MRI maps where registered to the MouseX-DW ALLEN Atlas and advanced markers of glia morphology were extracted by modelling different cylindrical and spherical compartments [4]. Immunostaining for microglia (Iba-1) was processed with QUINT workflow modified to match MouseX parcellation. **b) periplaque microglia load** (sum of positive pixels/total pixels per region) was quantified per each of the 44 grey matter regions, showing presence of inflammation in cortical and hippocampal regions, and minimum in internal nuclei**. c) both MRI and histological data were extracted under common anatomical division**, which allowed testing their correlation. Stick dispersion (KW) was reported to be significantly correlated to periplaque microglia accumulation per ROI (*Pearson correlation=-0.47; pvalue=0.031*).

References

[1] Yates S.C., Groeneboom N.E., Coello C., Lichtenthaler S.F., Kuhn P.H., Demuth H.U., Hartlage-Rübsamen M., Roßner S., Leergaard T., Kreshuk A., Puchades M.A., Bjaalie J.G. QUINT: Workflow for Quantification and Spatial Analysis of Features in Histological Images From Rodent Brain. Front. Neuroinform., 13:75 (2019).

[2] Martínez-Tazo P., Santos A., Kotb M.S., Espinós Soler E., De Santis S. Sex Matters: the MouseX DW-ALLEN Atlas for mice diffusion-weighted MR imaging. Neuroimage, in press (2024).

[3] Oshima T., Kater M.S.J., Huffels C.F.M., Wesseling E.M., Middeldorp J., Hol E.M., Verheijen M.H.G., Smit A.B., Boddeke E.W.G.M., Eggen B.J.L. Early amyloid-induced changes in microglia gene expression in male APP/PS1 mice. J. Neurosci. Res., 102(3):e25295 (2024).

[4] Garcia-Hernandez R., Cerdán Cerdá A., Trouve Carpena A., Drakesmith M., Koller K., D.K. Jones, Canals S, De Santis S. Mapping microglia and astrocytes activation in vivo using diffusionMRI.SciAdv.8,eabq2923 (2022).

[5] McIntosh A., Mela V., Harty C., Minogue A.M., Costello D.A., Kerskens C., Lynch M.A. Iron accumulation in microglia triggers a cascade of events that leads to altered metabolism and compromised function in APP/PS1 mice. Brain Pathol., 29(5):606–621 (2019).

Diet-induced obese mice show altered cerebral mean diffusivity and FA values during fasting

Marta Rodrigo[1,2], Adriana Ferreiro[1], Maya Holgado[1], Pilar López-Larrubia[1] and Blanca Lizarbe[1,2*]

[1]Instituto de Investigaciones Biomédicas Sols-Morreale, Madrid, Spain; [2]Department of Biochemistry, Universidad Autónoma de Madrid, Spain.

Abstract

INTRODUCTION: Obesity is a chronic disease linked to multiple comorbidities and it is associated with cerebral changes, including neuroinflammation and resistance to insulin and leptin, in cerebral regions involved in appetite regulation and energy homeostasis[1]. During fasting periods, the brain changes its metabolism, promotes the activity of hypothalamic orexigenic neurons and other regions, and regulates food-intake hormones[2]. In this study, we propose MRI to investigate *in vivo* the effects of short-term fasting on the brain in mice and how they are affected by obesity.
METHODS: MRI images were acquired using a 7T Bruker Biospec scanner after 20 weeks of low-fat low-sugar (LFLS, 10 kcal% Fat) diet or high-fat high-sugar (HFHS, 45kcal% Fat with 30 kcal% Sucrose) diet consumption (n=16 C57BL/6 mice for each diet group, 50% females), and after 4 hours of fasting during the dark phase. Their body weight was monitored weekly and their blood glucose levels were checked before the acquisition. MRI study included DTI (30 directions, TR/TE= 3000/37.56 ms, δ/Δ= 4/25ms, Mtx= 128×128, slice thickness= 1.25 mm, b-values= 800μm^2/s and 2500μm^2/s) and MTI ($MT_{ON/OFF}$, TR = 2500 ms, TE = 9.8 ms, and Av = 1) images that were processed using a python-based software to obtain mean diffusivity (MD), axial diffusivity (AD), radial diffusivity (RD) and fractional anisotropy (FA) maps using "patch2self" filter[3], and magnetization transfer ratio (MTR) maps using adaptive "soft coefficient matching filter"[3]. In each map the regions of interest were manually selected using ImageJ and a mouse brain atlas as a reference[4]. To investigate the effects of diet, sex and brain region on the MRI coefficients we fitted the data to a linear mixed-effects model using R software[5]. After selecting the best baseline model, ANOVA tests were performed to estimate the significance of each effect and interaction on the MRI variables, and pos-hoc t-test with Bonferroni correction when interactions where significant.
RESULTS & DISCUSSION: After a short fasting period, we found MD values changing significantly in a diet and brain region manner (diet:region interaction, $p < 0.05$) and an area effect ($p < 0.001$), with post-hoc tests showing significantly higher values in HFHS-fed mice in the NAc and ILA ($p_{adj} < 0.05$ both) **(Figure 1A)**. Regarding FA values, significant effects were found for diet, sex, and area ($p < 0.05$ all). An increase in FA values was noted in HFHS-fed animals **(Figure 1B)**. MTR values only showed a significant area effect ($p < 0.001$).
In summary, we report that, in both sexes, mice fed with a HFHS diet have increased MD values, more remarkably in the reward regions NAc and ILA, and increased FA, under fasting conditions, as compared to non-obese mice. This MRI results are in agreement with previous investigations that report neuroinflammation[6] and microgliosis[7] processes under obesity conditions. In order to investigate this effect in depth, H^1 HRMAS data will be acquired to examine the metabolic changes undergoing. In parallel, results will be compared to a non-fasting group.

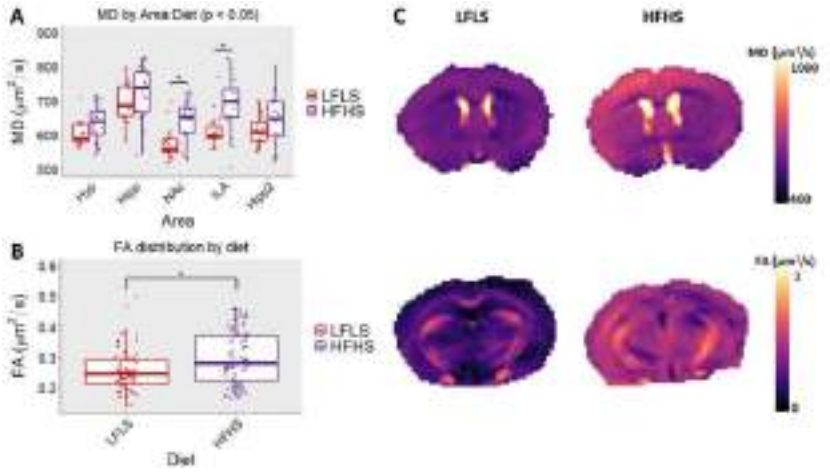

Figure 1 – A: Distribution of MD values by area and diet in LFLS-fed (red) and HFHS-fed (purple) mice in the four brain regions investigated: hypothalamus (Hyp), hippocampus (Hipp), Nucleus Accumbens (NAc) and Infralimbic Area (ILA) (**p < 0.05*). **B:** Distribution of FA values by diet in LFLS-fed (red) and HFHS-fed (purple) mice (**p < 0.05*). **C:** Representative MD (top) and FA (bottom) maps of LFLS-fed (left) and HFHS-fed (right) female animals in the slices containing the NAc /ILA (MD) and Hyp/Hipp.(FA).

References

1. Lizarbe B *et al*., *Front. Neuroenergetics*. 5 (2013); **2.** Bogdanov VB *et al*., *Psychoneuroendocrinology*. 112 (2020); **3.** Garyfallidis E *et al*., *Front Neuroinform.* 8 (2014); **4.** Allen Brain Atlas, *Reference Atlas* (2024); **5.** R Core Team, *R* (2021); **6.** Jais A *et al*., *J Clin Invest.* 127 (2017); **7.** Nguyen LT *et al*., *npj Metab Health Dis*. 2 (2024).

A Custom Bioreactor for dDNP-NMR Studies of 3D Cell Models

Lluís Mangas-Florencio[1, 2], Alba Herrero-Gómez[1], James Eills[1], Marc Azagra[1], Marina Batlló-Rius[2], Irene Marco-Rius[1]

[1]Institute for Bioengineering of Catalonia, Barcelona, Spain
[2]Vitala Technologies, S.L, Barcelona, Spain
lmangas@ibecbarcelona.eu

INTRODUCTION: Dissolution Dynamic Nuclear Polarization (dDNP) significantly enhances NMR sensitivity[1], enabling the real-time, non-destructive tracking of metabolic conversions and the study of cellular metabolism. We developed a bioreactor (BR) fabricated from biocompatible materials and equipped with a fluidic system to maintain optimal culture conditions during NMR acquisition in benchtop spectrometers. This platform has been designed for dDNP-NMR studies of 3D cell models and has been tested on two tissue-engineered models of cervical cancer and hepatocellular carcinoma.

METHODS: To characterize the BR-NMR signal distortion, an NMR tube was filled with 10% H2O/D2O. The different pieces of the BR were added one by one to the NMR tube in their correct position and 1H NMR spectra were acquired. To assess the capability of the BR for cell maintenance, the metabolic activity of the scaffolds was assessed via alamarBlue assay. The 3D construct was placed inside the BR with the circulation system connected to a media reservoir a peristaltic pump with a flow of 0.2mL/min. For dDNP-NMR experiments, 2x106 scaffolded cells in the BR were placed inside a 1.4 T benchtop NMR spectrometer. After dissolution of hyperpolarized 1-13C pyruvate[2], 1mL of growth media containing 3.2mM of 1-13C pyruvate was injected into the BR and 13C NMR spectra were acquired dynamically for 200s.

RESULTS & DISCUSSION: The compatibility of the presented BR materials with NMR acquisitions was studied by assessing the signal distortion caused by the addition of each BR piece close to the detection area. In Fig. 1 A, we show a comparison between line shapes after sequentially adding the BR pieces.

The efficiency of the cell media recirculation was examined to assess the suitability of the BR as a cell culture platform. As seen in Fig. 1C, the viability of the 3D cell models kept without media recirculation decreased by 45%, while the 3D models under flow maintained their viability. These results illustrate the suitability of the BR platform to maintain cell viability during analysis.

To validate the BR for dDNP-NMR analysis, the 3D cell models of HeLa and HepG2 cells were tested both in 2D and 3D (Fig 2). While HeLa show no significant difference between 2D and 3D conformation, HepG2 cells showed a 2.2-fold higher rate of lactate production compared with the cell suspensions.

Our findings suggest that this bioreactor platform effectively sustains and enables analysis of 3D cell models in NMR studies, providing a flexible and accessible tool for metabolic and biochemical research in tissue engineering. This platform integrates complex cellular models with NMR spectroscopy, establishing a solid foundation for future use in non-specialized laboratories.

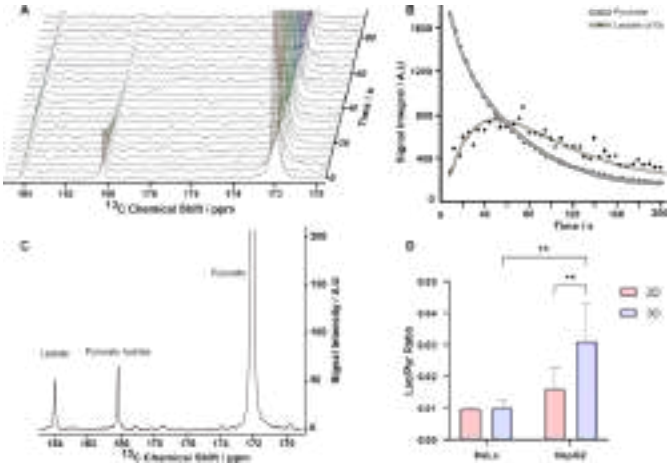

Figure 1 – Metabolic analysis of 3D cell models in the bioreactor. (A) Representative dynamic ^{13}C NMR spectra of 3D HepG2 acquired every 5 s after HP pyruvate injection. (B) Time-course plot of pyr and lac signal integrals. (C) Summed dynamic spectra showing metabolic data from panel A. (D) Lactate-to-pyruvate ratios for HeLa and HepG2 in 2D and 3D models (mean ± SD).

1. Adamson, E. B.; Ludwig, K. D.; Mummy, D. G.; Fain, S. B. Magnetic resonance imaging with hyperpolarized agents: methods and applications. Physics in Medicine and Biology 2017, 62, R81–R123.

2. Yeste J, Azagra M, Ortega MA, Portela A, Matajsz G, Herrero-Gómez A, Kim Y, Sriram R, Kurhanewicz J, Vigneron DB, Marco-Rius I. Parallel detection of chemical reactions in a microfluidic platform using hyperpolarized nuclear magnetic resonance. Lab Chip. 2023 Nov 21;23(23):4950-4958. doi: 10.1039/d3lc00474k.

Cerebral magnetic resonance imaging insights into bariatric surgery-induced changes in obese mice

Adriana Ferreiro[1], Maya Holgado[1], Raquel González-Alday[1], Pilar López-Larrubia[1] and Blanca Lizarbe[1,2]*

[1]Instituto de Investigaciones Biomédicas Sols-Morreale, CSIC-UAM, Madrid, Spain; [2]Department of Biochemistry, Autonomus University of Madrid, Madrid, Spain; *blanca.lizarbe@iib.uam.es

Abstract

INTRODUCTION: Obesity is a chronic disease associated with several pathologies such as type 2 diabetes, cardiovascular risk or neurodegeneration. Bariatric surgery (BS), initially a high-risk weight-loss procedure, is still the most successful approach at restoring non-obese body mass indexes (BMI) in an increasing range of population [1]. Beyond weight reduction, BS alters metabolism, gut microbiota, and brain function. [2,3]. Among available techniques, vertical Sleeve Gastrectomy (VSG) is one of the most common, removing 70%–80% of the stomach. This study aims to investigate VSG's effects in the brain on a rodent diet-induced obesity model using diffusion tensor imaging (DTI) and magnetization transfer imaging (MTI).

METHODS: 26 C57BL/6 mice (male and female) were fed with a high-fat high-sugar (HFHS, 45kcal% fat, 30 kcal% sucrose) diet (Research Diets Inc., D08112601i). After 20 weeks, obese mice were assigned to either a sham-operated or BS group. Post-surgery, animals were maintained on a liquid diet for 1 week, followed by a chow diet for 6 weeks. Body weight (BW) was followed daily. Brain diffusion tensor images (DTI, 30 directions, TR/TE= 3000/37.56 ms, δ/Δ= 4/25ms, Mtx= 128×128, slice thickness= 1.25 mm, b-values= 800μm^2/s & 2500μm^2/s) and magnetization transfer images (MTI, $MT_{ON/OFF}$, TR=2500ms, TE=9.8ms, and Av=1) were acquired pre-surgery and at 3- and 6-weeks post-surgery using a Bruker Biospec 7T system (Bruker Biospin, Ettlingen, DE). Image pre- and processing was performed using a software based on Dipy [4]. Parametric maps of mean, axial and radial diffusivities (MD, AD, RD), anisotropic fraction (FA) and MT ratio (MTR) were obtained, and regions of interest (ROI) from the hypothalamus (Hyp), hippocampus (Hipp), nucleus accumbens (NAc), and infralimbic area (ILA) selected. Statistical analyses were performed using R [5], and MR parameters were fitted to a variety of LME regression models using the "lme" function of "nlme" [6] package to evaluate the differences of the MR parameters between sham and BS groups over time.

RESULTS & DISCUSSION: The analysis of MR parameters in the Hyp and Hipp revealed significant variations in RD values associated with the "Type" (Sham/BS) and "State" (Pre, $Post_{3w}$ or $Post_{6w}$) interaction ($p<0.001$ and $p<0.01$, respectively). Specifically, in BS group, RD increased significantly and Sham group decreased (Pre Vs $Post_{6w}$) (**Figure A**). Additionally, in the Hipp, LME analysis of the FA also demonstrated a significant Type:State interaction ($p<0.001$), indicating that at week 6 the BS group had lower FA values, compared to the Sham (**Figure B**). Up sum, treatment with BS, which effectively reduced BW, resulted in decreased FA values and increased RD, on agreement with a successful reversal of the inflammatory state induced by obesity [7]. Currently our dataset comprises only *n* = 5 with the three time points. Future research will increase the n and expand the analysis to additional brain regions.

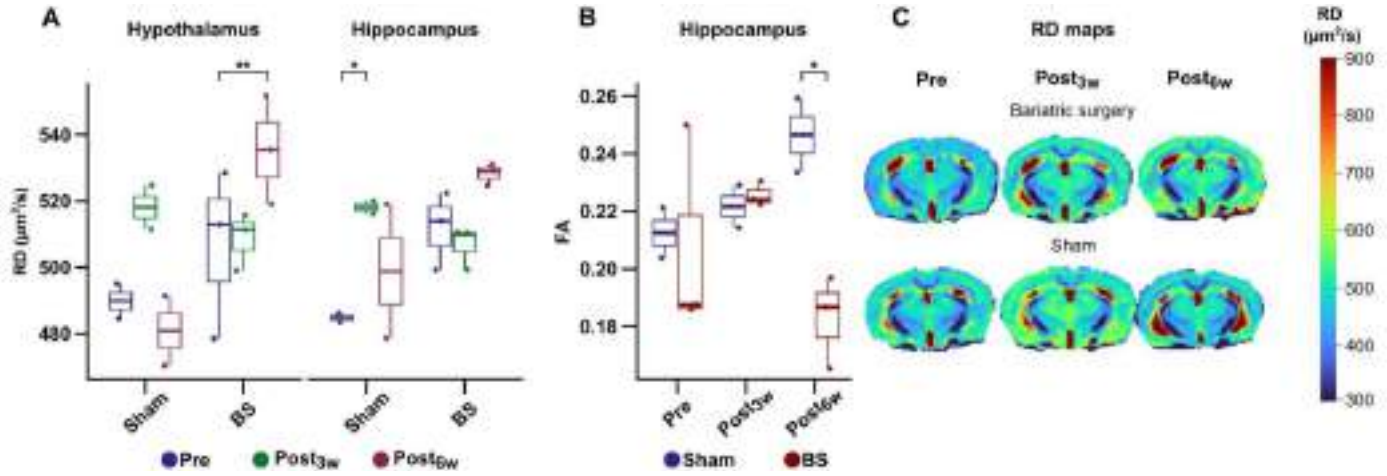

Figure 1 – (A) Boxplot of RD illustrating the comparative analysis across different time points for both the Sham and BS groups in the hyp and hipp. (B) Boxplot of FA values comparing the Sham and BS group in the different time points in the hipp. (C) Parametric maps of RD of the brain of a mice at different time points after a bariatric surgery (top) and a sham procedure (bottom) in the slice containing the hyp and hipp. (*p < 0.05, **p < 0.01, ***p < 0.001).

References

1. Ji, Y. et al., Biomolecules 11, 1582 (2021) **2.** Sinclair, P. et al., Nat Rev Gastroenterol Hepatol 10, 606-624 (2018) **3.** Chen, J. et al, Mol Metab 48,101214. (2021) **4.** Garyfallidis E, et al.Front Neuroinf. (2014); **5.**R Core Team. Vienna: R Core Team (2020) **6.** Pinheiro, J., Bates, D., R Core Team, Mol. Metab. 3.1-167 (1999) **7.** Anderson, M. A., et al., Neurosci. Lett. 565, 23–29 (2014).

Neuroinflammation and Metabolic changes induced by medium-term High-fat diet in an IL-1R1KO murine model: An MRI-based study

Darwin Córdova-Ascurra[1], Lidia Esteban-Merayo[1], Raquel González-Alday[1], Nuria Arias-Ramos[1], Jesús Pacheco-Torres[1], Pilar López-Larrubia[1*]

[1][Instituto de Investigaciones Biomédicas Sols-Morreale (CSIC-UAM) Madrid, Spain]; *[plopez@iib.uam.es]

Abstract

INTRODUCTION: Nowadays, obesity is a pathological condition with a high and increasing prevalence in society, due to the complex relationships between biological and socioeconomic influences; it has different comorbidities associated too, such as diabetes [1]. Chronic inflammation is strongly associated with obesity, moreover, high-fat diets (HFD) activate pro-inflammatory cascades in the brain because saturated fatty acids can cross the blood-brain barrier (BBB). Interleukin-1-receptor 1 (IL-1R1), a pro-inflammatory mediator, bridges the metabolic and inflammatory systems since previous studies have demonstrated that deletion of IL-1R1 signaling prevents the onset of insulin resistance in a mouse model of diet-induced obesity (DIO) [2]. In this context, our objective is to characterize the neuroinflammation by *in vivo* multiparametric MRI in an IL-1R1KO DIO murine model and *wild-type* mice (WT) both fed with standard diet (SD) and HFD. Also, we study the differences in mouse phenotyping between groups by using an indirect calorimetric assay.
METHODS: Male C57BL/6J *wild-type* mice (n=12) and male IL-1R1KO mice with the same genetic background (n=19) of 7-8 weeks of age were divided into 2 groups: mice fed with HFD for 10 weeks and with SD for 10 weeks. At the end of this diet period, multiparametric MRI studies were conducted using a Bruker Biospec 7T scanner; we acquired magnetization transfer (MT) images, diffusion tensor imaging (DTI), T_2 and T_2* maps. Subsequently, parametric maps were processed with an in-house Python-based software (Resomapper) and, using ImageJ software, 4 brain regions of interest (ROIs) were selected and quantified: cortex (Cx), hippocampus (HPC), thalamus (Thal) and hypothalamus (HTH). Linear mixed effects models were used to statistically assess the impact of diet and genotype (WT or KO) across areas on MRI parameters. Moreover, after 5 days from the MRI study, a metabolic and motor analysis system of cages (Phenomaster, TSE Systems GmbH) was used to study every mouse from each group (2 different genotypes with HFD or SD), which provided data on indirect calorimetry, motor activity and food intake, among other parameters.
RESULTS & DISCUSSION: WT mice gained weight faster than KO mice and both groups with HFD lost circadian oscillations of respiratory exchange ratio (RER). MRI studies have detected higher T_2 values in KO mice, which could indicate the occurrence of vasogenic edema in these mice. On the other hand, in the T_2* studies, the values are significantly higher in the Cx of obese WT mice suggesting microvascular changes, potentially due to inflammation. Also, we observe a difference between KO and WT -significantly higher values in HPC and Thal of WT- and this difference remains independent of diet. The absence of *Il1r1* gene in these mice might indicate an altered neuroinflammatory response, affecting homeostasis or oxygenation of brain tissue. This study is a work in progress; thus, we expect that the addition of new MRI studies with more WT mice and studying these groups after 20 weeks of SD and HFD, will help us to better understand the role of IL-1R1 in neuroinflammation caused by HFD.

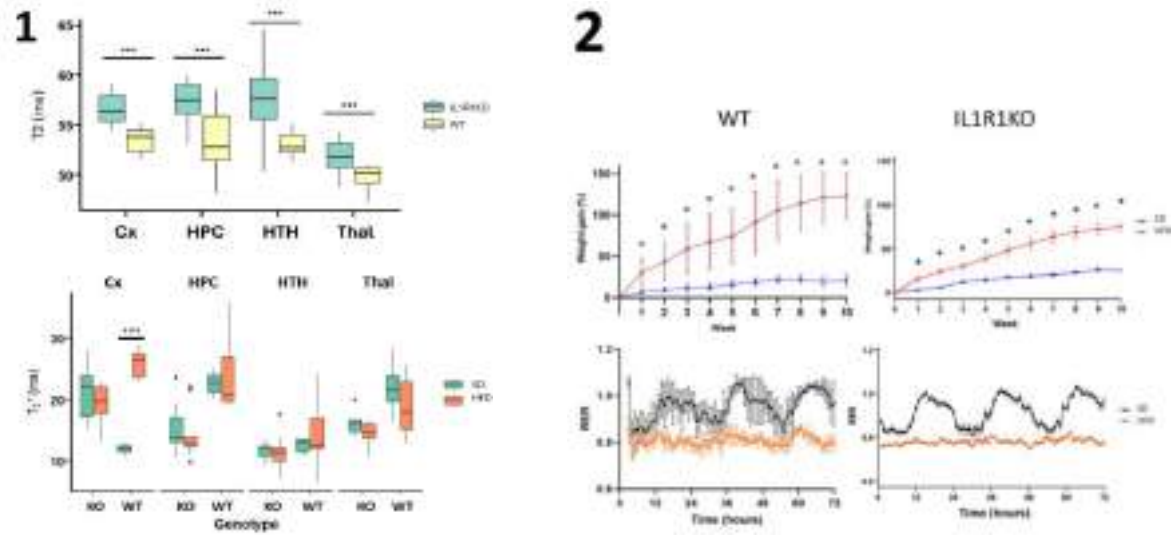

Figure 1 – Boxplots representing the quantification of T_2 values in the 4 regions comparing both genotypes (Above). Boxplots representing the quantification of T_2* values in the 4 regions according to genotype and diet (Below). **Figure 2 –** Representations of body weight increase in the experimental groups relative to the start of the diet (Above). Representations of Respiratory Exchange Ratio (RER) adjusted to 72 hours (Below).

References

1. Apovian CM. Am. J. Manag. Care, 2016 - 06;22(7 Suppl):176.
2. Finucane, O. M. et al. (2015). Monounsaturated fatty acid–enriched HFD impede adipose NLRP3 inflammasome–mediated IL-1β secretion and insulin resistance despite obesity. Diabetes 64, 2116–2128.

Towards Robust Diffusion MRI Biomarkers: A Reliability and Repeatability Study

Guillem París[1]*, Tomasz Pieciak[1], Santiago Aja-Fernández[1], Antonio Tristán-Vega[1]

[1]Laboratorio de Procesado de Imagen (LPI), Universidad de Valladolid, Valladolid, Spain; *guillem.paris@uva.com

Abstract

INTRODUCTION: Neuroimage studies are often obscured in their reliability assessment. In the diffusion MRI field, researchers are obtaining bigger datasets to evaluate the reliability of the developed methods. However, critics argue that better rather than bigger datasets should be acquired. This, together with the lack of a common framework for reliability evaluation limits the comparability between the developed markers. Extending the work in [1], we provide a thorough reevaluation of reliability assessment in region-based diffusion MRI studies, and evaluate the reliability of state-of-the-art EAP-based diffusion markers derived from DTI [2], AMURA [3], MiSFIT [4], MAPL [5], and HYDI-DSI-QP [6]. Also, we study the required sample size for different group tests.

METHODS: Two repeated-measures multishell datasets (MICRA [7] and ZJU [8]) are used to assess the repeatability and reliability of relevant diffusion metrics: the return probabilities (RTOP, RTAP, RTPP) [9], non Gaussianity (NG) [9], Mean Squared Displacement (MSD) and Q-space Inverse Variance (QIV). For a fairer comparison, MICRA dataset has been subsampled to mimic the ZJU's acquisition protocol.

RESULTS & DISCUSSION: EAP-based biomarkers show a different behavior for the two datasets. For MICRA, MiSFIT and HYDI-DSI yield the best results in terms of reliability across the different biomarkers. For ZJU, however, HYDI-DSI obtains the best results in all but two (RTPP and MSD) biomarkers. We conclude that only evaluating repeatability is not enough: restricted methods tend to score higher on repeatability given their lack of freedom when fitting the signal. HYDI-DSI and MiSFIT show a consistent high reliability, which may be due to the positivity constraints they impose. While the return probabilities and QIV seem to be the most robust measurements, NG performs slightly worse, and MSD is poor in terms of repeatability.

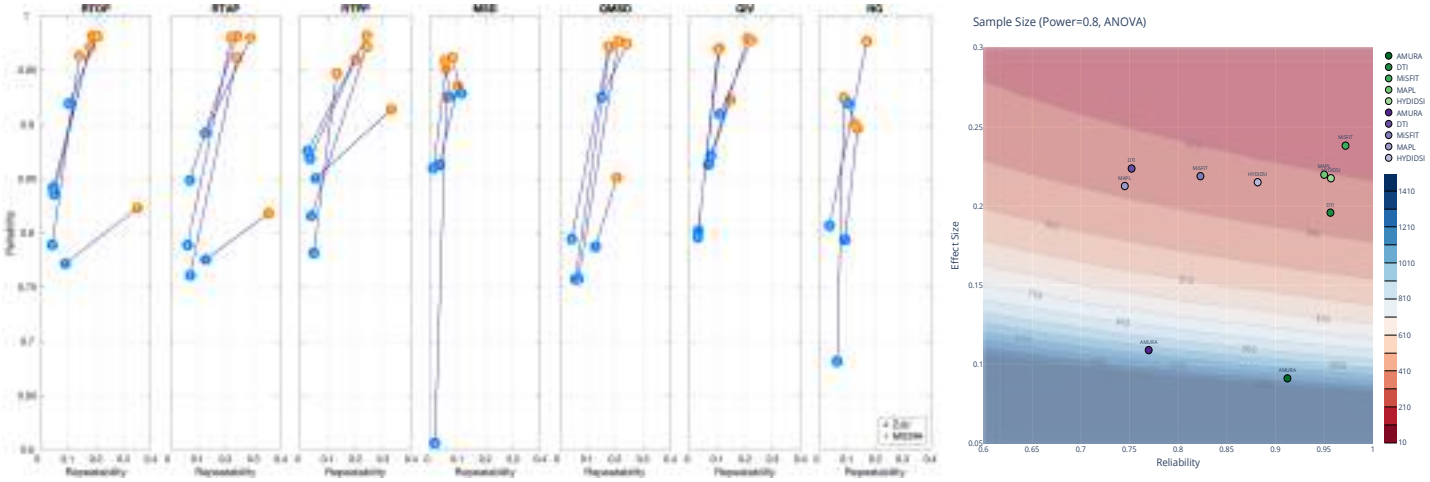

Figure 1 – (Left) Displacement of reliability vs. repeatability estimates across different datasets for different models: (1) AMURA, (2) DTI, (3) MiSFIT, (4) MAPL, (5) HYDI-DSI. Orange represents those estimates from MICRA, whereas blue represents ZJU. Even though the MICRA dataset has been subsampled for a fairer comparison, there still exists differences in the quality of the data, which have an effect on the reliability of their estimates. (Right) Required sample size for an ANOVA test using the data provided. The samples have been grouped across the different biomarkers. Green, therefore, represent the samples of MICRA, whereas purples are ZJU's. The background shows the required sample size for the given effect size in an ANOVA test. As it can be seen, MICRA's MiSFIT is the most reliable, and therefore, requires less samples to find statistical significant group differences.

References

[1] Zuo et al., 2008; Nature Communications. [2] Basser et al., 1994; Biophysical Journal. [3] Tristán-Vega et al., 2020; PLOS ONE. [4] Tristán-Vega et al., 2021; Neuroimage. [5] Fick et al., 2016; Neuroimage. [6] Tristán-Vega et al., 2022; MedIA [7] Koller et al., 2021; Neuroimage. [8] Tong et al., 2020. [9] Özarslan et al., 2013; Neuroimage.

Advanced AI strategies to estimate inflection point of response/relapse in preclinical GL261 glioblastoma using T2w MRI data

González Béjar, J[1], Vellido, A[1,3]*, Candiota, AP[2,3]

[1]Intelligent Data Science and Artificial Intelligence (IDEAI-UPC) Research Center, Barcelona; [2]Departament de Bioquímica i Biologia Molecular, Unitat de Biociències, Universitat Autònoma de Barcelona, Cerdanyola del Vallès, Spain; [3]CIBER de Bioingeniería, Biomateriales y Nanomedicina, ISCIII. *[avellido@cs.upc.edu]

Abstract

INTRODUCTION: Magnetic Resonance Imaging (MRI) enables disease progression and treatment monitoring in clinical practice. Identifying early imaging biomarkers predicting treatment response is crucial for improving prognosis in Glioblastoma (GB), a primary brain tumor with poor outcome. In this work, we harness the GL261 preclinical GB model, which allows for longitudinal explorations[1,2], providing a robust framework for evaluating treatment efficacy. In past work, we suggested that T2 weighted (T2w) MRI could identify response to Temozolomide (TMZ) independent of volume changes[3]. Here, we compared standard machine learning (ML) with feature extraction from T2w longitudinal MRI and deep learning techniques (DL), assessing their effectiveness in distinguishing between relapsing and cured TMZ-treated mice, prior to volume changes. **METHODS:** GL261 GB bearing mice were generated and TMZ-treated as described by us[1]. T2w MRI studies were performed at 7T with a RARE sequence (TR/TEeff = 4200/36 ms), every 2-3 days. Mice showing transient response were followed-up until endpoint. Mice were considered “cured” if tumor disappeared or remained as scar for one month after therapy halt, and control mice received TMZ vehicle. The dataset used was n=8 control mice (84 images), n=5 cured mice (66 images), and n=5 relapsing mice (232 images, representing different time points). For standard ML, radiomic features were extracted from tumor segmentations using PyRadiomics and models such as XGBoost were employed. Different data splitting and data augmentation strategies were approached to assess their impact on predictive performance. For DL, we implemented CNNs, LSTMs, and Transformers to capture both spatial and temporal tumor evolution. To enhance interpretability, we leveraged explainable AI techniques, including feature importance analysis in ML and Grad-CAM for visualizing DL model attention, examining whether the extracted features align with biological indicators. **RESULTS & DISCUSSION:** Our ML models achieved a mean accuracy of 67% and an AUC exceeding 74% using a 50-fold strategy. DL models significantly outperformed ML, achieving 94% accuracy and an AUC above 91%. Radiomic texture-based features played a key role in distinguishing between relapse and response/cure, particularly those from Gray Level Run Length Matrix (GLRLM), Gray Level Size Zone Matrix (GLSZM), and Neighbouring Gray Tone Difference Matrix (NGTDM) (Figure 1). GLRLM captures patterns of texture organization, with Run Entropy reflecting randomness in intensity distributions—higher values were observed in relapsing tumors, suggesting greater structural disorder. Gray Level Non-Uniformity was also more pronounced in cases with poor response. GLSZM quantifies gray level zones, with Size Zone Non-Uniformity indicating the variability of zone sizes. Non-uniformity is linked to irregular texture patterns, often associated with uncontrolled growth. NGTDM provides insights into spatial intensity relationships, and its Coarseness feature evaluates the smoothness of intensity transitions. Lower values, indicative of abrupt intensity changes, were matched to tumors prone to relapse, whereas higher values suggested more uniform, less aggressive structures. These features have been also described by authors investigating radiomics in GB response[4], suggesting that our findings are biologically sound and can pave the way for a future translational scenario, with the potential advantage of relying in single T2w MRI. The findings contribute to a better understanding of glioblastoma progression and highlight the role of AI-driven biomarkers in early relapse prediction and treatment stratification.

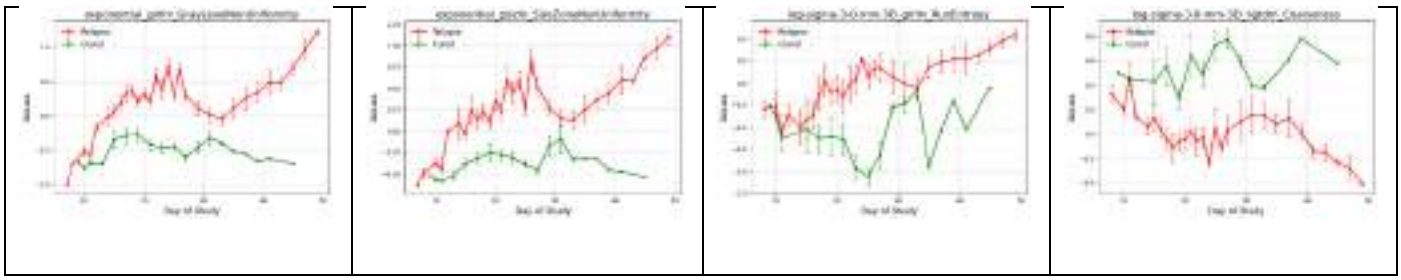

Figure 1 – Average trend of the GLRLM Gray Level Non-uniformity, GLSZ Size Zone Uniformity, GLRLM Run Entropy and NGTDM Coarseness features for relapsing tumours (red) and cured mice (green).

References

1.Wu S, et al. NMR Biomed. 2020;33(4):e4229; **2.** McKelvey KJ, et al. Front Oncol. 2021;11:633210; **3.** Núñez LM, et al. Sci Rep. 2020;10(1):19699. **4.** Sadeghinasab A, et al. Health Sci Rep. 2024;8(1):e70323.

T2* MRI hiperintensity in a rat model of intracerebral hemorrhage are related to dynamic changes in perilesional edema and clot formation

Clàudia Calvet-Soler[1], Sílvia Lope-Piedrafita[2,3], Santiago Rojas[1], Gemma Manich[1]*

[1]Department of Morphological Sciences, Autonomous University of Barcelona (UAB), Spain; [2]Department of Biochemistry and Molecular Biology. UAB; [3]CIBER de Bioingeniería, Biomateriales y Nanomedicina, Spain; *Gemma.Manich@uab.cat

Abstract

INTRODUCTION: Spontaneous acute intracerebral hemorrhage (ICH) accounts for 15-20% of strokes, but it is the deadliest and causes the highest disabilities [1]. Its clinical diagnosis and progression are done through MRI techniques [2]; however, the histopathological modifications related to specific lesion stages and their correlation with alterations in conventional MRI sequences are not well-known [3]. Therefore, our study aimed to characterize histological changes in hyper- and hypointensities in MRI T2 and T2*- weighted images during the acute, subacute, and chronic stages of an experimental animal model of ICH.

METHODS: Autologous blood was injected into the striatum of adult male and female Sprague-Dawley rats. After acquiring T2-weighted (RARE sequence; TEeff/TR=36ms/5s) and T2* weighted mages (FLASH sequence TE/TR/α=8ms/500ms/40º) with a Bruker BioSpec 70/30 small animal scanner at 2h, 24h, and 3, 7, and 21 days post-injury (dpi), the animals were euthanized, and brains were collected for histology. Brain tissue was stained with Hematoxylin-Eosin (HE), Perls, Martius Scarlet Blue (MSB), and Iba1 and GFAP immunohistochemistry, and sections were analyzed.

RESULTS & DISCUSSION: In T2 and T2* weighted images, the lesion volume and hypointensities progressively decrease through time. Lesion hyperintensities in both imaging types peak at 24h in the perilesional area and at 3 dpi also in the core, coinciding with the maximal lesion edema volume. Histological observations with HE and MSB show that, in the lesion core, erythrocytes are mainly lysed at 3 dpi, coinciding with the first appearance of mature fibrin. In the perilesional area, edema extends until 3 dpi, along with tissue vacuolation, and iron deposits accumulate intracellularly at 3 dpi and extracellularly at 7 and 21 dpi. Microglial/macrophage reactivity, which participates in erythrophagocytosis, peaks at 3 dpi and decreases later. Meanwhile, astroglial reactivity starts at 3 dpi and increases later, coinciding with glial scar formation. In general, brain hypointensities located in the lesion core at early time points in both T2 and T2* weighted images reflect the paramagnetic effect of iron produced by the injected autologous blood, which progressively reduces over time, an event dissociated from iron accumulation detected by Perls staining or hemosiderin deposits by HE. On the other hand, T2 and T2* hyperintensities at 24 h and 3 dpi mainly reflect two phenomena: brain edema in the perilesional area, as observed by tissue vacuolation, and clot formation, corresponding to mature fibrin detected in the lesion core and lesion margins. Overall, changes in T2 and T2* sequences in ICH reflect different histopathological phenomena depending on the lesion stage (acute, subacute, and chronic). Further studies are needed to correlate other main tissue changes to conventional MRI sequences and their relation to lesion outcomes.

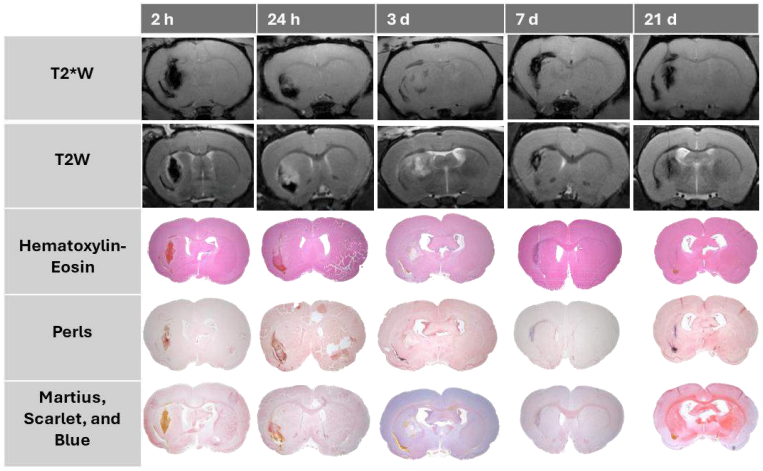

Figure 1 – MRI T2*w and T2w images and histological stained HE, Perls and MSB images at 2h, 24h, and 3, 7, and 21 days post autologous blood injection, modeling acute intracerebral hemorrhage.

References

1. Veltkamp R, Purrucker JC. Management of spontaneous intracerebral hemorrhage. *Curr Neurol Neurosci Rep*. 2017;17(10):80. doi:10.1007/s11910-017-0782-3.; **2.** Penckofer M. et al., *Front Neurosci*. 2024 May 9;18:1408288 **3.** Chaudhary et al., *J Cereb Blood Flow Metab*. 2019 Mar;39(3):562–4.

Bridging 3T and 7T MR: Towards Unified Metabolic Profiling for Preclinical Brain Tumor Studies

Ana Paula Candiota[1,2], Rui V. Simões[3], Silvia Lope-Piedrafita[1,2*]

[1]Universitat Autònoma de Barcelona, Departament de Bioquímica i Biología Molecular, Spain; [2]CIBER-BBN, Instituto de Salud Carlos III, Madrid, Spain;; [3] Institute for Research & Innovation in Health (i3S), University of Porto, Porto, Portugal. * [Silvia.Lope@uab.cat]

Abstract

INTRODUCTION: High-field 7T MRI provides good sensitivity and spectral resolution for treatment response assessment in preclinical brain tumor models[1,2]. As 3T MRI remains the standard for clinical translation, bridging the two magnetic field strengths requires careful evaluation of data comparability. In this study, we acquired an analyzed 3T and 7T MR spectra from a well-characterized phantom solution, to identify magnetic field-dependent differences and thus the feasibility of integrating data from both systems for metabolic profiling. **METHODS:** Phantoms studies were based on quality control assessment procedures implemented in the e-Tumour project[3]. A one-chamber metabolite solution was prepared, mimicking human brain MR spectra: N-acetyl aspartate, choline, creatine, glutamate, myo-inositol, lactate, and glutamate. Data was acquired at 3T (Bruker Biospec Maxwell 30/17, i3S, Portugal; using either a conventional single channel surface RF coil or a cryoprobe, both for the mouse brain) and 7T (Bruker Biospec 70/30, UAB, Spain; using a conventional single channel mouse brain surface RF coil) with a PRESS sequence: TE/TR 12/2500ms, sweep width 10.05 ppm, 2048 points, 128 averages, and voxel size 2.5-3mm[3]. Magnetic field homogeneity adjustments were performed within the PRESS voxel based on B0 mapping, with water FWHM 4.43 Hz, 1.95 Hz (3T with and without cryoprobe), and 1.96 Hz (at 7T). Data were processed in Topspin, with 1 Hz line broadening and baseline correction, and calibrated for the creatine peak at 3.03 ppm. Processed spectra were exported as text for unit length normalization, signal-to-noise (SNR) estimation, and plotting using a home-built R script. **RESULTS & DISCUSSION:** Conventional single channel RF coil data confirmed the lower signal-to-noise ratio (SNR) at 3T compared to 7T (approximately 46%). However, the cryoprobe enhanced 3T SNR up to 5-fold, remarkably surpassing 7T SNR by 2.4-fold (Figure 1). **CONCLUSIONS:** As expected, compatible RF coil configurations rendered better SNR and spectral resolution at 7T, revealing spectral multiplicity details not resolved at 3T. The latter are consistent with 3T clinical MR spectral profiles and should be taken into account in future pattern recognition studies integrating different magnetic field strengths, as recently reported for human brain tumors at 1.5T and 3T[4]. Importantly, the cryoprobe enhanced MR spectral SNR at 3Tby a factor of five , outperforming 7T sensitivity – a crucial parameter for developing metabolic pattern-based classifiers for automated assessment of treatment response. Unlike spectral fitting approaches for metabolic quantification, aimed at estimating specific concentrations, pattern recognition classifiers focus on regional changes in spectral vectors, less dependent on spectral resolution, as shown in class activation maps analyzed using Grad-Cam[5]. These preliminary results hold promise for future studies bridging 3T and 7T MR spectroscopy.

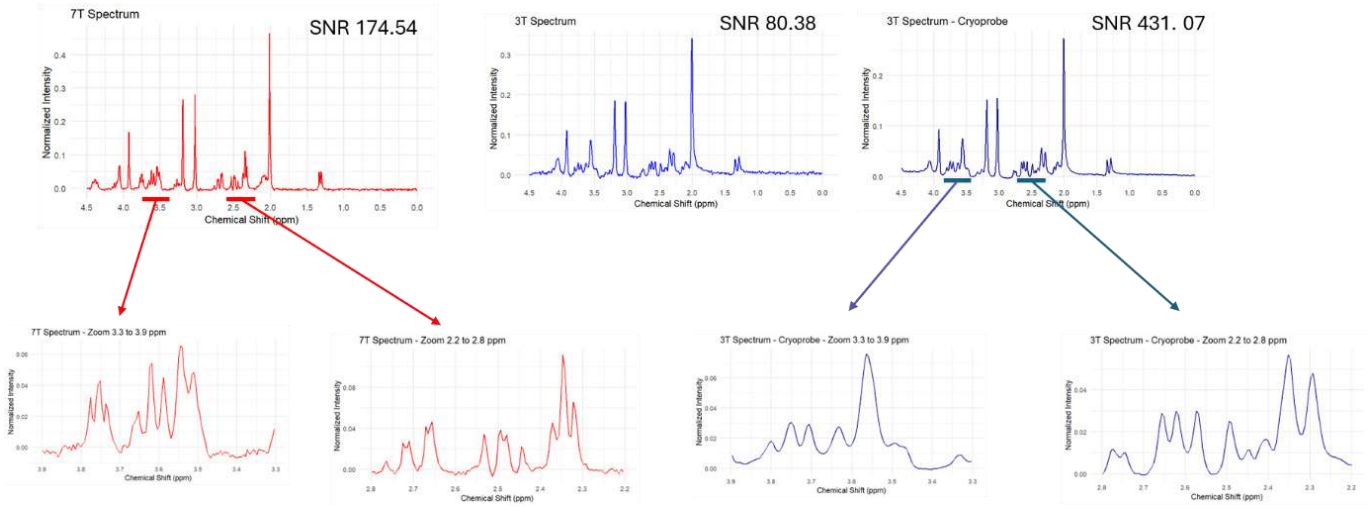

Figure 1 – Top: Unit-length normalized spectra from Phantom 1 acquired at 7T (red), 3T without (light blue) and with cryoprobe (dark blue), with the calculated SNR. Bottom: expansions for better appreciation of myo-Inositol (left) and glutamate (right) zones

References

1. Calero-Pérez P, et al. Cancers (Basel). 2021;13(11):2663; **2.** Wu S, et al. NMR Biomed. 2020;33(4):e4229 **3**. Julià-Sapé M, et al. Database (Oxford). 2012;2012:bas035. **4**. Ungan G, et al. Cancers (Basel). 2023;15(14):3709. **5.**Ortega-Martorell S, et al. Cancers (Basel). 2023;15(15):4002.

Fear conditioning pathways: Psychophysiological interaction analysis of the basolateral amygdala

Alejandro Hinojosa-Moscoso[1,*], Enric Vilajosana[1,2], Miquel Àngel Fullana[1], Carles Soriano-Mas[2], Emma Muñoz-Moreno[1,*]

[1] IDIBAPS, Barcelona, Spain; [2] IDIBELL, L'Hospitalet de Llobregat, Spain; [3] CIBERSAM, Madrid, Spain; [4] University of Barcelona, Barcelona, Spain; * AHINOJOSA@recerca.clinic.cat

INTRODUCTION: Fear is a psychological response to a stimulus that is perceived as a threat. Fear mechanisms have been long studied at a physiological level through the Pavlovian paradigm of fear conditioning, and it has been established that the amygdala is a key region to fear mediating circuits. Among the different nuclei forming the amygdala, the basolateral amygdala (BLA) has been known to be activated during fear learning, memory formation and fear response [1]. MRI-based Psychophysiological interaction (PPI) analysis can be helpful to identify which brain regions have task-dependent connectivity to a seed region of interest in a way to further understand neural pathways associated to a specific task [2]. In this work, we aim to identify the brain regions effectively connected to the BLA during the phases of a fear conditioning task.

METHODS: 188 healthy subjects were recruited and scanned with functional magnetic resonance imaging (fMRI) during a reversal fear conditioning task [3]. Pictures of blue and yellow spheres were used as the conditioned stimulus (CS) and an electric shock as the unconditioned stimulus (US). The fear conditioning task consisted of three phases. During pre-conditioning, the pictures with the CS were presented to the participants without US. During fear conditioning, the US was paired to one of the two spheres, with that sphere becoming CS+, with a 33% reinforcement rate. During fear reversal, the pairing of the US and CS was switched (un-signaled). Conditioning phase CS+ became the "new CS-" and the CS- became the "new CS+" (with US pairing). A PPI analysis with the left and right basolateral amygdalae as separated seed regions was performed for each of the phases of the task as first-level analysis. One-sample and two-samples T-test analyses were performed as a second-level analysis using FSL RANDOMISE with a grey matter mask and threshold-free cluster enhancement correction. Statistical significance was set at $p < 0.05$.

RESULTS & DISCUSSION: One-sample analysis during the fear conditioning phase showed a pattern of effective connectivity between the right BLA and a region comprising the right frontal operculum and insular cortex. In the comparison between pre-conditioning and fear conditioning phases, we found differences in effective connectivity with the right BLA in the right middle frontal gyrus. These results suggest two pathways related to the BLA and modulated by fear conditioning in line with previous knowledge of an increased connectivity of the amygdala with the insula as a response to negative images [4] or an association with regions of the prefrontal cortex related to threat processing and anxiety [5], [6].

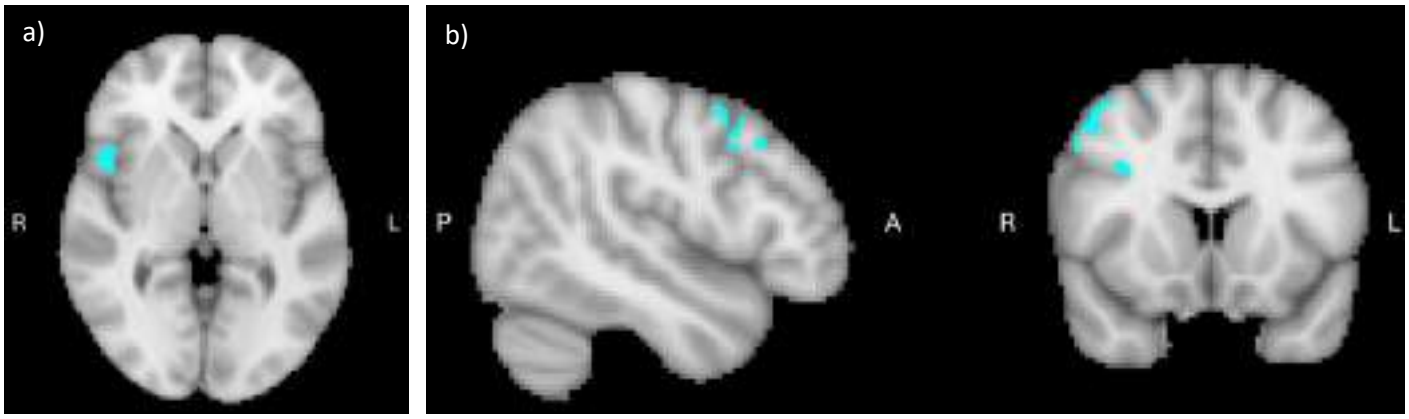

Figure 1 – Second-level analyses of PPI analysis of the BLA: a) One sample analysis of the fear conditioning phase. b) Comparison between pre-conditioning and fear conditioning phases. In blue, voxels with statistical significance thresholded at $p < 0.05$.

References.

[1] P. Sah, *et al*., *F1000Res*, vol. 9, p. F1000 Faculty Rev-53, 2020, doi: 10.12688/F1000RESEARCH.21201.1.
[2] K. J. Friston*, et al*. *Neuroimage*, vol. 6, no. 3, pp. 218–229, Oct. 1997, doi: 10.1006/NIMG.1997.0291.
[3] B. J. Harrison *et al.*, *Hum Brain Mapp*, vol. 36, no. 10, pp. 3950–3958, Oct. 2015, doi: 10.1002/HBM.22889.
[4] B. T. Denny *et al.*, *Soc Cogn Affect Neurosci*, vol. 9, no. 11, p. 1660, Sep. 2013, doi: 10.1093/SCAN/NST160.
[5] W. Z. Liu *et al.*, *Nature Communications 2020 11:1*, vol. 11, no. 1, pp. 1–15, May 2020, doi: 10.1038/s41467-020-15920-7.
[6] M. Alexandra Kredlow, et al. *Neuropsychopharmacology 2021 47:1*, vol. 47, no. 1, pp. 247–259, Sep. 2021, doi: 10.1038/s41386-021-01155-7.

T2 heterogeneity analysis of the infarcted region reveals a new aspect of cerebroprotection by SAHA in stroke

Andrea Díaz-Pérez[1,2,3], Clara Penas[2,3,4], Francesc Jimenez-Altayó[1,2,5]*, Silvia Lope-Piedrafita[6,7]*

[1]Dept. de Farmacologia, de Terapèutica i de Toxicologia, Universitat Autònoma de Barcelona (UAB), Spain; [2]Institute of Neurosciences, UAB, Spain; [3]Dept. de Biologia Cel·lular, de Fisiologia i d'Immunologia, UAB, Spain; [4]CIBER de Enfermedades Neurodegenerativas, Spain; [5]CIBER de Enfermedades Cardiovasculares, Spain; [6]Dept. de Bioquímica i Biología Molecular, UAB, Spain; [7]CIBER de Bioingeniería, Biomateriales y Nanomedicina, Spain. *Francesc.Jimenez@uab.cat & Silvia.Lope@uab.cat

Abstract

INTRODUCTION: Stroke is a major global health problem associated with focal neurologic brain deficits triggered by the interruption of blood supply. It represents the second leading cause of death and the third of adult disability in the world [1]. The potential benefits provided by several pharmacological strategies have been evaluated to reduce brain injury and ameliorate neurological deficits, with brain damage recovery typically assessed through infarct volume measurement using staining or magnetic resonance imaging [2]. In most stroke MRI studies, ADC, CBF, and/or T2 acquisitions are used to assess the response to treatment by comparing mean values of a region of interest (ROI) [3]. However, these quantitative comparisons, based solely on the dimension of the ischaemic region or in a mean value of a ROI, could mask the complex underlying events taking place within the lesion, particularly in the metabolically-active penumbra. In this way, the analysis of the heterogeneity within the infarcted pre-delimited ROI in MRI parametric maps like T2 may offer a novel strategy to assess an indirect measure of a wide range of severities within that injury region. In the present study, a set of adult male spontaneously hypertensive rats (SHR) were subjected to the intraluminal occlusion of the middle cerebral artery (90 min), and an epigenetic drug (suberoylanilide hydroxamic acid; SAHA) was administered 4 h after reperfusion onset. The infarct volume as well as the severity of the injury were evaluated through T2-weighted images and T2 mapping obtained at 24 h and 8 days post-insult. **METHODS:** The right MCA was occluded for 90 min using a nylon suture thickened at the end as described in [4]. MRI acquired at 7T (Bruker Biospec 70/30). High resolution T2w images acquired at two echoes with RARE sequence (TEeff, 36 ms and 136 ms; TR, 6.5 s; 30-1 mm slices; MTX 256x256; FOV, 32x32 mm^2). T2-maps acquired using a multi-slice multi-echo sequence (TE, 10 to 240 ms, TR,4000 ms, MTX, 128 x 128, and FOV,32x32 mm^2). T2 relaxation maps generated on a pixel-by-pixel basis using Paravision 5.1 software. Slices containing lesion components were identified, and ROIs were manually delineated to measure cortical and subcortical lesion areas in both hemispheres on each slice. Infarct volume was adjusted for oedema by dividing the lesion volume by the ratio of ipsilateral to contralateral volume. In T2 maps, pixel counts at different thresholds were computed to evaluate lesion severity. Given that T2 values in the ipsilateral brain regions ranged from 52 ± 5 ms, with a maximum T2 of 65 ms, three threshold ranges were defined to assess lesion severity: T2 < 70 ms (mild), 70 ms ≤ T2 ≤ 90 ms (moderate), and T2 > 90 ms (severe). **RESULTS & DISCUSSION:** In SAHA-treated animals, the cortical infarct showed a higher percentage of volume with T2 values between 70-90 ms, while most of the infarct volume in vehicle-treated animals had T2 values above 90 ms on both days 1 and 8 post-reperfusion (B). In a similar way, in the subcortical infarct of SAHA-treated animals, 1 day after injury, there was a trend (p = 0.08) toward a higher percentage of infarct volume with T2 values between 70-90 ms compared to vehicle-treated animals, though this difference was not observed at 8 days post-surgery. Furthermore, the percentage of infarct volume with T2 values above 90 ms was significantly reduced in the SAHA treated group compared to the vehicle-treated group on both days 1 and 8 post-insult (C). Notably, there was an increase in the percentage of volume with low T2 values in the treated rats on both days 1 and 8 in both cortical and subcortical regions (B, C). This alternative analysis may enhance the performance of therapeutic agents in the treatment of ischaemia-reperfusion injuries.

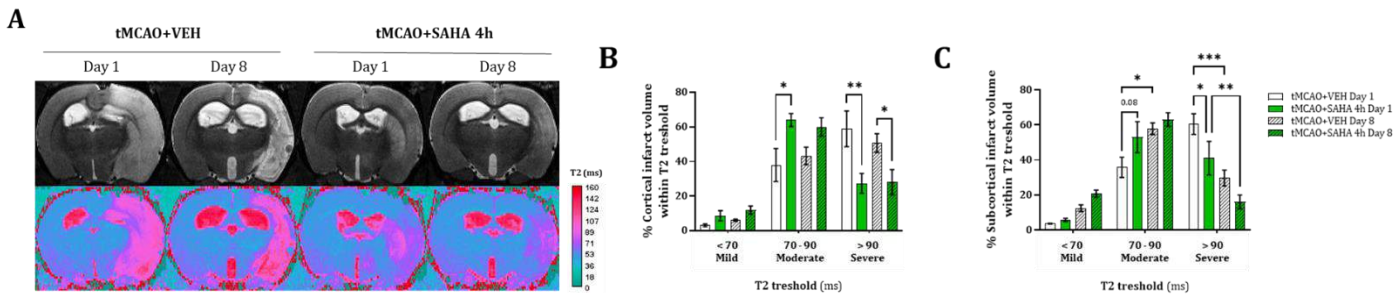

Figure 1 – Modulation damage severity within the infarcted region by SAHA treatment at 4 h of reperfusion, assessed at 1 and 8 days post-tMCAO. (A) Representative T2w images and corresponding T2 maps. Percentage of cortical (B) and subcortical (C) infarcted volume within T2 pre-stablished damage threshold. Results are the mean ± SEM *p<0.05; **p<0.01; ***p<0.001.

References

1. Li, et al. *EClinicalMedicine*. 2024;75:102758; **2.** Weber, et al. *Data Brief*. 2024;53:110188; **3.** Van Velthoven, et al. 2016 *J Neurosci Res*. 95:1225–36; **4.** Díaz-Pérez, et al. *Biomed Pharmacother*. 2024; 172:116287**.**

^{13}C metabolic imaging in chorioallantoic membrane (CAM) assays: methods development and optimisation

Gergo Matajsz[1], Eduard Salinero-Lozano[1], David Gomez-Cabeza[1], Patricia Fernandez Nogueira[2], Gemma Fuster Orellana[3], Paloma Bragado-Domingo[4], Almudena Porras-Gallo[4], Irene Marco-Rius[1]

[1]Institute for Bioengineering of Catalonia; [2]University of Barcelona; [3]University of Vic, [4]Complutense University of Madrid

Abstract

INTRODUCTION: The chorioallantoic membrane (CAM) assay is a versatile biological model for cancer studies. The fast angiogenesis of chicken embryos provides an optimal, borderline in-vivo physiological environment for tumour growth, achieving sizes comparable to 3–6-week-old mouse models within days [1]. Therefore, they provide a low-cost, high-turnover alternative for studies on real-time cancer metabolism via Hyperpolarized Magnetic Resonance Spectroscopic Imaging (HP-MRSI). Nevertheless, preclinical MRI scanners need further optimization for CAM assays as they are designed for rodents.

METHODS: We kept the CAM assays at 36 °C and 50% humidity in a rotating incubator until inoculating with MDA-MB-231 breast cancer cells on embryonic day (ED) 10. We grew the tumours until and performed HP-MRSI experiments on ED 17. We used a Hypersense (Oxford Instruments) polarizer for the dynamic nuclear polarization (DNP) of 1-^{13}C pyruvic acid (PA) substrates. We used a Bruker Biospec 3T MRI with commercial surface and volume coils to acquire spectroscopic data, and a custom-made Python code to process them. We held 25G stainless steel needles close to a bar magnet to inject the tumours directly [2]. We used Autodesk Fusion to generate egg holders and custom receiver coil 3D models. We used an Ender S3 Pro extrusion 3D printer to fabricate the holders from polylactic acid (PLA) filaments.

RESULTS & DISCUSSION: We encountered shimming challenges during HP-MRSI studies following ex-situ 1-^{13}C pyruvic acid (PA) injection in CAM assays. This occurred due to several factors: mispositioning our sample with respect to the MRI's B0 field, tilting of the radiofrequency (RF) surface coil due to twisted coaxial cables and movement of the chicken embryos. We used single pulse ^{1}H sequences with slice selection on unfertilized chicken eggs to recreate and troubleshoot this obstacle; with a custom 3D printed holder design, achieving similar signal-to-noise ratio (SNR) to high intensity volume coil scans (Fig.1. a-i).

To avoid shimming disturbances during future injections, we will use PEEK needles in-situ without removing CAM assays from the homogeneous B1 field. SNR may further be improved by reducing the distance between the receiver loop and our sample and increasing the filling factor arising from their different size. Hence, we propose an adjustable surface coil design descending into the CAM's window (Fig. 1. j-k). In this study we troubleshooted issues arising from using CAM assays during MRI experiments with instrumentation designed for rodents. Using 1H spectroscopy we highlighted several challenges with their implementation, i.e., consistent positioning and low SNR. We will investigate the proposed solutions during 13C metabolic imaging experiments to characterize and present the potential of CAM assays for HP-MRSI at the 2025 edition of the ISMRM Iberian Chapter.

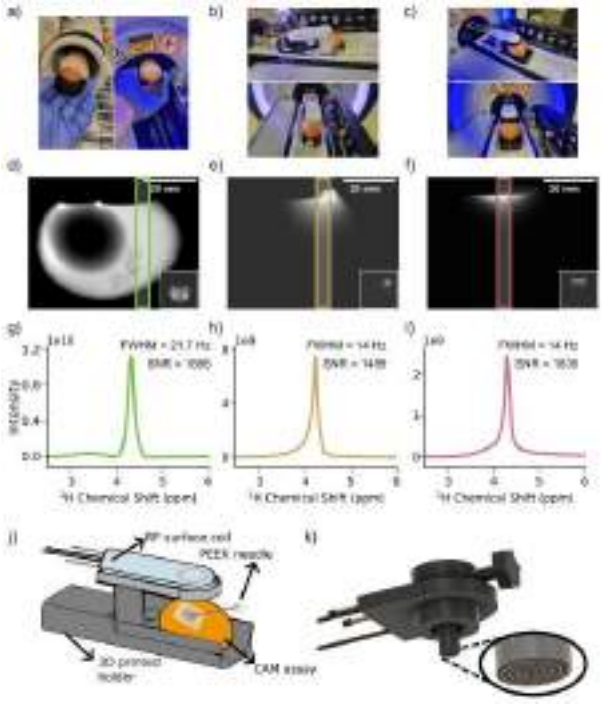

Figure 1 – *Single slice ^{1}H measurements with commercial volume and surface coils and proposed solutions for an optimised setup during HP-MRSI experiments with CAM assays. Experimental setup for volume coil measurements (a), surface coil measurements with handmade supports (b) and surface coil measurements with 3D printed coil holder (c). d-f) T2-weighted images highlighting the single slice selection for spectroscopic data collection in the order of a-c). Single pulse slice selection ^{1}H spectra for the volume coil (g), handmade setup (h) and 3D printed surface coil holder measurements (i). (j) 3D printed surface coil holder indicating the positioning of the components of the setup. (k) 3D model of the proposed adjustable-height surface coil for improving SNR via increased filling factor for CAM assays.*

References

1. Fischer, D., Fluegen, G., et. al. Cancers, 15(1), p.191

Advanced Diffusion MRI in the Mouse Brain in vivo at 3 Tesla

Joana P. Faria [1], Raquel Vale-Silva [1], Andrada Ianus [2], Rafael N. Henriques 3, João B Relvas [1],

& Rui V. Simões [1]*

[1] Neurobiology and Neurologic Disorders Program, Institute for Research and Innovation in Health (i3S), Porto, Portugal

[2] School of Biomedical Engineering & Imaging Sciences, King's College, London, UK

[3] Champalimaud Research, Champalimaud Center for the Unknown, Lisbon, Portugal.; ***rvsimoes@i3s.up.pt**

Abstract

INTRODUCTION: Mouse brain MRI typically relies on high magnetic field strengths for enhanced sensitivity, which often limits the translation of preclinical neuroimaging to clinical scanners. We recently described a novel 3T MRI configuration for mouse neuroimaging, demonstrating ex vivo high-quality microstructural images [1] and the ability to detect white matter lesions [2]. Here, we demonstrate its sensitivity and reproducibility for advanced mouse neuroimaging in vivo.

METHODS: Animal experiments were preapproved by institutional and national authorities, and carried out according to EU Directive 2010/63. Female C57BL6j mice (n=3, P90) underwent longitudinal MRI on a 3 Tesla Bruker BioSpec Maxwell scanner, equipped with high power gradients (900 mT/m) and a cryogenic RF coil. Mice were kept under isoflurane anesthesia and warmed during diffusion MRI, which was acquired with single-shot DTI-EPI: TR/TE, 2500/35 ms; 30 b0 values; 8 b-values (250-8000 s/mm^2); 24 directions; 118 µm in-plane resolution; 0.6 mm slice thickness; 18.5 min. Data were TPCA denoised [3] and analyzed for pixel-wise DKI fitting [4], SANDI modeling [5], and SNR assessment.

RESULTS & DISCUSSION: SNR maps indicate higher sensitivity in the upper brain region, due to the surface design of the cryogenic RF coil; and a consistent 10-fold SNR increase after TPCA denoising. DTI parameters were extracted from DKI fitting in the denoised data [4]; whereas SANDI fitting estimated spheres (intra-soma), sticks (intra-neurite), and water pools (extra-cellular) fractions, and cell sizes (radius) – Fig 1. DTI and SANDI maps were very reproducible across the 3 animals; and the SANDI maps were consistent with the literature [5], e.g. cell radius (8-9 µm).

CONCLUSION: Advanced diffusion MRI of the mouse brain is feasible in vivo at 3 Tesla, delivering high-quality and reproducible microstructural images at clinical field strength. This setup is ideally suited for translational mouse neuroimaging. Undergoing studies include: further improving the denoising pipeline; reproducing *in vivo* our initial *ex vivo* results [2], demonstrating reliable longitudinal MRI quantification of age- and treatment-dependent changes associated with de/re-myelination; and characterizing the brain tumor microenvironment and its progression.

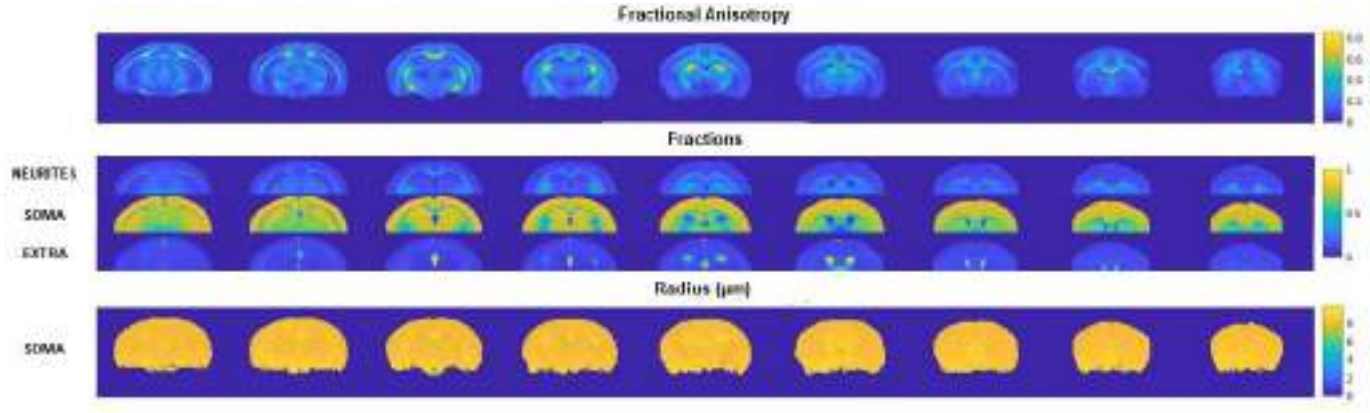

Figure 1 – Diffusion Maps (DTI and SANDI). DKI and SANDI fitting rendered good quality maps, as illustrated for Fractional Anisotropy, and compartment model estimates for cell fraction maps (soma, neurite, and extra-cellular) and cell sizes (soma radius), respectively.

References

1. Vale-Silva, R., et al. Harnessing 3 Tesla MRI for advanced microstructural imaging of the mouse brain. Proc. ESMRMB; 2024: 308. Barcelona, Spain. **2.** Vale-Silva, R., et al. MRI Characterization of Cuprizone-Induced Demyelination/Remyelination Proc. Iberian ISMRM; 2024: P22. Porto, Portugal. **3.** Henriques, R.N., et al., Efficient PCA denoising of spatially correlated redundant MRI data. Imaging Neuroscience, 2023. 1: p. 1-26. **4.** Henriques, R.N., et al., Diffusional Kurtosis Imaging in the Diffusion Imaging in Python Project. Front Hum Neurosci, 2021. 15: p. 675433. **5.** Ianus, A., et al., Soma and Neurite Density MRI (SANDI) of the in-vivo mouse brain and comparison with the Allen Brain Atlas. Neuroimage, 2022. 254: p. 119135.

micro-MRI as a tool to determine neurodevelopmental changes derived from Afadin protein perturbation

M. Carmen Martínez-Bisbal[1,2,3,4*], David de Agustín-Durán[5], Isabel Mateos-White[5], Jaime Fabra-Beser[5], Alba Marín[5], Carmen María Mateos-Martínez[5], Laura Veintimilla Escot[5], Cristina Gil-Sanz[5**]

[1] Instituto Interuniversitario de Investigación de Reconocimiento Molecular y Desarrollo Tecnológico (IDM), Universitat Politècnica de València - Universitat de València, Valencia, Spain; [2] Departamento de Química Física, Universitat de València, Valencia, Spain; [3] Unidad Mixta de Investigación en Nanomedicina y Sensores, Instituto de Investigación Sanitaria La Fe (IISLAFE), Universitat Politècnica de València, Valencia, Spain; [4] CIBER de Bioingeniería, Biomateriales y Nanomedicina, Instituto de Salud Carlos III, Spain; [5] Instituto de Biotecnología y Biomedicina (BIOTECMED), Departamento de Biología Celular, Universitat de València, Burjassot, Valencia, Spain; * carmen.martinez-bisbal@uv.es ** cristina.gil@uv.es

Abstract

INTRODUCTION: Afadin is a multimodal scaffolding protein with essential functions in cell-cell adhesion (1). It is part of adhesion complexes in epithelial cells, linking the activity of two types of cell-cell adhesion molecules, Nectins and Cadherins, which participate in the establishment of adherens junctions (2). Afadin has been described as playing important roles in cerebral cortex development, where its embryonic inactivation causes over-proliferation of neural stem cells and severe malformations, including cortical hyperplasia and the formation of subcortical band heterotopia or “double cortex” (3). However, a detailed characterization of the structural brain malformations in the conditional Afadin mutant mouse for the cerebral cortex is still lacking. In this study, we propose the use of MRI techniques to perform extensive anatomical measurements of these mutant mice.

METHODS: MRI was used to study the anatomy of mice brains from control and Afadin conditional mice (3). Adult mice were euthanized using pentobarbital and transcardially perfused with 4% of PFA. Heads were preserved in PBS at 4 C until the date of analysis. The heads underwent micro-MRI study in a 9.7 T spectrometer (Bruker Avance III 400 WB), a 400 MHz magnet with wide bore, equipped with a microimaging probe MIC WB40 for mouse applications (NMR section on Servei Central de Suport a la Investigació Experimental, SCSIE, Universitat de València, U26 NMR: Biomedical Applications II platform from Nanbiosis, Research Infrastructures & Services of CIBER-BBN). Each mouse head was placed at the bottom of a 2.5 cm diameter glass tube and inserted into the sample probe receptacle. The probe with the sample was inserted into the magnet and the necessary connections were made. After initial adjustments, low-resolution T1-weighted localization sequences were acquired in all three planes. Next, T2-weighted Turbo RARE 2D and 3D sequences were acquired. Temperature was kept at 15 C during the micro-MRI experiments.

RESULTS & DISCUSSION: MRI analysis of Afadin conditional brains revealed the previously described anatomical alterations observed with standard histology, including brain enlargement and ectopic white matter characteristic of subcortical band heterotopia, with high resolution. This approach enabled rapid and precise measurements across different brain axes and planes. Moreover, this non-invasive analysis allowed us to study ventricular alterations without potential sectioning artifacts. These alterations included changes in the ventricular surface, which appeared rough and uneven, along with an increase in ventricular size in the mutants. Finally, this technique allowed us to identify and describe significant alterations in axonal tracts, including corpus callosum agenesis and the near absence of the anterior commissure. Importantly, MRI provides a powerful tool for in vivo imaging, enabling the study of brain morphology in a two and three-dimensional context while preserving tissue integrity.

References

1. Rätze et al., J Pathol 2025, online ahead of print doi: 10.1002/path.6394; **2**. Takahashi et al., J Cell Biol (1999) 145:539 –549; **3.** Gil-Sanz et al., Journal of Neuroscience (2014) 34(32):10475–10487

New metal-free MRI contrast agents based on organic radical dendrimers.

Yufei Wu,[1] Rubén García-Costas,[1] Ehsan Shirdel,[1] Xuejiao Wang,[1] Chuanting Zhou, [1] Vega Lloveras,[1,2,*] José Vidal-Gancedo.[1,2,*]

[1]Institut de Ciència de Materials de Barcelona, ICMAB-CSIC, Campus UAB, 08193 Bellaterra, Spain.
[2] CIBER de Bioingeniería, Biomateriales y Nanomedicina, Instituto de Salud Carlos III, 08913 Bellaterra, Spain.
*j.vidal@icmab.es; vega@icmab.es

Magnetic resonance imaging (MRI) is a non-radiative and non-invasive imaging technique widely utilized for early diagnosis and monitoring of tumors and other pathologies. The most commonly used contrast agents (CAs) in MRI are Gd(III)-based chelates. However, alternatives to these metal-based CAs are needed due to their known toxicity.

Organic radicals present a promising alternative since they possess paramagnetic properties, allowing them to function as T_1 CAs similar to Gd-based CAs, while being organic and thus reducing concerns about toxic metal accumulation. Although isolated organic radicals generally have limited contrast-generating capabilities and are prone to rapid bioreduction, anchoring numerous organic radicals onto the surface of a dendrimer scaffold (creating radical dendrimers) can enhance contrast capacity and protect the radicals from bioreduction.

High water solubility, high ^{1}H water relaxivities, low toxicity and long *in vivo* lifetimes are essential requirements for this purpose. We have synthesized and characterized several families of water-soluble radical dendrimers that exhibit substantial contrast enhancement both *in vitro* and *in vivo* while maintaining low toxicity.[1-8].

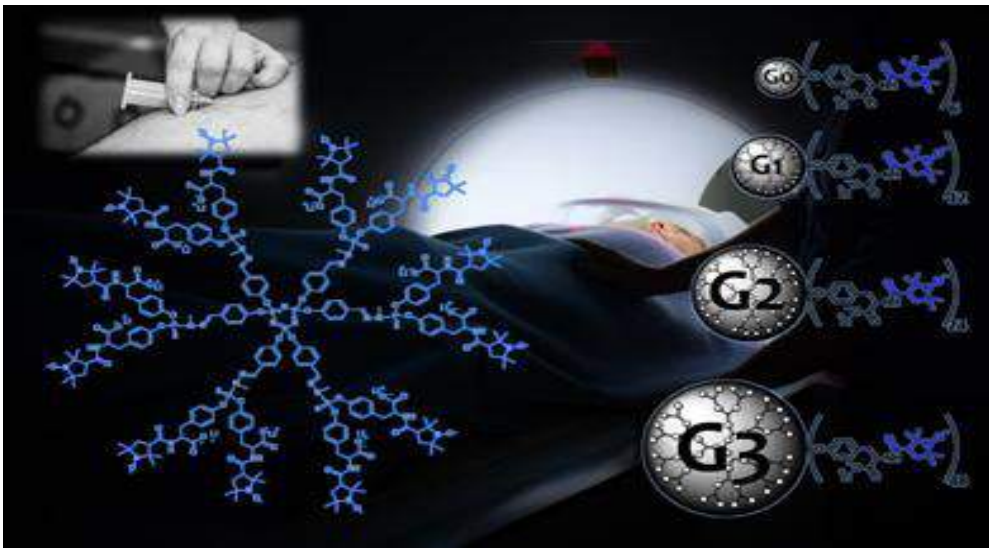

References:

1. L. Pinto, V. Lloveras, S. Zhang, F. Liko, J. Veciana, J.L. Muñoz-Gómez, J. Vidal-Gancedo. ACS *Appl. Bio Mater.* **2020**, *3*, 369.
2. S. Zhang, V. Lloveras, S. Lope, P. Calero, S. Wu, A. P. Candiota, J. Vidal-Gancedo. *Biomacromolecules* **2022**, *23*, 2767−2777.
3. S. Zhang, V. Lloveras, Y. Wu, J. Tolosa, J. C. García-Martínez, J. Vidal-Gancedo. *Pharmaceutics* **2023**, *15*, 1776.
4. Ch. Tian, S. Zhang, V. Lloveras, J. Vidal-Gancedo. *Adv. Ind. Eng. Polym. Res.* **2024**, *7*, 255-261.
5. Y. Wu, V. Lloveras, A. Morgado, E. Perez-Inestrosa, E. Babaliari, S. Psilodimitrakopoulos, Y. Vida, J. Vidal-Gancedo. *ACS Appl. Mater. Interfaces* **2024**,*16* (47), 65295-65306.
6. Y. Wu, V. Lloveras, S. Lope-Piedrafita, M. Mulero-Acevedo, A. P. Candiota, J. Vidal-Gancedo. *Acta Biomaterialia* **2025**,*192*, 461-472.
7. Y. Wu, V. Lloveras, S. Zhang, J. Tolosa, J. C García-Martínez, J. Vidal-Gancedo. *Dyes Pigm.* **2025**, *232*, 11248.
8. S. Zhang, V. Lloveras, Y. Wu, J. Vidal-Gancedo. *Eur. Polym. J.* **2025**, *235*, 113691.

2D Glioblastoma Segmentation in Rat and Mouse Models Using U-Net Architecture

Sara Ortega-Espina, Sabela Fernández-Rodicio, Ana Sampedro-Viana, Marcos Bazarra-Barreiros, María Teresa Abengoza-Bello, Pablo Hervella, Ramón Iglesias-Rey*

Neuroimaging and Biotechnology Laboratory (NOBEL), Clinical Neurosciences Research Laboratory (LINC), Health Research Institute of Santiago de Compostela (IDIS), Santiago de Compostela, Spain.

Ramon.Iglesias.Rey@sergas.es

Abstract

INTRODUCTION: Rodents are essential in preclinical brain disease research, including stroke, tumors, and degenerative disorders. Magnetic resonance imaging (MRI) plays a vital role in visualizing brain tissue at various timepoints, but accurate analysis requires segmentation [1-3]. We present a multi-task 2D U-Net, a convolutional neural network designed for the automated identification, segmentation, and quantification of brain regions or brain tumors in rodents using T_2-weighted imaging (T_2-wi).

METHODS: Our convolutional neural network models enable automatic segmentation and volume or T_2-relaxivity quantification across three MRI datasets: (i) multiple brain regions (striatum, neocortex, hippocampus, whole brain) in healthy rats using T_2-wi; and (ii) glioblastoma tumor segmentation using T_2-wi. We evaluated quantification accuracy by comparing our results against the ground truth obtained from traditional semi-automatic methods using Dice coefficient, Hausdorff distance, Sensitivity, and Volume ratio. Additionally, we compared our models with existing methods to validate their accuracy, robustness, and potential for preclinical and translational research applications

RESULTS & DISCUSSION: In total, 111 animals were studied, resulting in 1,949 images, which were expanded to 5,847 images after data augmentation. Our results are either comparable to or outperform those in the literature, demonstrating the strength of our segmentation framework. A detailed representation of the Spearman correlation between automated and semi-automated mask volumes across cohorts demonstrated a consistently high correlation (ρ= 0.99-0.82).
Our framework exhibits enhanced robustness and broader applicability across different brain regions, pathological conditions, and MRI acquisition settings. These tools will be valuable in overcoming issues related to inaccuracies, inter- and intra-rater variability, and time consumption when analyzing rodent brain MRI data.

References:

1. Barroso J., Branco P., Apkarian, A.V. Brain mechanisms of chronic pain: critical role of translational approach. Transl Res. 2021 Dec:238:76-89.
2. Carbone, L. Estimating mouse and rat use in american laboratories by extrapolation from animal welfare act-regulated species. Sci Rep. 2021 Jan 12;11(1):493.
3. Stringer, M.S., Lee H., Huuskonen M.T., et al. A review of translational magnetic resonance imaging in human and rodent experimental models of small vessel disease. Transl Stroke Res. 2021 Feb;12(1):15-30.

Diffusion MRI Simulation Takes Advantage of Higher Order Models than DTI

Justino R. Rodríguez-Galván[1]*, Pablo Villacorta-Aylagas[1], Susana Merino-Caviedes[1], Carlos Castillo-Passi[2], Pablo Irarrazaval[2], Antonio Tristán-Vega[1], Carlos Alberola-López[1]

[1]Laboratorio de Procesado de Imagen (LPI), Universidad de Valladolid, Valladolid (Spain)

[2]Pontificia Universidad Católica de Chile, Santiago (Chile); *jrodgal@lpi.tel.uva.es

Abstract

INTRODUCTION: Diffusion is a random phenomenon thermodynamically driven. Within this procedure, spins exchange positions leading to an overall signal loss. Without restrictions, free diffusion can be modeled as a 3D random walk, for whose case, a trivariate Gaussian probability density function suffices the mathematical characterization. This model is called diffusion tensor imaging (DTI) [1]. However, inside biological organs, diffusion is prone to be restricted, and consequently, DTI is not enough to fully describe this procedure. Higher order (HO) models than DTI, such as MAPL [2] or MiSFIT [3] have arisen to fill this gap.

Moreover, there is a plethora of scenarios, from radiologists' training to research, in which simulation of diffusion can be a differentiating factor. Focusing on research matters, simulation's accuracy is a key point to rely in whichever development built upon synthetic data. In this work, diffusion simulation will be assessed in terms of the model used to recreate the phenomenon, as well as the number of spins used in the simulation.

METHODS: Departing from three slices of a dense myocardial dMRI acquisition, composed by 192 DWIs equally distributed among six shells, with b-values in {300, 600, 900, 1200, 2000, 3600} s/mm^2 and a baseline acquisition. Each of those slices presents signs of ischemia.

All diffusion models presented beforehand were computed over these three slices, along with relaxometry maps namely, T1, T2 and PD. Spins' motion following each model distribution was computed throughout rejection method [4]. All relaxometry maps in combination with the computed motion was fed into Koma MRI simulator [5]. Simulated data, acquired with a simulation of the same sequence as in reality, was put against original data and pixelwise MSE and pixelwise correlation was computed using all three slices.

RESULTS & DISCUSSION: Results can be found in the figure, (a) subfigure depicts the overall pixelwise MSE for each model with a given number of spins, (b) subfigure shows the overall pixelwise correlation. As can be seen, each of these models got an improvement with the increase of spins for the simulation. Though differences in MSE are smaller, progression suggests that HO models get bigger improvements while DTI seems to be more stagnant. Correlation results suggest that HO models need more simulated spins to reflect their potential.

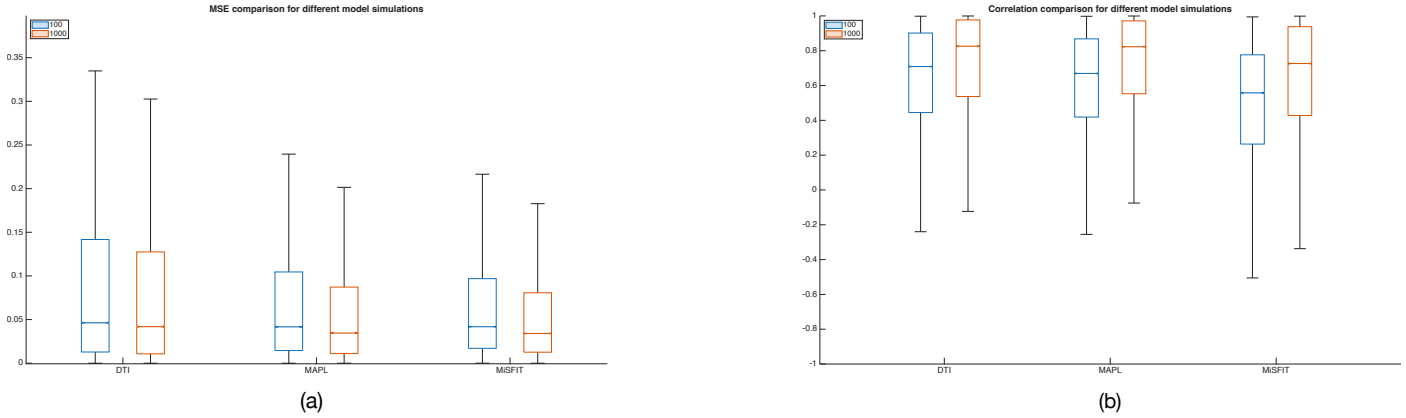

Figure 1 – Pixelwise MSE and pixelwise correlation metrics for a compound of three simulated slices of dMRI. (a) subfigure depicts the boxplots of MSE, grouped in the X axis by model. Blue boxplots depict the 100 spins results and orange boxplots depict de 1000 spins results. (b) subfigure depicts pixelwise correlation results for each model. X axis groups the results by model. 100 spins results are shown in blue while 1000 spins are shown in orange.

References

1. . J. Basser and C. Pierpaoli, "Microstructural and physiological features of tissues elucidated by quantitative-diffusion tensor MRI," Journal of magnetic resonance, vol. 213, no. 2, pp. 560–570, 2011.**2.** Fick, R. H., Wassermann, D., Caruyer, E., & Deriche, R. (2016). MAPL: Tissue microstructure estimation using Laplacian-regularized MAP-MRI and its application to HCP data. *NeuroImage*, *134*, 365-385. **3.** Tristán-Vega, A., & Aja-Fernández, S. (2021). Efficient and accurate EAP imaging from multi-shell dMRI with micro-structure adaptive convolution kernels and dual Fourier Integral Transforms (MiSFIT). *NeuroImage*, *227*, 117616. **4.** . Devroye, "Sample-based non-uniform random variate generation," in Proceedings of the 18th conference on Winter simulation, pp. 260–265, 1986. **5.** Castillo-Passi, C., Coronado, R., Varela-Mattatall, G., Alberola-López, C., Botnar, R., & Irarrazaval, P. (2023). KomaMRI. Jl: an open-source framework for general MRI simulations with GPU acceleration. *Magnetic Resonance in Medicine*, *90*(1), 329-342.

Acknowledgements: This work was supported in part by the spanish Agencia Estatal de Investigación, under Grants PID2020-15339RB-I00 TED2021-130090B-I00 and CPP2021-008880, and by ESAOTE Ltd (18IQBM).

Next edition

6th Iberian Chapter ISMRM Meeting

2nd and 3rd of July 2026

University of Coimbra

Sponsors

Institutional:

IBEC
Institute for Bioengineering of Catalonia

Platinum sponsors:

MR SOLUTIONS

Gold sponsors:

paralabbio Mediso

NVISION SIEMENS Healthineers

Silver sponsors:

BRUKER

Bronze sponsors:

neosooo biotecoooo Bionic

DEEPSPIN RSEQ Real Sociedad Española de Química